AMMONIA-BORANE BASED HYDROGEN STORAGE MATERIALS – A COMPUTATIONAL STUDY

VU VIET CUONG

NATIONAL UNIVERSITY OF SINGAPORE

2012

AMMONIA-BORANE BASED HYDROGEN STORAGE MATERIALS – A COMPUTATIONAL STUDY

VU VIET CUONG

(B. SCI. (HONS.))

National University of Hanoi

A THESIS SUBMITTED

FOR THE DEGREE OF DOCTOR OF PHILOSOPHY

IN CHEMISTRY

DEPARTMENT OF CHEMISTRY

NATIONAL UNIVERSITY OF SINGAPORE

2012

DECLARATION

The work in this thesis is the original work of **Vu Viet Cuong**, performed independently under the supervision of Professor Wong Ming Wah, Richard, (in the laboratory S5-02-18), Chemistry Department, National University of Singapore, between Aug 04th 2008 and Aug 05th 2012.

VU VIET CUONG Aug 05th 2012

ACKNOWLEDGEMENT

This dissertation would not have been possible without the guidance and the steady support of the kind people around me, who in one way or another have contributed and extended their valuable assistance in the preparation and completion of this study.

First and foremost, I would like to express my utmost gratitude to my supervisor, Professor Wong Ming Wah, Richard for his continuous support towards my Ph.D. study and research, for his patience, motivation, enthusiasm and immense knowledge. Prof. Wong has been my beacon of inspiration and motivation as I tackled through and overcame all the obstacles during the entire course of my research work. I could not have wished for a better advisor and mentor for my Ph.D. study.

I also wish to thank Professor Đặng Ứng Vận and Professor Lê Kim Long from the Hanoi University of Science, who gave me the initial opportunity to pursue computational quantum chemistry. Their guidance, enthusiasm, support and trust kept me going as they constantly encouraged me during my long leave of study.

In the course of my daily work, I have been blessed to have by my side many friendly and cheerful lab and school mates. I owe sincere and earnest thanks to Yang Hui, my senior who sat next to me in the lab. Ever since I first joined the group, I have learnt so much from him, from his vast experience and the professional way he did his research. I will also never forget Cao Ye, another lab mate of mine. She is one of the kindest and sweetest friends in Singapore I have met. She has impressed me with her willingness to learn and her ever determined thirst for new knowledge. I

benefited much from her advice and help (both in the scientific and technical aspects) when I was having difficulties. Particularly, I would also like to give special thanks to my very close and best Singaporean friend, Yeo Keng Leng, Trevor, who has devoted much of his precious time to read and rephrase my thesis. His revisions have significantly improved my thesis. I also want to thank Xie Huifang, Cho Bokun, Chen Serene, Yu Zongrong Wesley, Kok Sos Fuf, Xi Yu and Zhou Yujing for their deep and sincere friendship. We have shared many unforgettable moments together during our research, now we are like family members.

I would similarly like to acknowledge all the financial, academic and technical support from the National University of Singapore (NUS) as well as from the Department of Chemistry. NUS provided the necessary financial support for my four-year study in Singapore. The Department of Chemistry supplied me with the support and equipment I needed to successfully produce and complete my thesis.

Last but not least, I would like to thank my family: my father Vũ Trường Sơn and my mother Vũ Thị Thuý Hà, for giving birth to me in the first place and for relentlessly supporting me in their minds, hearts, and spirits.

Finally, I want to thank everyone who was important in one way or another to the successful realisation of this thesis and express my sincere apologies for not being able to mention each and every one of you here in this acknowledgement.

Cuong Vu Viet

Singapore, August 05th, 2012

TABLE OF CONTENTS

SUMMARY

Chapter 1 briefly presents some of the consequences stemming from the overutilisation of natural sources of energy such as fossil fuels. This, in turn, has stimulated the world to investigate intensely upon H_2 as one of the promising alternative, renewable, sustainable, and greener energy sources. Succinct literature review on physical and chemical hydrogen storage methods is introduced. The strengths and weaknesses of each method are highlighted. The purpose of my research is shown in this chapter.

Chapter 2 comprises the literature review, which includes a short history about the discovery and applications of hydrogen in conjunction with other relevant events. The physical and chemical properties of hydrogen are also given. The physical and chemical storage methods for storing hydrogen are discussed. Advantages and disadvantages associated with these methods are then analysed to elucidate why some particular chemical storage methods are more preferred than the physical methods. Finally, there is a comprehensive discussion about various hydrogen storage materials, which have been synthesised and examined thus far. The limitations of each material are also carefully analysed. Again, the purpose of my research is restated at the end of this chapter.

Chapter 3 gives an overview of the theoretical methods and models that were employed during the study of the various systems in this thesis. Formulations and descriptions of *ab initio* theory, density functional theory (DFT) and solvation models are discussed in this chapter.

Chapter 4 presents the mechanistic study on the dehydrogenation mechanism of lithium amidoborane ($LiNH_2BH_3$) in the gas phase and in the THF solvent. The key role of lithium metal in facilitating hydrogen release is explored and carefully analysed. Effect of the THF solvent on the kinetics of the dehydrogenation is also investigated.

Chapter 5 presents the study of a novel compound $Mg(NH_2BH_3)_2.NH_3$. This compound has gained much attention due to its high hydrogen content, up to 14.5 wt%, as well as its low temperature of dehydrogenation – first H_2 evolving at 50^oC – in contrast to the high temperature of decomposition of ammonia-borane. The study in this chapter will shed light on the role of the magnesium atom and the NH_3 group in the $Mg(NH_2BH_3)_2.NH_3$ compound.

Chapter 6 concentrates on the dehydrogenation of an intriguing compound known as $LiBH_4.MgCl_2.NH_3$, which includes two metals we have seen in two previous chapters. We then discuss in detail about how they actually support each other during dehydrogenation process

Chapter 7 presents the mechanistic study on the dehydrogenation of the newly explored composites poly(methyl acrylate)-confined ammonia-borane, PAB20 and PAB80. These composites were reported to present a significantly lower onset dehydrogenation temperature as compared to neat ammonia-borane. Additionally, they were reported to possess water-resistant properties and to be effective in suppressing harmful impurities such as diborane and borazine. Similar to previous

chapters, this chapter also investigates the possible dehydrogenation mechanisms of these composites. On a deeper level, the critical role played by the carbonyl functional group of these composites in the facilitation of H_2 elimination is elucidated. Their capability of suppressing detrimental impurities is also explained.

Chapter 8 examines the H_2 elimination of the system polymer-confined AB with varied polymers and predicts in advance the outcome with hopes for improving the dehydrogenation properties of the novel compound discussed in chapter 7.

Chapter 9 gives a final conclusion of the systems studied in this thesis and suggests possible avenues for future research in this area.

List of Tables

List of Figures

CHAPTER 1

INTRODUCTION

Our magnificent star, the Sun, it holds our entire solar system together; bestowing life-giving light, heat, and energy onto the Earth we call Home. During the advent of mankind, it was thought to be the only sole source of natural energy. Soon after, we realised another gift of energy from Mother Nature, the Wind and used it as another earliest source of energy for transportation and travelling [1] to explore new places. These natural sources were deemed to be infinite and were the chosen sources of energy for man until the onset of the industrial revolution. The main drawbacks pertaining to the usage of these natural sources include the intermittency of the energy production, and the difficulty in the energy storage and delivery. Solar and wind energy cannot be efficiently stored and delivered, their availability also greatly depends on the weather conditions at that moment in time. This led to the global desire of discovering more sustainable, viable sources of energy to exploit, deliver, and utilise. After which began the industrial revolution, where the mining and engineering of fossil fuels opened up a whole new page in history for mankind's energy needs.

Natural processes such as the anaerobic decomposition of dead buried organisms form fossil fuels, which include coal, petroleum and natural gases. Coal was initially used as a source of energy for mechanical power production as early as in the 1780s. It was later on in the 19th century that the internal combustion engine

was developed. Liquid petroleum was then exploited – first in North America and then across the world – and was refined to provide fuel for both petrol and diesel engines. During the middle of the 20th century, natural gas fields were discovered in abundance and became widely used ever since [2].

Fossil fuels have been of immense importance to mankind and the perfect candidate for an energy source for many industrial countries throughout the decades; they can produce a considerable amount of energy per unit weight. Furthermore, in contrast to natural energy sources, they can be easily stored and delivered. However, there are some inherent problems linked with fossil fuels that we cannot overcome. Firstly, fossil fuels take millions of years to form; they are thus non-renewable and unsustainable. To make matters worse, the current exploitation, which results from the ever increasing demand from our expanding global economy and population, has largely exceeded the reformation ability of the fossil fuels [3,4]. **Figure 1.1** shows the robust growth of energy demand of the world projected to the year 2035 [5].

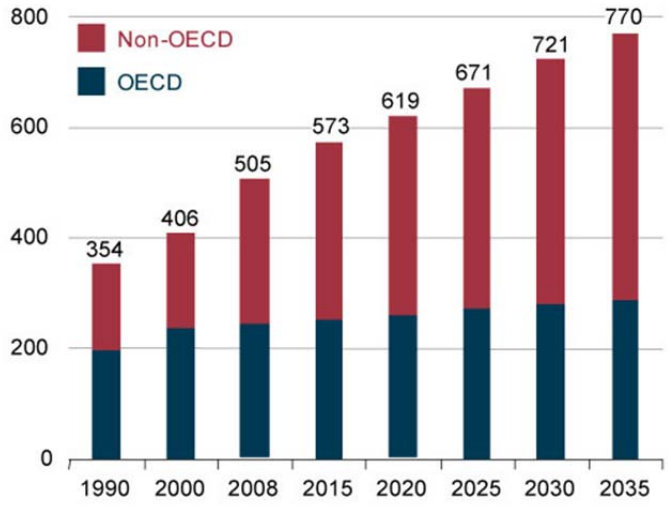

Figure 1.1 World energy consumption for years 1990-2035 (quadrillion Btu).

An average growth rate of 1.3% annually in conjunction with the increase in world population and industrialisation gives rise to an alarming amount of energy that will be consumed [5]. Consequently, the fossil fuel reserves will be depleted at an accelerated rate, posing a looming threat of global energy deficiency in the near future as we have predicted and feared. Secondly, the production and utilisation of fossil fuels have resulted in many environmental problems. The burning of fossil fuels contributes greatly to the overall carbon dioxide emitted into the atmosphere, as illustrated in **Figure 1.2** [6]. It produces around 21.3 billion tonnes of carbon dioxide (CO_2) per year; thankfully certain processes in nature absorb half of that amount. Thus, there is a net amount of 10.65 billion tonnes of atmospheric CO_2 introduced per year [7].

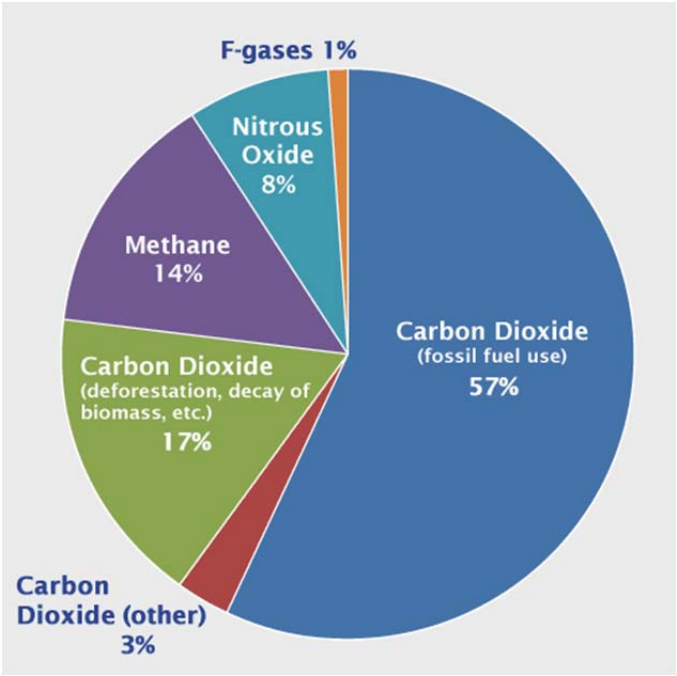

Figure 1.2 Global greenhouse gas emissions by gas

On a more serious note, global carbon emissions from fossil fuels have continued to increase rapidly since 1900, which is indicated in **Figure 1.3** [8]. Emission rate skyrocketed by over 16 times between 1900 and 2008 and continued to soar by about 1.5 times between 1990 and 2008.

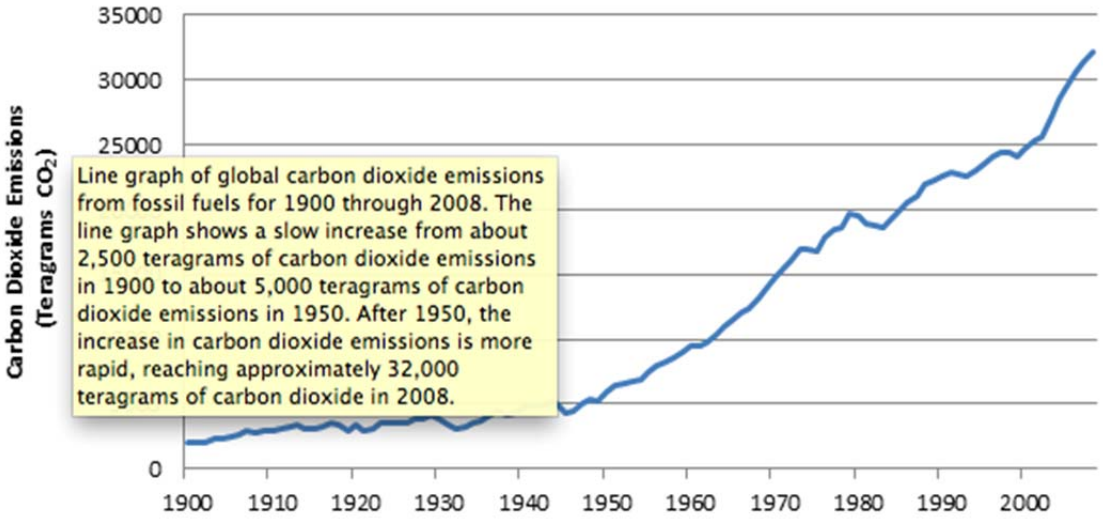

Figure 1.3 Global Carbon Dioxide (CO_2) emissions from fossil fuels 1900-2008.

CO_2 is known to be the main culprit that causes the greenhouse effect and contributes to global warming [9], triggering many other adverse effects such as higher temperature worldwide, increased tropical cyclone activities, glacier retreats and disappearances, rising global sea levels, as well as the increased incidences for natural disasters all over the globe.

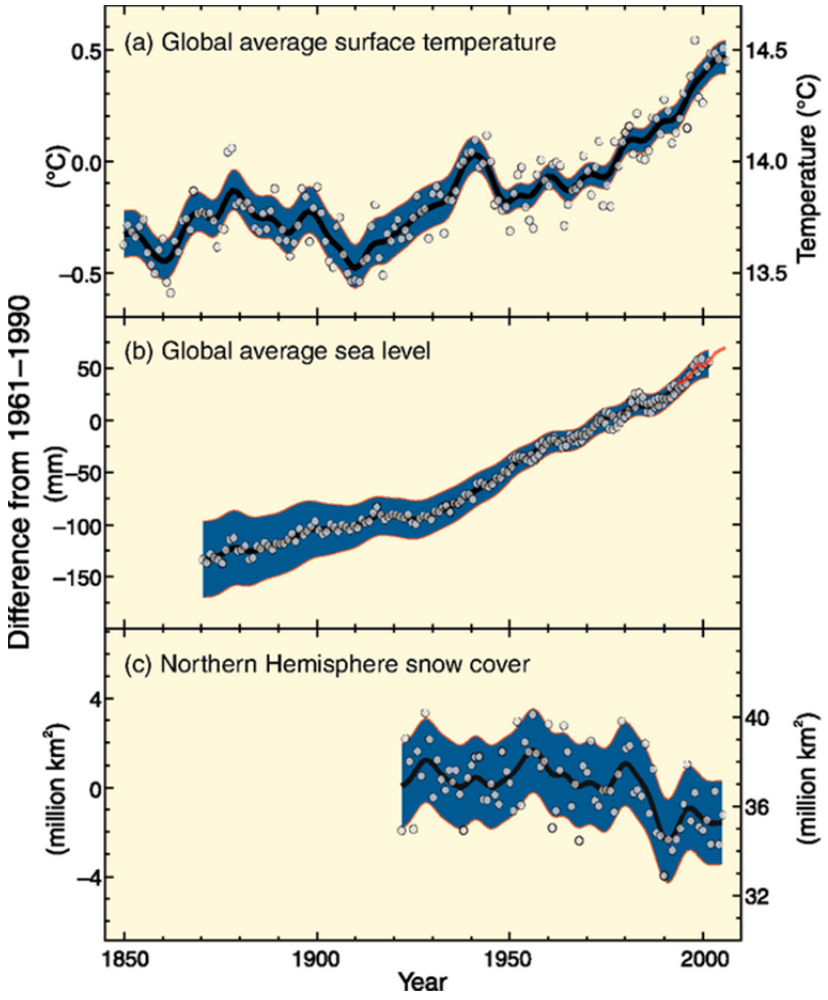

Figure 1.4 Observed changes in (a) global average surface temperature; (b) global average sea level from tide gauge (blue) and satellite (red) data and (c) Northern Hemisphere snow cover for March-April. All differences are relative to corresponding averages for the period 1961-1990. Smoothed curves represent decadal averaged values while circles show yearly values. The shaded areas are the uncertainty intervals estimated from a comprehensive analysis of known uncertainties (a and b) and from the time series (c).

It was reported that the period of 1995-2006 was recorded as the twelve warmest years in the instrumental record of global surface temperature (since 1850). Rising sea level is clearly observed to be consistent with global warming. Global average sea level has considerably increased since 1961 at an average rate of 1.8 mm/year and since 1993 at 3.1 mm/year. Additionally, satellite data since 1978 also indicated that annual average Arctic sea ice extent has shrunk by 2.7% per decade, which significantly contributes to the rise of sea level [10].

A thirst for energy alternatives to fossil fuel initially led human to the discovery of nuclear energy. Since its discovery, it has brought numerous benefits as an unlimited source of energy for man. Nuclear energy can provide a stable source of electricity with significantly low production cost [11-13]. **Figure 1.5** below clearly reveals the competitively lower production cost of nuclear energy in comparison with other traditional sources of energy such as oil, gas and coal in the United States during the period of 1995-2008.

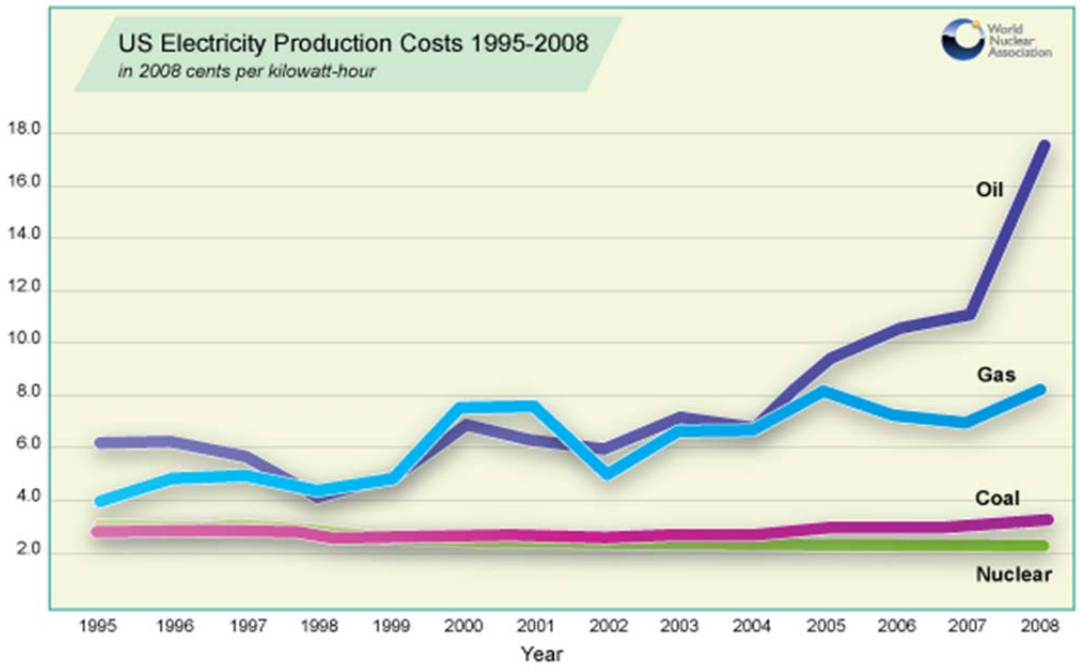

Figure 1.5 US Electricity Production Costs 1995-2008

In addition to that, nuclear energy is environmentally friendly as it hardly emits any greenhouse gases such as CO_2, CO, NO, etc. However, over the time, some issues have cropped up along with the usage of nuclear energy. Nuclear power is extremely dangerous if it is wrongly operated or affected by natural catastrophes. How will we ever forget the Chernobyl disaster in 1986, which was the consequence of a flawed

reactor design, coupled with inadequately trained personnel. Thousands of people have been affected by radioactivity since the Chernobyl station exploded. These harmful effects will continue on even after thousands of years later and will be passed on to our younger generations [14-16]. Last year in 2011, a massive earthquake and tsunami that struck Japan's Fukushima province caused another catastrophic nuclear accident as well. This resulted in nuclear meltdowns and dispersed radioactivity dust all over the world through mediums such as the wind, the sea, migratory animals, and even food [17,18]. Besides the danger of nuclear power, long-term radioactive waste storage problems have not yet been completely solved. With the aforementioned consequences of overusing fossil fuels, the various drawbacks of alternative energy sources, and the public outcry over the utilisation of nuclear energy; finding alternative, renewable, sustainable, and greener energy sources have become more urgent than ever before.

Recently, hydrogen has gained much attention as a promising candidate for a green and renewable fuel. Hydrogen is the simplest atom, consisting of one proton and one electron [19]. Hydrogen is by far-and-away the most abundant element in the universe, of which it constitutes 88.6% of the composition by weight. On earth, hydrogen is similarly the most abundant element. Its prevalent presence is in the form of water, which covers ¾ of the Earth's surface. Hydrogen atoms are very reactive and tend to form H_2 molecule. At ambient temperature, hydrogen is colourless, odourless, tasteless and nontoxic. It is important to note that burning hydrogen yields only water, which is totally harmless and friendly to the environment. Thus, hydrogen may just be our perfect fuel of the future. However, to be of practical use, several strict requirements must be satisfied when storing hydrogen on board. In January

2002, Freedom CAR Partnership between the United States Council for Automotive Research (USCAR) and the U.S. Department of Energy (D.O.E) set the 2010 and 2015 targets for the mobile hydrogen storage system [20], which includes all valves, tanks, regulators and hydrogen or hydrogen storage materials. The targets stipulate that a system capable of storing 6-10 wt% H_2 will be required to satisfy commercial demand.

Storing hydrogen can be divided into two conventional methods: physical and chemical storage. There are several disadvantages of using the physical storage approach. For instance, hydrogen storage using physical techniques such as high pressure carry a significant safety risk and the fuel would be available at a pressure dropping from 450 bars, i.e. when the tank is full of H_2, to zero over-pressure. As a result, additional pressure control is essential for this storage method. Conversely, condensation into liquid or even solid hydrogen offers an attractive solution to store H_2 from the point of view of increasing the mass per container volume. The densities of liquid and solid hydrogen are 70.8 kg m^{-3} and 70.6 kg m^3, respectively. However, the condensation temperature of hydrogen at 1 bar is 252^{o}C and the vaporisation enthalpy at the boiling point amounts to 452 kJ kg^{-1}. Hence, a sizable amount of energy is needed to maintain this system below the vaporisation temperature. In general, liquid hydrogen containers are built as open systems to prevent strong overpressure. Heat transfer through the container leads directly to the loss of hydrogen. Besides, the hydrogen storage capability of all physical storage systems is very far from the target set by D.O.E in which the system should contain at least 6-10 wt% hydrogen, it is very difficult to achieve that. For this reason, attention has shifted to chemical techniques of storing hydrogen in recent years.

In the early years, research on hydrogen storage materials focused on intermetallic hydrides such as $LaNi_5$ and TiFe, which showed very promising sorption and desorption kinetics but had low hydrogen storage capacities (below 2% of hydrogen by weight). Numerous attempts to increase their capacity and maintain good kinetics by synthesising polymetallic compositions with lightweight metals were unsuccessful [21].

Subsequently, strong interest was targeted at sodium aluminum hydride (or alumohydride, or alanate), $NaAlH_4$. Bogdanovic [22] discovered that titanium catalyst decreased the desorption temperature of $NaAlH_4$ and made the hydrogen release process reversible. This result suggested that those complex metal hydrides might be utilised as reversible hydrogen storage materials. Unfortunately, relatively low capacities of complex metal alumohydrides, except $LiAlH_4$ (10.5%), together the complexity of their decomposition pose serious problems to be resolved before their commercialisation. Aluminum hydride AlH_3, which contains 10 wt% of hydrogen, smoothly releases H_2 in one step at moderate temperature, it can however only be regenerated at a very high pressure of 24 Kbar.

Recently, ammonia-borane (NH_3BH_3, denoted as AB) has been paid much attention as another promising candidate for a hydrogen storage material due to its low molecular weight (30.7 $g.mol^{-1}$) and high gravimetric hydrogen capacity (19.6 wt%) [23-25]. However, its slow thermal kinetics below 100^oC and its the detrimental volatile byproducts which include borazine $(HNBH)_3$ and diborane (B_2H_6) are among the main hindrances to practical application. To overcome these obstacles, great

efforts have been made for the use of nanoscaffolds [26-28], transition metals [29-32], ionic liquids [33], and additives [34-36]. In spite of these significant achievements, new approaches remain to be developed so as to facilitate operation and practicality. Among these approaches, the method in which one hydrogen atom of AB is replaced by a metal such as Li, Mg has generated novel compounds with promising properties. These novel compounds such as $LiNH_2BH_3$, $Mg(NH_2BH_3)_2.NH_3$, $LiBH_4.NH_3.MgCl_2$ still have high hydrogen content. Additionally, they can start to release H_2 at as low as 75^oC in contrast to the high temperature of the decomposition of AB. Aside from that, these compounds have demonstrated their ability in the inhibition of the generation of volatile byproducts such as borazine and diborane, which are extremely harmful to vehicle motors. Apart from these novel compounds, another encouraging achievement comes from the successful synthesis of poly(methyl acrylate)-confined ammonia-borane [37]. Among its outstanding properties, water-resistant ability, suppressing harmful volatile products and low temperature of dehydrogenation have greatly attracted attention. Different from most other borohydride systems, which easily absorb water in air, leading to the system damage, this new water-resistant polymer-confined AB provides a more stable compound for better thermolysis performance. In particular, it still retains its low dehydrogenation temperature, which begins at as low as 70^oC. Moreover, this compound also can suppress the generation of detrimental boracic impurities. In conclusion, these two outstanding approaches, which lead to the synthesis of novel metal amidoboranes and polymer-confined AB have opened a new door and possibility for good hydrogen storage materials to be created. These will lay the foundation for further findings of better on-board hydrogen storage materials.

Due to the fact that these compounds are novel, their detailed dehydrogenation mechanisms have not been fully investigated and understood. Thus, understanding

these dehydrogenation processes in detail is the first critical step needed to approach closer to the production control, as well as to design better compounds in future. Modelling the hydrogenation mechanism of the newly explored hydrogen storage materials such as $LiNH_2BH_3$, $Mg(NH_2BH_3)_2.NH_3$, $LiBH_4.NH_3.MgCl_2$, polymer-confined AB will shed light on the critical roles of these metals and polymers in facilitating the hydrogen release of ammonia-borane. Based on this knowledge, new compounds may be synthesised to enhance the dehydrogenation properties. It will significantly contribute to the current tremendous efforts of finding better hydrogen storage materials. Therefore, it is of utmost importance to comprehensively grasp the molecular mechanisms of all relevant hydrogen reactions through the construction of the potential energy surfaces.

In the work presented in this thesis, we aim to investigate the energetic and mechanistic characteristics of the dehydrogenation of several promising hydrogen storage materials including $LiNH_2BH_3$, $Mg(NH_2BH_3)_2.NH_3$, $LiBH_4.NH_3.MgCl_2$ and polymer-confined AB. Density Functional Theory based on quantum mechanical calculations, which will be further reviewed in Chapter **3**, has been employed to obtain crucial information on chemical reactions such as the possible structures of intermediates, roles of the metals, kinetic, and thermodynamic properties. More specifically, the key role of lithium in facilitating hydrogen release will be explored and carefully analysed in Chapter **4**. Chapter **5** then continues investigation on the critical role of magnesium in the dehydrogenation of the compound $Mg(NH_2BH_3)_2.NH_3$. In particular, the role of NH_3 molecule will be elucidated. Chapter **6** will concentrate on the dehydrogenation of an intriguing compound known as $LiBH_4.MgCl_2.NH_3$, which includes two metals we would have seen in two previous

chapters. We will then discuss in detail how they support each other in the dehydrogenation. In Chapter **7**, a newly explored compound poly(methyl acrylate)-confined AB will be examined. Finally, in Chapter **8**, we will examine the H_2 elimination of system polymer-confined AB with varied polymers and predict in advance the outcome with hopes for improving the dehydrogenation properties of the novel compound discussed in chapter **7**. Chapter **9** will conclude the thesis and suggest possible avenues for future research in this area.

References

[1] "NEED Energy Infobooks, Vol.," *The National Energy Education Development Project* , p. available at http://www.need.org/EnergyInfobooks.php.

[2] P. Deborah and C. Anna N. Marylin, "Energy for Keeps: Electricity from Renewable Energy," 2005.

[3] R. M. Dell and Editors D. A. J. Rand, "Hydrogen energy: challenges and prospects," 2008.

[4] R. M. Dell and D. A. Rand, "Clean Energy, Vol.," 2004.

[5] "E.I. Administration in International Energy Outlook," 2012, available at http://205.254.135.7/forecasts/aeo/pdf/0383(2012).pdf.

[6] O. R. Davidson, P. R. Bosch, R. Dave, L. A. Meyer B. Metz, "Climate Change 2007: Mitigation of Climate Change".

[7] Károly Rényi, "The fossil-fuels and the global warming," in *World Energy Congress*.

[8] T. A., G. Marland and R. J. Andres Boden, "Global, Regional and National Fossil-Fuel CO2 Emissions," 2010.

[9] E. David, *Energy, Society and Environment* , 2003.

[10] Pachauri, R. K. and Reisinger, A. Core Writing Team, "Climate Change: 2007 Synthesis Report," p. 104.

[11] "Projected Costs of Generating Electricity," 2005.

[12] "The Cost of Generating Electricity," 2004.

[13] "Reference Costs for Power Generation," 2003, http://www.industrie.gouv.fr/energy/electric/cdr-anglais.pdf.

[14] Expert Group Health, World Health Organization, "Health Effects of the Chernobyl Accident and Special Health Care Programmes," 2006.

[15] United Nations Office for the Coordination of Humanitarian Affairs (OCHA), "Chernobyl - A Continuing Catastrophe," 2000.

[16] Malcolm Crick and Didier Louvat Mikhail Balonov, "Update of Impacts of the Chernobyl Accident: Assessments of the Chernobyl Forum (2003-2005) and UNSCEAR (2005-2008)," in *Proceedings of the Third European IRPA*

(International Radiation Protection Association) Congress, Helsinki, Finland, 2010.

[17] IAEA organisation. Fukushima Nuclear Accident: Information Sheet. [Online]. http://www.iaea.org/About/japan-infosheet.html

[18] World Health Organisation. Japan nuclear concerns. [Online]. http://www.who.int/hac/crises/jpn/faqs/en/index.html

[19] J. S. Rigden, "Hydrogen: The Essential Element;," p. 1, 2003.

[20] U.S. Department of Energy. Energy Efficiency & Renewable Energy. [Online]. http://www1.eere.energy.gov/hydrogenandfuelcells/storage/DoE

[21] Grigorii L. Soloveichik, "Metal Borohydrides as Hydrogen Storage Materials," *Material Matters*, vol. 2, p. 11, 2007.

[22] B. Bogdanovic and M. Schwickardi, *J. Alloys Compounds*, vol. 1, pp. 253-2541, 1997.

[23] V. Pons, R. T. Baker F. H. Stephens, *Dalton Trans*, vol. 25, p. 2613, 2007.

[24] X. B. Zhang, S. Han, H. S. Shioyama, Q. Xu J. M. Yan, *Angew. Chem. Int. Ed.*, vol. 47, p. 2287, 2008.

[25] W. L. Mao, H. K. Mao Y. Lin, *Proc. Natl. Acad. Sci USA*, vol. 106, p. 8113, 2009.

[26] A. Gutowska et al., *Angew. Chem. Int. Ed.*, vol. 44, p. 3578, 2005.

[27] A. Feaver et al., *J. Phys. Chem. B*, vol. 111, p. 7469, 2007.

[28] L. Li et al., *Adv. Funct. Mater.*, vol. 19, p. 265, 2009.

[29] C. A. Jaska, K. Temple, A. J. Lough, and I. Manners, *J. Am. Chem. Soc.*, vol. 125, p. 9424, 2003.

[30] M. C. Denney, V. Pons, T. J. Hebden, D. M. Heinekey, and K. I. Goldberg, *J. Am. Chem. Soc*, vol. 128, p. 12048, 2006.

[31] F. Y. Cheng, H. Ma, Y. M. Li, and J. Chen, *Inorg. Chem.*, vol. 46, p. 788, 2007.

[32] P.M. Zimmerman, A. Paul, Z. Zhang, and C. B. Musgrave, *Angew. Chem. Int. Ed.*, vol. 48, p. 2201, 2009.

[33] M. E. Bluhm, M. G. Bradley, R. Butterick, U. Kusari, and L. G. Sneddon, *J. Am. Chem. Soc.*, vol. 128, p. 7748, 2006.

[34] Z.T. Xiong et al., *Nat. Mater.*, vol. 7, p. 138, 2008.

[35] X. D. Kang et al., *Adv. Mater.*, vol. 20, p. 2756, 2008.

[36] J. Spielmann, G. Jansen, H. Bandmann, and S. Harder, *Angew. Chem. Int. Ed.*, vol. 47, p. 6290, 2008.

[37] Zhao. J. et al., *Adv. Mater.* , vol. 22, pp. 394-397, 2010.

CHAPTER 2

LITERATURE REVIEW

2.1 Introduction

This chapter first gives a brief history of hydrogen in Section 2.2. Then the physical and chemical properties of hydrogen are discussed in Section 2.3. Later, some outstanding physical and chemical hydrogen storage methods are introduced in Section 2.4. The strengths and weaknesses of these methods are carefully analysed. Toward the end of Section 2.4, the properties of all ammonia-borane-based materials examined in this research are presented. Lastly, the aims of my research are restated.

2.2 History of Hydrogen

The earliest discovery of the presence of hydrogen could be attributed to Turquet de Mayerne, who in ***1650*** discovered and described an "inflammable air" produced by the reaction of dilute sulfuric acid on iron. However, a British scientist, Henry Cavendish was the first to recognised hydrogen gas as a discrete substance after he conducted an experiment between zinc metal and hydrochloric acid to identify and isolate hydrogen in ***1766*** [2-5]. Seventeen years later, in ***1783***, a French physicist, Alexander Cesar Charles [3] invented the first hydrogen balloon, which was able to fly to an altitude of three kilometers. In the same year, a French chemist,

Antoine Lavoisier gave hydrogen its name, which was derived from the Greek words – "hydor" and "genes" meaning "water" and "born of" [6] when he and Laplace reproduced Cavendish's finding that burning hydrogen yielded water [3].

At the beginning of the nineteenth century, English scientists William Nicholson and Sir Anthony Carlisle reported electrolysis phenomenon in ***1800*** in which hydrogen and oxygen would be produced when applying an electric current to water.

Early in the twentieth century, a German chemist, Fritz Haber described a catalytic process, which enabled facile ammonia synthesis from hydrogen and nitrogen. This outstanding discovery brought him the prestigious Nobel Prize in chemistry. During the ***1920s*** – a German engineer, Rudolf Erren, invented an internal combustion engines for trucks, buses and submarines, which was fueled by hydrogen or hydrogen mixtures. Inspired by this invention, a British scientist and writer J. B. S. Haldane presented the concept of renewable hydrogen in his paper "Science and the Future", by forecasting that "there will be great power stations where during windy weather the surplus power will be used for the electrolytic decomposition of water into oxygen and hydrogen".

Unfortunately, the damage to hydrogen's reputation as a lifting gas happened after an accident in ***1937*** at Lakewood, New Jersey, USA [3]. After ten successful trans-Atlantic flights from Germany to United States, the Hindenburg, a dirigible inflated with hydrogen gas, was destroyed in a midair fire over New Jersey. However, hydrogen usage still increased strongly afterwards, particularly marked by NASA

decision to consistently use the liquid hydrogen, primarily for rocket propulsion and as a fuel for fuel cells. More interestingly, one year later, the first practical hydrogen-air fuel cell was developed in ***1959*** by Francis T. Bacon of Cambridge University in England, followed by the invention of the first fuel cell vehicle by Harry Karl Ihrig, an engineer of Allis-Chalmers manufacturing company. Further hydrogen fuel cell application based on Bacon's design was then employed to generate on-board electricity, heat and water for astronauts abroad the famous Apollo spacecraft and most subsequent space shuttle missions. The term "hydrogen economy" was first presented in ***1972*** by the electrochemist John O'M. Bockris in his paper "The Hydrogen Economy: An Ultimate Economy?"

In ***1990***, the world's first solar powered hydrogen production plant at Solar-Wasserstoff-Bayern, a research and testing facility in southern Germany, started operating.

Currently, hydrogen has gained much attention as a promising green and renewable energy for vehicles of the future. Tremendous efforts have been made to develop numerous methods for on-board hydrogen storage. In the next part, some crucial physical and chemical properties of hydrogen, which have laid the foundation for these methods, will be first reviewed.

2.3 Physical and Chemical Properties of Hydrogen

Hydrogen exists under three isotopes: protium, deuterium, and tritium. Notably, tritium is radioactive and emits very low energy β rays. The table below

displays some different physical properties of these isotopes, including nuclear, atomic and molecular.

Table 2.1 Some properties of hydrogen isotopes.

Isotope	Protium ^{1}H	Deuterium ^{2}D	Tritium ^{3}T
Atomic Mass (u)	1.007825	2.0140	3.01605
Natural Abundance (%)	99.985	0.015	0.000
Nuclide	1 proton (+) 1 electron (-)	1 proton (+) 1 electron (-) 1 neutron	1 proton (+) 1 electron (-) 2 neutrons
Half-Time (yr)	Stable	Stable	12.33
Ionisation energy (eV)	13.5989	13.6025	13.6038
Nuclear spin [h/2π]	+1/2	+1	+1/2

The elemental hydrogen can exist in several different forms such as monoatomic, diatomic gas, metallic conductor or plasma, depending on the ambient temperature. Monoatomic gas can be detected at very low densities while diatomic molecule is ample under ordinary conditions. A metallic conductor and ionised plasma can be generated at elevated temperature. All these states are found in different places in the Solar System, however, on earth, elemental hydrogen usually exists only as a molecule due to the reactive of monoatomic hydrogen. In the following part, we exclusively focus on the physical and chemical properties of the molecular hydrogen [7-10].

2.3.1 Physical Properties of Molecular Hydrogen

The combination of two highly reactive hydrogen atoms forms the molecule hydrogen, which is a very stable entity. The energy level of its electronic ground state, the singlet state $^1\Sigma_g^+$ lies lower than two separated atoms by E_0 = 4.748 eV (the binding energy). Particularly, the equilibrium separation is very short, being r_0 = 0.7416 Å. **Figure 2.1** [11] presents the electronic energy as a function of internuclear separation r (the adiabatic potential) and energy levels of the stretching vibration. For an H_2 molecule, the zero-point vibration energy is $E_v^0 = 0.372$ eV, thus, the dissociation energy is:

$$E_d = E_0 - E_v^0 = 4.476 \text{ eV}$$

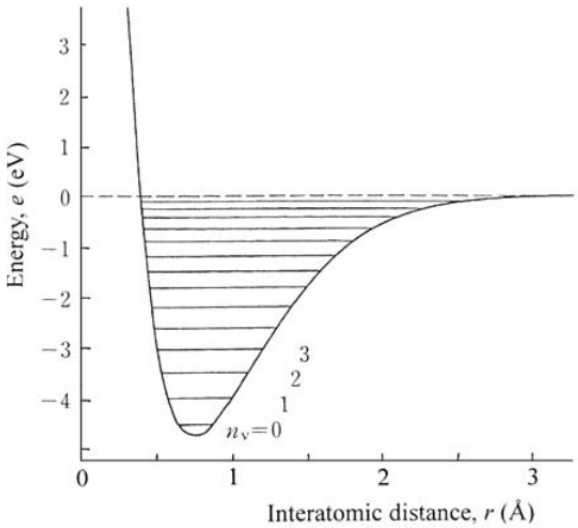

Figure 2.1 Adiabatic potential and energy levels of the stretching vibration of H_2.

Due to its extremely light mass, hydrogen has the second lowest boiling point and melting points of all substances, second only to helium. Hydrogen is a liquid below its boiling point of 20K (-253^{o}C) and a solid below its melting point of 14 K (-259^{o}C) and atmospheric pressure. It should be noted that, hydrogen has expansion

ratio of 1:848, which means hydrogen in its gaseous state at atmospheric conditions occupies 848 times more volume than it does in its liquid state. Thus, to be of practical use, it is of great importance to liquefy hydrogen. However, due to these strict conditions, storing liquid hydrogen is extremely difficult. This issue will be further analyzed in the later part of literature review.

Hydrogen has lowest atomic weight of any substance, thus it has extremely low density both as a gas and a liquid. Vapor and liquid densities of H_2 and other comparative substances such as methane and gasoline are listed in **Table 2.2**.

Table 2.2 Vapor and liquid densities of comparative substances.

Substance	Vapor Density (at 68^{o}F; 20^{o}C, 1 atm)	Liquid Density (at normal boiling point, 1 atm)
Hydrogen	0.005229 lb.ft^{-3} (0.08376 kg.m^{-3})	4.432 lb.ft^{-3} (70.8 kg.m^{-3})
Methane	0.0406 lb.ft^{-3} (0.65 kg.m^{-3})	26.4 lb.ft^{-3} (422.8 kg.m^{-3})
Gasoline	0.275 lb.ft^{-3} (4.4 kg.m^{-3})	43.7lb.ft^{-3} (700 kg.m^{-3})

Different from other fuels, hydrogen is odorless, colorless, tasteless and non-toxic. However, these seem-to-be-good properties will become dangerous once hydrogen leakage occurs. A risk of explosion is present whenever hydrogen mixes with oxygen in air. Thus, the propensity for hydrogen to leak dictates the current trend of using hydrogen storage materials as safe fuels instead of using liquefied pure hydrogen so as to avoid associated fire hazard. Prior to discuss further this issue in the

"physical hydrogen storage" part, the following part will review some critical properties of molecular hydrogen.

2.3.2 Chemical Properties of Molecular Hydrogen

Being the lightest element with a single proton and one electron, hydrogen atoms are extremely reactive. The driving force behind its reactivity lies on the unique $1s^1$ electron configuration of hydrogen atom. This half-filled valence shell allows hydrogen to pair with one extra electron to form a complete shell of the helium configuration $1s^2$ or to lose one electron to become the proton H^+.

Due to its high reactivity, hydrogen atom can form numerous chemical compounds with all the known elements except for the noble gases. The most abundant compounds include water, minerals, in particular hydrocarbons such as petroleum and natural gases. Besides, hydrogen can combine with metals to form hydrides such as NaH, CaH_2. It is also able to form covalent bonds with nonmetal elements such as S, N and halogens. Among these hydrogen compounds, there are strong acids such as $HClO_4$, HNO_3, H_2SO_4, etc. Interestingly, hydrogen can form strong covalent bonds with carbon to form hundreds of millions organic compounds such as glucose, protein, DNA, etc., which constitute the living world.

One of the most interesting characteristics of hydrogen is its possibility to form hydrogen bond [12], which is a strong intermolecular force of attraction. Hydrogen bonds are present when hydrogen is attached to a strongly electronegative heteroatom, such as nitrogen, oxygen, or fluorine, which has a partial negative charge. This electronegative element attracts the electron cloud around the hydrogen nucleus,

resulting in the hydrogen atom with a partial positive charge. This partial positive charge hydrogen, in turn attracts a lone pair of electrons on another heteroatoms of other molecules. The hydrogen bond can be represented as:

$$X^{\delta-}\text{-}H^{\delta+} + :Y \rightleftharpoons X\text{-}H\bullet\bullet\bullet :Y$$

Where X and Y are strongly electronegative atoms such as N, O, F… The X-H group is termed "hydrogen bond donor", while Y is the "hydrogen bond acceptor".

More interestingly, a negatively polarised hydrogen atom in $H^{\delta-}Z$ where Z is a less electronegative element than H such as boron, could be regarded as an unusual or nonconventional proton acceptor. The interaction in this case, which is termed a dihydrogen bond [13], will take the form:

$$X^{\delta-}\text{-}H^{\delta+} \bullet\bullet\bullet \quad H^{\delta-}Z$$

What makes this interaction so unusual is that the proton-accepting atom is also a hydrogen atom. This character is critical in understanding hydrogen release of some hydrogen storage materials, which will be further discussed in chapter 4, 5 and 6.

2.4 Hydrogen Storage Methods

The storage of hydrogen greatly depends on the purpose of application, resulting in different characteristics of materials used. In stationary application, including heating and air-conditioning of homes and buildings, electricity generation and varied industrial uses, hydrogen storage systems can be placed in a relatively large space and the weight of the system is not a major issue. In contrast, for on-board hydrogen storage, vehicles need compact, light, safe and affordable containment. Thus, in January 2002, Freedom CAR Partnership between the United States Council

for Automotive Research (USCAR) and U.S. Department of Energy (D.O.E) set the 2010 and 2015 targets for mobile hydrogen storage system [14], which includes all valves, tanks, regulators and hydrogen or hydrogen storage materials. Among these conditions are some critical requirements, including: (1) The target requires the system capability of 6-10 wt% H_2 storage to satisfy the commercial demand. (2) It has to provide rapid hydrogen release at operating temperature range from -20^{o}C to +85^{o}C via a chemical reaction [15,16].

There are several methods to store hydrogen including physical storage and chemical storage. As presented in section 2.3.1, hydrogen has a low density, thus to satisfy D.O.E target, in physical storage approach, hydrogen either needs compressing at elevated pressure or liquefying under extremely low temperature. The following part will first review these two methods. Then, chemical storage methods, which show more advantages, will be discussed in detail.

2.4.1 Compressed Hydrogen Gas

Compressed hydrogen gas is the gaseous state of the element hydrogen, kept under elevated pressure. Cylinders used to store hydrogen are made from new lightweight materials such as carbon-fiber-reinforced composites. Although hydrogen will be compressed under 350 or even 700 atm in the tanks, it still has a significantly lower energy content per volume than gasoline. Thus, the volume must be several times bigger to contain the same amount of energy content as in gasoline tanks. Additionally, depending on the pressure applied, hydrogen compression will consume the equivalent 10-15% of the energy contained in the hydrogen fuel [17]. Finally, this

method also carries high risk of explosion when hydrogen is kept under high pressure, thus it seems inappropriate for conventional transportation use.

2.4.2 Liquid Hydrogen Storage

To achieve higher safety and volumetric energy density, an alternative method is liquefying hydrogen. Liquid hydrogen is cryogenic and boils at 20K. Although cryogenic storage saves weight, it requires large liquefaction energies. Liquefaction process includes pressurizing and cooling steps, which consume intensive energies [18-20]. Furthermore, liquid hydrogen storage tanks must be well insulated to minimise vaporisation, which certainly adds more cost in operation. Additionally, there is a trade-off between the well-insulated tank and its mass, whose increase will reduce the fuel economy efficiency of this method. Finally, it is necessary to take into account materials of the tank since hydrogen is likely to diffuse through any liner material intended to contain it, resulting in the embrittlement, or weakening of the materials.

While physical hydrogen storage seems inappropriate to provide as a safe hydrogen carrier for vehicles, much attention has been paid to chemical hydrogen storage. Tremendous efforts have been devoted to synthesise and design novel compounds, which can satisfy the requirements of a good hydrogen storage material. The following part will review some outstanding and promising materials for chemical hydrogen storage.

2.4.3 Chemical hydrogen storage

In accordance with a definition elaborated by the USA Department of Energy, the term "chemical hydrogen storage" is used to describe storage technologies in which hydrogen can be stored in a chemical compound and released by a chemical reaction. Based on the strength of hydrogen bonding, hydrogen storage materials can be divided into three categories, (1) sorbent materials [21-26] where hydrogen is physisorbed and weakly bound to the substrate; (2) nanostructured materials [27-30] where hydrogen is held by an interaction that is intermediate between physisorption and chemisorption. These are composed of functionalised sorbent materials as well as nanoparticles of complex hydrides. (3) complex hydrides [31-33] where hydrogen is held in strong covalent bonds; these include light metal hydrides and chemical hydrides. The following part will discuss further about the progress made, advantages as well as disadvantages of these materials.

2.4.3.1 Sorbent Materials

Carbon-based materials are outstanding representatives for this category. They include nanotubes, fullerences, graphene, mesoporous silica, metal-organic frameworks (MOFs), and clathrates [21-26].

In the earliest report, Dillon and his collaborators [25] reported the promising hydrogen storage ability of carbon nanotubes that raised considerable hope and attention. However, subsequently, studies [22] indicated that these findings were flawed due to difficulties in accurate measurements and impurities in samples.

Although these materials show promising hydrogen storage capacities at 77 K, only less than 1 wt% of hydrogen can be stored at 298 K and 100 atm of pressure. Work on clathrate hydrates [21] also shows attractive results such as $(H_2)_4CH_4$ with 33.4% molecular hydrogen by mass or 50% total hydrogen if one includes the four hydrogen atoms within each methane molecule. However, its instability at ambient conditions is still the main issue. Recently, a new class of porous aromatic frameworks (PAFs) characterised by diamond-like structure has been investigated. It was reported that these compounds possessed higher gravimetric hydrogen density than conventional COF-102, namely, it can store 6.53 wt% hydrogen at 298 K and 100 bar [34].

2.4.3.2 Functionalised Nanostructures

Research on nanostructured materials also obtains significant achievement. One of the early works by Zhang, Yildrim, and their collaborator [27,28] demonstrated that transition-metal-doped C_{60} fullerene and carbon nanotubes can store hydrogen up to 9 wt% reversibly with favorable kinetics and thermodynamics. However, it was later reported that these materials might not be stable during repeated hydrogenation/rehydrogenation cycles as transition metal atoms are likely to cluster [29]. Their later work showed that this problem can be avoided either by choosing metal dopants that has more competitive binding affinity to the substrate than to each other or by having them replace a ligand site [35]. Some theoretical studies also indicated that Li [30] and Ca [36] atoms supported on C_{60} and nanotubes do not cluster, and up to 13 wt% hydrogen can be stored on $Li_{12}C_{60}$ [30]. The binding energy of hydrogen can be further improved by functionalisation of C_{60}. Recent theoretical work [37] also predicted that an external electric field might polarise H_2 molecules

just as metal cations can. This will lead to the ability of tailoring the thermodynamics of hydrogen storage by varying both the polarisability of the substrate as well as the electric field strength. However, more experiments are required to be conducted to verify these predictions.

2.4.3.3 Complex Hydrides

Complex hydrides comprise metal hydrides and chemical hydrides. MgH_2 and salts of $[AlH_4]^-$ (alanates), $[NH_2]^-$ (amides), and $[BH_4]^-$ (borohydrides) such as $NaAlH_4$, $LiNH_2$, Li_2NH, and $Mg(BH_4)_2$ belong to the former category [31] while $C_{10}H_{18}$, and NH_3BH_3 are classified as chemical hydrides [32,33].

Many metals and alloys are capable of absorbing large amounts of hydrogen such as Pd, Pt, $LaNi_5$, ZrV_2, FeTi, Mg_2Ni, TiV_2, etc. [38] In these metals and alloys, hydrogen is located in the form of atoms on interstitial sites of the host metal lattice. Therefore, the metal-hydrogen bond offers the advantage of very high hydrogen density. However, none of metallic systems satisfy the pressure and temperature range attractive for mobile storage (1-10 bar, 0-100^{o}C, corresponding to an enthalpy change between 15 and 24 kJ mol^{-1}) [39]. Thus, attention has shifted to intermetallic compounds such as $LaNi_5$, Mg_2Ni. Alloys derived from $LaNi_5$ demonstrated some very promising properties, including fast and reversible hydrogen sorption and good cycling life. The volumetric hydrogen density of $LaNi_5H_{6.5}$ at 2 bar is equivalent to the amount of gaseous molecular hydrogen at a pressure of 1800 bar. More interestingly, all these hydrogen molecules can desorb at a pressure of 2 bar. Thus, storage in these intermetallics allows very safe hydrogen handling. However, as

lanthanum and nickel are large elements, the proportion of hydrogen in $LaNi_5H_{6.5}$ remains below 2 wt % [40,41]. Therefore, it is not enough for hydrogen fuel tanks to be used. This low mass density is the general weakness of all known metal hydrides working near room temperature. Certainly, many intermetallic compounds and alloys were reported to form hydrides with up to 9 wt% hydrogen such as $Li_3Be_2H_7$ [42] and 4.5H atoms per metal atom such as $BaReH_9$ [43] but they are not reversible within the required range of temperature and pressure for on-board applications.

To obtain higher mass density, light elements such as calcium and magnesium were employed. Experimental data showed that Mg formed ionic, transparent MgH_2 containing 7.6 wt% hydrogen. However, its formation from bulk Mg and gaseous hydrogen is extremely slow, and in thermodynamic equilibrium a plateau pressure of 1 bar requires not room temperature but 300^{o}C. Despite tremendous efforts devoting to improve its properties such as precipitation from metal-organic solutions or high-energy balling of Mg [42,44,45] they still failed to lower the dehydrogenation temperature under 150^{o}C. Another approach was to alloy Mg prior to the hydride formation. In this case, Mg_2Ni forms a ternary complex hydride Mg_2NiH_4, which still contains 3.6 wt% hydrogen. The hydride formed fairly rapidly, probably due to the presence of Ni as a catalyst for the dissociation of molecular hydrogen, but thermodynamically it still required 280^{o}C for 1 bar hydrogen. Other alloys of Mg such as Mg_2Cu, $Mg_{17}La_2$ and MgAl have been successfully synthesised. Unfortunately, by incorporating heavy metals such as Cu or La into the alloys, they reduce dramatically the hydrogen mass density.

Subsequently, strong interest was targeted to other compounds containing higher hydrogen content such as alanates, amides, and borohydrides. However, the major issue of these compounds is theirs poor thermodynamics, kinetics, and reversibility. For example, $NaAlH_4$ undergoes dehydrogenation at elevated temperature 265^oC, giving rise to Al metal and NaH. The reaction is shown below:

$$NaAlH_4 \rightarrow NaH + Al + 3/2H_2$$

Further dehydrogenation occurs at even higher temperature above 400^oC. Later, Bogdanovic and Schwickardi [46] conducted systematic study on Ti-based catalysis. They reported that the addition of that catalysis could bring down the first dehydrogenation temperature in the solid state to 150^oC while simultaneously improving the conditions for rehydrogenation. Further studies have shown that (i) the absorption process is quite feasible when enhanced by a catalyst [46,47], (ii) Zi-based catalysts are inferior to Ti-based ones [48], (iii) mechanochemical synthesis (ball milling) significantly improves reversibility [42], and (iv) "dry-dopping" lowers the T_{dec} value to about 100^oC for $NaAlH_4$ [49].

Later, a spectacular result was achieved with $LiAlH_4$. It was indicated that mechanical processing of catalyst-supported $LiAlH_4$ results in hydrogen evolution even at room temperature [50,51]. This discovery paves a new way for the controlled design of efficient storing materials operating in the desired temperature range (60-90^oC).

Recently, a chemical hydride, ammonia-borane has been attracted great interests due to its promising hydrogen storage properties. It has an impressive gravimetric capacity of up to 19.6 wt% and is nonflammable and non-explosive under standard conditions, which makes it a good candidate for hydrogen storage [52-55].

Recent work has indicated that NH_3BH_3 can release more than 2 moles of H_2 when heating at moderate temperature (120-150^oC) in comparison with other metal hydrides. It was reported that in the first two steps, reaction of AB led to the formation of PAB, polyaminoborane, $(NH_2BH_2)_n$, followed by the formation of PIB polyiminoborane $(NHBH)_n$. The total amount of 12 wt% hydrogen was released during this process. The reactions of hydrogen evolution can be summarised as shown in equations:

$nNH_3BH_3 \rightarrow (NH_2BH_2)_n + (n-1)H_2$ (<120^oC) (intermolecular)

$(NH_2BH_2)_n \rightarrow (NHBH)_n + H_2$ (~150^oC) (intramolecular)

At a slightly higher temperature the cross-linking between molecules is observed to release additional hydrogen. These materials are common intermediates used as precursors to boron nitride, which is formed at temperatures much greater than 500^oC [56-60].

$2(NHBH)_n \rightarrow (NHB\text{-}NBH)_n + H_2$ (~150^oC) (cross linking)

$(NHBH)_n \rightarrow BN + H_2$ (>500^oC) (boron nitride)

It should be noted that when pure ammonia-borane is heated at 85^oC, which is the optimal condition for on-board application, it only gave a negligible amount of

hydrogen after 3h. The high temperature of dehydrogenation and slow kinetics make NH_3BH_3 inappropriate for automobile use. Furthermore, in solid state thermal decomposition, it is found that volatile product such as borazine has been generated in tandem with hydrogen release. Higher heating rates resulted in even greater quantities of volatile products such as borazine [56-58]. The formation of volatile products will be problematic for PEM fuel cells that are easily fouled by contaminants in the hydrogen stream.

To summarise, the challenges for ammonia-borane to be of practical use are high temperature of dehydrogenation, the long induction period, and harmful volatile by-products such as borazine. The next part will be dedicated to reviewing some current methods to improve the properties of ammonia-borane as well as some analyses on advantages and drawbacks of these methods.

Numerous methods have been examined to control hydrogen release at moderate temperatures and reasonable rates while not having to sacrifice the high gravimetric storage density of hydrogen and trying to depress the volatile byproduct borazine. In the early days, various groups mainly focused on the catalytic approaches including (1) Transition metal catalysed dehydrogenation; (2) Ionic liquid catalyzed dehydrogenation; (3) Solution phase thermal decomposition; (4) Hydrogen release facilitated by scaffolds. Although improvements have been obtained such as lowering the temperature, some drawbacks still remain in these methods.

Sneddon and co-workers [61] who carried out the thermolysis in an ionic liquid (bmim Cl = 1-butyl-3-methylimidazolium) reported that NH_3BH_3 started to

release hydrogen immediately and gave 0.95 equivalent after 3h at 85°C and even 1.5 equivalents after 3h at 95°C. Although this method succeeded in lowering the temperature of the thermal decomposition of ammonia-borane and the induction period is shortened, by introducing ionic liquids as solvents, the storage density of system has been dramatically reduced.

Interestingly, complexes of transition metals can be employed as good catalysts. Some impressive results were achieved such as shortening the induction period of NH_3BH_3 to release hydrogen. Denney and Goldberg [62] reported use of molecular complexes of transition metals (e.g. Ir) containing pincer ligands for dehydrogenation at room temperature in just 14 minutes, considerably faster than the previously reported rhodium complexes (dehydrogenation of dimethyl amino borane required 2-4 days at 45°C) [63]. Unfortunately, the reaction can occur in THF, which reduces considerably the gravimetric density of hydrogen.

In another attempt to lower the onset temperature, some achievements were obtained by using nanocomposites of a matrix with intercalated ammonia-borane. It was reported that a nanocomposite of mesoporous silica and ammonia-borane in a 1:1 mixture allowed the thermal decomposition of ammonia-borane at 50°C with a half-reaction time of 85 min in comparison with a half-reaction time of 290 min at 80°C for neat ammonia-borane [33]. More spectacularly, the decomposition temperature could be significantly decreased with a 24 wt % carbon cryogel/ammonia-borane nanocomposite [64]. In this case, hydrogen started to release at <80°C, with a decomposition peak at approximately 90°C, with no further decomposition peak at

higher temperature. However, similar to other approaches, the use of nanocomposites considerably lowers the hydrogen content of the whole system.

Due to these current drawbacks of catalytic approaches, recent attention has shifted to a further active area, which is the chemical modification of ammonia-borane to produce amidoboranes. Metal amidoboranes are a subclass of amine-boranes where one of the acidic protons on nitrogen has been replaced by a metal such as Lithium, Magnesium, and Calcium. Currently, these compounds are mainly being investigated for their hydrogen storage properties. However, the beginning results are very encouraging. Some of the systems including $LiNH_2BH_3$ and $Mg(NH_2BH_3)_2.NH_3$ will be discussed in detail.

Chen and co-workers were the first to report lithium amidoborane ($LiNH_2BH_3$) as a novel promising hydrogen storage material [65]. This compound were generated through the interactions of lithium hydride with ammonia-borane, which results in the replacement of one hydrogen atom of NH_3 group by a lithium:

$$NH_3BH_3(s) + LiH(s) \rightarrow LiNH_2BH_3(s) + H_2(s)$$

The overall hydrogen release from this compound are illustrated in the following reaction:

$$nLiNH_2BH_3(s) \rightarrow (LiNBH)_n(s) + 2nH_2(g) \quad 10.9\ wt\%$$

Chen, P. and co-workers also observed many substantially different and significantly improved properties as compared to ammonia-borane. While ammonia-borane was found to release hydrogen at 108^{o}C, $LiNH_2BH_3$ released more than 10 wt% of hydrogen cleanly at considerably lower temperature 92^{o}C. Moreover, formation of the unwanted by-product borazine was observed at 154^{o}C for ammonia-borane but could be reduced to levels below the detection threshold of mass spectrometry in the case of lithium amidoborane. In brief, this material offers significant advantages over their parent compound, ammonia-borane. Lithium amidoborane are also environmentally harmless, non-flammable, non-explosive and stable solids at ambient temperature and pressure. The replacement of one hydrogen atom by lithium has significantly changed the properties of amido-borane. It is of utmost importance to understand the role of lithium in this reaction. However, few studies have been done to shed light on this critical role. Recently, Kim et al. have reported the mechanism of this interesting compound [66]. However, they only report the mechanism of the first step of this dehydrogenation mechanism. Furthermore, the reported mechanism is based on gas-phase model which is quite simple and far from the reality. Thus, in chapter 4, comprehensive mechanism of dehydrogenation mechanism of lithium amido-borane will be discussed in detail. In particular, the solvent effect was also taken into account to better model this mechanism.

Apart from lithium amidoborane, the successful synthesis of magnesium amidoborane ammoniate ($Mg(NH_2BH_3)_2.NH_3$) has been reported [67]. Chen, P. and her collaborators synthesised $MgAB.NH_3$ via ball milling $Mg(NH_2)_2$ with 2 equiv. AB, which was proposed to have the compositional formula of $Mg(NH_2BH_3)_2.2NH_3$. Subsequently, $Mg(NH_2BH_3)_2.2NH_3$ solidified into a new phase at ambient

temperature while releasing slowly one equiv. NH_3, resulting in the formation of $MgAB.NH_3$. Notably, this compound showed some intriguing dehydrogenation properties that might be useful for hydrogen storage purpose. Quantitative measurements of hydrogen desorption from $MgAB.NH_3$ have shown impressive results: 5.3, 8.4, 9.7 and 11.4 wt% or 2.7, 4.2, 4.9 and 5.7 equiv. H_2 can be released at *ca.* 100, 150, 200 and 300^oC, respectively. Particularly, in each heating experiment, the NH_3 concentration was negligible and was undetectable at 300^oC. Due to the fact that, this compound is novel, up to present, there has been no report on the mechanism of this compound. Thus, it is of utmost importance to propose and investigate the detailed mechanism to shed light on the role of magnesium and gain further insight on how NH_3 plays in the dehydrogenation. Chapter 5 will be devoted to studying the dehydrogenation mechanism of this compound.

In addition to these metal amidoboranes, $LiBH_4.NH_3$ has been extensively researched over the years due to its attractive gravimetric capacity of 18.4 wt%, in particular, it has relatively good reversibility as compared to the other known boron-based storage materials [68]. However, the high dehydrogenation temperatures, slow rates have reduced partly the attractiveness of the compound. Recently, Gao *et al.* has reported that the addition of some metal halides such as $MgCl_2$, $ZnCl_2$ could improve dehydrogenation properties of the $LiBH_4.NH_3$ compound [69]. While $LiBH_4.NH_3$ mainly releases H_2 at 280 and 400^oC, the system $LiBH_4.NH_3.MCl_2$ (M=Mg, Zn) can start to release H_2 at as low as 150^oC. Furthermore, NH_3 release was reported to suppress successfully. Chapter 6 will investigate the system $LiBH_4.NH_3.MgCl_2$ to elucidate the role of lithium and magnesium in improving dehydrogenation properties and suppressing NH_3 release.

Another encouraging achievement comes from the successful synthesis of poly(methyl acrylate)-confined ammonia-borane (denoted as PMA-AB) [70]. The PMA-AB composite was generated through a simple solution-blending process. The PMA was initially dissolved in acetonitrile. Then, it was blended with AB and was stirred for 10 min at room temperature.

Among its outstanding properties, its water-resistant ability, inhibition of harmful volatile products and low temperature of dehydrogenation have greatly attracted attention. Different from most other borohydride systems, which easily absorb water in air, leading to the system damage, this new water-resistant AB-based polymer provides more stable compound for better thermolysis performance. In particular, it still remains its low dehydrogenation temperature, which starts at as low as 70^{o}C. Moreover, this compound can suppress the generation of detrimental boracic impurities. Chapter 7 will be devoted to investigate theoretically the dehydrogenation mechanism of this novel system. This study will shed light on the crucial role of the carbonyl group of the polymer in facilitating the hydrogen release. Then, chapter 8 will continue the study on the dehydrogenation of an analogous composite poly acrylamide-confined ammonia-borane. Finally, some new composites are suggested and a theoretical study will be carried out to systematically examine the dehydrogenation of these new materials with hopes for finding composites with better dehydrogenation properties.

2.5 Theoretical Studies on the dehydrogenation mechanism

In the previous sections, we have comprehensively reviewed some of the most outstanding hydrogen storage materials. Although they are promising candidates for future hydrogen storage materials, it is still desired to improve further the hydrogen storage and hydrogen release properties to make these compounds applicable in reality. To improve these properties, it is of utmost importance to understand the underlying mechanisms of hydrogen release processes. In turn, the mechanisms depends mainly on the structures of these compounds. However, it is quite difficult to investigate both the structures and mechanisms directly by experimental methods. Thus, many theoretical studies have been done to tackle these issues. Up to present, there have been many mechanistic studies on the dehydrogenation of various hydrogen storage materials. However, only those related to ammonia borane or relevant to the compounds of interests in this thesis such as metal amidoranes, polymer-confined ammonia borane will be reviewed.

Early researches focused on the structure determination of NH_3BH_3 both in the gas and solid phases [71-73]. Subsequent researches suggested that ammonia borane adducts might be a potential hydrogen storage materials with reversible hydrogen uptake [74]. Based on these findings, later theoretical studies were done to shed light on the dehydrogenation mechanisms of ammonia borane. Among earliest researches were the studies carried out by V. Son Nguyen *et al* [75-79]. They investigated several dehydrogenation pathways of NH_3BH_3, including monomer pathway, dimer pathway and catalyst pathway. In the monomer pathway, they proposed that BH_3 and NH_3 fragments were generated by decomposition of B-N bonds in BH_3NH_3. In turn,

these fragments, in particular BH_3 acted as an active bifunctional acid-based catalyst for H_2 formation. The B-N bond dissociation energy of 26 kcal/mol was found to be smaller than the energy barrier of 37 kcal/mol for the concerted H_2 elimination. Based on a difference of 11 kcal/mol in barrier heights, they speculated that the thermal decomposition of NH_3BH_3 was dominated by the bond cleavage channel. In the dimer pathway, they indicated that the hydrogen releases were likely to occur from either two starting reactants, including the conventional neutral dimer and two ion pair isomers. Their calculation showed that the most stable gaseous phase dimer **dim** results from a head-to-tail cyclic interaction and was stabilised by 14.0 kcal/mol with respect to the two **ab** monomers. Their studies indicated that the neutral dimer **dim** could generate one H_2 molecule through direct pathways with energy barrier near 45 kcal/mol, substantially higher than that needed in the monomer pathway. The pathway for loss of two H_2 molecules is even higher near 50 kcal/mol. These results were in good agreement with experimental data.

Later studies were devoted to investigating the mechanisms of ammonia triborane. Experimental data showed that oxidative hydrolysis of $NH_3B_2H_7$ in aqueous solution leads to the release of up to 8 equiv of H_2, upon addition of either acids or metal catalysis (such as $RhCl_3$) [80-83]. V. Son Nguyen *et al* applied electronic structure calculations to predict the energetic properties of this compound [84]. Their calculations showed that the molecular hydrogen release reaction was endothermic by 5.6 kcal/mol giving an aminotriborane ring. Subsequently, ammonia triborane can release one H_2 molecule via a direct 1,3-H_2 elimination pathway characterised by an energy barrier of 28.9 kcal/mol. In addition to 1,3-H_2 elimination pathway, H_2 can be released via 1,2-H_2 elimination pathway which was a less favoured process. In

particular, their calculations showed that the barrier height for H_2 release from $B_3H_7NH_3$ was slightly smaller than the B-N bond cleavage energy of 30.7 kcal/mol, which leads to the generation of B_3H_7 and NH_3.

To gain insight into the role of catalysts on the dehydrogenation of NH_3BH_3, V. Son Nguyen *et al* investigated the hydrogen release of this compound in the presence of AlH_3 [85,86]. Their calculations showed some interesting results. Firstly, the energy of the entire process ranges occurred within 20 kcal/mol. The transition state was only 2 kcal/mol above the starting reactants, showing that it was facile for the reaction to occur with the assistance of AlH_3. They concluded that alane could be a more efficient bifunctional catalyst for H_2 release from ammonia borane than BH_3.

In addition to ammonia borane, its derivatives such as $LiNH_2BH_3.NH_3BH_3$ have been investigated recently by Chen. P *et al* [87]. Experimental data showed that compared with lithium amidoborane ($LiNH_2BH_3$) and ammonia borane, this new ammonia borane derivative has better dehydrogenation kinetics and releases 14.8 wt% hydrogen with peak temperature at ca. 80 and 140 ^oC, respectively. Chen. P *et al* employed first principles calculations to reveal the differences in dehydrogenation properties of NH_3BH_3, $LiNH_2BH_3$ and $LiNH_2BH_3.NH_3BH_3$. Their study indicated that Li^+ cations played similar roles in $LiNH_2NH_3.NH_3BH_3$ as in $LiNH_2BH_3$ in destabilizing the B-H and N-H bonds, and the mechanism of the first step dehydrogenation of $LiNH_2BH_3.NH_3BH_3$ is likely via the dissociation and combination of hydridic H^- (B) from $LiNH_2BH_3$ molecule and protonic H^+(N) from the adjacent NH_3BH_3 molecule, leading to the desorption of H_2 at lower temperature.

Though many researches have been devoted to investigating various hydrogen storage systems, the dehydrogenation mechanisms of those compounds such as $Mg(NH_2BH_3)_2.NH_3$, $LiBH_4.NH_3.MgCl_2$ and NH_3BH_3-confined polymers are yet to be investigated theoretically. Thus, the following chapters will focus on the research of the dehydrogenation mechanisms with hope to fulfill these gaps.

References

[1] G. K. Surya Prakash A. G. George A. Olah, *Beyond Oil and Gas: The Methanol Economy*.: WILEY-VCH, 2006.

[2] "Hydrogen," in *Van Nostrand's Encyclopedia of Chemistry*.: Wylie-Interscience, 2005, pp. 797-799.

[3] John Emsley, *Nature's Building Blocks*.: Oxford University Press, 2001.

[4] "Why did oxygen supplant phlogiston?," in *Research programmes in the Chemical Revolution*.: Cambridge Books Online - Cambridge University Press, 2011.

[5] "Just the Facts - Inventions & Discoveries," in *School Specialty Publishing*., 2005.

[6] Albert Stwertka, *A Guide to the Elements*.: Oxford University Press, 1996, pp. 16-21.

[7] Roman J., Santhanam, K. S. V. Press, Miri M. J., A. V. Bailey, and G. A. Takacs, *Introduction to Hydrogen Technology*.: John Wiley & Sons, Inc., 2009.

[8] R. B. Gupta, *Hydrogen Fuel: Production, Transport, and Storage*.: CRC Press, 2009.

[9] P. Enghag, *Encyclopedia of the Elements*.: WILEY-VCH, 2004.

[10] Y. Fukai, *The Metal-Hydrogen System*.: Springer, 2005.

[11] "Springer Series in Materials Science," in *The Metal-Hydrogen System*.: Springer, 2005, vol. 21, pp. 1-8.

[12] S. J. Grabowski, *Hydrogen Bonding - New Insides*, vol. 3, p. 535, 2006.

[13] R. Custelcean and J. E. Jackson, *Chem. Rev.*, vol. 101, no. 7, pp. 1963-1980, 2001.

[14] U.S. Department of Energy. Energy Efficiency & Renewable Energy. [Online]. http://www1.eere.energy.gov/hydrogenandfuelcells/storage/DoE

[15] M. Dresselhaus, G. Crabtree, M. Buchanan, and Eds., "Basic research needs for the hydrogen economy," vol. Basic Energy Sciences, 2003.

[16] "Hydrogen Storage Technologies Roadmap," 2005.

[17] U. Bossel, B. Eliasson, and G. Taylor. (2003) The Future of the Hydrogen Economy: Bright or Bleak? [Online]. http://www.efcf.com/reports/

[18] "MRS Bulletin," vol. 27, pp. 675-716, 2002.

[19] F. Wetzel, *Int. J. Hydrogen Energy*, vol. 23, pp. 339-348, 1998.

[20] H. F. F. Michel, G. Meyer, and F. Theiben, *Int. J. Hydrogen Energy*, vol. 23, p.

191, 1998.

[21] W. L. Mao, C. A. Koh, and E. D Sloan, "Clathrate Hydrates under Pressure," *Phys. Today* , vol. 60, pp. 42-47, 2007.

[22] L. Wang and R. T. New Sorbents for Hydrogen Storage by Hydrogen Spillover - A Review Yang, "Energy Environ. Sci.," vol. 1, pp. 268-279, 2008.

[23] N. L. Rosi et al., "Hydrogen Storage in Microporous Metal - Organic Frameworks," *Science*, vol. 300, pp. 1127-1129, 2003.

[24] A. P. Côté et al., "Porous, Crystalline, Covalent Organic Frameworks," *Science*, vol. 310, pp. 1166-1170, 2005.

[25] A. C. Dillon et al., "Storage of Hydrogen in Single-Walled Carbon Nanotubes," *Nature*, vol. 386, pp. 377-379, 1997.

[26] C. Liu et al., "Hydrogen Storage in Single-Walled Carbon Nanotubes at Room Temperature," *Science*, vol. 286, pp. 1127-1129, 1999.

[27] Y. Zhao, Y. H. Kim, A. C. Dillon, M. J. Heben, and S. B. Zhang, "Hydrogen Storage in Novel Organometallic Buckyballs," *Phys. Rev. Lett.*, vol. 94, p. 155504, 2005.

[28] T. Yildirim and S. Ciraci, " . Titanium-Decorated Carbon Nanotubes as a Potential High-Capacity Hydrogen Storage Medium ," *Phys. Rev. Lett*, vol. 94, p. 175501, 2005.

[29] Q. Sun, Q. Wang, P. Jena, and Y. Kawazoe, "Clustering of Ti on a C60 Surface and Its Effect on Hydrogen Storage ," *J. Am. Chem. Soc.* , vol. 127, pp. 14582-14583, 2005.

[30] Q. Sun, P. Jena, Q. Wang, and M. Marquez, "First-Principles Study of Hydrogen Storage on Li12C60," *J. Am. Chem. Soc.*, vol. 128, pp. 9741-9745, 2006.

[31] S. Orimo, Y. Nakamori, J. R. Eliseo, A. Zuttel, and C. M. Jensen, "Complex Hydrides for Hydrogen Storage," *Chem. Rev.*, vol. 107, pp. 4111-4132, 2007.

[32] P. Chen, Z. Xiong, J. Luo, J. Lin, and K. L. Tan, "Interaction of Hydrogen with Metal Nitrides and Imides," *Nature*, vol. 420, pp. 302-304, 2002.

[33] A. Gutowska et al., "Nanoscaffold Mediates Hydrogen Release and the Reactivity of Ammonia Borane," *Angew. Chem., Int. Ed.*, vol. 44, pp. 3578-3582, 2005.

[34] J. Lan, D. Cao, W. Wang, T. Ben, and G. Zhu, "High-Capacity Hydrogen Storage in Porous Aromatic Frameworks with Diamon-like Structure.," *J.Phys. Chem. Lett.*, vol. 1, pp. 978-981, 2010.

[35] Q. Sun, Q. Wang, P. Jena, B., Reddy, and M. Marquez, "Hydrogen Storage in Organometallic Structures Grafted on Silsequioxanes.," *Chem. Mater.*, vol. 19, pp. 3074-3078, 2007.

[36] M. Yoon et al., "Calcium as the Superior Coatting Metal in Functionalization of Carbon Fullerenes for High-Capacity Hydrogen Storage.," *Phys. Rev. Lett.*, vol. 100, p. 206806, 2008.

[37] J. Zhou, Q. Sun, Q. Wang, P. Jena, and X. S. Chen, "Electric Field Enhanced Hydrogen Storage on Polarizable Materials Substrates.," *Proc. Natl. Acad. Sci. U.S.A.*, vol. 107, pp. 2801-2806, 2010.

[38] G. & Thomas, G. Sandrock, "The IEA/DOC/SNL on-line hydride databases.," *Appl. Phys. A*, vol. 72, pp. 153-155, 2001.

[39] Louis Schlapbach & Andreas Zuttel, "Hydrogen-storage materials for mobile

applications," *Nature*, vol. 414, November 2001.

[40] T., Natsuoka, M. & Iwakura, C. Sakai, "Rare earth intermetallics for metal–hydrogen batteries," *Handb. Phys. Chem. Rare Earths* , vol. 21, pp. 135-180, 1995.

[41] M., Percheron-Guegan, A. & Chabre, Y. Latroche, "Influence of cobalt content in MmNi(4.3–x)Mn0.3Al0.4Cox alloy (x = 0.36 and 0.69) on its electrochemical behaviour studied by in situ neutron diffraction," *J. Alloys Compounds*, no. 295, pp. 637-642, 1999.

[42] A. Zaluska, L. Zaluski, and J. O. Stroem-Olsen, "Structure, catalysis and atomic reactions on the nano- scale: a systematic approach to metal hydrides for hydrogen storage ," *Appl. Phys. A*, vol. 72, p. 157, 2001.

[43] K. Yvon, "Complex transition metal hydrides ," *Chimia*, vol. 52, pp. 613-619, 1998.

[44] E. Akiba and H. Iba, "Hydrogen absorption by Laves phase related BCC solid solution," *ntermetallics*, vol. 6, pp. 461-470, 1998.

[45] T. et al. Kuriiwa, "New V-based alloys with high protium absorption and desorption capacity," *J. Alloys Compounds*, no. 295, pp. 433-436, 1999.

[46] B. Bogdanovic and M. Schwickardi, "Ti-Doped Alkali Metal Aluminum Hydrides as Potential Novel Reversible Hydrogen Storage Materials," *J. Alloys Compd.*, vol. 253, pp. 1-9, 1997.

[47] J. Chen, N. Kuriyama, Q. Xu, H. T. Takeshita, and T. Sakai, *J. Phys. Chem. B*, vol. 105, p. 11214, 2001.

[48] R. A. Zidan, S. Takara, A. G. Hee, and C. M. Jensen, *J. Alloys Compd*, vol. 285, p. 119, 1999.

[49] C. M. Jensen, R. Zidan, N. Mariels, A. Hee, and C. Hagen, *Int. J. Hydrogen Energy*, vol. 24, p. 461, 1999.

[50] V. P. Balema, K. W. Denis, and V. K. Pecharsky, *Chem. Commun.*, p. 1665, 2000.

[51] V. P. Balema, J. W. Wiench, K. W. Denis, M. Pruski, and V. K. Pecharsky, *J. Alloys Compd.*, vol. 329, p. 108, 2001.

[52] Graetz, *J. Chem. Soc. Rev*, vol. 38, p. 73, 2009.

[53] P. Chen and M. Zhu, *Mater. Today* , vol. 11, p. 36, 2008.

[54] J. Irvine, *J. Mater. Chem.*, vol. 18, p. 2295, 2008.

[55] M. Felderhoff, C. Weidenthaler, R. von Helmolt, and U. Eberle, *Phys. Chem. Chem. Phys.*, vol. 9, p. 2643, 2007.

[56] F. Baitalow, J. Baumann, G. Wolf, K. Jaenicke-Rossler, and G. Leitner, *Thermochim. Acta*, vol. 391, p. 159, 2002.

[57] G. Wolf, J. Baumann, F. Baitalow, and F. P. Hoffmann, *Thermochi. Acta*, vol. 343, p. 19, 2000.

[58] G. Wolf, J. C. van Miltenburg, and U. Wolf, *Thermochim. Acta*, vol. 317, p. 111, 1998.

[59] J. Baumann, E. Baitalow, and G. Wolf, *Thermochim. Acta*, vol. 430, p. 9, 2005.

[60] V. Sit, R. A. Geanangel, and W. W. Wendlandt, *Thermochim.Acta*, vol. 113, p. 379, 1987.

[61] M. E. Bluhm, M. G. Bradley, R., III Butterick, U. Kusari, and L. G. Sneddon, *J.*

Am. Chem. Soc., vol. 128, p. 7748, 2006.

[62] M. C. Denney, V. Pons, T. J. Hebden, D. M. Heinekey, and K. I. Goldberg, "J. Am. Chem. Soc.," vol. 128, p. 12048, 2006.

[63] Y. S. Chen, J. L. Fulton, J. C. Linehan, and T. Autrey, *J. Am. Chem. Soc*, vol. 127, p. 3254, 2005.

[64] Feaver A. et al., *J. Phys. Chem. B*, vol. 111, p. 7469, 2007.

[65] Z. Xiong et al., *Nat. Mater*, vol. 7, p. 138, 2008.

[66] D. Y. Kim, N. J. Singh, H. M. Lee, and K. S. Kim, *Chem. Eur. J.*, vol. 15, p. 5598, 2009.

[67] Guotao Wu, Zhitao Xiong, Abhi Karkamkar, Jianping Guo, Mingxian Jian, Ming Wah Wong, Thomas Autrey and Ping Chen Yong Shen Chua, "Synthesis, structure and dehydrogenation of magnesium amidoborane monoammoniate," *Chem. Commun.*, vol. 46, pp. 5752-5754, 2010.

[68] L. L. Shaw, X. F. Wan, J. Z. Hu, J. H. Kwak, and Z. G. Yang, *Journal of Physical Chemistry C*, vol. 114, p. 8089, 2010.

[69] L. Gao, Y. H. Guo, Q. Li, and X. B. Yu, *Journal of Physical Chemistry C*, vol. 114, pp. 9534-9540, 2010.

[70] Zhao. J. et al., *Adv. Mater.* , vol. 22, pp. 394-397, 2010.

[71] D. West, S. Limpijumnong, B. S. Zhang, *Phys. Rev. B.* vol. 80, 064109, 2009.

[72] M. S. Kathmann, V. Parvanov, K. G. Schenter, C. A. Stowe, L. L. Daemen, M. Hartl, J. Linchan, J. N. Hess, A. Karkamkar, T. Autrey, *J. Chem. Phys.*, p. 130, 2009.

[73] A. C. Morrison, M. M. Siddick, *Angew. Chem., Int. Ed.*, vol. 43, p. 4780, 2004.

[74] A. Staubitz, M. Besora, N. J. Harvey, I. Manners, *Inorg. Chem.*, vol. 47, p. 5910, 2008.

[75] T. M. Nguyen, S. V. Nguyen, H. M. Matus, G. Gopakumar, A. D. Dixon, *J. Phys. Chem. A*, vol. 111, pp. 679-690, 2007.

[76] G. Gopakumar, S. V. Nguyen, T. M. Nguyen, *J. Mol. Struc.*, vol. 811, pp. 77-89, 2007.

[77] S.V. Nguyen, H. M. Matus, T. M. Nguyen, A. D. Dixon, *J. Phys. Chem. C*, vol. 111, pp. 9603-9613, 2007.

[78] S. V. Nguyen, H. M. Matus, J. D. Grant, T. M. Nguyen, A. D. Dixon, *J. Phys. Chem. A*, vol. 111, pp. 8844-8856, 2007.

[79] S. V. Nguyen, H. M. Matus, T. M. Nguyen, A. D. Dixon, *J. Phys. Chem. A* **2008**, vol. 112, pp. 9946-9954.

[80] W. C. Yoon, G. L. Sneddon, *J. Am. Chem. Soc.* **2006**, vol. 128, p. 13992.

[82] G. Kodama, W. R. Parry, C. J. Carter, *J. Am. Chem. Soc.* **1959**, vol. 81, p. 3534.

[83] F. E. Westrum, E. N. Levitin, *J. Am. Chem. Soc.* **1959**, vol. 81, p. 3544.

[84] S. V. Nguyen, H. M. Matus, T. M. Nguyen, A. D. Dixon, *J. Phys. Chem. A*, **2008**, vol. 112, p. 9946.

[85] S. V. Nguyen, H. M. Matus, T. V. Ngan, T. M. Nguyen, A. D. Dixon, *J. Phys. Chem. C*, **2008**, vol. 112, pp. 5662-5671.

[86] S. V. Nguyen, S. Swinnen, T. M. Nguyen, A. D. Dixon, *J. Phys. Chem. C*, **2009**, vol. 113, pp. 18914-18926.

[87] L. Wen, S. H. Ralph, C. M. Araújo, W. Guotao, B. Andreas, W. Chenzhang, A. Rajeev, F. P. Yuan, Chen. P, *J. Phys. Chem. C*, **2010**, vol. 114, pp. 19089-19095.

CHAPTER 3

THEORETICAL BACKGROUNDS

3.1 Introduction

Theoretical chemistry is the subfield of chemistry where mathematical methods combining with fundamental laws of physics are employed to investigate the processes of chemical relevance such as energies, reaction mechanisms, spectroscopic properties, etc. Nowadays, with the development of many fast supercomputers, the charming combination between theoretical chemistry and the power of supercomputers has formed a new branch, computational chemistry. It can aid chemists in understanding reaction mechanisms, making predictions or investigating the unknown reactions before running the actual experiments so that they can be better prepared for making observations. Currently, it rapidly becomes a useful way to explore novel materials, reactions that are inaccessible experimentally. This chapter will introduce some fundamental knowledge that computational chemistry based on to offer the aforementioned benefit and more importantly employed to serve my research on some novel hydrogen storage materials. The chapter begins by introducing the concept of potential energy surface (PES), which is of utmost importance in understanding geometry structures, kinetic and thermodynamic properties of any reaction. Then it explores the underlying principles of quantum chemical methods, in particular the Density Functional Theory method (DFT), which is employed in this thesis to establish the PES of dehydrogenation reactions. Subsequently, we

concentrate on explaining how this method will be used in Gaussian to calculate thermodynamic quantities such as enthalpy, free Gibbs energy. Finally, Natural Bond Orbital (NBO) analysis, solvation models will be succinctly presented.

3.2 Potential Energy Surface

A potential energy surface (PES) is a mathematical function that establishes the relationship between the geometry of a molecule and its corresponding energy. R. Marcelin [1] was the first to introduce this concept of the PES in his dissertation. His research laid the groundwork for transition-state theory 20 years before the much better known work of Eyring [2,3] who first calculated the PES, using a mixture of experiment and theory [4]. Currently, many important concepts that seem to be mathematically challenging can be grasped intuitively with the insight provided by the idea of the PES [5-7]. When discussing the PES of a reaction, we mainly focus on the following distinct points that characterise the PES:

1. Local Maxmima: the points that occupy the highest energy in a particular section or region of the PES and any small change in the geometry will lower the energy.

2. Global Maximum: the point that occupies the highest value in the entire PES.

3. Local Minima: the points that occupy the lowest value in a particular section or region of the PES and any small change in the geometry will increase the energy.

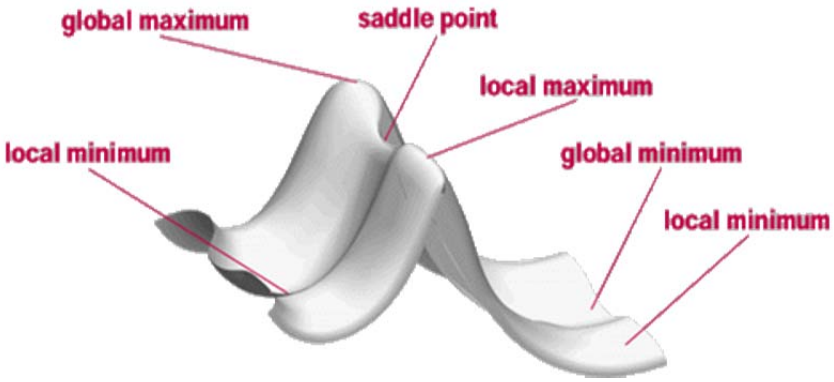

Figure 3.1 A potential energy surface.

4. Global Minimum: the point that occupies the lowest value in a particular section or region of the PES.

5. Saddle point: the point that is a maximum in one direction and a minium in all other directions.

In this thesis, only local minima and saddle points are of our interests because local minima correspond to reactant and product structures in reaction systems and saddle points correspond to the transition states. These species of interest are also called the stationary points on the PES. Regarding geometry, a stationary point on a PES is a point at which the surface is flat, i.e. parallel to the horizontal line corresponding to the one geometric parameter. Mathematically, a stationary point is one at which the first derivative of the potential energy with respect to each geometric parameter is zero:

$$\frac{\partial E}{\partial q_1} = \frac{\partial E}{\partial q_2} = \cdots = 0 \tag{3.1}$$

Partial derivatives in (3.1) emphasise that each derivative is with respect to just one of the variables q of which E is a function. It should be noted that although the first derivative of minima and saddle points is zero, their second derivatives take different values:

For a minimum:

$$\frac{\partial^2 E}{\partial q^2} > 0 \tag{3.2}$$

for all q.

For a transition state:

$$\frac{\partial^2 E}{\partial q^2} > 0 \tag{3.3}$$

for all q, except along the reaction coordinate, and

$$\frac{\partial^2 E}{\partial q^2} < 0 \tag{3.4}$$

along the reaction coordinate.

In summary, computational chemistry is essentially the study of the stationary points on a PES. When we study stable molecules such as reactants, products, intermediates, we focus on minima. When we examine chemical reactions, we

investigate the passage of a molecule from a minimum through a transition state to another minimum.

3.3 Geometry Optimisation

Geometry optimisation is the process of locating a stationary point on a potential energy surface. As discussed in the previous section, the stationary point of interest might be a minimum, a transition state, or, occasionally, a high-order saddle point. Locating a minimum is called an energy minimisation, and locating a transition state refers to specifically as a transition state optimisation. In this thesis, geometry optimisation is started with an input structure that is believed to resemble (the closer the better) the desired stationary point. Then the level of theory such as B3LYP and the 6-31+G(2d,p) basis set, which will be discussed later, are specified. Finally, submit this plausible structure to Gaussian 09. The program will initially calculate the energy and the gradient at that starting point to determine if it has reached a stopping point, which is convergence. If the convergence condition is not satisfied, the program will systematically change the geometry based on the size of the gradient. New integrals will be computed, new self-consistent field calculations are done, and a new energy and gradients are calculated. This process will continue until it has found a stationary point. In other words, the program terminates calculation when reaching convergence.

There are several algorithms for performing optimisation such as Berny, Fletcher-Powell, quasi-Newton etc. However, it is beyond the scope of this methodology, thus it will not be discussed in detail here. It should be noted that,

despite these powerful methods, the initial guess of the starting geometry is extremely important and thus require computational chemists to have a deep relevant knowledge on the researched molecules because the gradient calculations do not always find the stationary point intended. It is likely to converge to the stationary point that is close to the starting geometry on the potential energy surface.

3.4 Calculation Methods

3.4.1 Introduction

Currently, there are different computational methods to make calculations such as molecular mechanics, semi-empirical techniques, *ab initio*, density functional calculation and molecular dynamics.

Molecular mechanics employs classical physics to explain and interpret the behavior of atoms and molecules. Molecular mechanics treats a molecule as a collection of balls (atoms) held together by springs (bonds). If the normal spring lengths and the angels between balls (atoms) are known, the energy needed to stretch and bend the springs will be computed. Repeatedly changing the geometry until the lowest energy found allows us to perform a geometry optimisation, i.e. to find the ground state energy of a molecule. Of these three main methods, the molecular mechanics method requires least computer resources and produce fast results due to its simplicity in calculation in comparison with other two methods. For example, the optimisation result of a fairly big molecule like a disaccharide $C_{12}H_{22}O_{11}$ can be obtained in seconds on a powerful desktop computer. Thus, this method is the best

choice for large systems with thousands of atoms such as enzymes, DNA. However, this method has two main limitations. Firstly, each force field achieves good approximation for a limited class of molecules, which was parameterised. No force field can be generally applied to all molecular systems of interest. Secondly, molecular mechanics calculations don't explicitly treat the electrons in a molecular system. Thus, it is not proper for the systems or processes in which electron presence plays the crucial role such as breaking or forming of bonds.

To overcome this drawback of molecular mechanics, semi-empirical was developed. This method combines both the quantum physics and experimentally derived empirical parameters in its calculation. One the most advantages of this method is that it is capable of calculating transition states and excited states while it is less demanding computationally than the *ab initio* method, which will be discussed later. However, this method requires experimental data for parameters, which cannot be satisfied in many cases. In these cases, *ab initio* method is the best choice since it completely employs quantum physics without empirical parameters needed. This method is very useful for abroad range of systems. In particular, it is extremely useful when the finding of transition states or new compounds or intermediates are of concern.

Ab initio, which means "from scratch" in Latin, is a group of methods in which only Schrödinger equation [8], the values of the fundamental constants and the atomic numbers of the atoms present are employed to calculate molecular structures.

Density Functional calculation is similar to *ab initio* and semi-empirical methods in terms of applying the Schrödinger equation. However, different from the other two methods, instead of calculating a wave function, DFT derives the electron distribution (electron density function) directly. This method is faster than *ab initio*, but slower than semi-empirical. DFT methods are attractive since they take into account the effects of electron correlation to explain the fact that electrons in a molecular system react to others' motion and attempt to keep out of another's way.

In contrast to the previous four methods, which investigate the static molecules, molecular dynamics calculations explore the motion of the molecules. For example, the motion of an enzyme can be simulated as it changes shape on binding to a substrate.

The next part will provide deeper knowledge on quantum mechanics, which is the foundation of the *ab initio* methods. Then, DFT method will be carefully discussed.

3.4.2 Quantum Mechanics

3.4.2.1 The Schrödinger Equation

In the beginning of the last century, quantum mechanics was developed to describe the behavior of newly explored microscopic particles, which could not be elucidated by classical mechanics. The heart of quantum mechanics was the Schrödinger equation formulated by Erwin Schrödinger in 1926 [8]. The general

form of Schrödinger equation is the time-dependent equation, which describes the evolution of a system with time by calculating the future wave function of a system. The time-dependent Schrödinger equation can be expressed as:

$$\left(\frac{-\hbar^2}{2m}\nabla^2 + V\right)\Psi(\boldsymbol{r},t) = i\hbar\frac{\partial\Psi(\boldsymbol{r},t)}{\partial t} \tag{3.5}$$

Where ħ is the Planck's constant divided by 2π, m is the mass of the system, V is the potential energy operator, Ψ is the wave function of the system as a function of position, $\boldsymbol{r}$, and time, t. By solving Equation (3.5) for Ψ, the energy and other properties of the system can be determined.

However, in many problems of interest, the simpler time-independent Schrödinger can be derived based on the assumption that the potential energy V is not a function of time but depends solely on the coordinates, thus it takes the form:

$$\left(\frac{-\hbar^2}{2m}\nabla^2 + V\right)\Psi(\boldsymbol{r}) = E\Psi(\boldsymbol{r}) \tag{3.6}$$

This equation is expressed in the general form as:

$$H\Psi(\boldsymbol{r}) = E\Psi(\boldsymbol{r}) \tag{3.7}$$

where E is the total energy of the system and H is the Hamiltonian operator, which will be further discussed in the next part.

The solutions to Equation (3.7) yield the energy terms of the different states and other properties of the system. However, the exact solution to the Schrödinger equation cannot be achieved for any system larger than hydrogen atom or hydrogen-type atom. Thus, the ultimate goal of quantum chemistry is to establish some assumptions to obtain approximate solutions to the Schrödinger equation for these systems. Prior to discussing these assumptions, all the terms of Hamiltonian Operator will be explained in detail for further use.

3.4.2.2 The Hamiltonian Operator

The Hamiltonian operator, H, is the sum of a kinetic term, T, and a potential energy term, V:

$$H = T + V \tag{3.8}$$

The terms T and V has the form:

$$T = -\sum_{k} \frac{\hbar^2}{2m_k} \nabla_k^2 \tag{3.9}$$

$$V = \frac{1}{4\pi\varepsilon_0} \sum_{j} \sum_{k<j} \frac{e_j e_k}{\Delta r_{jk}} \tag{3.10}$$

The Hamiltonian in a molecular system, whereby there are interactions between the nuclei and electrons, can be expressed as:

$$H = -\sum_i \frac{\hbar^2}{2m_e}\nabla_i^2 - \sum_A \frac{\hbar^2}{2m_A}\nabla_A^2 - \sum_i \sum_A \frac{1}{4\pi\varepsilon_0}\frac{Z_A e^2}{\Delta r_{iA}} + \sum_i \sum_{j<i} \frac{1}{4\pi\varepsilon_0}\frac{e^2}{\Delta r_{ij}} + \sum_A \sum_{B<A} \frac{1}{4\pi\varepsilon_0}\frac{Z_A Z_B e^2}{\Delta R_{AB}}$$

$$= H_{elec}^{KE} + H_{nuclei}^{KE} + H_{elec-nuclei}^{PE} + H_{elec-elec}^{PE} + H_{nuclei-nuclei}^{PE} \quad (3.11)$$

where i and j represent electrons, A and B represent nuclei, m_e is the mass of the electron, m_A is the mass of the nucleus, $\Delta \boldsymbol{r_{ab}}$ is the distance between 2 particles a and b, e is the charge of the electron and Z is the atomic number.

In the Equation (3.11), the first two terms represent the kinetic of the electrons and the nuclei. The third term describes the coulomb attraction between the electrons and the nuclei. The remaining two terms refer to the potential energy from nuclear-nuclear repulsion.

3.4.2.3 Born-Oppenheimer Approximation

Born-Oppenheimer approximation is the first assumption to simplify the Schrödinger equation, thus yields an approximated solution to the system larger than hydrogen atom [9]. This approximation is based on the fact that nuclei is thousands of times larger than that of electrons, thus the electrons can be approximated to move much faster than the nuclei, and able to react instantaneously with nuclear motion. Based on this assumption, the nuclear and electronic motions can be separated and the electronic energies can be computed for fixed nuclei positions. The Schrödinger equation can thus be simplified by ignoring the kinetic energy of the nuclei and

approximating the nuclear-nuclear interaction to a constant. The simplified Schrödinger equation now can be expressed as the electronic Schrödinger equation:

$$H_{elec}\Psi_{elec} = \varepsilon_{elec}\Psi_{elec} \tag{3.12}$$

where

$$H_{elec} = -\sum_i \frac{1}{2}\nabla_i^2 - \sum_i \sum_A \frac{Z_A e^2}{\Delta r_{iA}} + \sum_i \sum_{j<i} \frac{e^2}{\Delta r_{ij}}$$

$$= H_{electrons}^{KE} + H_{electrons-nuclei}^{PE} + H_{electrons-electrons}^{PE} \tag{3.13}$$

The electronic wave function in Equation (3.12) describes the motion of electrons as a function of its coordinates, but has a parametric dependence on the nuclear coordinates. Thus, the nuclear-nuclear repulsion term, which is added as a constant, must be included in the total energy:

$$\varepsilon_{tot} = \varepsilon_{elec} + \sum_A \sum_{B<A} \frac{Z_A Z_B e^2}{\Delta R_{AB}} \tag{3.14}$$

Similarly, the motion of nuclei can be solved under the same assumptions. The nuclear Hamiltonian can be created for the motion of nuclei in an average field of electrons since the electrons move much faster than the nuclei. Solving the nuclear Schrödinger equation produces the vibrational, rotational and translational states of the nuclei.

3.4.2.4 Corrections to the Potential Energy Surface

It should be noted that, the energies obtained from solving the Schrödinger equation based on the Born-Oppenheimer approximation are the electronic energies. However, the total molecular energy must include the nuclear repulsion energies. This approximation did not consider the quantum mechanical nature of nuclear vibrations. According to the uncertainty principal, molecular vibrations still persist even at zero Kelvin and never go to zero [10]. The amount of vibrational energy retained at 0K is called the zero-point correction energy. Summing up the zero-point correction energies to electronic energies is critically important to get closer to the realistic values of total energy. In most modern computational software packages, zero-point corrections are calculated based on the harmonic-oscillator assumption. Another available method is to scale computed zero-point energies to match the experimentally determined values.

3.4.2.5 Hartree-Fock Theory

A second assumption to simplify the Schrödinger equation is Hartree-Fock method. This method is based on the assumption that the many-body wave function can be represented by a single Slater determinant. Employing an iterative algorithm, which gives the method another name "Self-Consistent Field Method", the resulting non-linear equations can be solved to yield the HF wave function and energy [11,12]. Though having many limitations, particularly the inadequate treatment of electron correlation, this method has established the foundation for most *ab initio* quantum

mechanical methods. The derivation of the HF theory will be described in the following subsections.

Hartree-Product Wave Function

The Halmitonian for a system with non-interacting electrons can be expressed as a sum of single-electron Hamiltonians:

$$H = \sum_{i=1}^{N} h_i \tag{3.15}$$

The wave function Ψ can also expressed as a product of one-electron wave function, forming the Hartree-product wave function:

$$\begin{aligned} \Psi(\boldsymbol{r}) &\approx \Phi(\boldsymbol{r}) \\ &= \varphi_1(\boldsymbol{r})\varphi_2(\boldsymbol{r}) \dots \dots \varphi_n(\boldsymbol{r}) \end{aligned} \tag{3.16}$$

where Ψ must satify the normalised and orthogonal requirements.

However, the Hartree-product wave function is non-symmetric. Since electrons have half-integer spin, inter-exchanging 2 electrons should cause a change in sign of the wave function, but the Hartree-product wave function does not satisfy this principle.

The Wave Function as a Slater Determinant

To satisfy the anti-symmetric principle, the wave function Ψ can be expressed as a determinant of spin orbitals, known as a Slater determinant. A spin orbital is the product of the molecular orbital and spin coordinate, α and β. Taking a system with 2 electrons with the same spin, α, the Hartree-product can be written as:

$$\Phi_{HP}(r_1, r_2) = \varphi_1(\boldsymbol{r_1})\alpha(1)\varphi_2(r_2)\alpha(2) \tag{3.17}$$

To satisfy the anti-symmetric principle, the wave function is expressed with a determinant, termed the Slater determinant:

$$\Phi(r_1, r_2) = \frac{1}{\sqrt{2}}\begin{vmatrix} \varphi_1(\boldsymbol{r_1})\alpha(1) & \varphi_2(\boldsymbol{r_1})\alpha(1) \\ \varphi_1(\boldsymbol{r_2})\alpha(2) & \varphi_2(\boldsymbol{r_2})\alpha(2) \end{vmatrix} \tag{3.18}$$

For an N-electron system, the Slater determinant can be written as:

$$\Phi(\mathbf{r}) = \frac{1}{\sqrt{N!}}\begin{vmatrix} \varphi_1(\boldsymbol{r_1})\alpha(1) & \varphi_1(\boldsymbol{r_1})\beta(1) & \varphi_2(\boldsymbol{r_1})\alpha(1) & \varphi_2(\boldsymbol{r_1})\beta(1) & \cdots & \varphi_{N/2}(\boldsymbol{r_1})\alpha(1) & \varphi_{N/2}(\boldsymbol{r_1})\beta(1) \\ \varphi_1(\boldsymbol{r_2})\alpha(2) & \varphi_1(\boldsymbol{r_2})\beta(2) & \varphi_2(\boldsymbol{r_2})\alpha(2) & \varphi_2(\boldsymbol{r_2})\beta(2) & \cdots & \varphi_{N/2}(\boldsymbol{r_2})\alpha(2) & \varphi_{N/2}(\boldsymbol{r_2})\beta(2) \\ \vdots & \vdots & \vdots & \vdots & \ddots & \vdots & \vdots \\ \varphi_1(\boldsymbol{r_N})\alpha(N) & \varphi_1(\boldsymbol{r_N})\beta(N) & \varphi_2(\boldsymbol{r_N})\alpha(N) & \varphi_2(\boldsymbol{r_N})\beta(N) & \cdots & \varphi_{N/2}(\boldsymbol{r_N})\alpha(N) & \varphi_{N/2}(\boldsymbol{r_N})\beta(N) \end{vmatrix} \tag{3.19}$$

An implication of anti-symmetrizing a Hartree-product to yield a Slater determinant is the exchange correlation, where 2 electrons of the same spin has a lowered probability of being close to each other.

In using a single Slater determinant to represent a many-electron system, it is assumed that each electron experiences an average potential due to the rest of the electrons, rather than explicit electron-electron interactions.

3.4.3 Density Functional Theory

3.4.3.1 Principles of Density Functional Theory

Density Functional Theory is based on the two Hohenberg-Kohn theorems [13]. The first Hohenberg-Kohn theorem [14] states that all the properties of a molecule in a ground electronic state are determined by the ground state electron density function $\rho_0(x, y, z)$. The second Hohenberg-Kohn theorem [14] defines an energy functional for the system and proves that the correct ground state electron density minimises this energy functional.

The first theorem says that there exists the relationship between the ground state electron density function $\rho_0(x, y, z)$ and any properties of a molecule such as the energy E_0, thus, this relationship can be represented as:

$$\rho_0(x, y, z) \rightarrow E_0 \tag{3.20}$$

$$E_o = F[\rho_0] = E[\rho_0] \tag{3.21}$$

Although this theorem assures that molecular properties calculation from the electron density is possible, it should be noted that the first theorem is "merely" an existence theorem: it states that a functional F exists, but does not demonstrate how to find it; thus it is the main problem with DFT.

The second Hohenberg-Kohn theorem implies that any trial electron density function will give an energy value higher than (or equal to, if it were exactly the true electron density function) the true ground state energy. The second theorem can thus be stated:

$$E_v[\rho_t] \geq E_0[\rho_0] \tag{3.22}$$

where ρ_t is a trial electronic density and $E_0[\rho_0]$ is the true ground state energy, corresponding to the true electronic density ρ_0. The trial density must meet the following requirements: (1) $\int\rho_t(r)dr = n$, where n is the number of electrons in the molecule; (2) $\rho_t(r) \geq 0$ for all r since the number of electrons per unit volume cannot be a negative value. This theorem assures us that any value of the molecular energy calculated from the Kohn-Sham equations will be greater than or equal to the true energy. However, it should be noted that this statement is true only if the functional used were exact. In practice, the exact functional is unknown, so actual DFT calculations use approximate functionals. Thus, they are not variational; they can yield an energy below the true energy.

3.4.3.2 The Kohn-Sham Approach to DFT Calculations

There are two fundamental ideas behind the Kohn-Sham approach to molecular DFT calculations: (1) The molecular energy will be displayed as a sum of terms, only one of which, a relatively small term, involves the unknown functional. Thus, even when this small term encountered large errors, these errors will not affect significantly to the total energy. (2) Initial guess of the electron density ρ in the KS

equations will be employed to compute an initial guess of the KS orbitals; in turn, this first guess is then utilised to refine these orbitals. The final KS orbitals obtained will be used to calculate an electron density, which aids in calculating the system energy.

To obtain the equation for the ground state energy of our molecule, we initially propose a fictitious non-interacting reference system, defined as one in which there are no interactions between electrons and in which the ground state electron density ρ_r is exactly identical as in our real ground state system: $\rho_r = \rho_0$. It is noted that, we regard the energy of our molecule as a deviation from an ideal energy of the reference system, which can be computed exactly later; the relatively small discrepancy contains the unknown functional, whose approximation is our main issue. The energy mentioned here is only the electronic energy of the molecule; the total internal "frozen-nuclei" energy of our molecule can be calculated later by adding the internuclear repulsions and the 0 K total internal energy by further adding the zero-point energy.

The following equation indicates the terms forming the ground state electronic energy, including electron kinetic energies, the nucleus-electron attraction potential energies, and the electron-electron repulsion potential energies and each is a functional of the ground-state electron density:

$$E_0 = \langle T[\rho_0] \rangle + \langle V_{Ne}[\rho_0] \rangle + \langle V_{ee}[\rho_0] \rangle \tag{3.23}$$

The middle term can be expressed as:

$$\langle V_{Ne} \rangle = \int \rho_0(r) v(r) dr \tag{3.24}$$

So, equation (1.1) takes the form:

$$E_0 = \int \rho_0(r) v(r) dr + \langle T[\rho_0] \rangle + \langle V_{ee}[\rho_0] \rangle \tag{3.25}$$

Unfortunately, these other two terms, $\langle T[\rho_0] \rangle$ and $\langle V_{ee}[\rho_0] \rangle$, are not known, thus equation (3.25) cannot be used at this point. However, the idea of a reference system will be employed to solve this issue. Two quantities $\Delta\langle T[\rho_0] \rangle$ and $\Delta\langle V_{ee}[\rho_0] \rangle$ are defined as the deviation of the real kinetic energy from that of the reference system and the real electron-electron repulsion energy from a classical charge-cloud Coulomb repulsion energy, respectively. Thus, these two quantities will be expressed in the following equations:

$$\Delta\langle T[\rho_0] \rangle \equiv \langle T[\rho_0] \rangle - \langle T_r[\rho_0] \rangle \tag{3.26}$$

and

$$\Delta\langle V_{ee}[\rho_0] \rangle = \langle V_{ee}[\rho_0] \rangle - \frac{1}{2} \iint \frac{\rho_0(r_1)\rho_0(r_2)}{r_{12}} dr_1 dr_2 \tag{3.27}$$

Introducing (3.26) and (3.27) to equation (3.23), equation (3.23) now can be written as:

$$E_0 = \int \rho_0(r)v(r)dr + \langle T_r[\rho_0]\rangle + \frac{1}{2}\iint \frac{\rho_0(r_1)\rho_0(r_2)}{r_{12}} dr_1 dr_2 + \Delta\langle T[\rho_0]\rangle + \Delta\langle V_{ee}[\rho_0]\rangle \quad (3.28)$$

The sum of two terms $\langle T[\rho_0]\rangle$ and $\Delta\langle V_{ee}[\rho_0]\rangle$ is called the exchange-correlation energy functional or the exchange-correlation energy, E_{XC}.

$$E_{XC} = \Delta\langle T[\rho_0]\rangle + \Delta\langle V_{ee}[\rho_0]\rangle \quad (3.29)$$

Using equation (3.29), equation (3.28) can be expressed as:

$$E_0 = \int \rho_0(r)v(r)dr + \langle T_r[\rho_0]\rangle + \frac{1}{2}\iint \frac{\rho_0(r_1)\rho_0(r_2)}{r_{12}} dr_1 dr_2 + E_{XC} \quad (3.30)$$

In this equation, the first three terms are readily calculated while the last term, which is the exchange-correlation energy functional, $E_{XC}[\rho_0]$ is unknown and requires some methods of calculation to be devised. The next part will briefly discuss some methods used to treat this exchange-correlation energy functional.

3.4.3.3 The Exchange-Correlation Functionals

The major problem with DFT is that the exact functionals for exchange and correlation are not known except for the free electron gas. Thus, many DFT methods with different functionals for exchange and correlation have been proposed with varying effectiveness. These methods, thus can be classified according to how they "guess" this functional. Some outstanding groups of DFT methods include the Local

Density Approximation (LDA), the Generalised Gradient Approximation (GGA), the meta-GGA, and the Hybrid DFT methods.

LDA methods are based on the assumption that the exchange-correlation functional depends solely on the electron density at each point in space. Most LDA methods take advantages of the Homogenous Electron Gas (HEG) model, which split the exchange-correlation energy into separate exchange and correlation parts. The exchange functional in HEG model takes a simple analytic form while the correlation functional has limited expression and various different correlation functionals have been devised. Some of the most known LDA correlation functionals are VWN, PZ81, CP and PW92.

Currently, the most widely used hybrid functional and in fact the most popular DFT functional is based on an exchange-energy functional developed by Becke in 1993, and further improved by Stevens *et al.* in 1994 by introduction of the LYP 1988 correlation-energy functional. This exchange-correlation functional, called the Becke3LYP or B3LYP functional [15] takes the form:

$$E_{xc}^{B3LYP} = (1 - a_0 - a_x)E_x^{LSDA} + a_0E_x^{HF} + a_xE_x^{B88} + (1 - a_c)E_c^{VWN} + a_cE_c^{LYP} \quad (3.31)$$

In this equation, E_x^{LSDA} is the pure DFT LSDA non-gradient-corrected exchange functional. E_x^{HF} is the KS-orbital-based HF exchange energy functional, E_x^{B88} represents the Becke 88 exchange functional mentioned earlier, E_c^{VWN} is the Vosko, Wilk, Nusair function which contributes to the accurate functional for the homogeneous electron gas of the LDA and the LSDA, and E_c^{LYP} is the LYP

correlation functional mentioned above; The three parameters, a_0, a_x and a_c are determined by fitting the predictions of the method to a set of calculated thermodynamic data such as atomisation energies, ionisation potentials and proton affinities. Among those functionals that have been comprehensively examined, the B3LYP is the most useful one [16]. However, B3LYP is known to perform poorly for predictions of reaction kinetics and for geometries and energies of molecules with long-range interactions.

Another family of hybrid DFT methods are the M05 and M06 [17] methods developed by Truthlar and Zhao. The exchange-correlation functionals of these methods take the form:

$$E_x^{Hyb} = \frac{X}{100} E_x^{HF} + \left(1 - \frac{X}{100}\right) E_x^{DFT} + E_c^{DFT} \tag{3.32}$$

The first term represents the exchange energy from Hartree-Fock method. The next two terms refer to the local DFT exchange and correlation energies. X is the contribution percentage of HF exchange in the methods. It is calculated by benchmarking the methods' results against selected thermodynamic databases. The M05 and M06 family of DFT methods perform well for conjugated π systems and weak for non-covalent interactions. Particularly, M06-2X was known to perform the best among the family for π-π stacking interactions.

3.4.3.4 Strengths and Weakness of DFT

Strengths

In contrast to other wave function methods, DFT takes into account electron correlation in its theoretical basis, thus it gives better calculation results for geometries and relative energies in comparison with MP2 calculations, in roughly the same time as needed for HF calculations. Furthermore, DFT appears to be a good candidate for geometry and energy calculations on transition metal compounds, for which conventional *ab initio* calculations often give poor results [18-20].

DFT employs the concept of electron density, which can be measured and is easily intuitively grasped [21] whereas wave function, which is commonly used in other methods is a mathematical entity whose physical meaning is still controversial.

Weaknesses

The major problem in DFT method is the unknown exchange-correlation functional $E_{XC}[\rho_0]$ which must be "guessed". Moreover, there is currently no method to systematically improve the approximation results. In contrast, in *ab initio* method, accuracy in energies may be achieved by using bigger basis sets and by expanding the correlation method: MP2, MP3 or more determinants in the CI approach. Currently, with the aid of experience and intuition, along with checking the calculations against experiment, the accuracy of DFT is being gradually improved.

3.4.4 Basis Sets

3.4.4.1 Introduction

To compute certain properties of a molecule such as electronic energy, bond formation energy, an understanding on molecular orbitals is needed. Molecular orbitals, in turn, are typically built based on the atomic orbitals, although the functions are not necessarily conventional atomic orbitals; they can be any set of mathematical functions that facilitate manipulation and which in linear combination produce good approximations of MOs. To approximate atomic orbitals, computational chemists employ basis sets. By definition, a basis set is a set of mathematical functions (basis functions), linear combinations of which yield molecular orbitals. In other words, several (usually) basis functions describe the electron distribution around an atom and the combination of atomic basis functions represents electron distribution in the molecule as a whole. Basis sets may be classified into two general categories: Minimal basis sets, which describes only the most basic aspects of the orbitals and extended basis sets, which describes the orbital in more detail. Prior to discussing two categories of basis sets, the next part will briefly discuss about Slater and Gaussian functions, which are employed to establish basis sets functions.

3.4.4.2 Slater and Gaussian Functions

The electron distribution around an atom can be represented in several ways. Hydrogen-like functions based on solutions of the Schrödinger equation for the hydrogen atom can be employed. However, Schrödinger equation can only be exactly solved for hydrogen or hydrogen-type atom due to the fact that this equation involves

solving partial differential equations. Thus, John Slater devised a set of 6 empirical rules to approximate wave functions including:

(1) Array orbitals: 1s, 2s, 2p, 3s, 3p, 3d, …
(2) Only the orbital containing the electron in question and the one below it is taken into account.
(3) Electrons lower than (2) are interior orbitals.
(4) Electrons higher than (2) are exterior orbitals.
(5) Electrons designated s (1s, 2s, etc.) have a screening constant of 0.30.
(6) Electrons in the same orbital have a screening constant of 0.85.

One example of a Slater function has the following form:

$$\emptyset(r) = re^{-\frac{-(Z-s)}{na_0}} \tag{3.33}$$

This function involves the radial distance in units of Bohrs, r/a_0, a negative exponential $e^{-\frac{-(Z-s)}{na_0}}$ where n is the principal quantum number such as 1, 2, 3 for H, He, and the first two full rows of the periodic table, and a_0 is the Bohr radius, Z is the nuclear charge. It should be noted that this equation involves only the radial part for the first two full rows in the periodic table, while the spherical harmonics are ignored. One the main advantage of STOs is to resemble the atomic orbitals of the hydrogen atom closely, thus being able to provide accurate description of the wave function. The cusp condition at the nucleus is accurately described by the exponential term $e^{-\zeta r}$ in the functional of an STO, which is given by:

$$\chi_i(r,\theta,\phi;\zeta,n,l,m) = Nr^{n-1}e^{-\zeta r}Y_l^m(\theta,\phi) \tag{3.34}$$

where r, θ, ϕ are spherical coordinates; n is the principal quantum number; l is the angular momentum quantum number; m is the magnetic quantum number; ζ is the Slater orbital exponent; N is the constant for normalisation; $Y_l^m(\theta,\phi)$ is the spherical harmonic functions which describes the orbital shape.

Another advantage of Slater function is its simplicity, particularly for the first three rows of the table, thus it would be the natural choice for *ab initio* basis functions. However, the problem lies in the calculation. During STO calculation of a molecule, the evaluation of certain two-electron integrals requires excessive computer time if Slater functions are used. To solve this issue, S. F. Boys developed a method of using combination of Gaussian Type orbitals in order to express the STO equation. The Gaussian Type Orbital (GTO) equation has the form:

$$g(x,y,z;\alpha,i,j,k) = Ne^{-\alpha r^2}x^i y^j z^k \tag{3.35}$$

where x, y, z are spherical coordinates; α is the Gaussian orbital exponent; i, j and k are integral exponents at Cartesian coordinates; $r^2 = x^2 + y^2 + z^2$.

Although GTOs have the advantage of fast 2-electron integral calculations, when being used to represent an individual atomic orbital, there are large deviations between GTOs and STOs at r=0 and at large r. At the nucleus, where r=0, GTOs lack the cusp condition, which is present in STOs and in real hydrogenic atomic orbitals. At large r, the $e^{-\alpha r^2}$ Gaussian function falls off more rapidly than the $e^{-\zeta r}$ Slater

function. To have a better approximation, a contraction scheme can be carried out, where a linear combination of GTOs are contracted to create the basis functions, instead of using one GTO. The contraction exponent and coefficients can be assigned such that the cusp and decay conditions can be satisfied to resemble a STO. This combines the computational efficiency of GTOs with the proper shape of STOs for good approximations.

3.4.4.3 Types of Basis Sets

As said earlier in the introduction, there are two types of basis sets: minimal basis set and the extended basis set. Minimal basis sets only give basic descriptions of molecular orbitals while extended basis sets give more detailed descriptions of molecular orbitals by considering the higher orbitals of the molecule and account for size and shape of molecular charge distributions. An example of a minimal basis set is the STO-3G [22].

The "STO" means we are attempting to represent a STO equation for our molecule. The 3G means that in order to form that STO equation, 3 Gaussian primitives are combined. All basis set equations in the form of STO-NG are minimal basis sets. There are several types of extended basis sets, including:

- Double-Zeta, Triple-Zeta, Quadruple-Zeta
- Split-Valence
- Polarised Sets
- Diffuse Sets

Double-Zeta, Triple-Zeta, Quadruple-Zeta

The minimal basis sets describes all orbitals to be of the same shape. However, this description is not accurate. To have a more accurate representation of the orbitals, the double-zeta basis set is needed since it allows treating each orbital separately when Hartree-Fock calculation is conducted. To express each atomic orbital, two terms which are two Slater-type orbitals are used. These two terms are similar except for the value of ζ_1 and ζ_2. The zeta value represents how diffuse (large) the orbital is. These two terms are then added in some proportion, to reflect the extent each term contributes to the final orbital. As a result, the size of the atomic orbital can range between the values of either of the two terms. The following equation expresses a 2s orbital:

$$\phi_{2s}(r) = \phi_{2s}^{STO}(r, \zeta_1) + d\phi_{2s}^{STO}(r, \zeta_2) \tag{3.36}$$

In this equation, the first term represents the Slater Orbital 1, the second term represents the Slater Orbital 2. The constant "d" accounts for the percentage of the second Slater Orbital contributing to the final orbital 2s. The triple and quadruple-zeta basis sets work similarly, except they use three and four terms in the equations, respectively.

Split-Valence

Obviously, calculating a double-zeta for every orbital will cost much time and effort. Furthermore, it is unnecessary to apply this calculation on the inner-shell

electrons, which have less contribution on the overall orbital properties of atom. Thus, it is suggested that calculating a double-zeta should only be used for valence orbital. This approach is named **split-valence basis set.** Some common basis sets frequently used are 3-21G, 4-31G and 6-31G.

The first number in these notations represents the number of Gaussian functions summed to describe the inner shell orbital. The second number reveals the number of Gaussian functions that comprise the first term (the first STO) of the double zeta. The third number tells us the number of Gaussian functions summed in the second term (the second STO). For example, 3-21G basis set reveals that we are summing 3 Gaussians for the inner shell orbital, two Gaussian for the first STO of the valence orbital and 1 Gaussian for the second STO.

Polarised Sets and Diffuse Sets

Previous basis sets only treat atomic orbitals as existing only as "s", "p", "d", "f" orbitals, etc. However, in fact, these orbitals may hybridise with each other, such as orbital s and p, giving rise to the hybridised orbitals, which have the characteristics of both s and p orbital. Thus, a better approximation requires the addition of polarisation functions. Polarisation functions are functions with one orbital angular momentum quantum number higher than the atomic orbital, e.g. functions with p orbital character for an s orbital. Taking into account polarisation functions results in more flexibility in space of the atomic orbitals, in particular, satisfy the requirement for an accurate calculation of molecular geometry. For anions or atoms with lone pairs, electrons occupy a larger spatial extent than provided with a standard basis set.

A diffuse function, a very shallow orbital with low electron density, thus, is necessary to allow the electrons to occupy great spatial extent. In the Pople notation, a polarisation function is denoted by a * and a diffuse function a +. The first * will add polarisation functions to all atoms heavier than hydrogen and the second add p orbital to hydrogen. Similarly, the first + will add diffuse functions to heavy atoms and the second to hydrogen.

3.4.4.4 Opt for an Optimal Theoretical Methodology

As previously presented, the best results that DFT method can generate appear to come from the so-called hybrid functionals, which include some contributions from HF type exchange, using KS orbitals. Thus, the DFT method, which uses the B3LYP (Becke three-parameter Lee-Yang-Parr) functional, was chosen. In many cases, the results obtained from B3LYP can be compared to MP2 method. Although it was reported that B3LYP may underestimate the activation energies in case the barrier "below 10 kcal mol^{-1}" [23,24], results obtained when barriers "above 10 kcal mol^{-1}" was said to be reliable [25].

In this thesis, B3LYP in conjunction with the basis sets 6-31+G(2d,p) was employed to optimise geometries and calculate kinetic and thermodynamic quantities though many researches have showed that B3LYP/6-31G* is enough to achieve excellent geometries and good thermodynamic quantities for a large number of molecules. Any significantly larger basis sets than the one chosen can be 6-311+G(2df,2p), 6-311++G(3df, 3p), etc. Certainly, larger basis sets may increase the accuracy further, but the increase in time may not make this worthwhile. It is due to

the fact that DFT calculations appear to be "saturated" more quickly by using bigger basis sets than are *ab initio* calculations: Merrill *et al.* noted that "Once the double split-valence level is reached, further improvement in basis set quality offers little in the way of structural or energetic improvement." [26]; Stephens *et al.* reported that "Our results also show that B3LYP calculations converge rapidly with increasing basis set size and that the cost-to-benefit ratio is optimal at the 6-31G* basis set level. 6-31G* will be the basis set of choice in B3LYP calculations on much larger molecules [than $C_4H_6O_2$]." [27]

Although our choice of the basis set 6-31+G(2d,p) is supported by numerous studies mentioned above, the reliablity of this basis set on our systems as compared to higher basis sets such as 6-311++G(2df,2pd) and 6-311++G(3df,3pd) has been further confirmed by a benchmark study performed on the hydride transfer step of the system $LiBH_4.NH_3.MgCl_2$. The hydride transfer step has been selected since it is later shown (see Chapter 4, 5 and 6) to be the rate-determining step, which is thus the critical step in most of the reactions studied in this thesis. The results of the basis set study are indicated in **Table 3.1.**

Table 3.1 Benchmark of the activation barrier of the hydride transfer step with various basis sets. Basis set employed in this thesis is indicated in bold.

Basis set	**Activation Barrier (kJ mol^{-1})**
6-31G	69.9
6-31+G	78.2
6-31+G(2d,p)	**82.5**
6-311+G(2d,p)	82.7
6-311++G(2d,p)	82.9
6-311++G(2df,2pd)	83.8
6-311++G(3df,3pd)	83.6

Table 3.1 clearly shows that the activation barrier starts to converge at the basis set 6-31+G(2d,p). Much higher basis sets such as 6-311++G(3df,3pd) or 6-311++G(2df,2pd) do not produce significant change in the activation barrier while these high basis sets will demand more computing sources. Thus, 6-31+G(2d,p) seems to be the optimal basis set for our systems.

After specifying all the necessary inputs such as B3LYP, 6-31+G(2d,p) basis sets to run calculations, we obtain some results from Gaussian including energy, entropy, enthalpy. It's necessary to understand how Gaussian computes these thermodynamic quantities, thus the following part will be devoted to explaining carefully how various thermochemical values such as Free Gibbs energy, Entropy, Enthalpy are treated in Gaussian. Gaussian thermochemistry output would be succinctly discussed.

3.5 Thermochemistry in Gaussian

This part will briefly discuss the equations used for computing thermochemical data in *Gaussian*. All these equations presented in this section, are covered in detail in "Molecular Thermodynamics" (McQuarrie and Simon - 1999).

3.5.1 Sources of Components for Thermodynamic Quantities

Thermodynamic quantities such as entropy, energy and heat capacity are calculated through the four contributions of four components including: translational motion, electronic motion, rotational motion and vibrational motion. The starting

point for these calculations is the partition function *q(V,T)* for the corresponding component of the total partition function. The following section will present how the partition function *q(V,T)* will be used to compute entropy, internal thermal energy and heat capacity.

To determine the entropy contribution *S* from any of four components, the following equation will be used:

$$S = Nk_B + Nk_B ln\left(\frac{q(V,T)}{N}\right) + Nk_B T\left(\frac{\partial lnq}{\partial T}\right)_V \tag{3.37}$$

It should be noted that the form used in Gaussian is a special case. Firstly, molar values are given, $n = N/N_A$, thus we can replace N by nN_A and substitute $N_A k_B = R$. The first term also can be moved into the logarithm (as $lne = 1$), which finally leaves (with $n = 1$):

$$\begin{aligned} S &= R + Rln\big(q(V,T)\big) + RT\left(\frac{\partial lnq}{\partial T}\right)_V \\ &= Rln(q(V,T)e) + RT\left(\frac{\partial lnq}{\partial T}\right)_V \\ &= R\left(\ln(q_t q_e q_r q_v e) + T\left(\frac{\partial lnq}{\partial T}\right)_V\right) \end{aligned} \tag{3.38}$$

The internal thermal energy *E* can also be computed from the partition function:

$$E = Nk_B T^2\left(\frac{\partial lnq}{\partial T}\right)_V \tag{3.39}$$

More importantly, the energy will later be used to calculate the heat capacity:

$$C_V = \left(\frac{\partial E}{\partial T}\right)_{N,V} \tag{3.40}$$

The following part will discuss in detail how these three equations are used to derive four components of thermodynamic quantities calculated by Gaussian.

3.5.2 Contributions from Translation

The translational partition function has the form:

$$q_t = \left(\frac{2\pi m k_B T}{h^2}\right)^{3/2} V \tag{3.41}$$

For an ideal gas, we have the relationship $PV = NRT = \left(\frac{n}{N_A}\right) N_A k_B T$ thus $V = \frac{k_B T}{P}$.

Therefore,

$$q_t = \left(\frac{2\pi m k_B T}{h^2}\right)^{3/2} \frac{k_B T}{P} \tag{3.42}$$

The partial derivative of q_t with respect to T can be written:

$$\left(\frac{\partial ln q_t}{\partial T}\right)_V = \frac{3}{2T} \tag{3.43}$$

This equation will be used to calculate the translational entropy:

$$S_t = R\left(ln(q_t e) + T\left(\frac{3}{2T}\right)\right)$$

$$= R\left(lnq_t + 1 + \frac{3}{2}\right) \tag{3.44}$$

The contribution to the internal thermal energy resulting from the translational motion is:

$$E_t = N_A k_B T^2 \left(\frac{\partial lnq}{\partial T}\right)_V$$

$$= RT^2\left(\frac{3}{2T}\right)$$

$$= \frac{3}{2}RT \tag{3.45}$$

The constant volume heat capacity is derived:

$$C_t = \frac{\partial E_t}{\partial T}$$

$$= \frac{3}{2}R \tag{3.46}$$

3.5.3 Contributions from Electronic Motion

The electronic partition function has the form:

$$q_e = \omega_0 e^{-\frac{\epsilon_0}{k_B T}} + \omega_1 e^{-\frac{\epsilon_1}{k_B T}} + \omega_2 e^{-\frac{\epsilon_2}{k_B T}} + \cdots \tag{3.47}$$

where ω is the degeneracy of the energy level, $\epsilon_n$is the energy of the *n*-the level. Gaussian assumes that the first electronic excitation energy is much greater than $k_B T$. Thus, the first and higher excited states are assumed to be inaccessible at any temperature. Additionally, the energy of the ground state is set to zero. These assumptions simplify the electronic partition function to:

$$q_e = \omega_0 \tag{3.48}$$

This simple equation displays the electronic spin multiplicity of the molecule.

The entropy resulting from electronic motion is:

$$S_e = R\left(lnq_e + T\left(\frac{\partial lnq_e}{\partial T}\right)_V\right)$$

$$= R(lnq_e + 0) \tag{3.49}$$

Since there are no temperature dependent terms in the partition function, the electronic heat capacity and the internal thermal energy will be zero when the partial derivative with respect to T is taken.

3.5.4 Contributions from Rotational Motion

Depending on the number of atoms and geometry of molecule, the equation for rotational motion will vary. It can be divided into three cases: single atoms, linear polyatomic molecules, and general non-linear polyatomic molecules. For single atom, q_r = 1. Since q_r does not depend on the temperature, the contribution of rotation to the internal thermal energy, its contribution to the heat capacity and its contribution to the

entropy are all zero. For a linear molecule, the rotational partition function can be expressed:

$$q_r = \frac{1}{\sigma_r}\left(\frac{T}{\Theta_r}\right) \tag{3.50}$$

where $\Theta_r = \frac{h^2}{8\pi^2 I k_B}$. I is the moment of inertia.

The rotational contribution to the entropy is displayed:

$$\begin{aligned} S_r &= R\left(lnq_r + T\left(\frac{\partial lnq_r}{\partial T}\right)_V\right) \\ &= R(lnq_r + 1) \end{aligned} \tag{3.51}$$

The rotational contribution to internal thermal energy is:

$$\begin{aligned} E_r &= RT^2\left(\frac{\partial lnq_r}{\partial T}\right)_V \\ &= RT^2\left(\frac{1}{T}\right) \\ &= RT \end{aligned} \tag{3.52}$$

The contribution of rotation to the heat capacity is:

$$C_r = \left(\frac{\partial E_r}{\partial T}\right)_V = R \tag{3.53}$$

For the general case for a nonlinear polyatomic molecule, the rotational partition function can be written:

$$q_r = \frac{\pi^{\frac{1}{2}}}{\sigma_r}\left(\frac{T^{\frac{3}{2}}}{\left(\Theta_{r,x}\Theta_{r,y}\Theta_{r,z}\right)^{\frac{1}{2}}}\right) \tag{3.54}$$

If we take partial derivative of q_r with respect to T, we then have:

$$\left(\frac{\partial lnq}{\partial T}\right)_V = \frac{3}{2T} \tag{3.55}$$

Thus, the entropy for this partition function is expressed as:

$$\begin{aligned} S_r &= R\left(lnq_r + T\left(\frac{\partial lnq_r}{\partial T}\right)_V\right) \\ &= R(lnq_r + \frac{3}{2}) \end{aligned} \tag{3.56}$$

Finally, the internal thermal energy resulted from this partition function can be written as:

$$\begin{aligned} E_r &= RT^2\left(\frac{\partial lnq_r}{\partial T}\right)_V \\ &= RT^2\left(\frac{3}{2T}\right) \\ &= \frac{3}{2}RT \end{aligned} \tag{3.57}$$

and the contribution to the heat capacity is expressed as:

(3.58)

$$C_r = \left(\frac{\partial E_r}{\partial T}\right)_V$$

$$= \frac{3}{2}R$$

It should be noted that the average contribution to the internal thermal energy from each rotational degree of freedom is $\frac{RT}{2}$ while the contribution to the heat capacity is $\frac{R}{2}$.

3.5.5 Contributions from Vibrational Motion

The contributions of vibrational motions to the partition function, entropy, internal energy and heat capacity at constant volume consists of a sum of the contributions from each vibrational mode, *K*. In this calculation, only the real modes are taken into account while imaginary frequencies are not considered. Each of the $3n_{atoms} - 6$ (or $3n_{atoms} - 5$ for linear molecules) modes has a characteristic vibrational temperature, $\Theta_{v,K} = \frac{h\nu_K}{k_B}$.

Depending on where the zero of energy is chosen as a reference point, there are two ways to compute the partition function. In case the zero reference point is the bottom of the well, the contribution to the partition function from a given vibrational mode can have the following mathematical form:

$$q_{v,K} = \frac{e^{-\Theta_{v,K}/2T}}{1 - e^{-\Theta_{v,K}/T}} \tag{3.59}$$

and the overall vibrational partition function has the form:

$$q_v = \prod_K \frac{e^{-\Theta_{v,K}/2T}}{1 - e^{-\Theta_{v,K}/T}} \tag{3.60}$$

If the first vibrational energy level is chosen to be zero of energy (V=0), then the partition function for each vibrational level will be:

$$q_{v,K} = \frac{1}{1 - e^{-\Theta_{v,K}/T}} \tag{3.61}$$

and the overall vibrational partition function is

$$q_v = \prod_K \frac{1}{1 - e^{-\Theta_{v,K}/T}} \tag{3.62}$$

Gaussian chooses the bottom of the well as the zero reference point to compute other thermodynamic quantities, however, it still prints out the V=0 partition function. The only difference between the two references is the addition factor of $\Theta_{v,K}/2$ (which corresponds to the zero point vibrational energy) in the equation for the internal energy E_v. It should be noted that, this factor will disappear in the expression for heat capacity and entropy when differentiation with respect to temperature T is taken.

The total entropy contribution from the vibrational partition function has the form:

$$S_r = R\left(lnq_r + T\left(\frac{\partial lnq_r}{\partial T}\right)_V\right)$$

$$= R\left(\ln(q_v) + T\left(\sum_K \frac{\Theta_{v,K}}{2T^2} + \sum_K \frac{(\Theta_{v,K}/T^2)e^{-\Theta_{v,K}/T}}{1-e^{-\Theta_{v,K}/T}}\right)\right)$$

$$= R\left(\sum_K \left(\frac{\Theta_{v,K}}{2T} + ln\left(1 - e^{-\Theta_{v,K}/T}\right)\right) + T\left(\sum_K \frac{\Theta_{v,K}}{2T^2} + \sum_K \frac{(\Theta_{v,K}/T^2)e^{-\Theta_{v,K}/T}}{1-e^{-\Theta_{v,K}/T}}\right)\right)$$

$$= R\left(\sum_K ln\left(1 - e^{-\Theta_{v,K}/T}\right) + \left(\sum_K \frac{(\Theta_{v,K}/T)e^{-\Theta_{v,K}/T}}{1-e^{-\Theta_{v,K}/T}}\right)\right)$$

$$= R\sum_K \left(\frac{\Theta_{v,K}/T}{e^{\Theta_{v,K}/T}-1} - ln\left(1 - e^{-\Theta_{v,K}/T}\right)\right) \quad (3.63)$$

The contribution of molecular vibration to internal energy is

$$E_v = R\sum_K \Theta_{v,K}\left(\frac{1}{2} + \frac{1}{e^{\Theta_{v,K}/T} - 1}\right) \quad (3.64)$$

The contribution of molecular vibration to constant volume heat capacity is

$$C_v = R\sum_K e^{\Theta_{v,K}/T}\left(\frac{\Theta_{v,K}/T}{e^{-\Theta_{v,K}/T} - 1}\right)^2 \quad (3.65)$$

3.5.6 Thermochemistry Output of Gaussian

To compute reaction enthalpies, activation barrier, etc. it is of great importance to calculate accurate geometries for reactants, transition states, intermediates and products. When the optimised structures for these compounds are obtained, the geometries will be used to calculate rotational constants and in turn the rotational contribution to the so-called partition function will be calculated. From the

vibrational frequencies, the zero-point frequencies will be obtained, and the vibrational contributions to the partition function will be achieved. In Gaussian, this information is computed whenever vibrational frequencies are calculated. A table containing translational, rotational and vibrational corrections to the enthalpy at standard temperature (298.15 K) and pressure (1 atm) will be printed out.

Thermodynamic properties in the output of Gaussian, which are shown in **Figure 3.2**, include default temperature and pressure used for calculation (298.15 K and 1 atm); zero-point correction; thermal correction to energy, enthalpy and Gibbs Free Energy; and sum of electronic with each of zero-point energy, thermal energies, thermal enthalpies, and thermal Free energies. The zero-point energy is a correction to the electronic energy of the molecule to account for the effects of molecular vibrations, which persist even at 0 K.

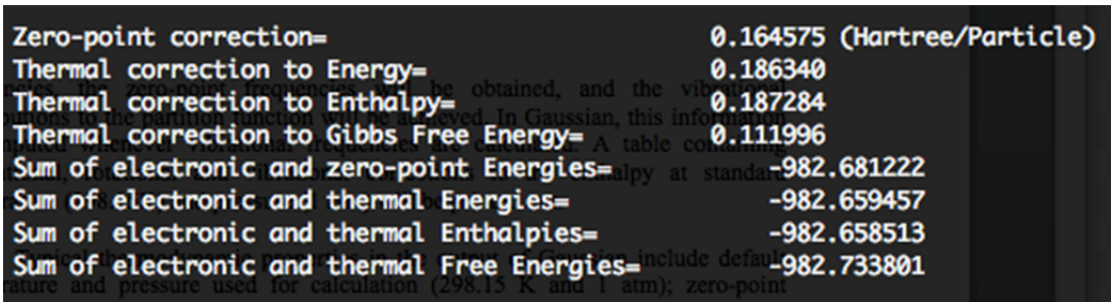

Figure 3.2 An example of partial Gaussian output file

Sum of electronic and zero-point Energies can be written in term of mathematical equation:

$$E_0 = E_{elec} + ZPE. \tag{3.66}$$

Sum of electronic and thermal Energies has the form:

$$E = E_0 + E_{vib} + E_{rot} + E_{transl} \tag{3.67}$$

Sum of electronic and thermal Enthalpies will be expressed as:

$$H = E + RT \tag{3.68}$$

Finally, sum of electronic and thermal Free Energies is:

$$G = H - TS \tag{3.69}$$

3.6 Natural Bond Orbital (NBO) Analysis [28]

Natural Bond Orbitals (NBOs) are localised few-center orbitals which may typically consist of 1, 2 or more centers that describe the Lewis-like molecular bonding pattern of electron pairs (or of individual electrons in the open-shell case) in optimally compact form. More precisely, NBOS are an orthonormal set of localised "maximum occupancy" orbitals whose leading *N/2* members (or N members in the open-shell case) give the most accurate possible Lewis like description of the total *N*-electron density.

Natural Orbitals (NOs) are the unique orbitals chosen by the wave function itself as optimal for its own description. Mathematically, the NOs $\{\theta_i\}$ of a wave

function Ψ can be defined as the *eigen*orbitals of the first-order reduced density operator Γ,

$$\hat{\Gamma}\theta_k = q_k\theta_k \tag{3.70}$$

which is formed by 'reducing' the wave function probability distribution to the single particle level,

$$\hat{\Gamma} = N\int \Psi(1,2,\dots,N)\Psi^*(1,2,\dots,N)d\tau_1 \dots d\tau_N \tag{3.71}$$

and whose eigenorbitals are hence 'natural' to Ψ itself. As indicated by Löwdin [29] and others, rigorous quantum-mechanical questions involving subsystems of an N-particle system are best formulated in terms of reduced density operators. In particular, the squared probability amplitude $|\langle\Psi(1,2,\dots,N)|\phi(1)\rangle|^2$ that an electron of Ψ(1,2,…,N) is 'in' orbital Φ (i.e., the population of ϕ(1) in the wave function) is rigorously expressed, for any possible orbital ϕ, as:

$$q_\Phi = \langle\phi|\hat{\Gamma}|\phi\rangle \tag{3.72}$$

The occupancies q_Φ are intrinsically non-negative and limited by the Pauli exclusion principle, e.g., for spatial orbital ϕ(r),

$$0 \le q_\Phi \le 2 \tag{3.73}$$

(The analogous restriction $q_\Phi \leq 1$ applies to spin orbitals). The sum of occupancies q_k over any complete orthonormal set $\{\phi_k\}$ accounts for all *N* electrons,

$$\sum_k \langle \phi_k | \hat{\Gamma} | \phi_k \rangle = \sum_k q_k = Tr\{\hat{\Gamma}\} = N \tag{3.74}$$

The Mulliken populations generally fail to satisfy the physical constraints

The chemist's idealised Lewis structure picture describes the *N/2* electron pairs as localised in one-centre (lone pair) or two-centre (bond) regions of the molecule. The natural bond orbital (NBO) algorithm [30,31] leads to an optimal set of one- and two-centre orbitals b_i that are in close correspondence with this picture. In effect, the algorithm searches the density matrix for the set of *N/2* localised Lewis-type lone pair and bond orbitals of near double occupancy that best describe the given wave function, with the residual weakly occupied non-Lewis type antibonding and *Rydberg orbitals* representing small corrections to delocalisation.

3.7 Solvation Methods

To simplify the calculations, most theoretical calculations are initially conducted without taking into account the presence of the solvents. These calculations, called the gas phase calculations, are only valid and acceptable when the solvent used are relatively non-polar so that the interactions between the solvents and the solutes do not change the nature of the reaction, and thus are negligible. However, when there exists a strong interaction between the solvents and the solutes such as when a polar solvent like THF or H_2O is used, the approximated geometry and

energies from the gas phase calculation might be significantly different from the experimental data. In these cases, solvent effect is of utmost importance to give a better prediction of molecular properties such as geometry and energy.

Currently, there are four methods for treatment of solvation: supermolecule, molecular mechanics, continuum models and recently a new method called various hybrid constructions has been developed. In the supermolecule approach, some solvent molecules are placed together with solutes in one QM calculation. Although it can give some insights on solvent effects even with limited number of solvent molecules, the quantitative results require a large number of solvent molecules to be included, thus it is very computationally demanding and beyond the present day limits. In the second approach, molecular mechanics method, the simplicity of the atom-atomic force field allows us to take into account a reasonable number of solvent molecules into consideration at cheap price. However, the simplicity of the MM approach does not allow this method to provide an adequate description of many processes such as bond breaking in chemical reactions. In the continuum model theory, solvent is described in terms of macroscopic properties. Solvent is dielectric medium, characterised by the dielectric constant ε_0. Polarisation of solvent is expressed in terms of the surface charge density on the cavity surface. Polarisation generates the electric field in the cavity making an effect on solute. Dispersion-Repulsion and Cavitation are added separately, or ignored. The Onsager model and the PCM model are two widely used models within this approach.

3.7.1 The Onsager Solvation Model

The simplest of all implicit solvation models is Onsager Solvation Model [32,37]. In this model, solvent is implicitly treated as a polarisable continuum characterised by its dielectric constant ε. The solute molecule is then put inside a spherical cavity inside the continuum field. The dipole of solute molecule will induce a reaction field in the surrounding medium, which in turn will induce an electric field in the cavity that interacts with the solute dipole. One of the advantages of this model is its simplicity to implement and analytical expressions for both the first and the second derivatives are available. However, there are some inherent disadvantages involving this method. Since the Onsager Solvation Model only includes the interaction between the molecular dipole moment and reaction fields, this gives rise to the zero value of the solvation energy for all those systems whose dipole moment is zero. The total energy in solution is thus identical to the total energy in the gas phase. Furthermore, treatment of the solute molecule inside a spherical cavity is only good if the molecule shape is spherical or close to spherical. This issue has been addressed in the polarised continuum model.

3.7.2 The Polarisable Continuum Model (PCM)

Tomasi and coworkers have developed the PCM [38-41] to tackle the disadvantages of the Onsager Solvation Model. In contrast with Onsager Model, PCM uses overlapping Van der Waals surfaces of atoms and groups to construct the solute cavity instead of using single sphere for the whole molecule. Cavity surface is then

split into a number of small surface elements of size ΔS. Based on this cavity, this model computes the molecular free energy in solution as the sum over three terms:

$$G_{sol} = G_{es} + G_{dr} + G_{cav} \tag{3.75}$$

in which, G_{es} reprents the electrostatic, G_{dr} describes the dispersion-repulsion contributions to the energy, and the cavitation energy is presented through G_{cav}.

Variations of the PCM model are available too, such as isodensity polarised continuum model (IPCM) [42] and self-consistent isodensity polarised continuum model (SCIPCM) [43]. In the IPCM model, the cavity is defined as an isosurface of the total electron density of the solute molecule. To determine this isodensity, the program performs an iterative process in which a SCF cycle is calculated and converged using the current isodensity cavity. The resultant wave function is then employed to compute an updated isodensity surface, and the cycle is repeated until the cavity shape no longer changes upon completion of the SCF. To further improve the IPCM model, the SCIPM model was designed to include the effect of solvation of the solution of the SCF problem. This procedure solves for the electron density which minimises the energy including the solvation energy and which itself depends on the cavity, which in turn depends on the electron density.

In general, due to taking more effects into account, these models offer more reliable results than the simple Onsager mode. However, it's worth noting that these models only investigate electrostatic interaction between the solvent and the solute while in some solvents, other non-electrostatic interactions might dominate.

References

[1] R. Marcelin, "Potential energy surface," in *Annales de Physique*., 1915, p. 158.

[2] P. Atkins, *Physical Chemistry*, 6th ed. New York: Freeman, 1998.

[3] H. Eyring, *J. Chem. Phys.*, vol. 3, p. 107, 1935.

[4] H. Eyring and M. Polanyi, *Z. Physik Chem. B.;*, vol. 12, p. 279, 1931.

[5] S. S. Shaik, H. B. Schlegel, and S. Wolfe, *Theoretical Aspects of Physical Organic Chemistry: the Sn2 Mechanism*.: Wiley, New York, 1992.

[6] R. A. Marcus, *Science*, vol. 256, p. 1523, 1992.

[7] J. I. Steinfeld, J. S. Francisco, and W. L. Hase, *Chemical Kinetics and Dynamics*, 2nd ed. New Jersey: Prentice Hall, 1999.

[8] E. Schrodingder, *Phys. Rev*, vol. 28, p. 1049, 1926.

[9] M. Born and R. Oppenheimer, *Ann. Phys*, vol. 389, p. 457, 1927.

[10] R. W. James, I. Waller, and D. R Hartree, *Proc. R. Soc. London Ser. A*, vol. 118, p. 334, 1928.

[11] D. R Hartree, *Proc. Camb. Phil. Soc.*, vol. 24, p. 89, 1928.

[12] D. R Hartree, *Proc. Camb.Phil. Soc.*, vol. 24, p. 111, 1928.

[13] I. N. Levine, *Quantum Chemistry*, 5th ed. New Jersey: Prentice Hall, Upper Saddle River, 2000.

[14] P. Hohenberg and W. Kohn, *Phys. Rev. B*, vol. 136, p. 864, 1964.

[15] F. J. Devlin, C. F. Chablowski, and M. J. Frisch P. J. Stephens, *J. Phys. Chem*, vol. 98, p. 11623, 1994.

[16] A. D. Becke, and R. G. Parr W. Kohn, *J. Phys. Chem*, vol. 100, p. 12974, 1996.

[17] Y. Zhao and D. G. G. Truhlar, *Theor. Chem. Acc.*, vol. 120, p. 215, 2008.

[18] Jr., A. Ricca, H. Partridge, and S. R. Langhoff C. W. Bauschlicher, "Recent Advances in Density Functional Methods. Part II," 1995.

[19] G. Frenking, *J. Chem. Soc*, p. 1653, 1997.

[20] W. Koch and M. Holthausen, "A Chemist's Guide to Density Functional Theory," 2000.

[21] G. P. Shusterman and A. J. Shusterman, *J. Chem. Educ.,* , vol. 74, p. 771, 1997.

[22] J. B. Collins, R. R. Schleyer, J. S. Binkley, and J. A. Pople, *J. Chem. Phys.*, vol. 64, p. 5142, 1976.

[23] M. N. Glukhovtsev, R. D. Bach, A. Pross, and L. Radom, *Chem. Phys. Lett.,* vol. 260, p. 558, 1996.

[24] R. L. Bell, D. L. Tavaeras, T. N. Truong, and J. Simons, *Int. J. Quantum Chem.*, vol. 63, p. 861, 1997.

[25] B. S. Jursic, *Recent Developments and Applications of Modern Density Functional Theory*. Amsterdam: Elsevier, 1996.

[26] G.N. Merrill, S. Gronert, and S. R. Kass, *J. Phys. Chem. A*, vol. 101, p. 208, 1997.

[27] P. J. Stephens, F. J. Devlin, C. F. Chablowski, and M. J. Frisch, *J. Phys. Chem.*, vol. 98, p. 11623, 1994.

[28] P. V. R. Schleyer et al., *Encyclopedia of Computational Chemistry*, vol. 3, p. 1792, 1999.

[29] P. O. Lowdin, *Phys. Rev.*, vol. 97, p. 1474, 1955.

[30] J. P. Foster and F. Weinhold, *J. Am. Chem. Soc.*, vol. 102, p. 7211, 1980.

[31] A. E. Reed and F. Weinhold, *J. Chem. Phys.*, vol. 78, p. 4066, 1983.

[32] J. G. Kirkwood, *J. Chem. Phys.*, vol. 2, p. 351, 1934.

[33] L. Onsager, *J. Am. Chem. Soc.*, vol. 58, p. 1486, 1936.

[34] M. W. Wong, M. J. Frisch, and K. B. Wiberg, *J. Am. Chem. Soc.*, vol. 113, p. 4776, 1991.

[35] M. W. Wong, K. B. Wiberg, and M. J. Frisch, *J. Chem. Phys.*, vol. 95, p. 8991, 1991.

[36] M. W. Wong, K. B. Wiberg, and M. J. Frisch, *J. Am. Chem. Soc.*, vol. 114, p. 523, 1992.

[37] M. W. Wong, K. B. Wiberg, and M. J. Frisch, *J. Am. Chem. Soc.*, vol. 114, p. 1645, 1992.

[38] V. Barone, M. Cossi, and J. Tomasi, *J. Chem. Phys.*, vol. 107, p. 3210, 1997.

[39] R. Cammi, M. Cossi, and J. Tomasi, *J. Chem. Phys.*, vol. 104, p. 4611, 1996.

[40] E. Cances, B. Mennucci, and J. Tomasi, *J. Chem. Phys.*, vol. 107, p. 3032, 1997.

[41] M. Cossi, V. Barone, R. Cammi, and J. Tomasi, *J. Chem. Phys. Lett.*, vol. 255, p. 327, 1996.

[42] J. B. Foresman; T. A. Keith; K. B. Wiberg; J. Snoonian; M. J. Frisch, *J. Phys. Chem.,* vol. 100, 1996

[43] T. A. Keith; M. J. Frisch, *manuscript in preparation.*

CHAPTER 4

A MECHANISTIC STUDY ON THE DEHYDROGENATION OF $LiNH_2BH_3$

4.1 Introduction

As presented in Literature Review (see Chapter 2), various types of materials composed of hydrogen bound to light elements, including borohydrides [1], amide-hydride combination systems [2-4], and ammonia-borane [5-7] are discovered. Among these compounds, ammonia-borane, due to its impressive high hydrogen content, has gained much attention since 2005. Initial efforts were concentrated on understanding the structure and physical properties of ammonia-borane and the dehydrogenation of this species. It soon emerged that ammonia-borane exhibited a slow kinetics below 100^{o}C and generated borazine as a by-product [5-7]. Several approaches based on catalysis usage have been suggested in order to enhance hydrogen generation at lower temperature and faster rates. These approaches range from transition metal catalysis [8,9], to acid and base catalysis [10,11], to the use of ionic liquids and catalysed solvolysis [5]. Another promising avenue, which has been explored recently, is the chemical modification of ammonia-borane to produce metal amidoboranes [12-14].

These compounds not only have high hydrogen content but also have strong potentials to meet D.O.E targets. Among them are the systems MNH_2BH_3, where M =

Li and Na. $LiNH_2BH_3$ and $NaNH_2BH_3$ could release 10.9 and 7.5 wt% of H_2, respectively, with no significant byproducts and the hydrogen release occur at reasonably low temperature of 90^oC. More importantly, $LiNH_2BH_3$ and $NaNH_2BH_3$ are friendly to environment and stable solids at room temperature and normal pressure [15]. It is, therefore, crucial for us to understand the dehydrogenation mechanism of these materials for further development towards making successful hydrogen storage materials.

The mechanism of thermal decomposition of lithium amidoborane in the gas phase has been studied computationally by Kim *et al.* [16] However, while $LiNH_2BH_3$ could release two moles of H_2, only the mechanism of the first mole of H_2 release from this compound was examined. Thus, the critical role that lithium atom might play in the second mole of H_2 release was not fully elucidated. Furthermore, the solvent effect on the dehydrogenation of the $LiNH_2BH_3$ compound was not taken into consideration. Therefore, in this study, to fulfill their research gaps, we will model the dehydrogenation reactions that may occur to release two moles of H_2 from lithium amidoborane. In particular, the solvent effect will be investigated. The results of this study will provide a comprehensive understanding on the role of lithium in the dehydrogenation of $LiNH_2BH_3$. Moreover, they may shed light on the effect of a dielectric medium on the thermodynamics and kinetics on the hydrogen release processes. These results will be useful for further development and design of future hydrogen storage materials.

4.2 Computational Methods

Density Functional Theory (DFT) calculations based on hybrid B3LYP functional together with 6-31+G(2d,p) basis set were carried out for optimisations of all equilibrium structures and transition states in the gas phase and THF solvent. Intrinsic reaction coordinates (IRC) were used to confirm the identity of the linking reactant and product from a transition state. Effects of solvent were investigated using an implicit solvation model, polarisable continuum model (PCM). THF solvent (ε = 7.58) was employed as experimental study on THF solvent has been reported recently. All DFT calculations were performed using the Gaussian 09 suite of programs.

4.3 Results and Discussions

The dehydrogenation of solid state $LiNH_2BH_3$ was first experimentally investigated by P.Chen *et al.* [17] Their experiments showed that $LiNH_2BH_3$ decomposed directly approximately two molar equivalents of H_2 on heating, with vigorous hydrogen release at around 92^{o}C; no borazine byproduct was detected. It was also reported that the final solid product has the chemical composition of LiNBH. High-resolution X-ray powder diffraction data indicated that the final product is a borazine-like or poly-borazine-like compound. Based on these experimental data, we will propose some possible mechanisms for the dehydrogenation.

4.3.1 Mechanism for Hydrogen Release using $(LiNH_2BH_3)_2$ Dimer Model

Initially, we examined the hydrogen release of $LiNH_2BH_3$ using a monomer model in the gas phase. The monomer of $LiNH_2BH_3$ is predicted to have a bridge structure with the lithium atom bridged between the nitrogen and boron atoms. The calculated activation barriers of hydrogen release are fairly high. For instance, it requires above 200 kJ mol^{-1} for the first mole of H_2 release. The structure of $LiNH_2BH_3$ and the computed energetics of hydrogen release suggest that the monomer model is not satisfactory to model this reaction in condensed phases. Next, we examine the dimer model. Interestingly, the optimised geometry of $LiNH_2BH_3$ dimer is very close to that observed in X-ray crystallography [18]. Thus, the dimer structure may provide a more realistic model for the solid-state reaction.

We propose the dehydrogenation reactions to occur in four stages of hydrogen release with a similar two-step mechanism for each molecule of H_2 release. The two-step mechanism consists of a hydride transfer (step **a**) initially, followed by H_2 release (step **b**). In step **a**, one lithium atom plays an important role to attract and remove one hydrogen atom (H^1) from the second molecule to form a Li□H bond. In step **b**, the dimer system changes its conformation so that the second hydrogen atom could approach the new Li□H moiety and then one hydrogen molecule is being released. The general form of this two-step mechanism, hydride transfer and H_2 release, is illustrated in **Figure 4.1**.

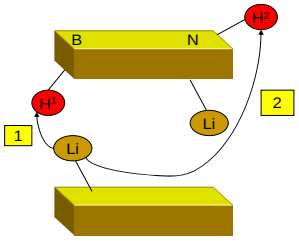

Figure 4.1 A simplified model of the hydrogen release reaction.

The four stages of hydrogen release are summarised in the following reactions:

Stage **1**: $(LiNH_2BH_3)_2 \rightarrow LiNH_2BH_3 + LiNHBH_2 + H_2$

Stage **2:** $LiNH_2BH_3 + LiNHBH_2 \rightarrow 2LiNHBH_2 + H_2$

Stage **3:** $2LiNHBH_2 \rightarrow LiNHBH_2 + LiNBH + H_2$

Stage **4**: $LiNHBH_2 + LiNBH \rightarrow 2LiNBH + H_2$

Overall reaction: $(LiNH_2BH_3)_2 \rightarrow 2LiNBH + 4H_2$

A schematic potential energy diagram for the release of the first mole of H_2 from lithium amidoborane, i.e. Stage **1**, involves step **1a** and **1b**, is shown below (**Figure 4.2**).

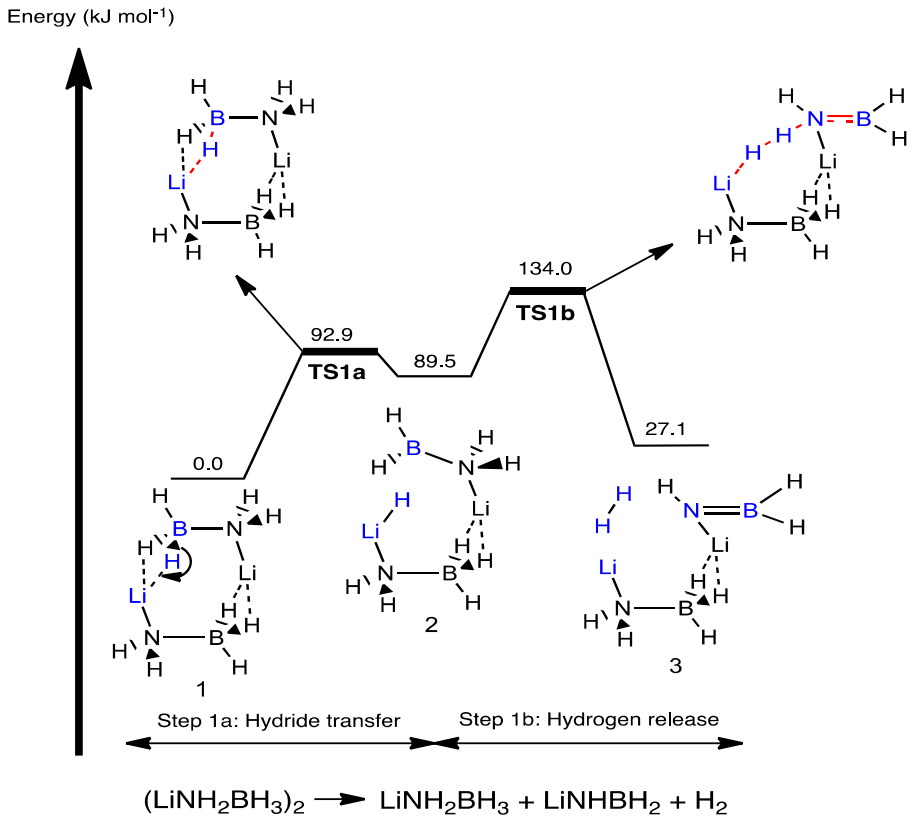

Figure 4.2 Schematic reaction profile for Stage **1** of H_2 release of $LiNH_2BH_3$.

In step **1a**, one hydrogen atom is transferred from boron to lithium, via transition state **TS1a**, to form an intermediate **2** (**Figure 4.3**). This intermediate is characterised by a hydrogen bridged between 2 strongly positively-charged lithium atoms (Li- -H- -Li). In step **1b**, two hydrogen atoms, one from Li-H and one from N-H, are lost together as H_2 molecule, via transition state **TS1b** (**Figure 4.4**). Hence, the Li atom in $LiNH_2BH_3$ serves as an important role to assemble the hydrogen atoms for dehydrogenation. The calculated activation barriers for steps **1a** and **1b** are 92.9 and 44.6 kJ.mol^{-1}, respectively. The higher barrier in step **1a** may be attributed to two reasons: (i) In the first structure, the bond breaking between the boron and the hydrogen atoms is difficult because of less polar bond whereas in the second structure, the bond breaking between the nitrogen and the hydrogen atoms is easier

because of more polar bond; (ii) The second step is a redox reaction, which is relatively facile since two hydrogen atoms are of opposite charges.

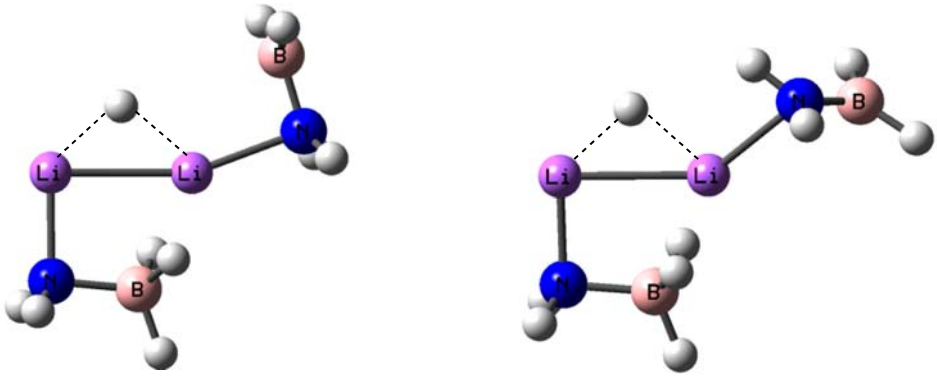

Figure 4.3 B3LYP/6-31+G(2d,p) optimised structures of transition state **TS1a** (left) and intermediate **2** (right).

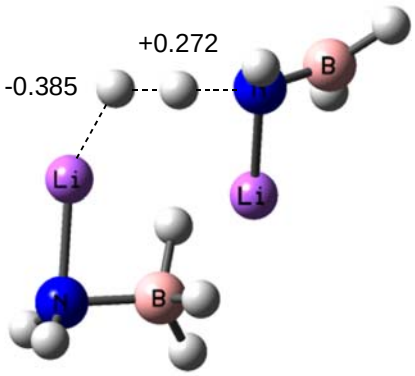

Figure 4.4 B3LYP/6-31+G(2d,p) optimised structures of transition state **TS1b** showing two hydrogens with opposite charges.

To gain a better insight on the driving force of this two-step mechanism, NBO analysis was also carried out to compute the atomic charge of each atom (**Figure 4.5**).

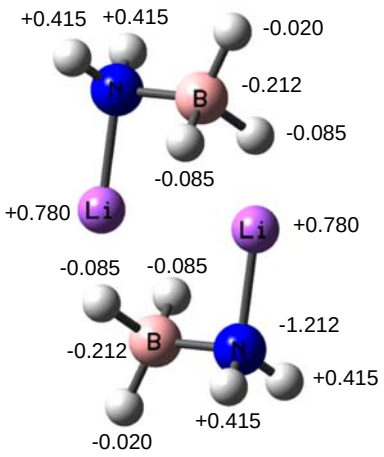

Figure 4.5 NBO atomic charges of $(LiNH_2BH_3)_2$.

In the optimised dimer structure, the two monomer units are in the opposite direction and there is strong electrostatic attraction between the lithium atom of one molecule and the boron hydrogens of another molecule. NBO analysis readily confirms that two negatively charged boron hydrogen atoms attract the positively charged lithium atom of the other monomer. The atomic charge of lithium is +0.78, which shows the high ionic character of two lithium atoms, which contribute to the electrostatic stabilisation of the dimer structure.

The release of second mole of H_2, i.e. Stage **2**, involves steps **2a** and **2b**, corresponds to the reaction: $LiNH_2BH_3 + LiNHBH_2 \rightarrow 2LiNHBH_2 + H_2$. The schematic energy profile for this stage is given in **Figure 4.6**. The chemistry occurs in steps **2a** and **2b** is similar to that in steps **1a** and **1b**. Again, one boron hydrogen is transferred via the lithium atom, and then the second nitrogen hydrogen approaches this Li-H atom and one H_2 molecule is being released via intermediate **4**. The transition states involved in steps **2a** and **2b** are **TS2a** and **TS2b**, respectively. Computed $\Delta G^{\ddagger}$ for steps **2a** and **2b** are 102.2 and 37.1 kJ mol^{-1}, respectively. These

$\Delta G^{\ddagger}$ values suggest that the release of second H_2 molecule is more difficult than the release of the first H_2 molecule.

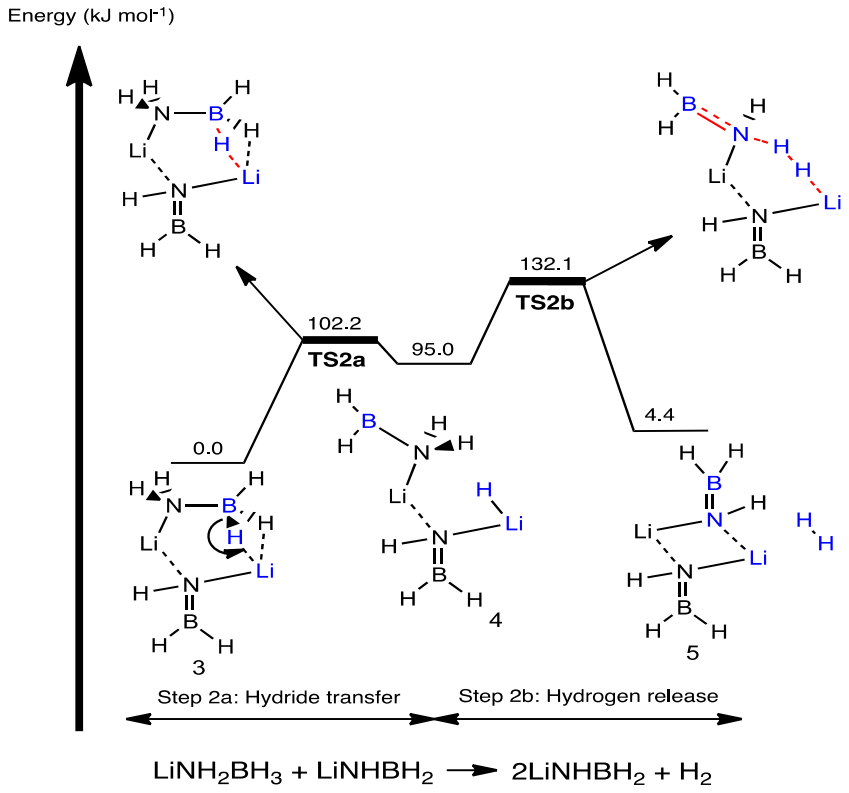

Figure 4.6 Schematic reaction profile for Stage **2** of H_2 release of $LiNH_2BH_3$.

The third mole of H_2 release, i.e. Stage **3**, via steps **3a** and **3b**, corresponds to the reaction: $2LiNHBH_2$ → $LiNHBH_2 + LiNBH + H_2$. $\Delta G^{\ddagger}$ for steps **3a** and **3b** are 75.5 and 36.1 kJ mol^{-1}, respectively. Interestingly, the value of $\Delta G^{\ddagger}$ for these steps is lower than two previous steps. This is perhaps due to the fact that **6** has a cyclic structure where nitrogen and boron are bonded together. The close proximity facilitates both the hydrogen transfer and H_2.

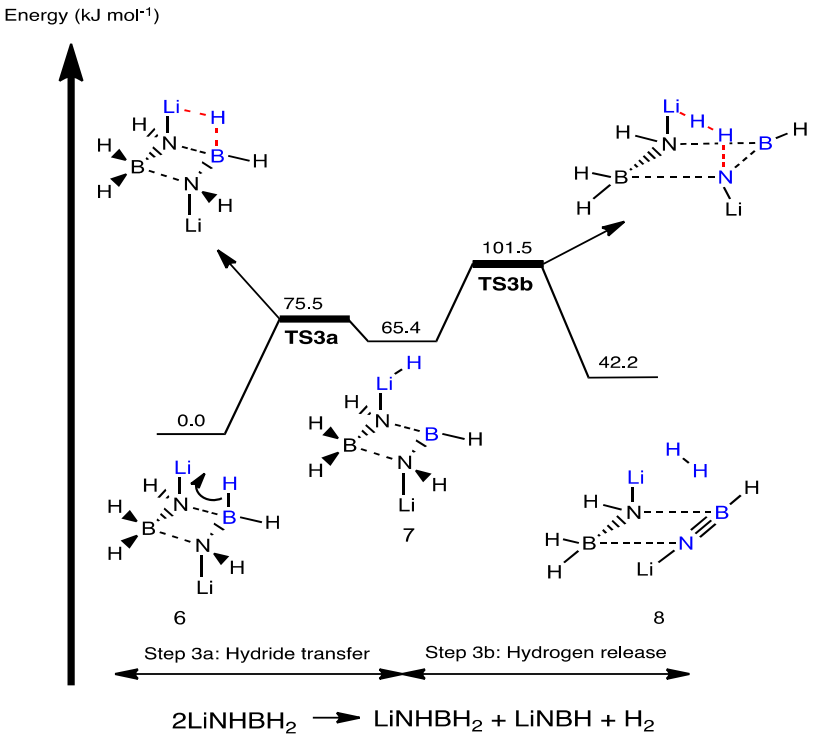

Figure 4.7 Schematic reaction profile for Stage **3** of H_2 release of $LiNH_2BH_3$.

A schematic energy profile for Stage **4** of H_2 release, involving steps **4a** and **4b**, is shown in **Figure 4.8**. Computed $\Delta G^{\ddagger}$ values for steps **4a** and **4b** are 116.5 and 201.7 kJ mol^{-1}, respectively. The considerably high activation barriers indicate that the last mole of hydrogen release is difficult, in accord with the experimental observation [17].

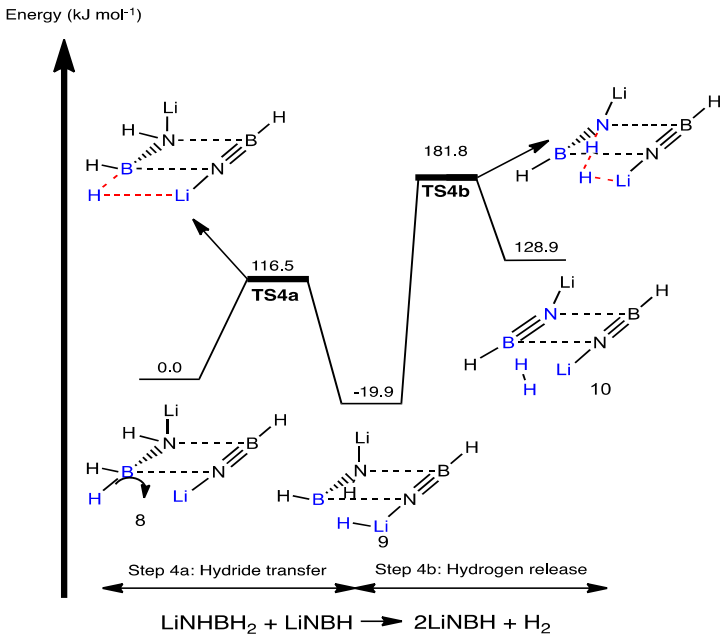

Figure 4.8 Schematic reaction profile for Stage **4** of H_2 release of $LiNH_2BH_3$.

4.3.2 Calculations for the Dimer System in THF Solvent using PCM Model:

Based on experimental study of LiH-NH_3BH_3 using ^{11}B NMR spectroscopy in THF, $LiNH_2BH_3$ is being first formed. The LiH-NH_3BH_3 samples in THF collected at different reaction intervals shown that the boron species at □23.9 ppm is present throughout the course of the dehydrogenation; however, the intensity did not change significantly with time while that of the $LiNH_2BH_3$ species obviously decrease. Although there is no authentic compound to confirm the identity of this minor species, a quartet in the ^1H NMR spectra indicate that it is likely the terminal BH_3 in a partially dehydrogenated dimerised $LiNH_2BH_3$, such as $Li_2[NHBHNHBH_3]$. This finding lends strong confidence to our use of the dimer structure to model this dehydrogenation reaction in THF solvent.

Table 4.1 Calculated reaction enthalpies (kJ mol^{-1}) in gas phase and THF solvent at 298 K.

Calculated reaction enthalpies (kJ mol^{-1}) in the gas phase and THF solvent at 298 K		
	Gas phase	THF solvent
Stage **1**	40.3	44.7
Stage **2**	38.2	45.3
Stage **3**	61.1	59.9
Stage **4**	146.9	105.7

The calculated reaction enthalpies of the 4 stages of hydrogen release in the gas phase and in THF solvent are summarised in **Table 1**. In general, there is a slight increase of reaction enthalpy on going from stage **1** to stage **4** in both phases. This upward trend indicates that it requires more energy for H_2 release as the reaction proceeds. The difference among the first three stages is not large (in THF solvent). In other words, it is relatively straightforward to release the first three molecules of H_2. However, the reaction enthalpy of the last step is twice larger the previous steps. Our calculated energetic is in pleasing agreement with the experimental observation that it is difficult to release the last mole of hydrogen molecule. We note that the effect of solvation is relatively small for the first 3 stages but very large for stage **4**. The reaction enthalpy reduces by 41 kJ mol^{-1} on going from the isolated state to THF solvent.

Kinetics of these dehydrogenation reactions in THF solvent has also been studied. The computed rate constants at each stage for each step are tabulated in **Table 2**, with computed the rate constants in the gas phase are also listed for comparison.

Table 4.2 Kinetics of dehydrogenation reactions in gas phase and in THF solvent.

	$\Delta G^{\ddagger}$ (kJ mol^{-1})	$\Delta G^{\ddagger}$ in THF (kJ mol^{-1})	rate constant (50^{o}C)	rate constant (THF at 50^{o}C)	$t_{1/2}$ (s) in THF	note*
Steps **1a** & **1b**	92.9	90.4	6.5x10^{-3}	1.6x10^{-2}	44.5	rds
	44.4	47.3				
Steps **2a** & **2b**	102.1	101.7	2.0x10^{-4}	2.3x10^{-4}	2987.7	rds
	37.2	33.9			= 49.8 min	
Steps **3a** & **3b**	75.3	47.7	4.2			
	36.0	78.2		1.5	0.5	rds
Steps **4a** & **4b**	116.3	109.6				
	201.7	159.8	1.6*10^{-20}	9.6*10^{-14}		rds

* rds = rate-determining step

The step, which has the highest activation energy ($\Delta G^{\ddagger}$), is the rate-determining step. In THF solvent, the first steps (hydride transfer) are the rate-determining steps for stages **1** and **2**. Conversely, the second step (H_2 loss) is the rate-determining step for stages **3** and **4**.

The rate constants (k) of the rate-determining steps are calculated using the following equation[7]:

$$k(T) = \frac{k_B T}{hc^0} e^{\frac{-\Delta G^{\ddagger}}{RT}} \tag{4.1}$$

In equation (4.1), the temperature used to calculate rate constants is 50^{o}C (323.15 K). The calculated $\Delta G^{\ddagger}$ as well as the rate constants clearly show that THF facilitates the dehydrogenation reactions. THF is a moderately polar solvent, with dipole moment of 1.63 D, therefore, it helps to stabilise the more polar equilibrium structure or transition state.

In stage **1**, the $\Delta G^{\ddagger}$ of the first stage (rate-determining stage) in THF is smaller than in gas phase. It is due to the fact that the transition state (**TS1a**) is more polar (1.03 D) than the reactant **1** (0.02 D). The differential solvent stabilisation effect leads to a lower activation free energy. Similarly, in stage **2**, the $\Delta G^{\ddagger}$ of the first step (rate-determining stage) in THF is smaller than in the gas phase. In this case, **TS2a** has a significantly dipole moment (3.24 D) than reactant **3** (2.89 D). The stronger solvation effect in stage 1 than stage **2** is readily attributed the greater difference in dipole moment between **TS1a** and **1**.

Interestingly, the first step (**3a**) is the rate-determining step for stage **3** of H_2 release. In sharp contrast, the second step becomes the rate-determining stage in THF solvent. The dipole moments of **TS3b** and **7** are 4.75 and 16.90 D, respectively. THF solvent strongly stabilises the very polar intermediate **7**. Consequently, the second step becomes the rate-determining step in a dielectric medium.

It is worth noting that stage **4** has very small value of rate constant (corresponds to very large $\Delta G^{\ddagger}$). That implies that it is difficult for the last hydrogen molecules to release.

It is instructive to see how fast the reaction occurs in THF by calculating the half life, i.e. the time required for the reactant concentration to fall to one half its initial concentration ($t_{1/2}$). The half life of the dehydrogenation reaction is calculated using the simple equation applied for the first order-reaction:

$$t_{\frac{1}{2}} = \frac{ln2}{k} \qquad (k - \text{rate constant}) \qquad (4.2)$$

The computed half lives show that it takes the system nearly 50 minutes to release 2 equivalents of H_2 and the molar of $LiNH_2BH_3$ reduces half. This result is indeed in good accord with the experimental data [17] and is more reasonable than the results reported by *Kim et al.* [16] They showed that rate constant *k* in the gas phase for the first step is approximately 1.6 min^{-1} at 90°C. With this value of rate constant, it would take the reaction only nearly 0.5 s to finish half whereas the experiment data shows approximately 1.4 molar equivalents of H_2 are released within approximately 1 hour. Therefore, the system modelled in THF solvent gives significantly better results that match well with the observed rate constants. In summary, THF facilitates the dehydrogenation reactions by stabilizing the transition states, which is generally more polar than the corresponding reactant involved. Therefore, we predict that the rates of these reactions can be improved further by using more polar solvent such as DMSO.

4.4 Conclusions

The thermodynamic and kinetic properties of the dehydrogenation of $LiNH_2BH_3$ both in the gas phase and in the THF solvent have been comprehensively studied by DFT calculations at B3LYP/6-31+G(2d,p) level. Our results have showed that *dimer*-$LiNH_2BH_3$ model is more realistic and it gives better results as compared to the observed experimental kinetics. The reaction enthalpy of each mole of hydrogen release increases with the number of H_2 lost from previous steps. In particular, the last step has a significantly higher value of enthalpy compared to the three previous steps. These calculated results are consistent with the experimental

observation that the last mole of H_2 release is difficult. Rate constants for this reaction have been calculated and are in good agreement with the results obtained from the experimental data.

In this study, we learnt that the lithium atom of lithium amidoborane plays an important role of a catalyst to facilitate the hydrogen release. Interestingly, the solvent-effect calculations show that THF has good potential to improve the rate of this reaction. In this dielectric medium, the solvent helps to stabilise the polar transition states more than the less polar ground states, which in turn reduces the activation barrier of the hydrogen release.

References

[1] R. Cerny, Y. Filinchuk, H. Hagemann and K. Yvon, *Angew. Chem., Int. Ed.,* vol. 46, p. 5765, 2007.

[2] F. E. Pinkerton, G.P. Meisner, M. S. Meyer, M. P. Balogh and M. D. Kundrat, *J. Phys. Chem. B*, vol. 109, p. 6, 2005.

[3] (a) G. Wolf, J. Baumann, F. Baitalow and F. Hoffmann, *Thermochim. Acta,* vol. 243, p. 29, 2000; (b) X. Gutowska, L. Y. Li, Y. S. Shin, C. M. M. Wang, X. H. S. Li, J. C. Linehan, R. S. Smith, B. D. Kay, B. Schmid, W. Shaw, M. Gutowski and T. Autrey, *Angew. Chem., Int. Ed.,* vol. 44, p. 3578, 2005; (c) A. C. Stowe, W. J. Shaw, J. C. Linehan, B. Schmid and T. Autrey, *Phys. Chem. Chem. Phys.,* vol. 9, p. 1831, 2007; (d) M. Gutowski and T. Autrey, *Abtr. Pap. Am. Chem. Soc.,* vol. 227, p. 1088, 2004.

[4] M.C. Denney, V. Pons, T. J. Hebden, M. Heinekey and K. L. Goldberg, *J. Am. Chem. Soc.,* vol. 128, p. 12048, 2006.

[5] M. E. Bluhm, M. G. Bradley, R. Butterick, U. Kusari and L. G. Sneddon, *J. Am. Chem. Soc.,* vol. 128, p. 7748, 2006.

[6] M.G. Hu, R. A. Geanangel and W. W. Wendlandt, *Thermochim. Acta*, vol. 23, p. 249, 1978.

[7] Z. T. Xiong, C. K. Yong, G. T. Wu, P. Chen, W. Shaw, A. Karkamkar, T. Autrey, M. O. Jones, S. R. Johnson, P. P. Edwards and W. I. F. David, *Nat. Mater.*, vol. 7, p. 138, 2008.

[8] (a) Q. Xu, M. Chandra, *J. Alloys Compd.*, vol. 729, pp. 446-447, 2007; (b) P. Wang, X. D. Kang, *Dalton Trans.*, p. 5400, 2008; (c) T. Umegaki, J. M. Yan, X. B. Zhang, H. Shioyama, N. Kuriyama, Q. Xu, *Int. J. Hydrogen Energy*,

vol. 34, p. 2303, 2009.

[9] S. Özkar, *Appl. Surf. Sci.*, vol. 256, p. 1272, 2009.

[10] H. F. Stephens, T. R. Baker, H. M. Matus, J. D. Grant, A. D. Dixon, *Angew. Chem., Int. Ed.*, vol. 46, p. 746, 2007.

[11] M. J. A. Miller, E. J. Bercaw, *Chem. Commun.*, vol. 46, p. 1709, 2010.

[12] S. De Benedetto, M. Carewska, C. Cento, P. Gislon, M. Pasquali, S. Scaccia, P. P. Prosini, *Thermochim. Acta*, vol. 441, p. 184, 2006.

[13] M. E. Bluhm, M. G. Bradley, L. G. Sneddon, *Prepr. Symp.-Am. Chem. Soc., Div. Fuel Chem.*, vol. 51, p. 571, 2006.

[14] H.V. K. Diyabalanage, R. P. Shrestha, T. A. Semelsberger, B. L. Scott, M. E. Bowden, B. L. Davis, A. K. Burrell, *Angew. Chem., Int. Ed.*, vol. 46, p. 8995, 2007.

[15] Z. Xiong, C. K. Yong, G. Wu, P. Chen, W. Shaw, A. Karkamkar, T. Autrey, M. O. Jones, S. R. Johnson, P. R. Edwards and W. I. F. David, *Nature Materials*, vol.7, pp. 138-141, 2007.

[16] D. Y. Kim, N. J. Singh, H. M. Lee and K. S. Kim, *Chemistry – a European Journal*, vol. 15, pp. 5598-5604, 2009.

[17] Z. Xiong, Y. S. Chua, G. Wu, W. Xu, P. Chen, W. Shaw, A. Karkamkar, J. Linehan, T. Smurthwaite and T. Autrey, *Chem. Commun*., vol. 43, pp. 5595-5597, 2008.

[18] H. Wu, W. Zhou and T. Yildirim, *J. Am. Chem. Soc.,* vol. 130, pp. 14834-14839, 2008.

CHAPTER 5

A MECHANISTIC STUDY ON THE DEHYDROGENATION OF $Mg(NH_2BH_3)_2.NH_3$

5.1 Introduction

In the previous chapter, we have discussed in detail the dehydrogenation mechanisms of $LiNH_2BH_3$. Our calculations have clearly indicated that Li cation plays a crucial role in lowering considerably H_2 desorption temperature in comparison with the dehydrogenation of the parent NH_3BH_3 compound. This result suggests that other cations such as calcium and magnesium may have the same ability in facilitating the H_2 release from amidoborane compounds. $Ca(NH_2BH_3)_2$, which is capable of releasing 8 wt% of H_2, has been successfully synthesised [1]. This compound was reported to release H_2 at moderate temperature [2] [3]. However, calcium has a higher molecular weight than magnesium. Thus, numerous attempts later have been made to introduce magnesium into ammonia-borane to increase the hydrogen weight percentage. Unfortunately, initial effort failed to synthesise this kind of compound [3]. Recently, a novel compound, $Mg(NH_2BH_3)_2.NH_3$ (denoted as MgAB.NH_3) has been reported to be successfully synthesised via ball milling $Mg(NH_2)_2$ with 2 equiv. AB. $Mg(NH_2BH_3)_2.2NH_3$ was initially formed and released NH_3 slowly at ambient temperature and solidifies into a new phase upon removing 1 equiv. NH_3 [4] This compound was regarded as a promising candidate for hydrogen storage material due

to many outstanding properties such as low H_2 desorption temperature and high hydrogen content. The temperature-programmed desorption method combined with mass spectrometric (TPD-MS) analysis on $MgAB.NH_3$ indicated that H_2 started to release at as low as 50^{o}C, peaked at as low as 74^{o}C and tailed to 300^{o}C. Furthermore, the harmful byproduct, borazine was undetectable and only a small amount of NH_3 was co-produced during the reaction course. More interestingly, quantitative measurements of hydrogen desorption from $MgAB.NH_3$ in a closed system revealed that ca. 5.3, 8.4, 9.7 and 11.4 wt% or 2.7, 4.2, 4.9 and 5.7 equiv. H_2 could be released at ca. 100, 150, 200 and 300^{o}C, respectively [4].

The chemistry involved in the dehydrogenation of $MgAB.NH_3$ is of great importance as it may give rise to the development of a new class of high hydrogen content compounds and provides insights to the bonding nature of B-H, N-H and B-N. Thus, much effort has been made to characterise the dehydrogenation reaction of $MgAB.NH_3$. However, only a limited number of information about some intermediates and final products has been attained in the experiments and the comprehensive mechanism is still unknown [4]. Therefore, it is of utmost importance to have a theoretical mechanistic study on the dehydrogenation reactions of $MgAB.NH_3$ to shed light on the role of magnesium cation as well as the function of NH_3 in this reaction. The focus of this chapter is on the following three questions: (1) How can $MgAB.NH_3$ release approximately 6 moles of H_2? (2) Is the role of magnesium cation similar to lithium cation in the previous chapter in facilitating the H_2 release? (3) How does NH_3 take part in the reaction? To address these questions, this chapter will investigate comprehensively the mechanisms, kinetic and thermodynamic properties of the dehydrogenation reactions of $MgAB.NH_3$.

5.2 Computational Methods

In this mechanistic study on the system MgAB.NH_3, all geometries were optimised at the B3LYP level of theory in conjunction with 6-31+G(2d,p) basis set. Frequency calculations were performed at the same level of theory for all stationary points, with zero imaginary frequencies at all intermediate structures and one imaginary frequency representing a saddle point for transition states. Transition state structures were then verified to ensure they connect their respective reactants and products using intrinsic reaction coordinate (IRC) calculation performed at the same level of theory. All these calculations were carried out using Gaussian 09 suite of programs.

5.3 Results and Discussions

We propose the dehydrogenation reactions to occur in four stages, shown in **Scheme 5.1**. Stage **1** and **2** involves the dehydrogenations of monomer, resulting in 2 moles of H_2 released. Subsequently, stage **3a** and **3b** involve the dimerisation and trimerisation of intermediates to form the four and six-membered ring with alternate NH-BH_2. Then, in stage **4a** and **4b**, the dehydrogenations of the previously formed dimer and trimer will occur to further release up to 4 moles of H_2.

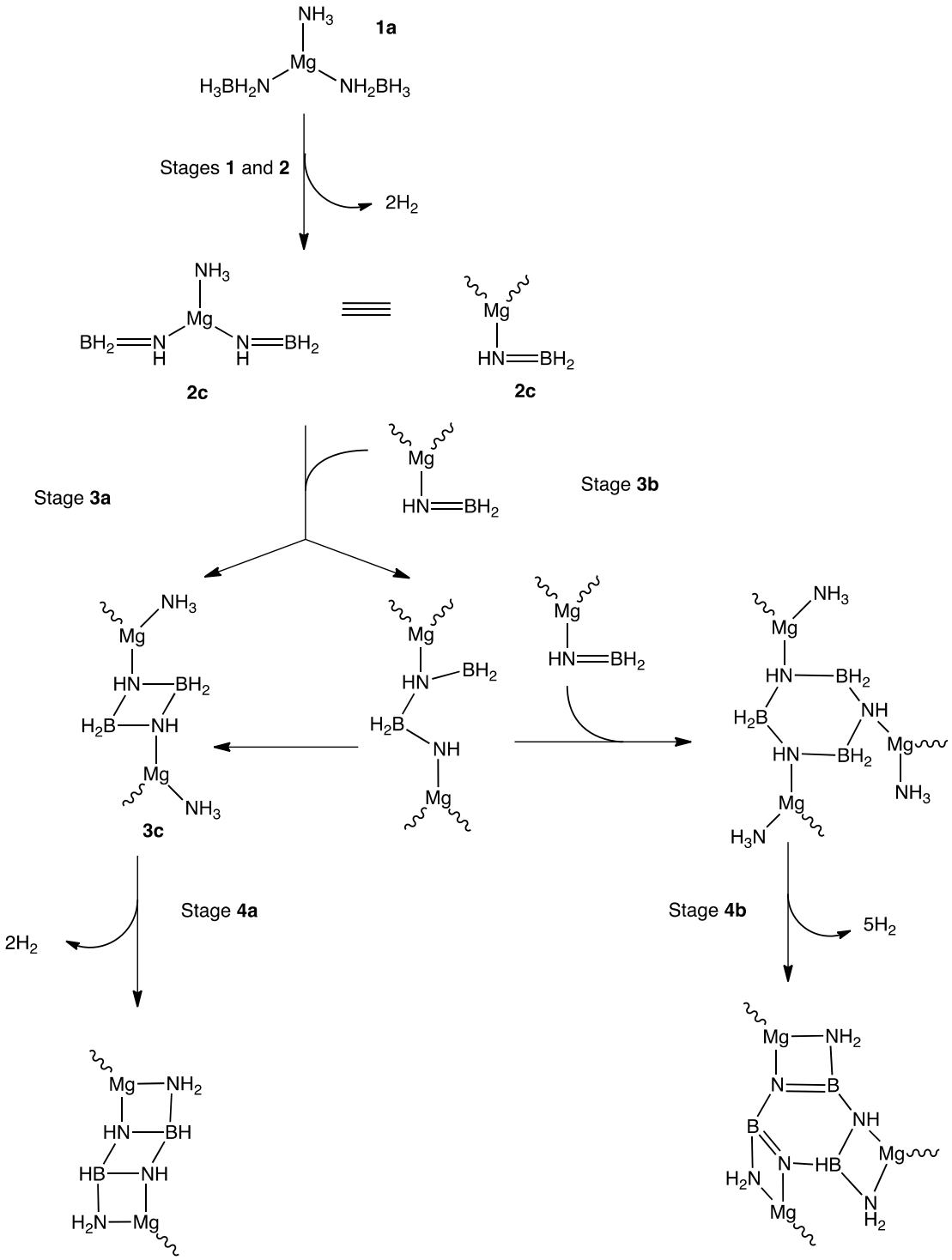

Scheme 5.1. Overall scheme for the dehydrogenation of MgAB.NH_3. The reaction begins with the monomer. Then, subsequent steps involve dimerisation and trimerisation processes. Finally, further hydrogen molecules are released from these dimer and trimer models.

The four stages of hydrogen release are summarised in the following reaction equations:

Stage **1**: $Mg(NH_2BH_3)_2.NH_3 \rightarrow Mg(NHBH_2)(NH_2BH_3).NH_3 + H_2$

Stage **2**: $Mg(NHBH_2)(NH_2BH_3).NH_3 \rightarrow Mg(NHBH_2)_2.NH_3 + H_2$

Stage **3a**: $2Mg(NHBH_2)_2.NH_3 \rightarrow [Mg(NHBH_2)_2.NH_3]_2$

Stage **3b**: $3Mg(NHBH_2)_2.NH_3 \rightarrow [Mg(NHBH_2)_2.NH_3]_3$

Stage **4a**: $[Mg(NHBH_2)_2.NH_3]_2 \rightarrow [Mg(NHBH)(NHBH_2).NH_2]_2 + 2H_2$

Stage **4b**:

$[Mg(NHBH_2)_2.NH_3]_3 \rightarrow [Mg(NHBH_2)(NHBH)_{1/3}(NB)_{2/3}.NH_2]_3 + 5H_2$

5.3.1 Hydrogen Release from the Monomer Model

Stage **1** and Stage **2** involve the dehydrogenations of the two groups NH_2BH_3 of $MgAB.NH_3$, which generate two moles of H_2. For each H_2 molecule being released, the NH_2 group will provide one proton to combine with one hydride of the BH_3 group.

Monomer $MgAB.NH_3$, which has a symmetric structure, possesses two similar groups NH_2BH_3, as shown in **Figure 5.1**. As a result, the dehydrogenation mechanisms of these two groups are likely to be analogous. Thus, we propose the same dehydrogenation mechanism for both stage **1** and stage **2**: (i) the concerted mechanism and (ii) the two-step mechanism.

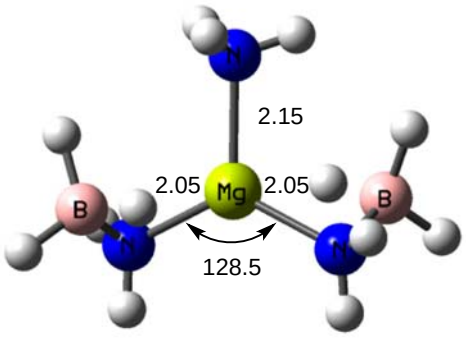

Figure 5.1 B3LYP/6-31+G(2d,p) geometrical parameters of the optimised monomer structure of $MgAB.NH_3$. Bond lengths are given in angstrom and bond angles in degree.

The dehydrogenation, kinetic and thermodynamic properties of stage **1** based on these two proposed mechanisms will be first carefully presented in the following section. Then, we mainly focus on the analysis of kinetic and thermodynamic differences between two stages when stage **2** is discussed.

5.3.1.1 Stage 1 of Hydrogen Release

In the first mechanism, the breakage of two bonds B-H and N-H occur simultaneously with the formation of H-H bond via transition state **TS1a1**, shown in **Figure 5.2**. The activation barrier $\Delta G^{\ddagger}$ required is 207.6 kJ mol^{-1}.

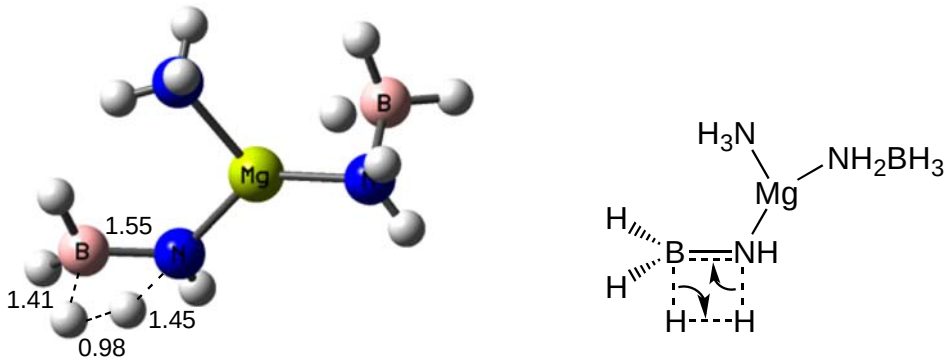

Figure 5.2 B3LYP/6-31+G(2d,p) geometrical parameters of transition state **TS1a1** of the one-step mechanism. Bond lengths are given in angstrom and bond angles in degree.

The second mechanism proceeds through two steps: (1) initially, one hydride of the BH_3 group is transferred to the magnesium atom to form Mg-H bond; (2) subsequently, this hydride interacts with one proton of the NH_2 group to release one hydrogen molecule through the redox reaction. Two transition states formed in this two-step mechanism are shown in **Figure 5.3**. The activation barrier of the first step is 100.7 kJ mol^{-1} while the activation barrier of the second step is significantly lower, which is 37 6 $kJ.mol^{-1}$. Thus, the first step is the rate-determining step in this two-step mechanism.

The difference between these two activation energies may be due to two reasons: (i) the bond breakage between boron and hydrogen is difficult because of less polar bond whereas in the second structure, the bond breaking between nitrogen and hydrogen is easier because of more polar bond; (ii) the second step is the redox reaction between the hydride carrying negative charge and the proton carrying the partial positive charge.

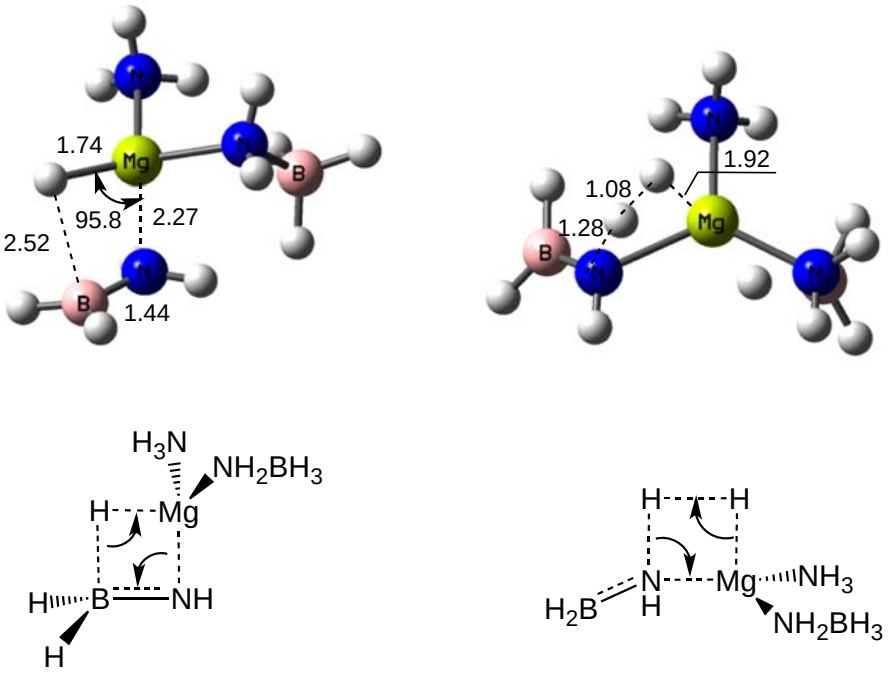

Figure 5.3 B3LYP/6-31+G(2d,p) geometrical parameters of two transition states **TS1a** and **TS1b** of the two-step mechanism. Bond lengths and bond angles are given in angstrom and degree, respectively.

The potential energy profiles for the two possible mechanisms are shown in **Figure 5.4**. Notably, this figure reveals that the transition state formation in the one-step mechanism requires a considerably higher activation barrier than in the two-step mechanism. It may be attributed to the fact that breaking two covalent bonds N-H and B-H simultaneously requires more energy than breaking one covalent bond in each separate step. In addition, partial charges on atoms involved such as the proton of NH_2 group, the hydride of BH_3 group and magnesium are likely to affect the activation barrier.

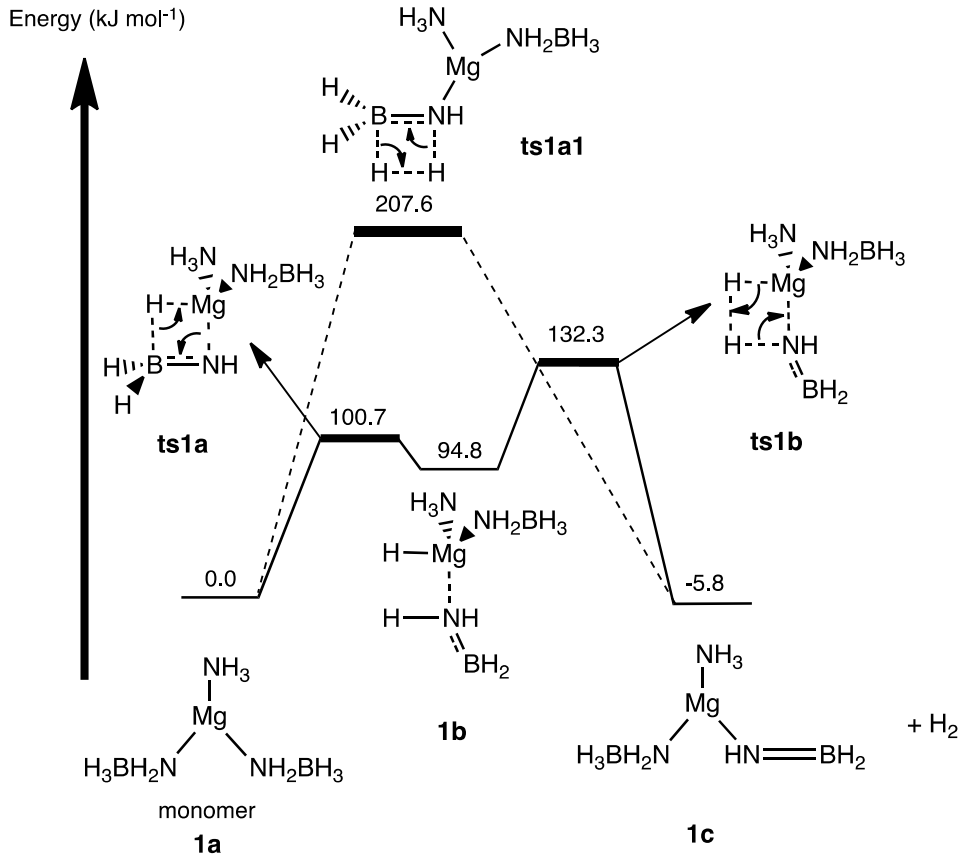

Figure 5.4 Schematic potential energy profile showing two possible pathways through which the monomer may proceed to release the first H_2 from the monomer $MgAB.NH_3$. Relative Gibbs free energies at 298.15 K and 1 atm given in kJ mol^{-1} from B3LYP/6-31+G(2d,p).

To further explore the effect of atomic charges on the activation barrier of these two mechanisms, NBO charge analysis has been carried out to compute the atomic charge of each atom of the monomer **1a** and the intermediate **1b**. **Figure 5.5** clearly indicates that magnesium atom in the monomer **1a** carries a considerably positive charge, which is +1.420; meanwhile, the proton of NH_2 group is much less positive, which is +0.430. Thus, magnesium attracts the negatively charged hydride stronger than the proton of NH_2 group does. Consequently, the activation barrier required to transfer the hydride to magnesium (in the two-step mechanism) is significantly lower than that needed to transfer the hydride to the proton of the NH_2 group (in the concerted mechanism).

The atom charge in the intermediate **1b** further elucidates the reason why in the two-step mechanism, the second activation barrier is considerably low. The hydride attached to Mg carries a negative charge, which is -0.512. On the contrary, the proton of NH_2 group carries a positive charge, which is +0.457. Thus, it can be deduced that these two opposite charges favours the interaction between the hydride and the proton, resulting in the low activation barrier.

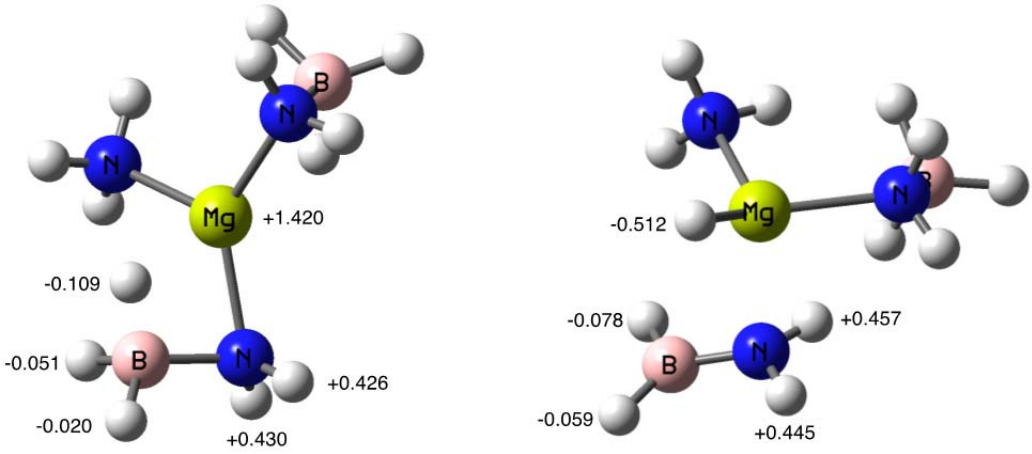

Figure 5.5 NBO atomic charges of monomer MgAB.NH_3 and its intermediate in the second mechanism.

Regarding the thermodynamic properties, the calculated enthalpy of the dehydrogenation of stage **1** increases by an amount of 33.4 kJ mol^{-1}, which indicates that this reaction is slightly endothermic. However, due to the release of H_2, the entropy of the system will also increase. This leads to the enthalpy-entropy compensation effect, resulting in a fairly small Gibbs free energy of the reaction. Indeed, the calculated Gibbs free energy is nearly zero, -5.8 kJ mol^{-1}. This small Gibbs free energy implies that the dehydrogenation occurred in stage **1** is readily reversible. This outstanding thermodynamic property is very critical for any hydrogen

storage material to be of practical use since it opens the way to restore the used material.

In summary, we have analysed two possible mechanisms of the dehydrogenation in stage **1**: (i) the concerted mechanism and (ii) the two-step mechanism. Our calculations have shown that in the two-step mechanism, the participation of magnesium is of utmost importance since it aids in lowering significantly the overall activation barrier, thus facilitate the hydrogen release. We also indicate that the first dehydrogenation of $MgAB.NH_3$ is a reversible reaction, which is important for any hydrogen storage material to be of practical use.

5.3.1.2 Stage 2 of Hydrogen Release

Similar to stage **1**, in stage **2**, the dehydrogenation reaction can proceed through two mechanisms. In the first mechanism, the direct interaction between the proton of NH_2 and the hydride of BH_3 group leads to H_2 release. Alternatively, H_2 may be released through two-step mechanism as described in the first stage. A schematic potential energy profile for stage **2** is given in **Figure 5.6**.

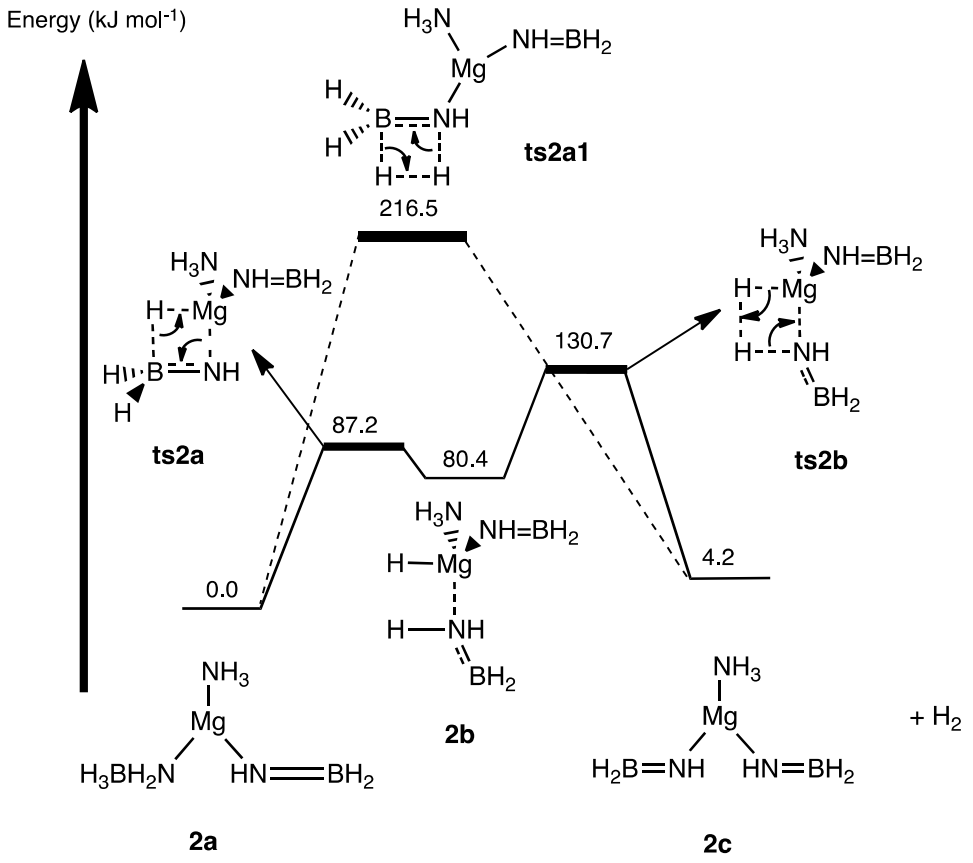

Figure 5.6 Schematic potential energy profile showing two possible pathways through which $Mg(NHBH_2)(NH_2BH_3).NH_3$ may proceed to release the second H_2. Relative Gibbs free energies at 298.15 K and 1 atm given in kJ mol^{-1} from B3LYP/6-31+G(2d,p).

Activation barrier for the first mechanism is 216.5 kJ mol^{-1}, which is quite similar to the calculated activation barrier of the same mechanism of stage **1**. Notably, in the second mechanism, the activation barrier of the rate-determining step, which is the hydride transfer step, is 87.2 kJ mol^{-1} compared to 100.7 kJ mol^{-1} at stage **1**. This significantly lower barrier may be attributed to the inductive effect of the newly formed $NH=BH_2$ group after stage **1**. To verify this, NBO charge analysis has been carried out to compute charges on atoms of **2a**.

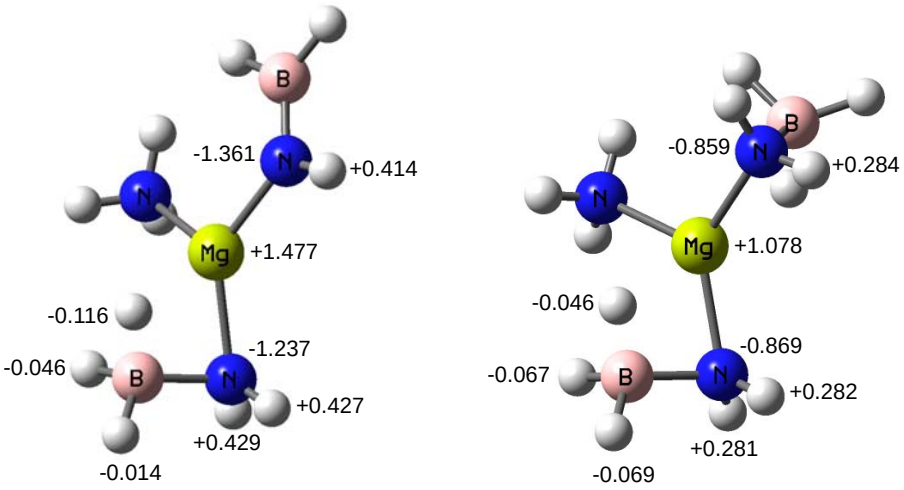

Figure 5.7 NBO atomic charges of **2a** (left) and **1a** (right) clearly indicates the inductive effect caused by $NH{=}BH_2$ group on magnesium charge. Bond lengths are given in angstrom and bond angles in degree.

Figure 5.7 reveals the considerable increase of the NBO atomic charge on the magnesium atom, from +1.078 to +1.477 after the first H_2 release. This is caused by the change of the hybridisation of the nitrogen atom from sp^3 in the NH_2-BH_3 group to sp^2 in the $NH{=}BH_2$ group. The sp^2 nitrogen atom is more electronegative than the sp^3 nitrogen. Consequently, this newly formed sp^2 nitrogen strongly withdraws the electron cloud between the magnesium and the nitrogen atoms, causing magnesium to be more positive. This more positively charged magnesium, in turn, attracts the hydride of the BH_3 group easier, leading to the lower activation barrier.

Concerning the thermodynamic properties of stage **2**, the calculated enthalpy and Gibbs free energy are 41.4 kJ mol^{-1} and 4.2 kJ mol^{-1}, respectively, which are merely slightly higher than those of stage **1**. Similar to stage **1**, the fairly small Gibbs free energy is due to the enthalpy-entropy compensation effect. Again, this small Gibbs free energy implies the reversible dehydrogenation reaction in stage **2**.

Based on the potential energy profiles of stage **1** and **2**, it is readily realised that the thermodynamic properties of stage **2** resembles those of stage **1**. Additionally, the calculated kinetics of stage **2** has indicated the even lower activation barrier of the rate-determining step than that of stage **1**. These findings imply that the first and second H_2 can be released at the same temperature. Interestingly, this result is in excellent agreement with the experimental data, which shows that the release of the first two moles of H_2 occurs simultaneously at 90^{o}C [4].

In summary, we have examined two possible mechanisms for the dehydrogenations of stage **1** and stage **2**: (i) the concerted mechanism and (ii) the two-step mechanism. In both the two cases, the activation barriers required in the two-step mechanism are significantly lower than those of the concerted mechanism. Thus, it can be deduced that the dehydrogenation is likely to proceed through the two-step mechanism. Our thermodynamic calculations have shown that both the two stages are readily reversible.

5.3.2 Dimerisation and Trimerisation of $Mg(NH=BH_2)_2.NH_3$

Our calculations in the previous section have indicated that the dehydrogenation reactions in stage **1** and **2**, which produce $Mg(NH=BH_2)_2.NH_3$, are kinetically favourable. However, any further H_2 released from the newly formed $NH=BH_2$ group of the monomer is likely to involve an extremely high activation energy. The energetic difficulties, which are demonstrated in the **Scheme 5.2** below, lie at the highly constrained structure of the $NH=BH_2$ group when the transition state, if possible, is formed.

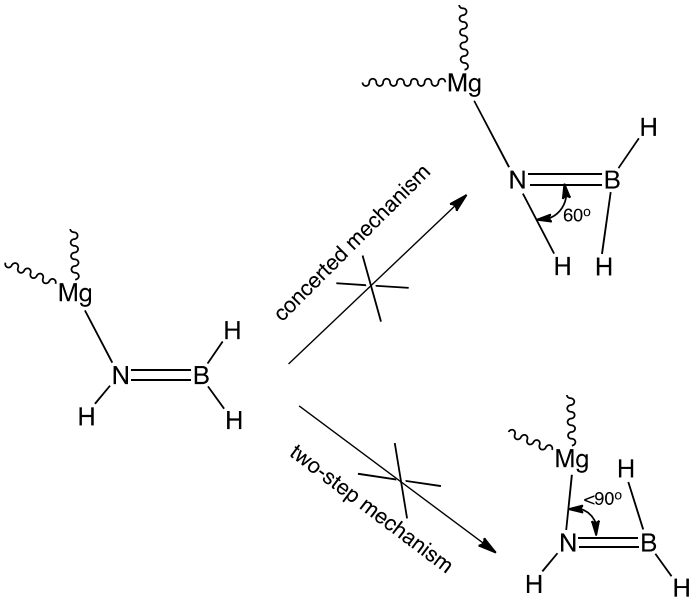

Scheme 5.2 The highly constrained transition states are unexpected to form

Scheme 5.2 clearly shows that in order to form the transition state in both mechanisms, the angles of H-N-B, H-B-N and Mg-N-B must be constrained to small angles, which are in the range of 60-90^{o}. These angles are much smaller than the ideal angles required for the sp^2 hybridisation, which is approximately 120^{o}. Thus, these highly constrained transition states are not likely to form.

While the hydrogen elimination reaction from the double bond is extremely difficult, the addition reactions occurring on the double bond $NH=BH_2$ are readily to happen due to the particular characteristics of this double bond. The $NH=BH_2$ bond is very different from other commonly found double bond such as ethylene because the π bond of the group $NH=BH_2$ in $Mg(NH=BH_2)_2.NH_3$ is polar, shown in **Figure 5.8** and easily polarised to having a lone pair localised on N and an empty boron orbital [5]. The polarities accessible to N=B double bonds creates a considerable contrast between the kinetic stability of carbon double bonds and the inherent reactive nature of N=B double bonds. It was reported that the thermal decomposition of ammonia-

borane in the solid state produced NH_2=BH_2 at approximately 125^{o}C. NH_2=BH_2 had been tentatively identified in the gas phase by mass spectrometry but was highly unstable and formed polyaminoboranes at around 155^{o}C [6] [7]. Thus, we suppose that the dimerisation and trimerisation processes of $Mg(NH=BH_2)_2.NH_3$, which are based on the reactions of the reactive N=B double bonds, are likely to occur. Subsequently, H_2 will further release from these dimer and trimer. Prior to describing the detailed dehydrogenation mechanisms of the dimer and trimer, we firstly explore the dimerisation and trimerisation mechanisms.

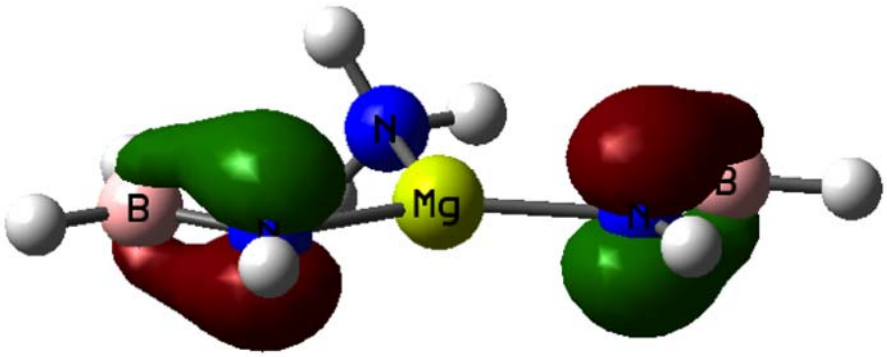

Figure 5.8 Molecular Orbital showing the polarisation of the π-orbital of $NH=BH_2$ onto the nitrogen in $Mg(NH=BH_2)_2.NH_3$.

We have examined two possible mechanisms of dimerisation: (i) the concerted mechanism and (ii) the two-step mechanism. In the first mechanism, two NH=BH2 groups of two monomers react in a concerted way, resulting in the formation of four-membered ring. On the contrary, in the second mechanism, two B-N bonds between two monomers are formed in two separate steps, leading to the formation of the same four-membered ring.

In the concerted mechanism, two monomers initially arrange in a parallel way to facilitate the coupling of two NH=BH_2 groups. Subsequently, two new N-B bonds are formed concomitantly via transition state **TS3a1**, shown in **Figure 5.9**, giving rise to dimer **3c** characterised by a four-membered ring with alternate NH-BH_2. The activation barrier required for this step is 86.2 kJ mol^{-1}.

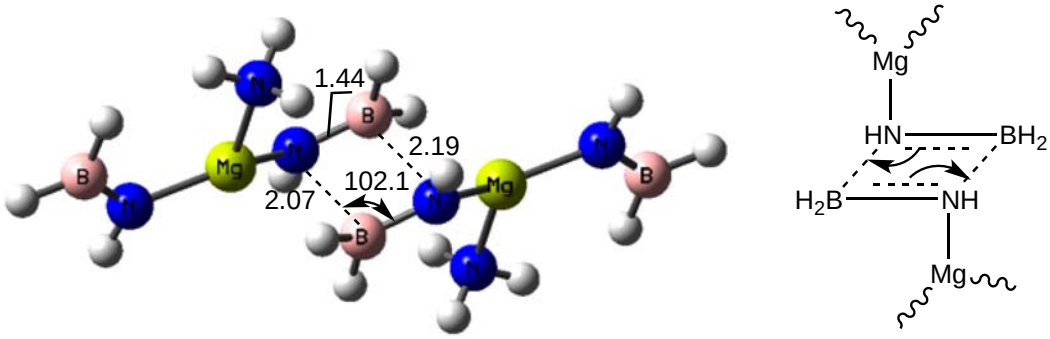

Figure 5.9 B3LYP/6-31+G(2d,p) geometrical parameters of transition states **TS3a1**. Bond lengths are given in angstrom and bond angles in degree.

The second mechanism, in contrast to the first one, does not require parallel alignment of the two monomers to occur. The first bond between two monomers is formed by the reaction of NH group of the first monomer to BH_2 group of the second monomer via the transition state **TS3a2** or **TS3a2'** (**Figure 5.10**), leading to the generation of intermediate **3b2**. This intermediate then will close the free BH_2 and NH group, via the transition state **TS3b2** (**Figure 5.10**), to form the four-membered ring.

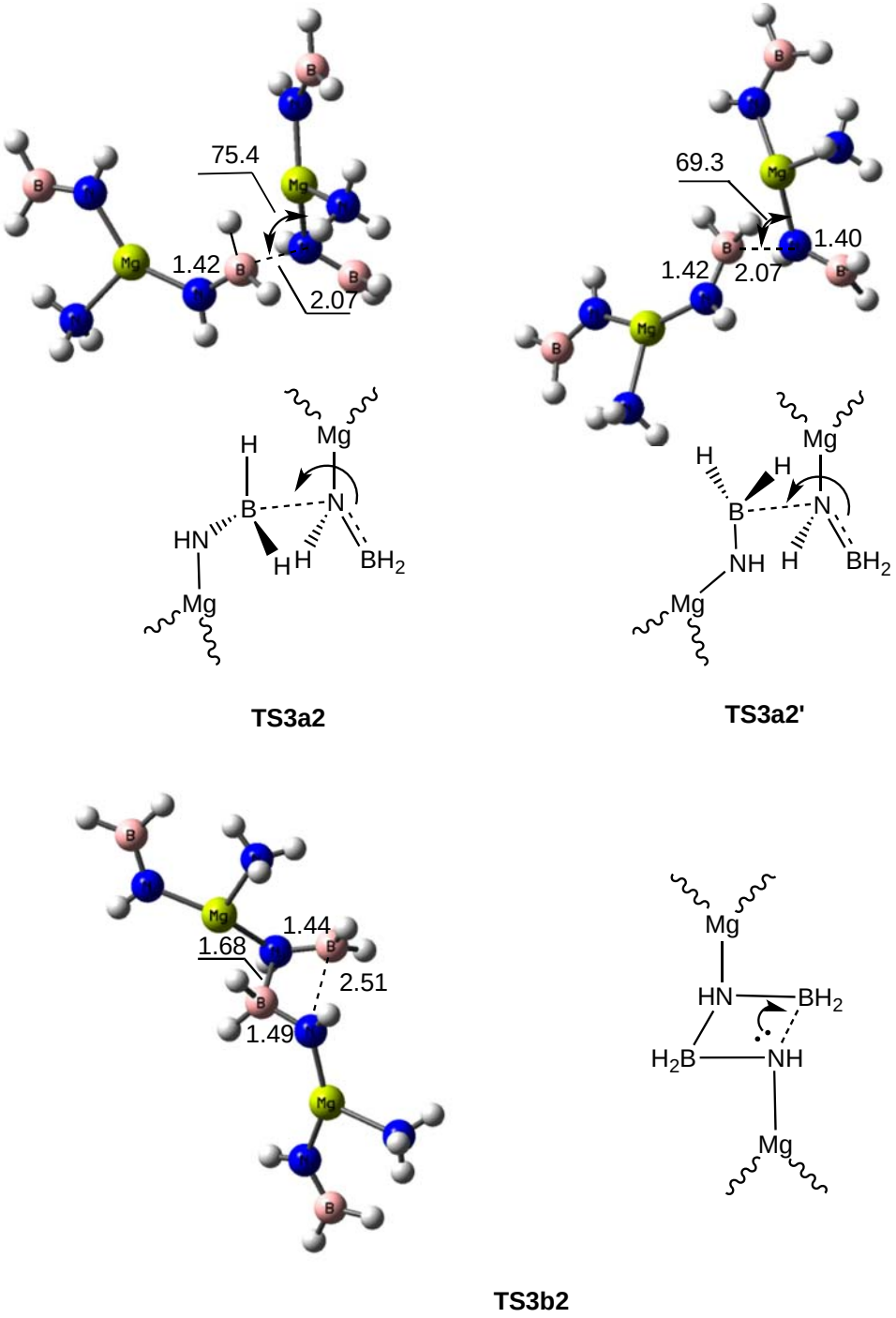

Figure 5.10 B3LYP/6-31+G(2d,p) geometrical parameters of three transition states in the two-step mechanism. Bond lengths are given in angstrom and bond angles in degree.

The activation energy required for the first B-N bond formation is 66.0 - 66.6 kJ mol^{-1} while the second N-B bond formation only needs an amount of 30.5 kJ mol^{-1}. In general, the low governing energetic barriers for the four-membered ring formation in

both mechanisms show that the dimerisation can occur very rapidly whenever two groups $NH=BH_2$ of two monomers are in favourable orientation and close proximity, which lies in a range of 2.07 to 2.19 Å as shown in **Figure 5.9**. Potential energy profile for two mechanisms is given in **Figure 5.11** below.

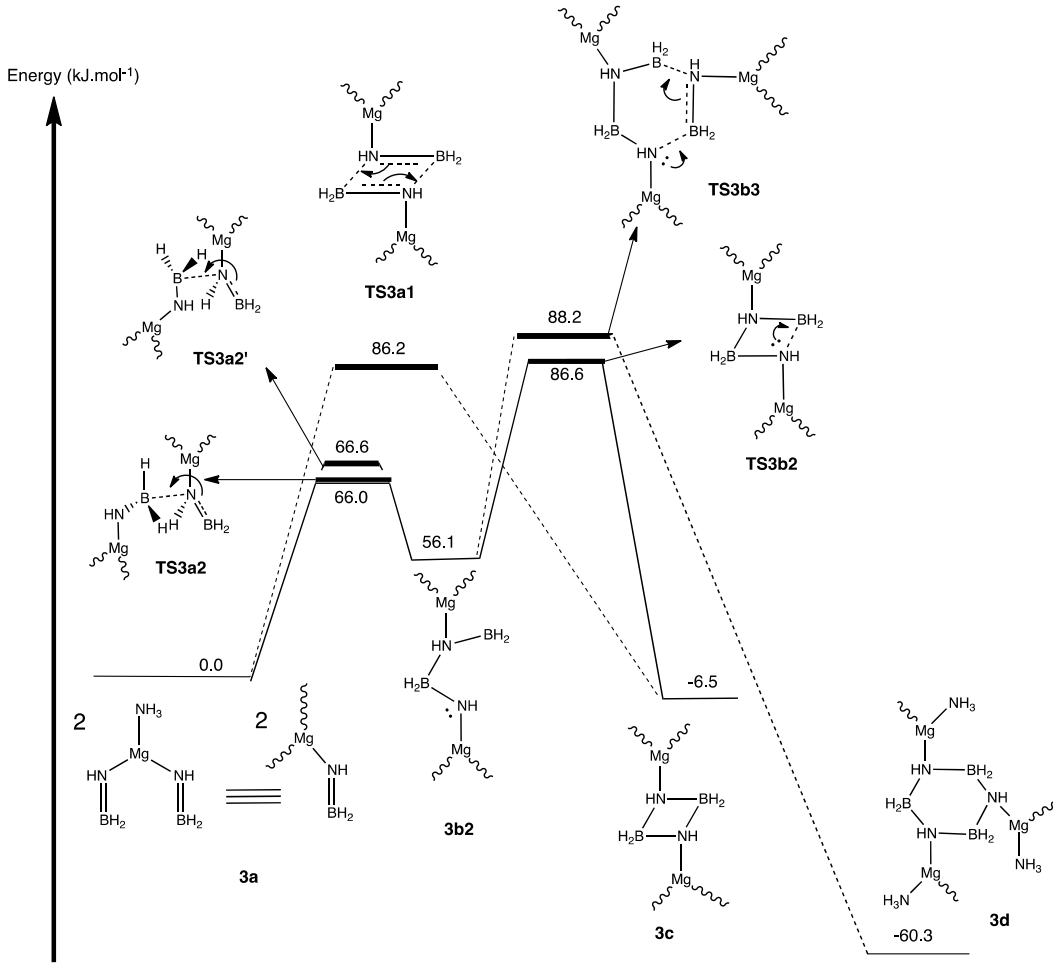

Figure 5.11 Schematic potential energy profile showing some possible mechanisms through which the monomer **3a**, $Mg(NH=BH_2)_2.NH_3$ proceed to transform to dimer **3c** or trimer **3d**.

Surprisingly, according to the energy profile, the pathway through the well-packed and aligned transition state **TS3a1** of the first mechanism is not energetically preferred since its activation barrier lies considerably higher than the two activation barriers of the two-step mechanism in which the structure are less-aligned. Molecular

orbital analysis has been carried out to explore the cause of this activation barrier difference between the two mechanisms.

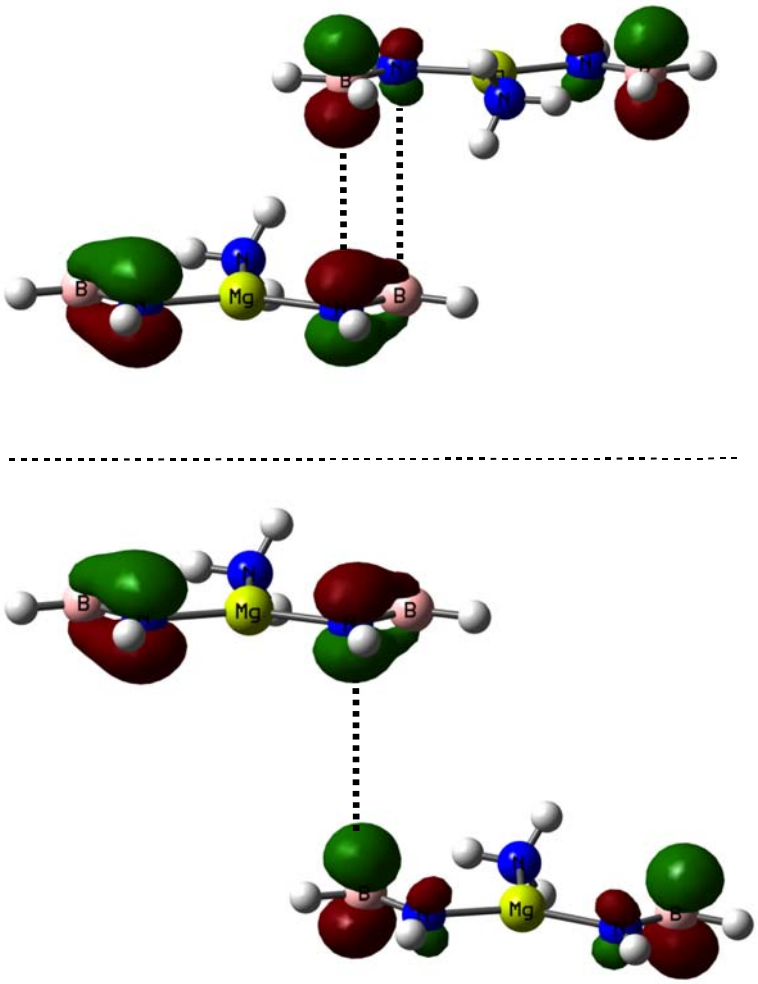

Figure 5.12 Interactions between the MO-π and the LUMO in the concerted mechanism (above) and in the two-step mechanism (below).

Figure 5.12 clearly shows that in the two-step mechanism, the overlap between the lobe of the MO-π at the B=N bond and the lobe of the LUMO at the boron atom are favourable since these two lobes have the same sign (represented as green color). However, in the step-wise mechanism, the overlap is energetically less

favourable since the lobe of the MO-π at the boron atom is of opposite sign against the lobe of the LUMO at the nitrogen atom. Consequently, the activation barrier of the concerted mechanism is higher than that of the one step mechanism.

Regarding the thermodynamic properties of the current system, the calculated enthalpy for the dimer formation at the standard condition (298 K, 1 atm), which is -73.4 kJ mol^{-1}, suggests that the dimerisation is an exothermic reaction. This can be attributed to the formation of new two σ-bonds B-N between two monomers. However, the dimer formation has caused the significant loss of entropy, thus the computed Gibbs free energy is fairly small, which is -6.5 kJ mol^{-1}.

Competing with the dimerisation pathway is the trimerisation pathway. The trimerisation comprises two separate steps. The first step proceeds through the intermediate **3b2** as in the dimerisation. However, instead of the internal cyclisation to form the dimer, the intermediate **3b2** may further combine with the third monomer $Mg(NH{=}BH_2)_2.NH_3$ to generate the trimer. **Figure 5.13** shows the transition state of trimer formation in which the third molecule approaches and aligns its $NH{=}BH_2$ group with the two free NH and BH_2 groups of the previously formed open-chained dimer.

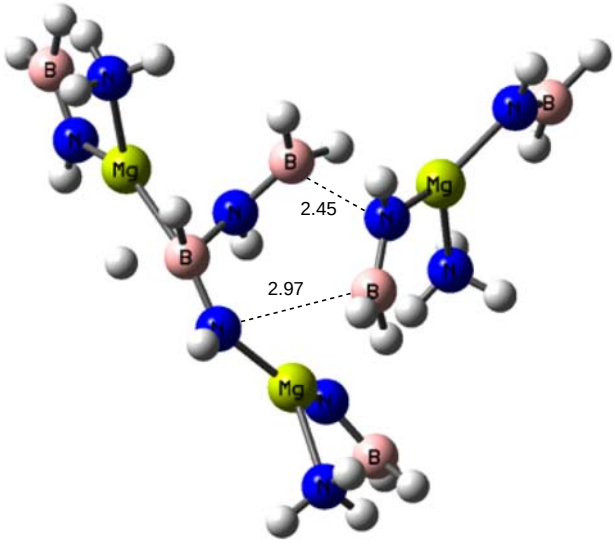

Figure 5.13 B3LYP/6-31+G(2d,p) optimised structure of transition state **TS3b3**. Bond lengths are given in angstrom.

As indicated in the energetic profile in **Figure 5.11**, this process requires an activation barrier of 32.1 kJ mol^{-1} which only lies slightly higher by 1.6 kJ mol^{-1} than the transition state **TS3b2** that leads to the dimer formation. Therefore, the trimerisation competes kinetically with the dimerisation.

Additionally, our calculations have indicated that the trimer formation is a highly exothermic reaction, which yields 186 kJ mol^{-1} while the dimer formation only can produce 73.4 kJ mol^{-1}. It may be attributed to two reasons: (i) there are three new σ-bonds B-N formed as compared to only two bonds formed in the dimer generation; (ii) the six-membered ring is much less constrained than the four-membered ring.

Although a great loss of entropy is expected after the trimer formation, Gibbs free energy (**Figure 5.11**) demonstrates that trimer structure is still thermodynamically more stable than dimer structure by 53.8 kJ mol^{-1} due to the

compensation of the enthalpy. Based on these kinetic and thermodynamic calculations, it can be deduced that, the trimer formation is more energetically favourable than the dimer formation.

In summary, this section suggests that the monomer $Mg(NH=BH_2)_2.NH_3$ is able to further dimerise and trimerise to form the dimer and trimer, respectively. We have investigates two possible mechanisms for the dimerisation, the concerted and two-step mechanism. Our calculations have shown that the two-step mechanism in which two B-N bonds between two monomers are formed in separate steps, is more kinetically favourable than in the concerted mechanism. In the trimerisation, the monomer is proposed to initially proceed through the same first step as in the two-step mechanism of the dimerisation. The later formed intermediate continues to further react with the third monomer to generate the trimer. Our kinetic and thermodynamic comparisons between the dimer and trimer formation have clearly indicated that the trimer formation is more favourable than trimer. In the following section, we will consider the thermal dehydrogenation of the newly formed dimer and trimer.

5.3.3 Hydrogen Release from the Dimer and the Trimer Models

The structures of the dimer and trimer are basically similar. As shown in **Figure 5.14**, their structures are characterised by two main components: the ring with alternate $NH\text{-}BH_2$ groups and the branch groups $Mg(NH=BH_2).NH_3$.

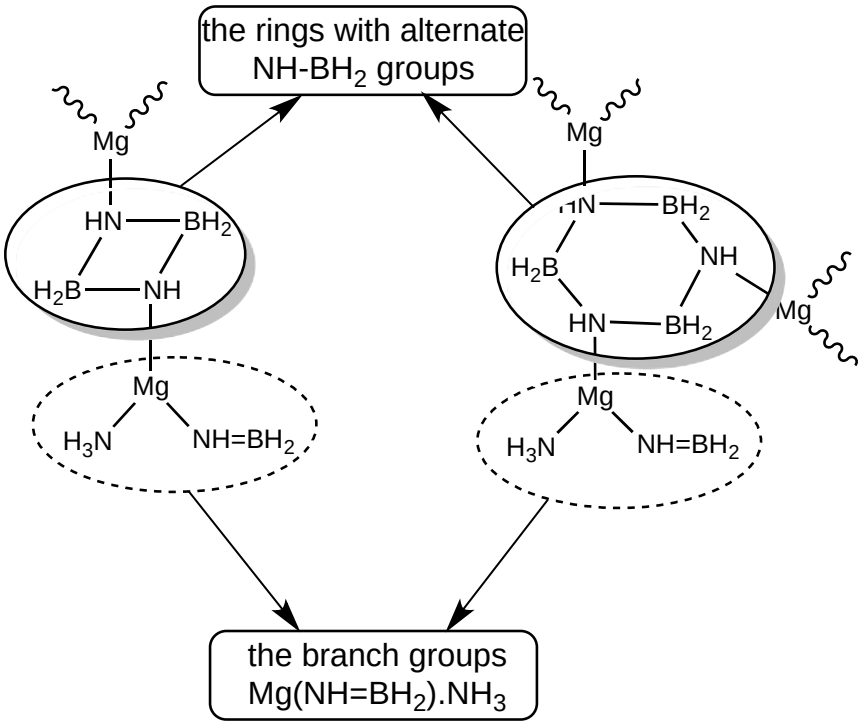

Figure 5.14 The structures of the dimer and trimer are basically similar.

Due to these structural similarities, the chemistry associated with the dehydrogenation of these two dimer and trimer models are supposed to be analogous. Thus, we propose the same two stages for the dehydrogenation reactions of these models: (i) the first stage i.e. Stage **4a1** in the case of the dimer model and Stage **4b1** in the case of the trimer model, includes all the reactions between the NH_3 groups of the branch groups $Mg(NH=BH_2).NH_3$ and the BH_2 groups of the ring, leading to the formation of four-membered rings and H_2 molecules being released; (ii) the second stage i.e. Stage **4b2** in the case of trimer model involves the H_2 eliminations as a result of the interactions between the protons and hydrides of the NH and BH_2 groups respectively, of the ring.

5.3.3.1 Stage 4a1 and 4b1

At stages **4a1** and **4b1**, the NH_3 group of the branch group $Mg(NH=BH_2).NH_3$ play a critical role in providing one proton to combine with one hydride contributed by the BH_2 group the ring, resulting in one hydrogen molecule being released. Since our dimer and trimer models possess two and three $Mg(NH=BH_2)_2.NH_3$ groups thus, two and three H_2 molecules can be released from these models, respectively.

We have envisaged two possible mechanisms for the H_2 release from the NH_3 group of $Mg(NH=BH_2).NH_3$ and the BH_2 group of the ring. The first H_2 molecule being released from the dimer model has been chosen to illustrate these two mechanisms **(Figure 5.15)**. In the first mechanism, the hydrogen elimination occurs in one step through the concerted interaction between the proton of the NH_3 group and the hydride of the BH_2 group of the ring. The sole transition state **4a_tsa1** involved in this mechanism is shown in **Figure 5.15**. The second mechanism is the familiar two-step mechanisms we've proposed in the previous sections. This mechanism consists of two steps, an initial hydride transfer, followed by a H_2 release. In the first step, one hydride is transferred from the BH_2 group of the four-membered ring to the magnesium atom of the $Mg(NH=BH_2).NH_3$ group via transition state **4a_tsa2** (**Figure 5.15**), giving rise to the formation of intermediate **4b2**. Then, the hydride from Mg-H and one proton from the NH_3 group are lost simultaneously as a H_2 molecule via transition state **4a_tsb2** (**Figure 5.15**).

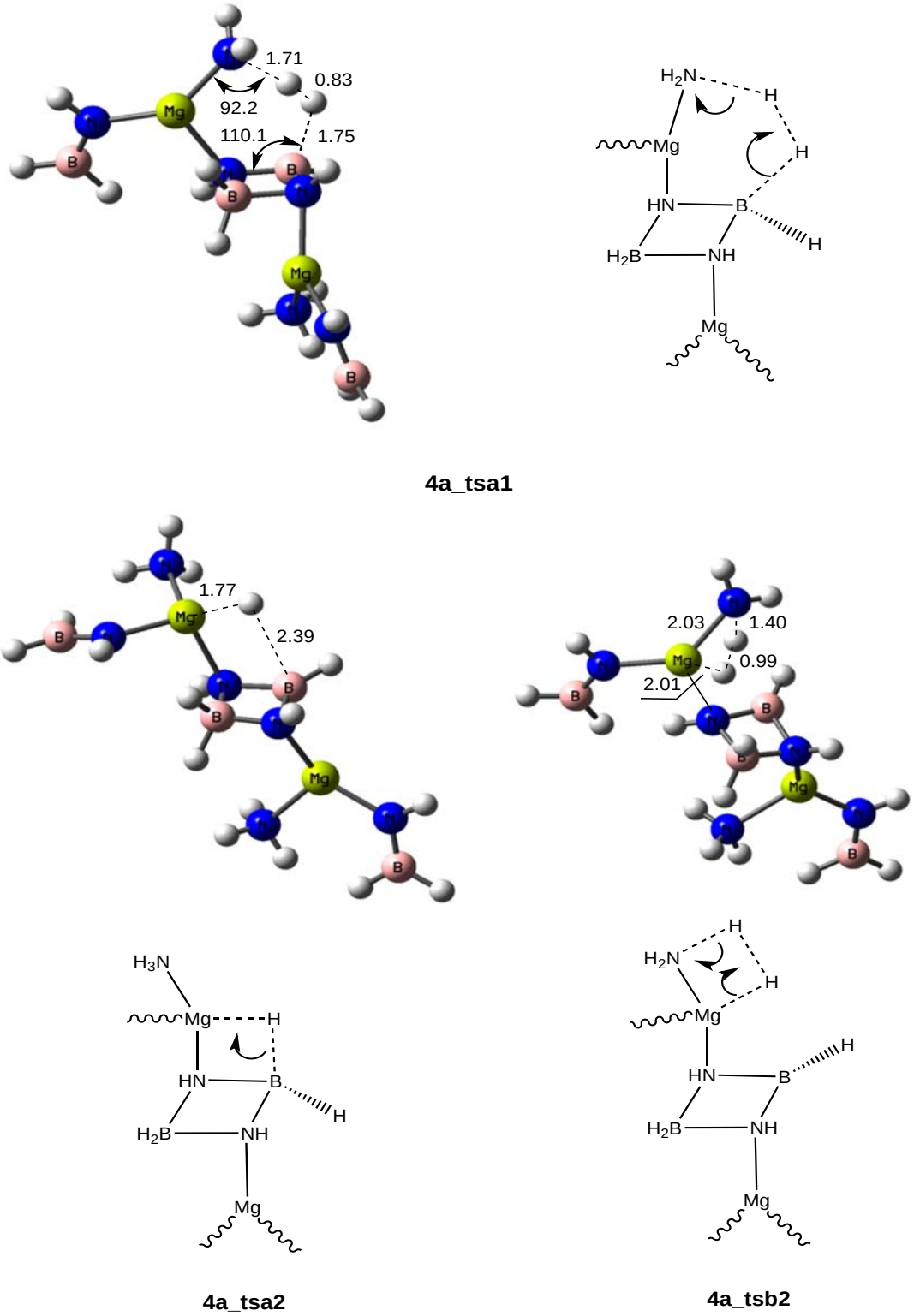

Figure 5.15 B3LYP/6-31+G(2d,p) optimised structures of the three transition states: **4a_tsa1** (in mechanism 1); **4a_tsa2** and **4a_tsb2** (in mechanism 2). Bond lengths and bond angels are given in angstrom and degree, respectively.

A schematic potential energy profile for these two mechanisms is shown in **Figure 5.16**. Similar to the schematic potential energy profiles corresponding to the first and second H_2 release at Stages **1** and **2**, this profile, again, confirms the critical role of the magnesium in facilitating the hydrogen release. In contrast to the one-step mechanism which requires a high activation barrier of 133.0 kJ mol^{-1}, the participation of the magnesium atom in the two-step mechanism effectively lowers the activation barrier to 70.9 kJ mol^{-1} and 81.3 kJ mol^{-1}.

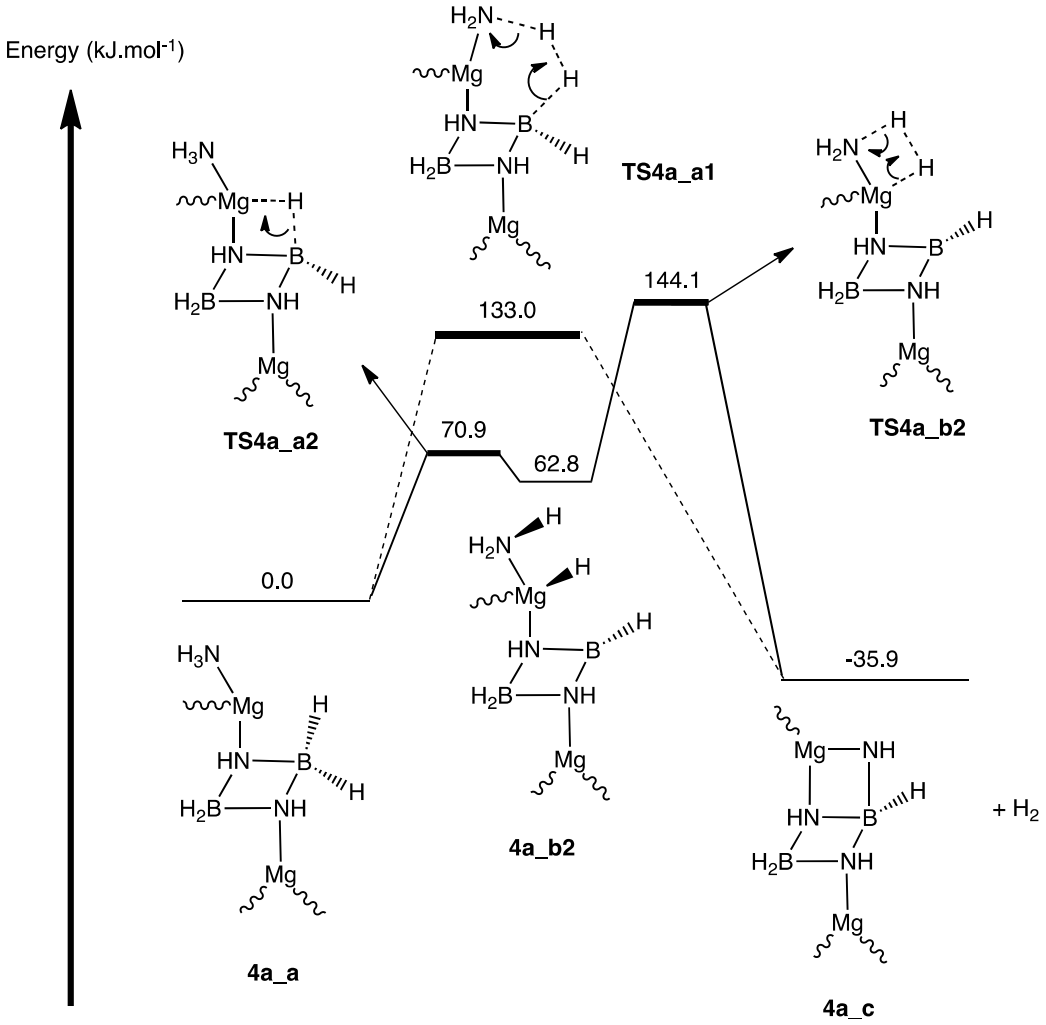

Figure 5.16 Schematic potential energy profile for the first H_2 release from the dimer model. Relative Gibbs free energies at 298.15 K and 1 atm are given in kJ mol^{-1} from B3LYP/6-31+G(2d,p).

Activation barriers required in each step of the two mechanisms for the first and second H_2 releases from the dimer and trimer models are shown in **Tables 5.1** and **5.2**. These results indicated in these two tables reveal that in both the dimer and trimer models, the one-step mechanism always requires significantly higher activation barrier than the two-step mechanism. Comparing the activation barriers of the two-step mechanism between the dimer and trimer models, we have found out that the energies needed to release H_2 via the two-step mechanism are similar. It is due to the similarity in the structures of the dimer and trimer models as earlier analysed.

Table 5.1 Activation barriers (kJ mol^{-1}) required in each step of the two mechanisms for the first and second H_2 releases from the dimer $[Mg(NH{=}BH_2)_2.NH_3]_2$.

Stage	$\Delta G^{\ddagger}$ of the one-step mechanism (kJ mol^{-1})	$\Delta G^{\ddagger}$ of the two-step mechanism (kJ mol^{-1})	
		Hydride Transfer Step	Hydrogen Release Step
First H_2 release	133.00	70.9	81.3
Second H_2 release	133.95	73.2	79.9

Table 5.2 Activation barriers required in each step of the two mechanisms for the first and second H_2 releases from the trimer $[Mg(NH{=}BH_2)_2.NH_3]_3$.

Stage	$\Delta G^{\ddagger}$ of the one-step mechanism (kJ mol^{-1})	$\Delta G^{\ddagger}$ of the two-step mechanism (kJ mol^{-1})	
		Hydride Transfer Step	Hydrogen Release Step
First H_2 release	125.2	61.5	79.8
Second H_2 release	126.1	62.1	81.2
Third H_2 release	126.5	64.3	79.3

5.3.3.2 Stage 4b2

After stage **4a1** of the dimer, we initially supposed that two more hydrogen molecules could be released from the four-membered ring characterised by two NH-BH groups. However, we failed to locate any transition states for these hydrogen eliminations. It might be due to the high constraint of this four-membered ring that prevents any further hydrogen release, which if occurs, will certainly add more ring constraint. In contrast with this four-membered ring, the six-membered ring of the trimer, which has no ring constraint, could continue release hydrogen.

At this second stage, each BH group of the ring will contribute its final hydride, while the NH group of the ring will also provide its final proton to release. We propose all the H_2 eliminations at this stage proceed through the concerted mechanism. We have successfully located two transition states, corresponding to the generation of another two moles from this six-membered ring. Our calculations have shown that the first H_2 release from this six-membered ring requires 215.6 kJ mol^{-1}, while the second H_2 release only needs 181.1 kJ mol^{-1}. It might be due to the inductive effect of the new B=N formed after the first H_2 release. However, these two activation barriers at **Stage 4b2** are considerably higher than that of previous stages investigated, implying that these final hydrogen molecules are difficult to release.

5.4 Conclusions

This chapter has provided a comprehensive understanding on different possible pathways $Mg(NH_2BH_3)_2.NH_3$ may undergo to release H_2. Based on the

monomer model of $Mg(NH_2BH_3)_2.NH_3$, we have shown that up to two moles of H_2 could readily release via two feasible mechanisms: the concerted mechanism and the step-wise mechanism. Our calculated results were consistent with the experimental observation when they indicated that two moles of H_2 could be release simultaneously at the same temperature of 90^oC. Then, we have shown that further H_2 release from the compound $Mg(NH=BH_2)_2.NH_3$ was energetically unfavourable due to high energy needed to break hydrogen sp^2 from double bond of the group $NH=BH_2$. Thus, we proposed the formation of dimer and trimer, which then facilitated hydrogen release. Based on these two models, we have envisaged two possible mechanisms to transform the monomer into the dimer and the trimer: (i) the concerted mechanism and (ii) the step wise mechanism. Notably, the stepwise mechanism in both cases is kinetically more competitive than the concerted one. The activation barrier for the step wise mechanism is found to be similar in dimerisation and trimerisation, which indicate the rate of formation of these two species are equal. However, thermodynamic calculations have clearly shown that the trimer model was much more thermodynamically stable than the dimer, thus the trimer formation was likely to predominate the dimer. More hydrogen molecules were shown to be able to release from the dimer and the trimer models. The mechanisms of the hydrogen elimination from the dimer and the trimer models were similar to what we have observed at the previous stages. H_2 release processes could proceed through either the concerted or the step-wise mechanism, in which the step-wise mechanism always required lower activation barrier.

Apart from these kinetic and thermodynamic results, we have learnt that magnesium atom plays an important role of a catalyst to facilitate the hydrogen

release. This finding in combination with our results in the previous chapter, once again, offers the compelling evidence for the critical role of the metal ions such as lithium and magnesium in improving the dehydrogenation properties of ammonia-borane based compounds. Besides, the important role of NH_3 as a protic supplier to release more H_2 was also elucidated.

In the next chapter, we will explore the dehydrogenation mechanisms of an intriguing newly synthesised compound $LiBH_4.MgCl_2.NH_3$, which contains lithium, magnesium atom and NH_3 group discussed in the latest two chapters. Will they collaborate in facilitating hydrogen release or will they take different roles? These questions will be answered shortly in the following chapter.

References

[1] Y. S. Chua, G. T. Wu, Z. T. Xiong, T. He, and P. Chen, *Chem. Mater.*, vol. 21, p. 4899, 2009.

[2] Jan Spielmann, Georg Jansen, Heinz Bandmann, and Sjoerd Harder, "Calcium Amidoborane Hydrogen Storage Materials: Crystal Structures of Decomposition Products," *Angewandte Chemie*, vol. 120, pp. 6386-6391, Aug 2008.

[3] Hui Wu, Wei Zhou, and Taner Yildirim, "Alkali and Alkaline-Earth Metal Amidoboranes: Structure, Crystal Chemistry, and Hydrogen Storage Properties," *J. Am. Chem. Soc.*, vol. 130, no. 44, pp. 14834-14839, 2008.

[4] Yong Shen Chua et al., "Synthesis, structure and dehydrogenation of magnesium amidoborane monoammoniate," *Chem. Commun.*, vol. 46, pp. 5752-5754, 2010.

[5] D. J. Grant and D. A. Dixon, *J. Phys. Chem. A*, vol. 110, pp. 12955-12962, 2006.

[6] R. A. Geanangel and J. W. Rabalais, *Inorg. Chim. Acta*, vol. 97, p. 59, 1985.

[7] A. Staubitz, P. M. Robertson Alasdair, and Ian Manners, "Ammonia-Borane and Related Compounds as Dihydrogen Sources," *Chem. Rev.*, vol. 110, pp. 4079-4124, 2010.

CHAPTER 6

A MECHANISTIC STUDY ON THE DEHYDROGENATION OF $LiBH_4.NH_3.MgCl_2$

6.1 Introduction

In the preceding chapters, we have examined the dehydrogenation mechanisms, thermodynamic and kinetic properties of some promising hydrogen storage materials, which included $LiNH_2BH_3$ and $Mg(NH_2BH_3)_2.NH_3$. Apart from these two examples, lithium borohydride has also been extensively researched over the years to possess a similarly deep potential. Besides its high gravimetric capacity of 18.4 wt%, it also has relatively good reversibility as compared to the other known boron-based storage materials [1]. However, this compound only contains hydrides while it has been demonstrated that the presence of both hydridic (H^-) and protic (H^+) atoms are critical for facile H_2 elimination via redox reactions [2-4]. Thus, to make $LiBH_4$ a better hydrogen storage material, one approach is to introduce protic atom-containing compounds into it.

It was reported almost fifty years ago that lithium borohydride could absorb ammonia to form a series of ammonia-lithium borohydride complexes such as $LiBH_4.NH_3$, $LiBH_4.2NH_3$ and $LiBH4.3NH_3$ [5]. Among these compounds, $LiBH_4.NH_3$ contains the highest hydrogen capacity of 18.0 wt%; in particular, the hydrogens on the nitrogen and boron exhibits protic and hydridic character,

respectively [6-19], making it a very promising candidate for a hydrogen storage material. Unfortunately, it has been revealed recently that $LiBH_4.NH_3$ mainly released ammonia rather than hydrogen during heating [20]. It was also reported that the compound remained un-decomposed until 300^oC [21].

In this context, some promising solutions have been proposed to tackle these problems; these include nanoengineering and also usage of additives [1]. Recently, Gao *et al.* has reported that by adding $MgCl_2$ to $LiBH_4.NH_3$, its dehydrogenation would be significantly improved [22]. Their experimental results indicated that while the dehydrogenation of $LiBH_4.NH_3$ mainly occurred at the range of 300 - 400^oC, the system $LiBH_4.NH_3.MgCl_2$ had a significantly lower dehydrogenation temperature, which was as low as 150^oC (hydrogen release peak at 240^oC). Moreover, it was observed that a significant amount of the NH_3 released during dehydrogenation of $LiBH_4.NH_3$ was successfully suppressed within the $LiBH_4.NH_3.MgCl_2$ molecule. Their research indicated that $LiBH_4.NH_3.MgCl_2$ released 2.91 equiv of H_2, accompanied by only 0.08 and 0.1 equiv of NH_3 emission, corresponding to a 91.6% NH_3 conversion. However, both the exact dehydrogenation mechanism and the role of $MgCl_2$ have remained unknown. Thus, it is of utmost importance to perform a mechanistic study to examine the dehydrogenation mechanism and shed light on the role of magnesium chloride in this reaction. The findings of this research may aid in finding better compounds than $MgCl_2$ in improving dehydrogenation properties.

In this chapter, the monomer and dimer models of $LiBH_4.NH_3.MgCl_2$ will be employed to model the hydrogen release reaction and explore how magnesium chloride affects the kinetic and thermodynamic properties of the dehydrogenation.

Subsequently, experimental data will be used to examine which model better matches the experimental data.

6.2 Computational Methods

DFT calculations based on the hybrid functional in conjunction with the 6-31+G(2d,p) basis set were employed to optimise all equilibrium structures and transition states in the gas phase of the system $LiBH_4.NH_3.MgCl_2$. Additionally, the activation barrier, $\Delta G^{\ddagger}$, and the enthalpy, ΔH of the reaction at the standard condition, 298 K, 1 atm were also computed. Intrinsic reaction coordinates (IRC) were utilised to confirm the identity of the linking reactant and product from a transition state. All DFT calculations were performed using the Gaussian 09 suite of programs.

6.3 Results and Discussions

6.3.1 Mechanism for Hydrogen Release using the Monomer Model

We first examine the dehydrogenation mechanism of $LiBH_4.NH_3.MgCl_2$ using a monomer model in the gas phase. The monomer of $LiBH_4.NH_3.MgCl_2$, which is shown in **Figure 6.1**, is predicted to have a two-bridge structure in which the anion BH_4^- and Cl^- bridges between two cations, Li^+ and Mg^{2+}. Notably, this is the unique monomer structure found after performing optimisations on many other intended input structures. The explanation for this structure might be because it possesses good stability, since the two most negatively charged anions, BH_4^- and Cl^- are trapped between the two most positively charged cations, Li^+ and Mg^{2+}.

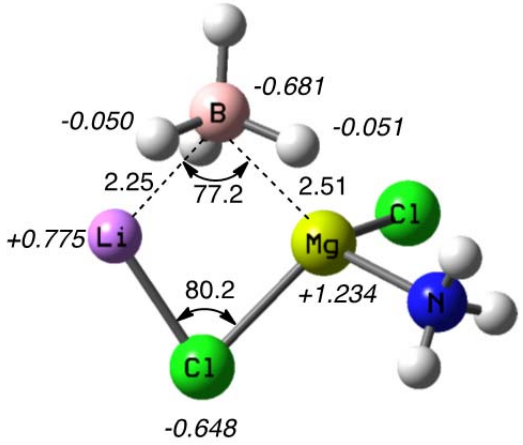

Figure 6.1 B3LYP/6-31+G(2d,p) geometrical parameters of the optimised monomer structure of $LiBH_4.NH_3.MgCl_2$. Bond lengths are given in angstrom and bond angles in degree. NBO charges (in *italic*) are also indicated.

We envisage the dehydrogenation reactions to occur in three stages of hydrogen release, corresponding to three moles of H_2 release, with a similar two-step mechanism as presented in the previous two chapters. It should be noted that the concerted mechanism has also been investigated. However, the calculations show that the barrier energies are considerably high (~ 250 kJ mol^{-1}), which are similar to those results obtained with previously examined hydrogen storage systems. Thus, this section only focuses on the two-step mechanism. The two-step mechanism consists of an initial hydride transfer (step **a**), followed by a H_2 release (step **b**). In step **a**, both the lithium and magnesium atoms play a critical role to attract and remove one hydride from the borohydride group to form a Li-H-Mg bond. Subsequently, in step **b**, the monomer system slightly changes its conformation so that the proton from the ammonia group could approach the new Li-H-Mg moiety, with one hydrogen molecule being released.

The three stages of hydrogen release are summarised in the following reaction equations:

Stage **1**: $LiBH_4.NH_3.MgCl_2 \rightarrow LiBH_3.NH_2.MgCl_2 + H_2$

Stage **2**: $LiBH_3.NH_2.MgCl_2 \rightarrow LiBH_2.NH.MgCl_2 + H_2$

Stage **3**: $LiBH_2.NH.MgCl_2 \rightarrow LiNBH.MgCl_2 + H_2$

Overall reaction: $LiBH_4.NH_3.MgCl_2 \rightarrow LiNBH.MgCl_2 + 3H_2$

A potential energy profile for the release of the first mole of H_2 from $LiBH_4.NH_3.MgCl_2$, i.e. Stage **1**, involves step **1a** and **1b**, is shown below.

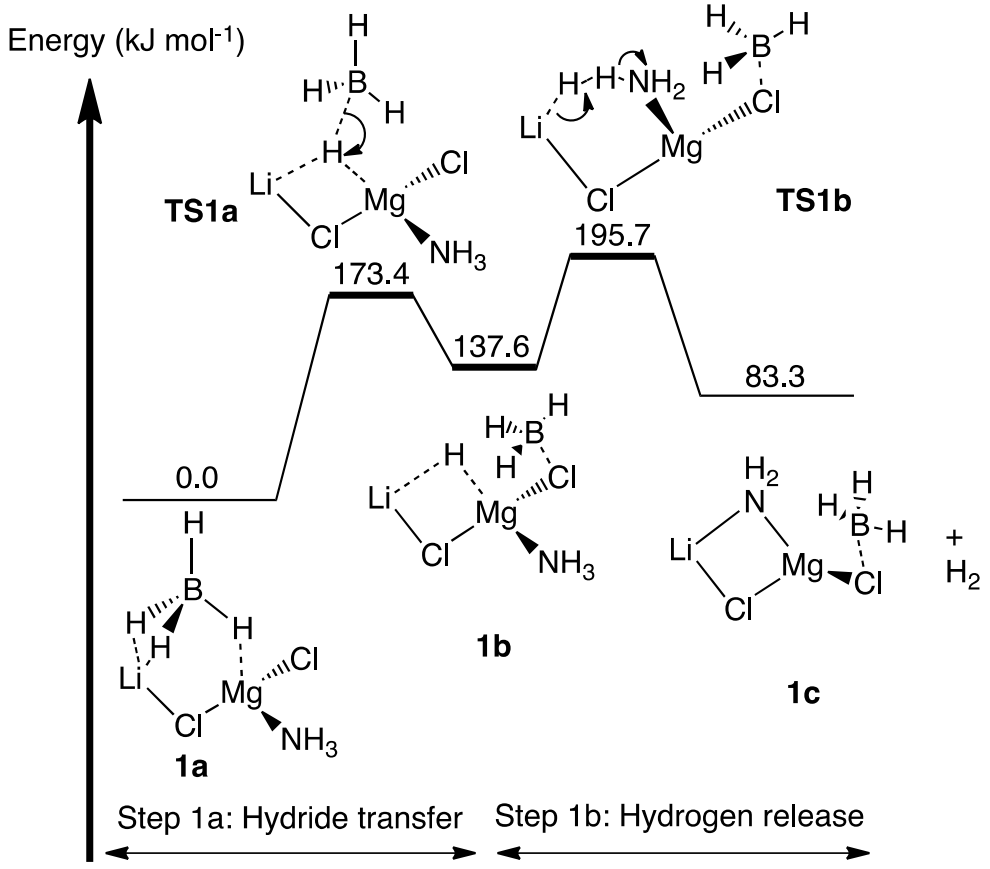

Figure 6.2 Schematic potential energy profile for Stage **1** of the H_2 release from $LiBH_4.NH_3.MgCl_2$. Relative Gibbs free energies at 298.15 K and 1 atm are given in kJ mol^{-1} from B3LYP/6-31+G(2d,p).

In step **1a**, one hydride is transferred from the borohydride group to the centre of the lithium and magnesium atoms, via transition state **TS1a** (**Figure 6.3**), giving rise to the formation of the intermediate **1b**. Notably, this intermediate is characterised by a hydride bridged between 2 strongly positively charged lithium and magnesium atom (Li---H---Mg). Subsequently in step **1b**, the intermediate **1b** alters its conformation slightly to orient the ammonia group towards the hydride for facilitating the hydrogen release. Then, the hydride from Li-H-Mg and the proton from N-H are lost simultaneously as a H_2 molecule, via transition state **TS1b** (**Figure 6.3**).

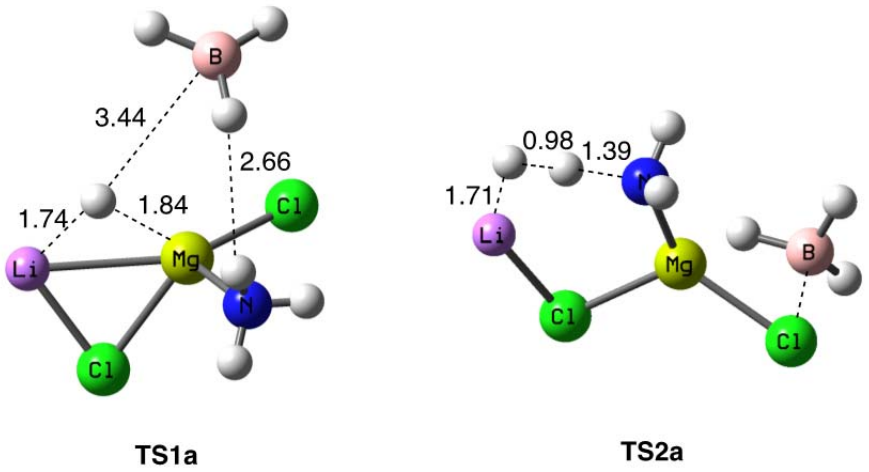

Figure 6.3 B3LYP/6-31+G(2d,p) geometrical parameters of transition state **TS1a** and **TS1b**. Bond lengths are given in angstrom.

At this stage, the Li and Mg atoms play a critical role to assemble the hydrogen atoms for dehydrogenation. The calculated activation barriers $\Delta G^{\ddagger}$ for step **1a** and **1b** are 173.4 and 58.1 kJ mol^{-1}, respectively. The considerably higher barrier in step **1a** may be due to two reasons: (i) In the first structure, the bond breaking between boron and hydrogen is more difficult because of the presence of a less polar bond whereas in the second structure, the bond breaking between nitrogen and hydrogen is easier because of the more polar bond between them; (ii) The second step

is a redox reaction, which would occur easily as the two hydrogen atoms are of opposite charge.

The second H_2 release at Stage **2**, involves steps **2a** and **2b**, corresponding to the reaction: $LiBH_3.NH_2.MgCl_2$ → $LiBH_2.NH.MgCl_2 + H_2$. A schematic energy profile for this stage is shown in **Figure 6.4**.

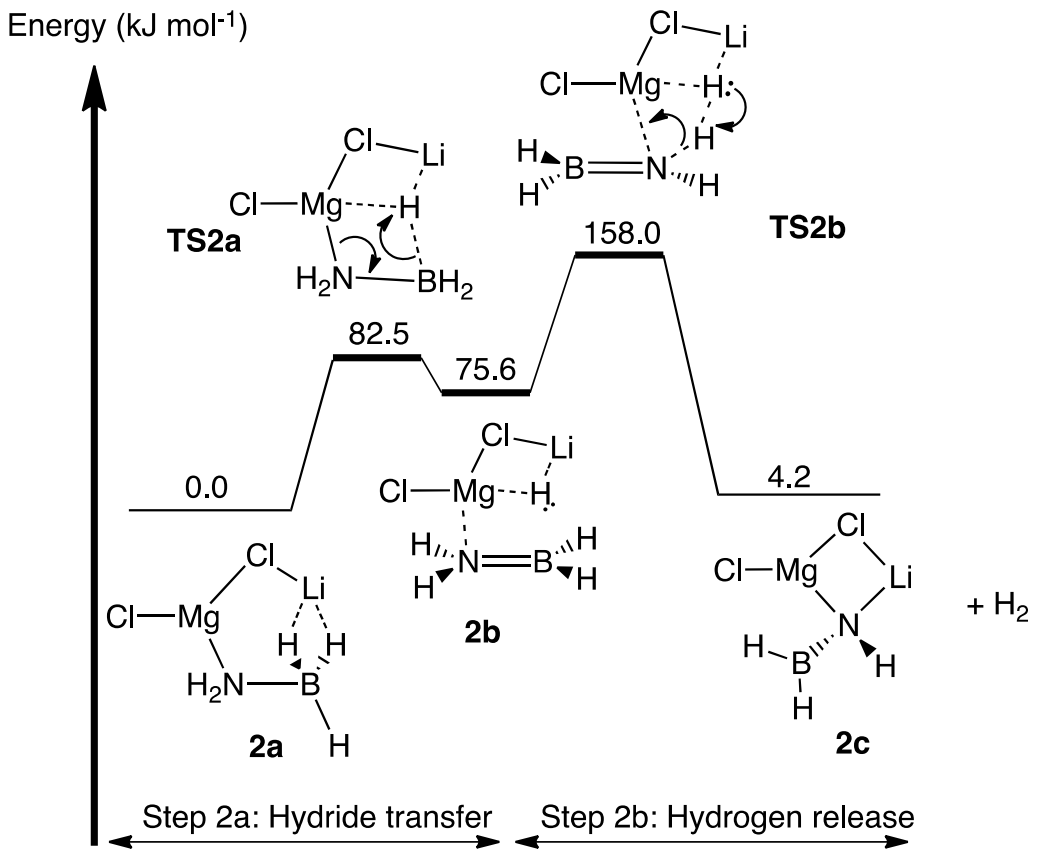

Figure 6.4 Schematic potential energy profile for Stage **2** of the H_2 release from $LiBH_4.NH_3.MgCl_2$. Relative Gibbs free energies at 298.15 K and 1 atm are given in kJ mol^{-1} from B3LYP/6-31+G(2d,p).

The relevant chemistry associated with steps **2a** and **2b** is analogous to which have occurred in steps **1a** and **1b**. Again, one hydride from the borohydride group is transferred to the centre of the lithium and magnesium atoms via transition state **TS2a**

as shown in **Figure 6.5**. Then, the proton from the ammine group approaches this hydride via transition state **TS2b** as given in **Figure 6.5**, resulting in a second H_2 released via intermediate **2b**.

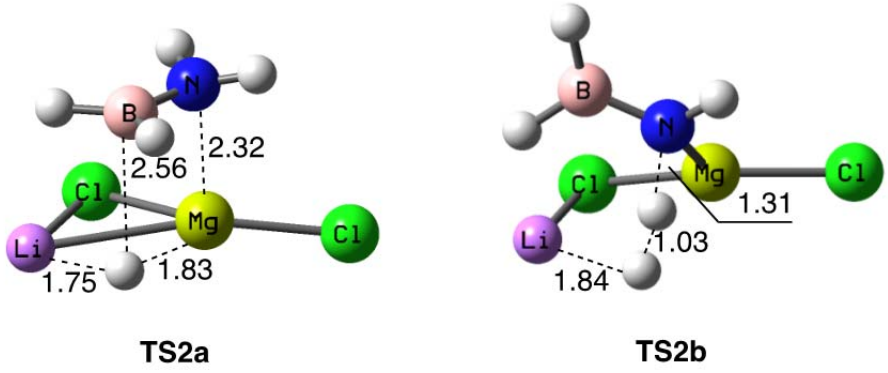

Figure 6.5 B3LYP/6-31+G(2d,p) geometrical parameters of two transition states, **TS2a** and **TS2b**. Bond lengths are given in angstrom.

The activation barriers $\Delta G^{\ddagger}$ required for these two steps are 82.5 and 82.4 kJ mol^{-1}, respectively. Surprisingly, the activation barrier for the hydride transfer step, which is the rate-determining step, is considerably lower, at 82.5 kJ mol^{-1} compared to 173.4 kJ mol^{-1} of the same step in Stage **1**. This may be attributed to the particular structure of monomer **1a**, as shown in **Figure 6.6**. In this structure, three out of four hydrides of the borohydride group, which rest on the same plane, are attracted strongly by two positively charged metal ions. On the contrary, in the structure **2a**, only two hydrides of the borohydride group are in close proximity to, and thus, attracted by the lithium atom. Therefore, when the transition state **TS1a** or **TS2a** formation occurs, two types of energy will be required: (i) the energy to break the bond between boron and the first hydride; (ii) the energy needed to move the remaining borohydride group away, resulting in the breakage of the static interactions between the other two hydrides with two metal ions in case of **TS1a** and only one hydride with one metal ion in the case of **TS2a**. Consequently, the formation of the

transition state **TS1a** will require considerably higher energy than the formation of the transition state **TS2a**.

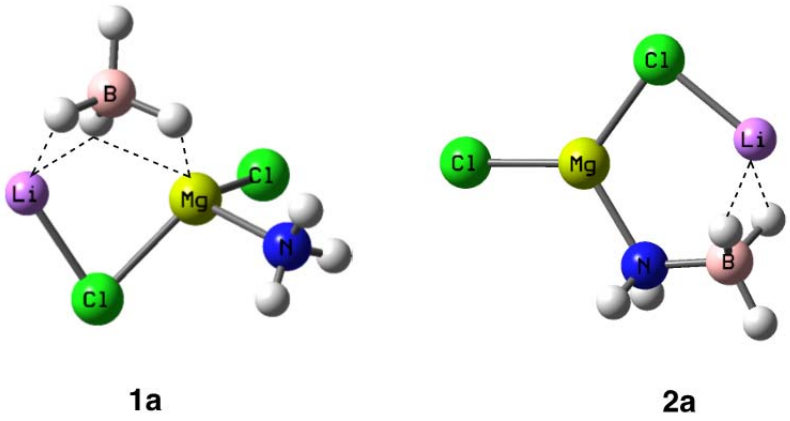

Figure 6.6 1a, which has more hydride-metal interactions; it thus requires more energy to form the transition state than **2a** does.

Another surprise comes from the second step, which has an unexpectedly higher activation barrier of 82.4 kJ mol^{-1}, as compared to 58.1 kJ mol^{-1} at the same hydrogen release step of Stage **1**. This may be attributed to the large constraint in the structure when forming the transition state **TS2b**. As presented in **Figure 6.7**, in the intermediate **2b**, Mg remains as an sp^3 hybridisation, which has an ideal angle of 109.1^o in H-Mg-N. However, the subsequent formation of the transition state **TS2b** requires this angle to become restrained at a much smaller angle, i.e. 63.2^o. This leads to a considerably higher activation barrier for the second step.

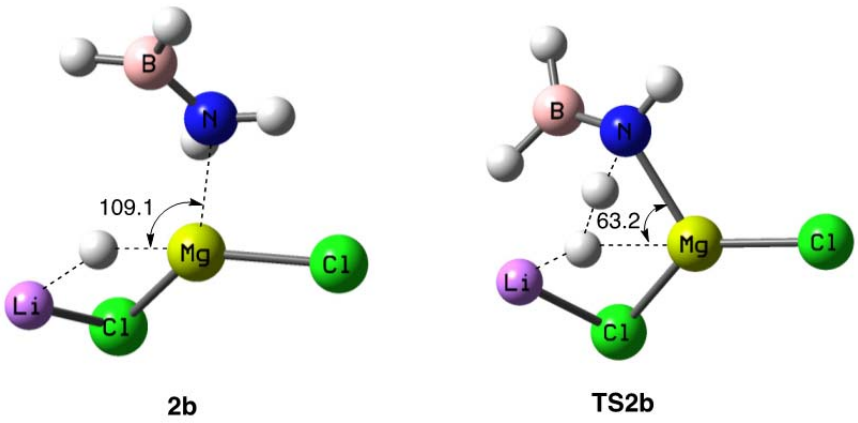

Figure 6.7 Angles of H-Mg-N in intermediate **2b** and transition state **TS2b**. Bond angles in degree.

Our calculations thus far have shown a noteworthy point: the activation barrier of the hydride transfer step of stage **2** is lower than that of stage **1**. Since the hydride transfer step is the rate-determining step in both cases, this result suggests that two moles of H_2 could have been released simultaneously, since the energy needed for the first H_2 release is more than sufficient to compensate for the second H_2 release. This is in good accord with the experimental data. Gao *et al.* conducted the thermogravimetric analysis and mass spectrometry (TGA-MS) profile for the hydrogen and ammonia release of $LiBH_4.NH_3.MgCl_2$ [22]. Their experimental data indicated that the main H_2 desorption peak appeared at 240^{o}C with an infinitesimally small NH_3 peak at 227^{o}C. Based on the TGA and volumetric results, the quantitative decomposition capacities of H_2 and NH_3 released were calculated and it demonstrated that this main peak corresponded to two moles of H_2 released. Furthermore, the TGA chart showed a significantly rapid decrease in the mass of the system at around 240^{o}C. These experimental results clearly revealed that two moles of H_2 were released simultaneously at the same temperature.

It should be noted that, in addition to this two-step mechanism, a concerted mechanism for stage **2** is also possible, in which the breaking of the N-H and B-H

bonds and the formation of the H-H occurs simultaneously as shown in **Figure 6.8**, leading to the formation of a H_2 molecule. However, the activation barrier $\Delta G^{\ddagger}$ required is seen to be considerably high, which is 202.5 kJ mol^{-1}. The energetic difficulty lies in the breakage of the N-H and B-H bonds, which contain sp^2 hybridised N and B atoms. Due to the considerably higher activation barrier, the reaction is thus less likely to proceed via this pathway.

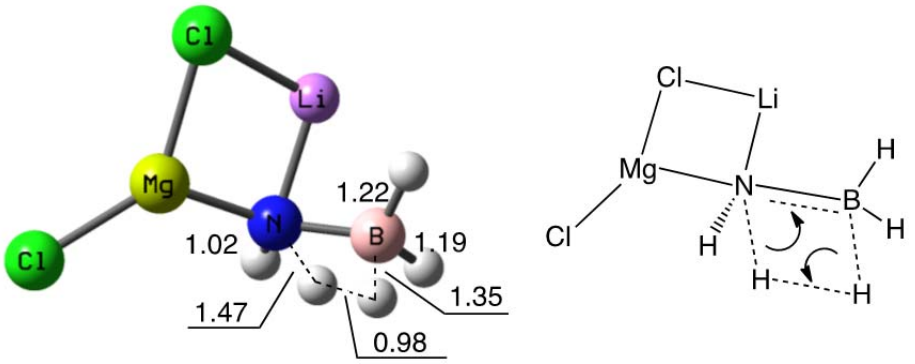

Figure 6.8 B3LYP/6-31+G(2d,p) optimised structure of the transition state in the concerted mechanism. Bond lengths are given in angstrom.

The third mole of H_2 release, i.e. Stage **3**, via steps **3a** and **3b**, corresponds to the reaction: $LiBH_2.NH.MgCl_2 \rightarrow LiNBH.MgCl_2 + H_2$. A schematic potential energy profile for the release of three moles of H_2 is given in **Figure 6.9** below. Similar to Stages **1** and **2**, the reaction begins by transferring a hydride from the borohydride group to the centre of the lithium and magnesium atoms via transition state **TS3a**; it is followed by the hydrogen release step via transition state **TS3b** as shown in **Figure 6.10**. The activation barriers $\Delta G^{\ddagger}$ for steps **3a** and **3b** are 172.2 and 116.0 kJ mol^{-1}, respectively. These high barrier values suggest that the release of the third H_2 molecule is much slower than the release of the second H_2. The result agrees well with the TGA-MS profile, which indeed showed a slower rate of H_2 release after two moles of H_2 were released at 240^{o}C.

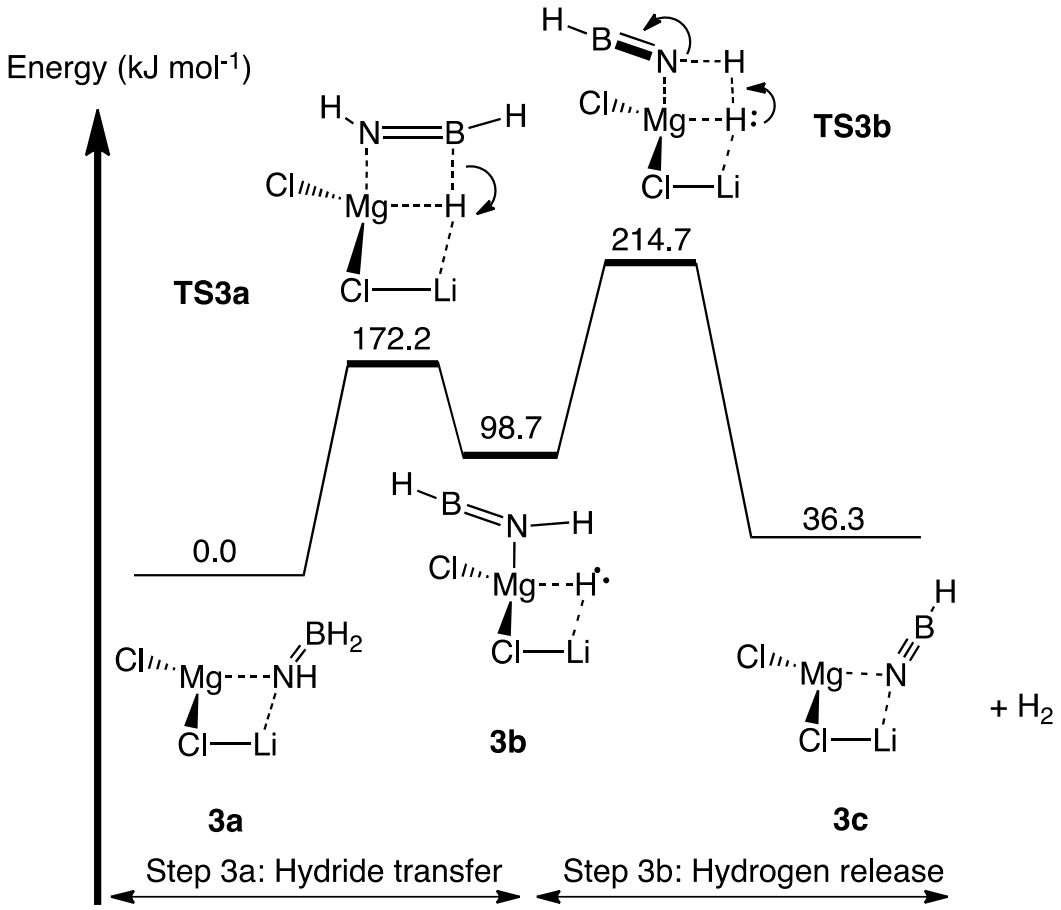

Figure 6.9 Schematic potential energy profile for Stage **3** of the H_2 release from $LiBH_4.NH_3.MgCl_2$. Relative Gibbs free energies at 298.15 K and 1 atm are given in kJ mol^{-1} from B3LYP/6-31+G(2d,p).

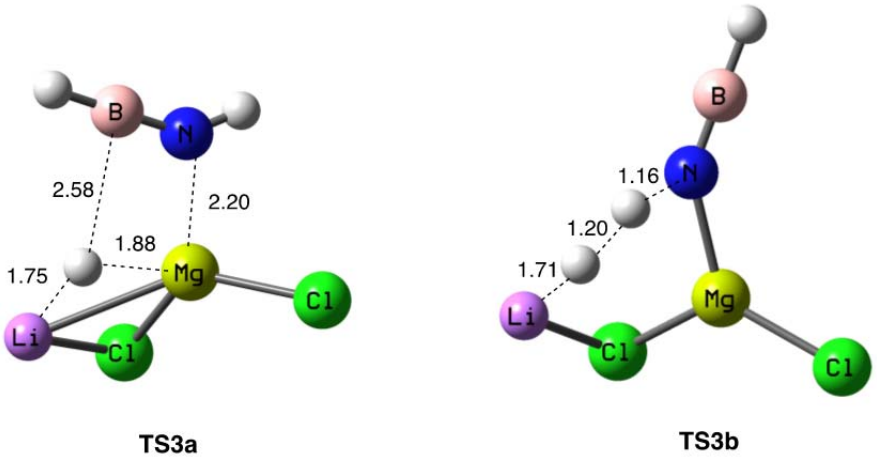

Figure 6.10 B3LYP/6-31+G(2d,p) geometrical parameters of two transition states, **TS2a** and **TS2b**. Bond lengths are given in angstrom.

Regarding the thermodynamic properties of the reactions, our calculations have shown that the first stage, whose $\Delta H^{0}_{298.15\,K}$ = 22.7 kJ mol^{-1}, is an endothermic reaction. The enthalpies of stages **2** and **3** are 61.2 and 74.9 kJ mol^{-1}, respectively, which suggest that more energy is required for H_2 release as the reaction proceeds, in particularly at stage **3**. In addition, this thermodynamic data implies that among these three stages, the hydrogen release at stage **3** is the most difficult. This result is in good agreement with the experimental data, which showed that the temperature needed to release the last mole of H_2 was approximately at 385^{o}C [22].

In summary, we have used the monomer structure to model three hydrogen release stages for $LiBH_4.NH_3.MgCl_2$ based on the two-step mechanism. In this mechanism, both the lithium and magnesium atoms play a critical role in attracting and removing hydrides from the borohydride group to facilitate the hydrogen release. Regarding the kinetic properties, our calculations have shown that the first two moles of H_2 could have been released simultaneously. Finally, the calculated enthalpies have indicated that more energy is needed when the reaction proceeds to stage **3**. Both of these kinetic and thermodynamic properties are in good agreement with the experimental data.

6.3.2 Mechanism for Hydrogen Release using the Dimer Model

It should be noted that in reality, the reaction actually occurs in the solid state at which molecules are in close proximity, thus possibly leading to the interaction between these molecules such as dimerisation of $LiBH_4.NH_3.MgCl_2$. Consequently, one molecule may play a critical role as a catalyst for the other as we observed in

Chapter 4 on the $LiNH_2BH_3$ system. Therefore, in this section, we have employed the dimer model to investigate another possible pathway for the dehydrogenation of $LiBH_4.NH_3.MgCl_2$.

We propose that $MgCl_2$ may play an important role as the linkage between two monomers. In $MgCl_2$, magnesium still has two empty valence orbitals $2p_y$ and $2p_z$, which can readily accept another lone pair of electrons from the chloride of the second $LiBH_4.NH_3.MgCl_2$.

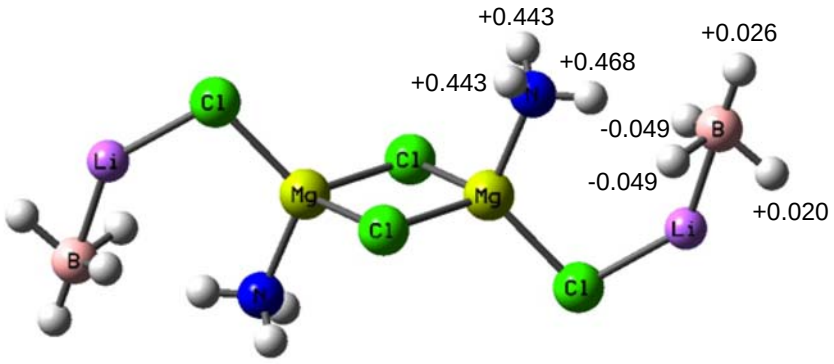

Figure 6.11 Optimised structure of the dimer $(LiBH_4.NH_3.MgCl_2)_2$ at B3LYP/6-31+G(2d,p). NBO charges are shown on the hydrides of the borohydride group and the protons of the ammonia group.

The Gibbs free energy of the dimer formation has a negative value of -39.6 kJ mol^{-1}; this suggests that the dimerisation process is energetically favourable and spontaneous. It is interesting to observe that in this optimised dimer structure as shown in **Figure 6.11**, two $MgCl_2$ molecules are predicted to form the four-membered ring. It is also worth noting that, this structure helps bring the NH_3 group and the BH_4^- group in a closer proximity, at 3.36 Å compared to 3.97 Å in the monomer model. Also, in contrast with the monomer structure, one proton of the NH_3 group in the dimer structure orients toward the hydrides of the borohydride group. Due to these

two reasons, this structure is predicted to be able to facilitate the first hydrogen release. To confirm this, the following section will examine the kinetic and thermodynamic properties of the first hydrogen release from this dimer.

Since this dimer has a symmetric structure, the dehydrogenation mechanism will be examined based on only half of the molecule as the rest is supposed to proceed through the same pathway. We propose that the first hydrogen release occurs in one step through the concerted interaction between a proton of the NH_3 group and a hydride of the BH_4^- group. The transition state and its subsequent product structure are displayed in **Figure 6.12**.

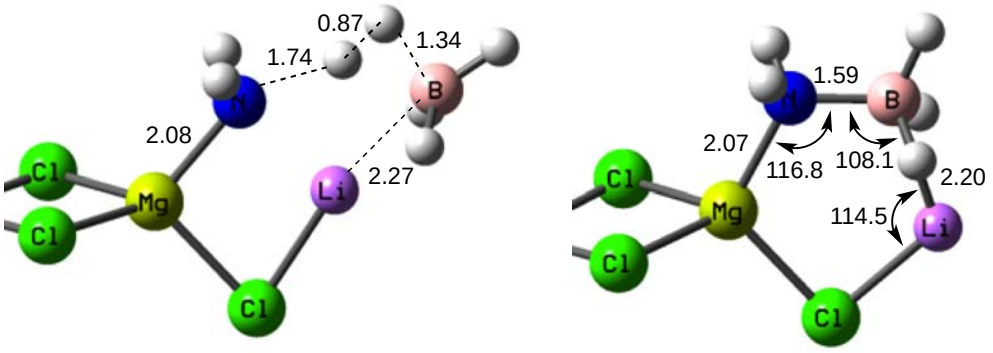

Figure 6.12 B3LYP/6-31+G(2d,p) geometrical parameters of transition state **dimer_ts1a** (left) and the product **1b** (right). Bond lengths are given in angstrom and bond angles in degree.

Figure 6.13 shows a schematic potential energy profile for the dimerisation process and the first hydrogen release from the dimer model. The calculated activation barrier for this dehydrogenation stage is only 108.1 kJ mol^{-1} as compared to 173.4 kJ mol^{-1} at the same stage of the monomer structure. This calculation confirms the earlier prediction that the dimer structure facilitates the hydrogen release.

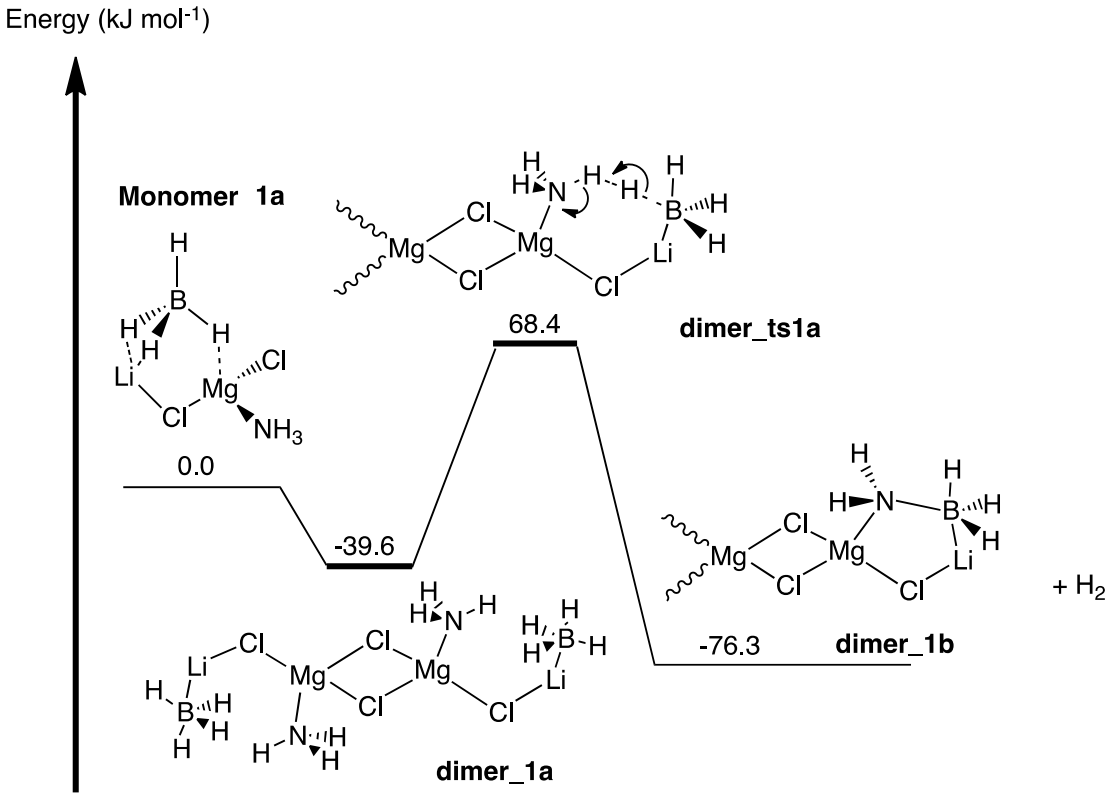

Figure 6.13 Schematic potential energy profile for Stage **1** of the H_2 release from the calculated dimer $(LiBH_4.NH_3.MgCl_2)_2$. Relative Gibbs free energies at 298.15 K and 1 atm are given in kJ mol^{-1} from B3LYP/6-31+G(2d,p).

It should be noted that, the structural differences between the monomer and the dimer might lead to changes in the partial charges of other atoms such as the hydrides of the BH_4^- group and the protons of the NH_3 group. These changes in the charges might be a critical factor that affects the activation barriers of the hydrogen release reaction thus it needs to be taken into serious consideration. NBO charge analysis has also been carried out to compute the atomic charge of each atom. Notably, the calculated charges shown in **Figure 6.14** reveal that there are no significant differences between the charges of the protons and hydrides in the dimer structure with the charges of the protons and hydrides in the monomer structure. With these results, we can conclude that, the facile hydrogen elimination in the dimer structure is only aided by the proper orientation and close proximity between the

ammonia and the borohydride groups, which are made possible by the particular structure of the dimer $MgCl_2$.

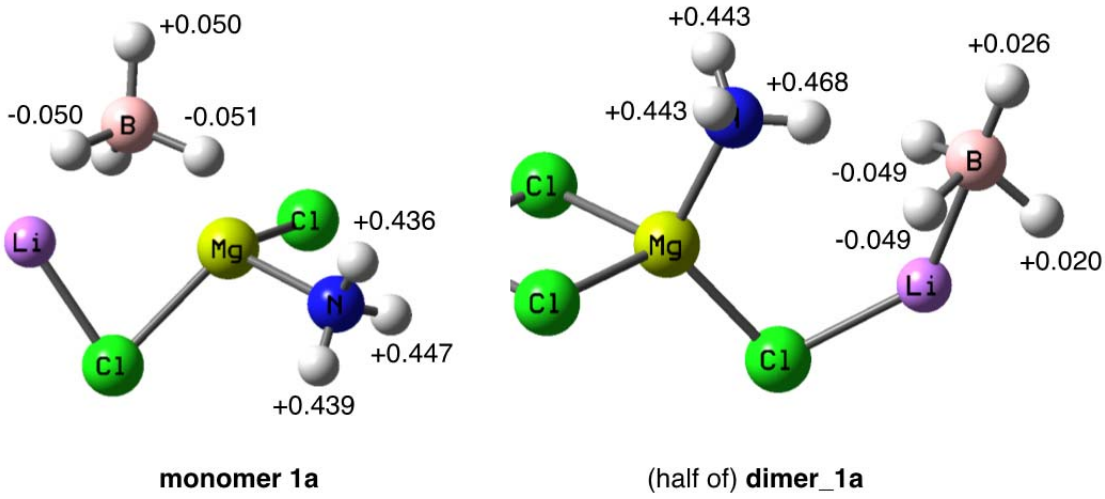

monomer 1a (half of) **dimer_1a**

Figure 6.14 NBO charges of protons and hydrides of **monomer 1a** and **dimer_1a**.

The release of the second H_2 occurring in Stage **2**, involves steps **2a** and **2b**. In step **2a**, one hydrogen atom is transferred from the boron to the centre of the lithium and magnesium atoms, via transition state **dimer_ts2a**, to form an intermediate **dimer_2b** as shown in **Figure 6.15**. This intermediate is characterised by the hydrogen atom bridged between two positively charged lithium and magnesium atoms (Li---H----Mg). In step **2b**, the NH_2-BH_2 group of the newly formed intermediate **dimer_2b** slightly changes its conformation so that the proton of the NH_2 group could approach the hydride via transition state **dimer_ts2b** as shown in **Figure 6.15**, resulting in the release of the second H_2.

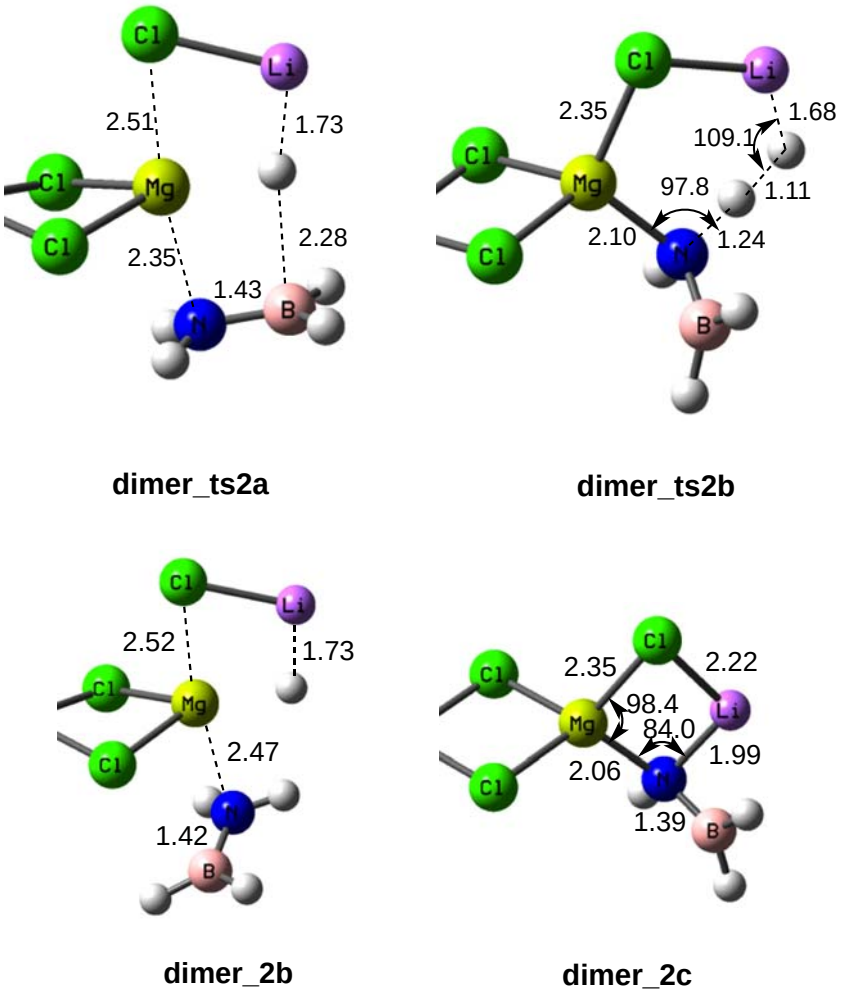

Figure 6.15 B3LYP/6-31+G(2d,p) geometrical parameters of two transition states **dimer_ts2a, dimer_ts2b**, intermediate **dimer_2b** and product **dimer_2c**. Bond lengths are given in angstrom and bond angles in degree.

The release of the third mole of H_2, i.e. Stage **3**, involves steps **3a** and **3b**. The chemistry that occurs in step **3a** and **3b** is similar to that in steps **2a** and **2b**. Again, one boron hydrogen is transferred to the centre of lithium and magnesium atoms via transition state **dimer_ts3a**, and then the second nitrogen hydrogen approaches this hydride and one H_2 molecule is eliminated via transition state **dimer_ts3b**.

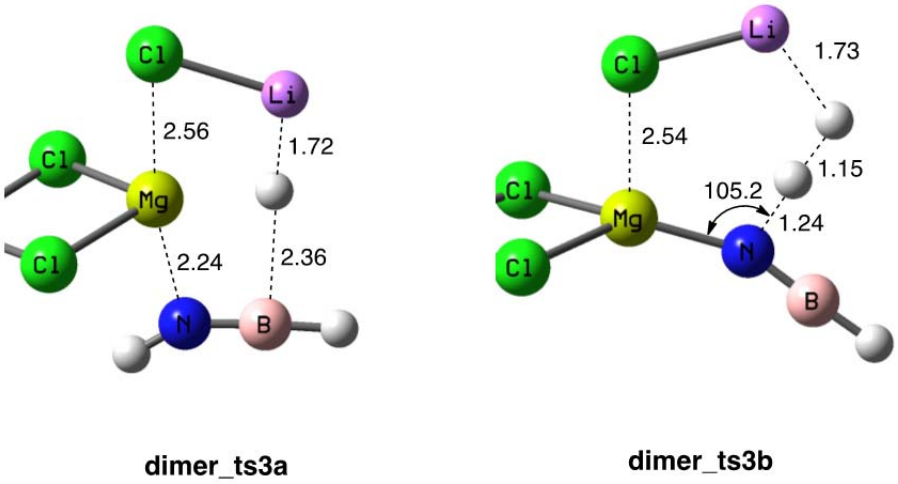

Figure 6.16 B3LYP/6-31+G(2d,p) geometrical parameters of two transition states **dimer_ts3a** and **dimer_ts3b**. Bond lengths are given in angstrom and bond angles in degree.

The activation barriers of two steps, the hydride transfer and the hydrogen release steps at stages **2** and **3** are summarised in **Table 6.1** below. It should be noted that the hydride transfer step is the rate-determining step in both stage **2** and stage **3**. This step has a significantly higher activation barrier than the hydrogen release step due to the same reasons explained in section **6.3.1**.

TABLE 6.1 Activation barriers for stage **2** and stage **3** of the dehydrogenation of the dimer $(LiBH_4.NH_3.MgCl_2)_2$.

Stage	*Hydride Transfer (kJ mol^{-1})*	*Hydrogen Release (kJ mol^{-1})*
2	111.8	-1.6
3	205.6	4.2

Interestingly, the rate-determining step of stage **2** has a slightly higher activation barrier of 111.8 kJ mol^{-1} as compared to 108.1 kJ mol^{-1} at stage **1**. Similar to the

conclusion at the section **6.3.1**, this result suggests the simultaneous release of two moles H_2 and thus agrees well with the experimental data.

With regards to the thermodynamic properties, the calculated reaction enthalpies of stages **1**, **2** and **3** are -9.5, 40.9 and 78.6 kJ mol^{-1}. Among the three stages, stage **1** is the only endothermic stage. It should be noted that this calculated enthalpy of stage **1** is in contrast with that of stage **1** of the monomer pathway, which is 22.7 kJ mol^{-1}. This is certainly due to the differences in the structure of the monomer and dimer.

In summary, our calculations have shown that the dimer $(LiBH_4.NH_3.MgCl_2)_2$ is thermodynamically more stable than two separate monomers. More importantly, the particular structure of the dimer $MgCl_2$, which aids in bringing the ammonia and borohydride groups in close proximity, has significantly lowered the activation barrier of the first hydrogen release. Thus, it can be deduced that, $LiBH_4.NH_3.MgCl_2$ and the dehydrogenation reactions are more likely to proceed through the dimerisation pathway.

6.4 Conclusions

We have comprehensively investigated the dehydrogenation mechanisms of $LiBH_4.NH_3.MgCl_2$. In addition, the thermodynamic and kinetic properties of these reactions have also been carefully examined.

Two possible pathways have been discovered: the monomer pathway which proceeded through the dehydrogenation reactions of monomer $LiBH_4.NH_3.MgCl_2$,

while the dimer pathway began with the dimerisation of the aforementioned monomer, followed by the dehydrogenation of the dimer $(LiBH_4.NH_3.MgCl_2)_2$. Both pathways occurred in three stages, corresponding to three moles of H_2 being released. In the monomer pathway, we have proposed the two-step mechanism for the three stages: Initially, a hydride was transferred to the centre of the lithium and magnesium atoms, which was then followed by the release of one H_2 molecule. In the dimer pathway, we have examined the concerted mechanism for Stage **1**, in which H_2 was released via the direct interaction between the proton of the ammonia group and the hydride of the borohydride group. For Stages **2** and **3**, we have proposed the two-step mechanism, which was analogous to the dehydrogenation mechanism of the monomer pathway. We have learnt that in two pathways, lithium and magnesium played critical roles as catalysts to facilitate the hydrogen release. In particular, in the dimer pathway, the dimer $(MgCl_2)_2$ played a critical role as a fixed frame to assemble the ammonia and the borohydride groups so that hydrogen release became more facile.

Regarding the kinetics of each pathway, our calculations have shown that:

1. In the monomer pathway, Stage **1** had a considerably higher governing activation barrier of 173.4 kJ mol^{-1} as compared to that of Stage **2**, which was 82.5 kJ mol^{-1}. This finding suggested that two moles of H_2 could have been released simultaneously since the energy required for the first H_2 release was more than sufficient for the second H_2 release. This result was in good accord with the experimental data.

Stage **3** had a considerably higher governing activation barrier than Stage **2**, which was 172.2 kJ mol^{-1}. This suggested that the third H_2 release was the slow stage. Needless to say, this result also agreed with the experimental data as well.

2. In the dimer pathway, the first stage had a slightly lower governing activation barrier of 108.1 kJ mol^{-1} as compared to 111.8 kJ mol^{-1} at the second stage. This result still suggested that two moles of H_2 could have been released simultaneously since the energies required were almost equivalent once again. In contrast to Stages **1** and **2**, Stage **3** was determined to have considerably higher governing activation barrier. Thus, the release of the third H_2 was the slowest stage.

3. Comparing the monomer and the dimer pathways, it was worth noting that the particular structure of the dimer helped significantly lower the governing activation barrier of the first stage in the dimer pathway. The two $MgCl_2$ molecules established a fixed frame for $LiBH_4$ and NH_3, so that the ammonia and the borohydride groups could come into close proximity, thus facilitating the hydrogen release.

Analysing the thermodynamic properties:

In both pathways, the hydrogen elimination enthalpies increased as the reactions proceeded towards Stage **3**, suggesting that the last mole of H_2 was difficult to eliminate.

Comparing the stability between the dimer and the monomer, our calculations showed that the dimer was 39.6 kJ mol^{-1} thermodynamically more stable than the monomer. Thus, the reaction was more likely to proceed via the dimer pathway.

In summary, our comprehensive study proposed two possible pathways for the dehydrogenation mechanisms of $LiBH_4.NH_3.MgCl_2$. Both the monomer and dimer model seems to be sufficient in explaining some of the most important experimental data, particularly with regards to the kinetic and thermodynamic properties. More importantly, the critical role of the lithium and magnesium atoms, and also the dimer $MgCl_2$ in facilitating the H_2 elimination has been shown.

References

[1] L. L. Shaw, X. F. Wan, J. Z. Hu, J. H. Kwak, and Z. G. Yang, *Journal of Physical Chemistry C*, vol. 114, p. 8089, 2010.
[2] R. Hoffmann, *J. Chem. Phys.*, vol. 40, p. 2474, 1964.
[3] W. T. Klooster, T. F. Koetzle, P. E. M. Siegbahn, T. B. Richardson, and R. H. Crabtree, *J. Am. Chem. Soc*, vol. 121, p. 6337, 1999.
[4] C. A. Morrison and M. M. Siddick, *Angew. Chem., Int. Ed.,* vol. 43, p. 4780, 2004.
[5] E. A. Sullivan and S. Johnson, *J. Phys. Chem.*, vol. 63, p. 233, 1959.
[6] Z. Xiong et al., *Nat. Mater.*, vol. 130, p. 14834, 2008.
[7] X. Kang et al., *Adv. Mater.*, vol. 20, p. 2756, 2008.
[8] T. J. Groshens and R. A. Hollins, *Chem. Commun.*, p. 3089, 2009.
[9] T. Hugle, M. F. Kuhnel, and D. Lentz, *J. Am. Chem. Soc.*, vol. 131, p. 7444, 2009.
[10] G. Soloveichik et al., *Inorg. Chem.*, vol. 47, p. 4290, 2008.
[11] X. Kang et al., *Phys. Chem. Chem. Phys.*, vol. 11, p. 2507, 2009.
[12] P. Wang and X. D. Kang, *Dalton Trans*, p. 5400, 2008.
[13] H. V. K. Diyabalanage et al., *Angew. Chem. Int. Ed.*, vol. 46, p. 8995, 2007.
[14] A. Feaver et al., *J. Phys. Chem. B.*, vol. 111, p. 7469, 2007.
[15] T. He et al., *Chem. Mater.*, vol. 21, p. 2315, 2009.
[16] V. Pons and R. T. Baker, *Angew. Chem. Int. Ed.*, vol. 47, p. 9600, 2008.
[17] J. Spielmann and S. Harder, *J. Am. Chem. Soc.*, vol. 131, p. 5064, 2009.
[18] C. W. Yoon and L. G. Sneddon, *J. Am. Chem. Soc.*, vol. 128, p. 13992, 2006.
[19] Y. Nakamori et al., *J. Power Sources*, vol. 155, p. 447, 2006.

[20] S. R. Johnson et al., *Chem. Asian J.*, vol. 4, pp. 849-854, 2009.

[21] Y. Guo, G. Xia, Y. Zhu, L. Gao, and X. Yu, "Hydrogen release from amminelithium borohydride, LiBH4.NH3," *Chem. Commun.*, vol. 46, pp. 2599-2601, 2010.

[22] L. Gao, Y. H. Guo, Q. Li, and X. B. Yu, "The Comparison in Dehydrogenation Properties and Mechanism between MgCl2(NH3)/LiBH4 and MgCl2(NH3)/NaBH4 Systems," *Journal of Physical Chemistry C*, vol. 114, pp. 9534-9540, 2010.

CHAPTER 7

POLY(METHYL ACRYLATE)-CONFINED AMMONIA-BORANE: A COMPUTATIONAL STUDY

7.1 Introduction

As presented in Literature Review (see Chapter 2), among various types of materials composing of hydrogen bound to light elements, N-B-based materials such as ammonia-borane (NH_3BH_3, denoted as AB) has still attracted great interests as a promising hydrogen storage material. It has low molecular weight (30.7 g mol^{-1}) and high gravimetric hydrogen capacity (19.6 wt%) [1-3]. However, the properties of the neat AB, such as slow kinetics below 100^oC, volatile byproducts, e.g. borazine $(HNBH)_3$, have prevented AB from being practical application. Great efforts have been devoted to exploring numerous approaches in order to overcome those barriers such as the use of nanoscaffolds [4-6], transition metals [7-10], ionic liquids [11], and additives [12-14]. In the preceding three chapters, we have investigated one interesting approach in which alkali and alkaline earth metals such as lithium, magnesium, are employed to replace one N-H hydrogen atom in AB, resulting in metal amidoboranes e.g. $LiNH_2BH_3$, $Mg(NH_2BH_3)_2.NH_3$ and $LiBH_4.MgCl_2.NH_3$. Our calculations based on these promising metal amidoboranes have confirmed that the replacement of one hydrogen atom by a metal could significantly improve the dehydrogenation properties. Additionally, these compounds also succeeded in suppressing the generation of detrimental boracic impurities. Despite these great

advantages, more improvements are still needed to approach closer to the practicable hydrogen storage material. Among necessary improvements, the water-resistant is one of the important properties. Metal amidoboranes are known to have hygroscopic properties and water solubility [15-17], which may cause them to absorb moisture in air or water generated during the H_2 burning process. Thus, they will negatively affect their thermolysis performance. Nevertheless, these effects have hardly been taken into consideration.

Recently, a new AB-based hydrogen storage system with water-resistant has just been successfully synthesised by using poly(methyl acrylate) (PMA) to confine AB [15]. J. Chen *et al.* reported two PMA-AB composites, denoted as PAB20 and PAB80, corresponding to 20 mg and 80 mg of AB introduced into 100 mg PMA. Notably, while commercial AB is a white powder at ambient conditions, the prepared PAB20 was a semitransparent rubbery material and was able to be fabricated in a form of a transparent film. The obtained PAB80 was opaque and soft. Their further investigations showed that PAB20 had an amorphous structure, which showed the comprehensive dispersion of AB into the polymeric composite. On the contrary, in PAB80, partial AB exists in the form of a crystalline phase in the polymeric composite. It was likely that the amount of AB exceeded the dispersive saturation, resulting in a partial recrystallisation of AB [15].

These materials were reported to have some outstanding properties over the neat AB. Firstly, these materials efficiently lowers the hydrogen release temperature. While the neat AB starts to release hydrogen at above 90^oC with decomposition peak centred at 106.0^oC and 153.5^oC, both the PAB20 and the PAB80 presented a

significantly lower onset temperature of 70^{o}C and 81.1^{o}C, respectively. Furthermore, approximately two equivalents of H_2 were generated during the isothermal decomposition of PAB20 and PAB80 at 90^{o}C. Secondly, these compounds succeeded in suppressing the generation of detrimental boracic impurities. It was reported that no MS signals of borazine or diborane were observed during the thermolysis process for PAB20 and PAB80. Finally, these materials possessed water-resistant property, which may make these materials more practicable. J. Chen *et al.* observed that a considerable amount of H_2 was able to produce from heating the polymeric composites that drowned in water even for 30 minutes while an equivalent amount of neat AB had already been dissolved under the same condition [15].

However, the mechanisms of AB decomposition in these composites have remained unknown. Thus, the main aim of this study is to propose some possible mechanisms on hydrogen release processes occurring in these composites. In particular, the critical role of the carbonyl functional group of the composites in facilitating H_2 elimination will be elucidated. Additionally, we will provide an explanation on how these composites may suppress the detrimental boracic impurities. The results of this present study may have significant impacts on both understanding the dehydrogenation mechanisms of the composite and designing better composite materials.

7.2 Computational Methods

Density Functional Theory (DFT) calculations based on hybrid B3LYP functional together with the 6-31+G(2d,p) basis set were carried out for optimisations

of all equilibrium structures and transition states in the gas phase. Intrinsic reaction coordinates (IRC) were used to confirm the identity of the linking reactant and product from a transition state. All DFT calculations, which produced Gibbs free energy, and enthalpy of reaction at 298.15 K, 1 atm, were performed with the Gaussian 09 suite of programs.

7.3 Results and Discussions

To model the dehydrogenation reactions of the two composites PAB20 and PAB80, the main polymer chain is replaced with a methyl group. Thus, our calculations will be based on the molecule CH_3COOCH_3. This replacement helps considerably reduce a great amount of optimisation calculations on the unnecessary moiety, i.e. the main polymer chain. Nevertheless, this replacement is unlikely to change the nature of the dehydrogenation reactions of PAB composites since they may mainly occur at the carbonyl functional group of the polymer. Besides, in accordance to the reported amount of AB introduced into PAB20 and PAB80, we have calculated that the molar ratios of methyl acrylate to AB in PAB20 and PAB80 are 1:1 and 1:2, respectively. Thus, to examine the dehydrogenation of PAB20, Model **1**, which comprises one molecule CH_3COOCH_3 and one molecule AB, will be utilised while in the case of PAB80, Model **2**, which includes one molecule CH_3COOCH_3 and two molecules AB, will be employed.

J. Chen *et al*. have reported that both the PMA-AB composites, PAB20 and PAB80, could release up to 2 equivalent moles of H_2 when the systems were heated from 70^{o}C to 200^{o}C [9]. Based on these experimental evidences, we have envisaged

the dehydrogenation reactions to occur in two stages, corresponding to two equivalent moles of H_2 being released. Stage **1** in conjunction with Stage **2a** and **2b**, as shown in **Scheme 7.1**, present the dehydrogenation of Models **1** and **2**, respectively. In all these stages, the NH_3 group plays an important role as a proton provider while the BH_3 group contributes its hydrides, leading to the generation of H_2 molecules.

At Stage **1**, the first reaction between CH_3COOCH_3 and AB proceeds through two possible mechanisms (see Section **7.3.1**), leading to the formation of the two possible intermediates **1a4** and **1b4**, accompanied by the first H_2 release. Both **1a4** and **1b4** then may proceed through an intramolecular cyclisation in Stage **2a** (see Section **7.3.2**), forming the four-membered ring intermediate **2a2**. Finally, this four-membered ring undergoes the elimination of the second H_2 via two feasible mechanisms. The first mechanism involves the direct interaction between one proton of the N-H group and one hydride of the B-H group, which is followed by one molecule H_2 being released. More interestingly, the second mechanism proceeds through two steps in which the CH_3O group plays a critical role in transferring one proton of the N-H group to one hydride of the B-H group to facilitate the hydrogen release.

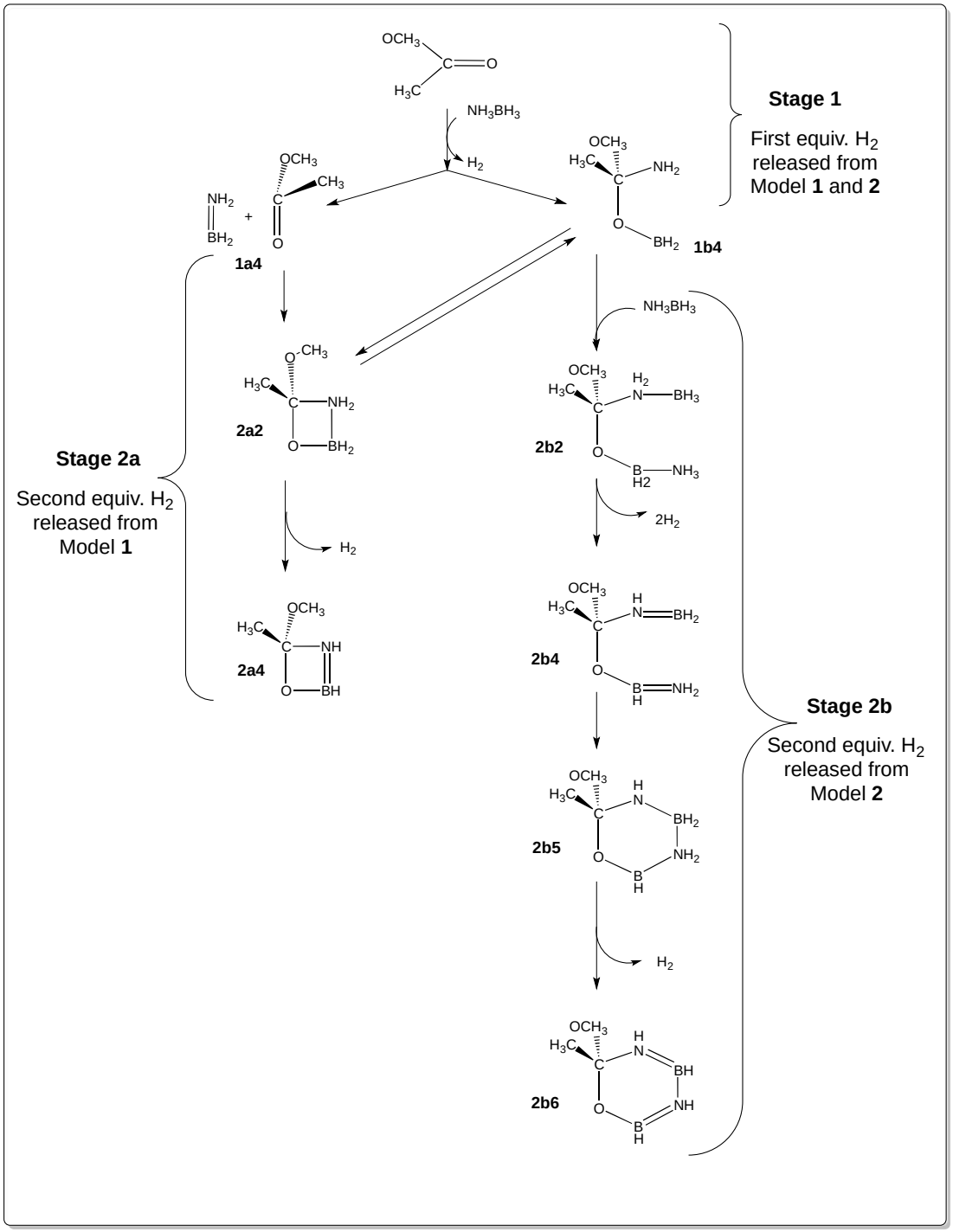

Scheme 7.1 Overall schemes for the dehydrogenation of the CH_3COOCH_3-AB and CH_3COOCH_3-2AB systems in the Models **1** and **2**.

In the case of Model **2**, the presence of the second AB molecule opens Stage **2b** (see Section **7.3.3**) for another three moles of H_2 being released. Initially, the second AB is added onto the intermediate **1b4**, which has been formed at the end of

Stage **1**, to generate the intermediate **2b2**. This intermediate, which is characterised by two AB-based groups, NH_2-BH_3 and BH_2-NH_3, readily eliminates two moles of H_2, resulting in the formation of the intermediate **2b4**. This intermediate, which includes two reactive N=B double bonds (discussed in Chapter **6**), readily undergoes an intramolecular cyclisation to produce the six-membered ring intermediate **2b5**. Finally, the intermediate **2b5** further releases one mole of H_2.

The dehydrogenation of Models **1** and **2** can be summarised in the following reaction equations:

Model **1**: $CH_3COOCH_3 + NH_3BH_3 \rightarrow CH_3CO(NH{=}BH)OCH_3 + 2H_2$

Model **2**: $CH_3COOCH_3 + 2NH_3BH_3 \rightarrow CH_3CO(NH{=}BH)_2OCH_3 + 4H_2$

The following sections will explore the details of dehydrogenation mechanisms involved in Stages **1**, **2a** and **2b** summarised above.

7.3.1 Stage 1 of Hydrogen Release

At Stage **1**, we have investigated two possible mechanisms. In the first mechanism, the interaction between the carbonyl group of CH_3COOCH_3 with the N head of the AB molecule leads to the formation of a tetrahedral intermediate. Subsequently, this intermediate slightly alters its conformation to facilitate the hydrogen release, which occurs at the final step of this mechanism. Alternatively, in the second mechanism, the initial step is the interaction between the carbonyl group of CH_3COOCH_3 with the B head of the AB molecule. This reaction also leads to the

formation of a tetrahedral intermediate. Finally, one hydrogen molecule is eliminated from this intermediate. The two possible mechanisms **1** and **2** are summarised in the **Scheme 7.1** below.

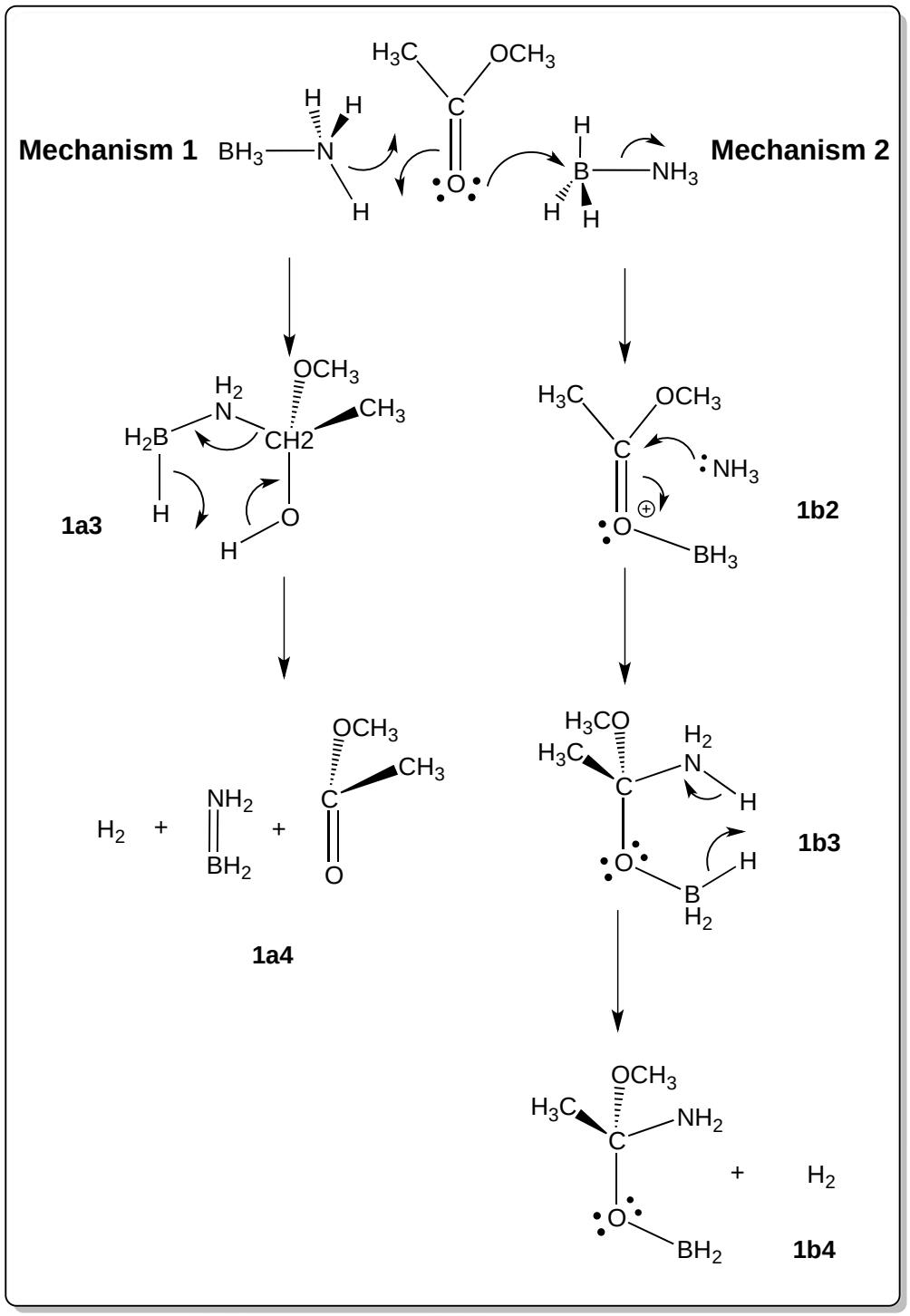

Scheme 7.2 Overall scheme for two feasible mechanisms of the dehydrogention of the CH_3COOCH_3-AB system at Stage **1**.

As shown in **Scheme 7.2**, step **1** of the mechanism **1** involves the concomitant formation of two bonds O-H and C-N via transition state **TS1a1**, as shown in **Figure 7.2**. Electrons from π bonds of the carbonyl group donate to the σ bond of the N-H of AB, forming the O-H σ bond. In the meantime, the interaction between the nitrogen atom of the AB molecule and the carbon atom of the carbonyl group of the CH_3COOCH_3 gives rise to the formation of a C-N σ bond. This first step, which requires a high activation barrier of 246.1 kJ mol^{-1}, results in the formation of the intermediate **1a2a**, as indicated in **Figure 7.1**. The initially formed intermediate **1a2a** then proceeds through several minor conformation changes in which the NH_2-BH_3 group rotates at the C-N σ bond and the H atom rotates at the O-H σ bond, leading to the formation of the two intermediates **1a2b** (step **2a**) and **1a3** (step **2b**) (**Figure 7.1**), respectively. These minor changes result in the close proximity of the proton of the OH group and the hydride of the NH_2 group. Consequently, step **3**, in which one hydrogen molecule is released via transition state **TS1a3** (**Figure 7.2**), has a considerably low activation barrier of 52 kJ mol^{-1}.

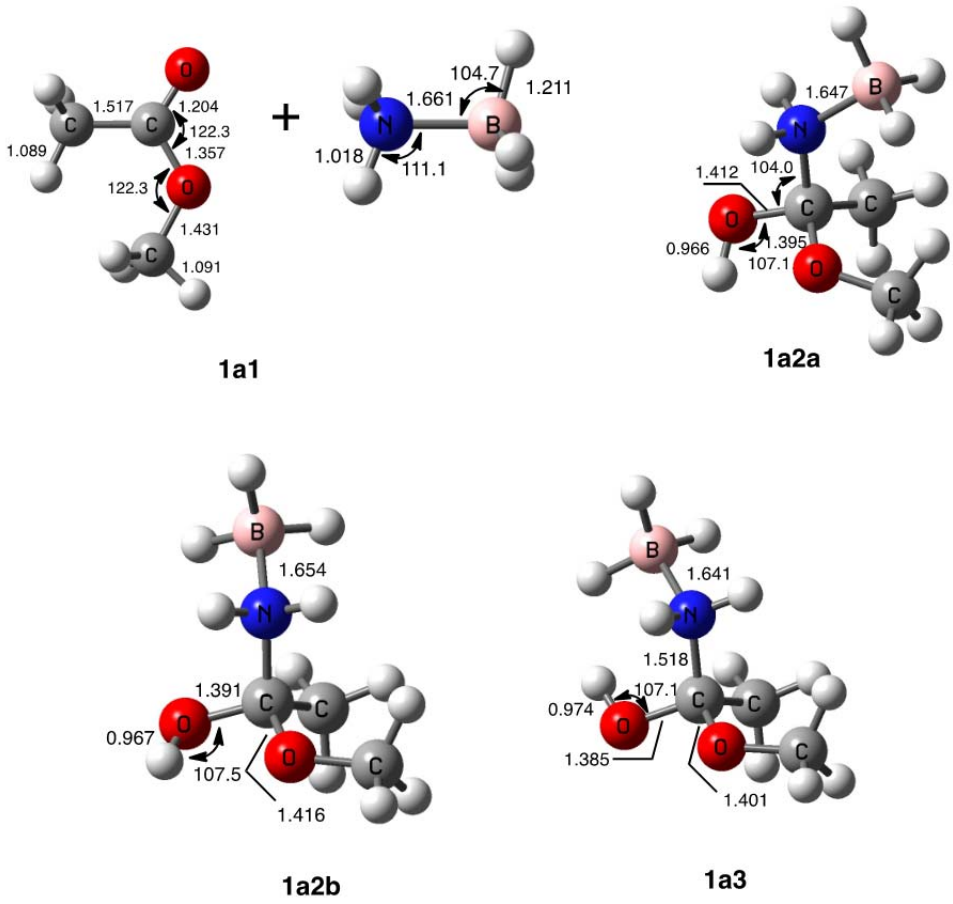

Figure 7.1 B3LYP/6-31+G(2d,p) geometrical parameters of all equilibrium structures in mechanism 1. Bond lengths are given in angstrom and bond angles in degree.

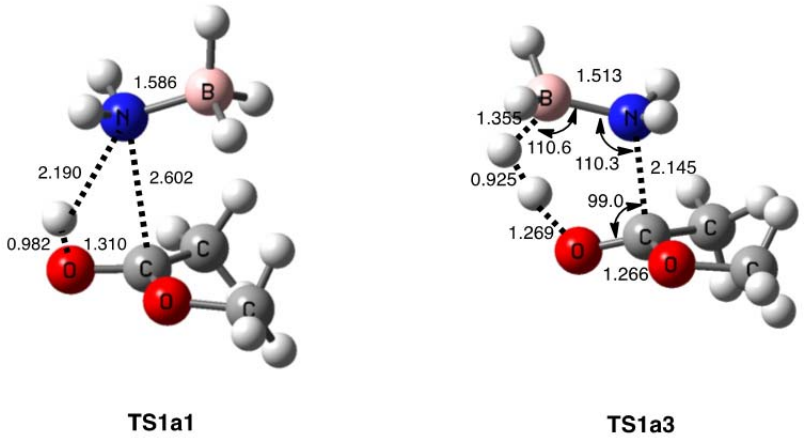

Figure 7.2 B3LYP/6-31+G(2d,p) geometrical parameters of transition states **TS1a1** and **TS1a3** in mechanism 1. Bond lengths are given in angstrom and bond angles in degree.

A schematic potential energy profile for the first mole of H_2 being released via mechanism 1 is shown in **Figure 7.3** below. It is clearly observed that the first step is the rate-determining step. It has a significantly higher activation barrier than all other steps. Regarding the thermodynamic properties, **Figure 7.3** shows that the Gibbs free energy of the first release of H_2 via mechanism 1 is -85.6 kJ mol^{-1}, and thus is thermodynamically favourable. It may be attributed to the release of H_2, which increases the overall entropy of the system.

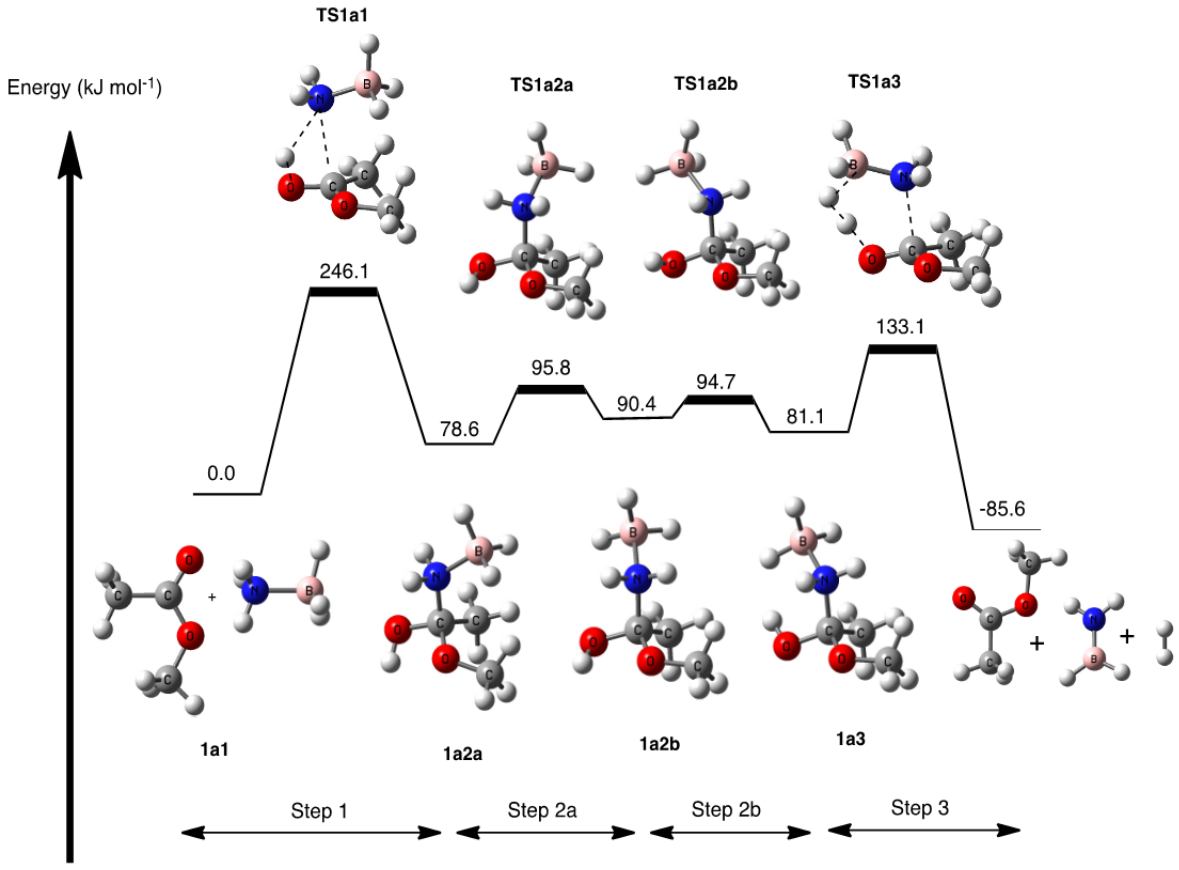

Figure 7.3 Schematic potential energy profiles showing the first H_2 release from the CH_3COOCH_3-AB system via mechanism 1. Relative Gibbs free energies are given in kJ mol^{-1} from B3LYP/6-31+G(2d,p).

In addition to the mechanism 1, the first mole of hydrogen can be released via mechanism 2. Mechanism 2 comprises three steps. The geometrical

parameters of all equilibrium structures and transition states involved in these three steps computed at B3LYP/6-31+G(2d,p) are listed in **Figure 7.4** and **7.5**, respectively. The first step is the nucleophilic attack of the lone pair of electrons on the oxygen of the carbonyl group of the CH_3COOCH_3 molecule to the BH_3 group of the AB molecule to produce the intermediate **1b2** via transition state **TS1b1**. An ammonia molecule is released during this first step and then participates in the second step, which is the addition reaction to form a new C-N σ* bond at the expense of the C=O π bond, resulting in the formation of the tetrahedral intermediate **1b3** via transition state **TS1b2**. It should be noted that the intermediate **1b3** is a zwitterion since it contains both the positively and negatively charged groups, which are NH_3^+ and BH_3^- groups, respectively. Finally, the third step is the hydrogen release from this zwitterion. In this step, the BH_3^- group provides one hydride and the NH_3^+ group contributes one proton, forming one H_2 molecule via transition state **TS1b3**.

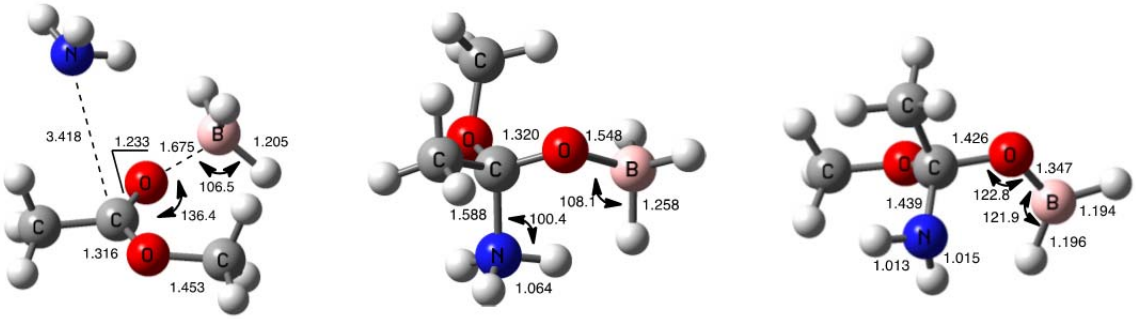

1b2 **1b3** **1b4**

Figure 7.4 B3LYP/6-31+G(2d,p) geometrical parameters of all equilibrium structures in the mechanism 2. Bond lengths are given in angstrom and bond angles in degree.

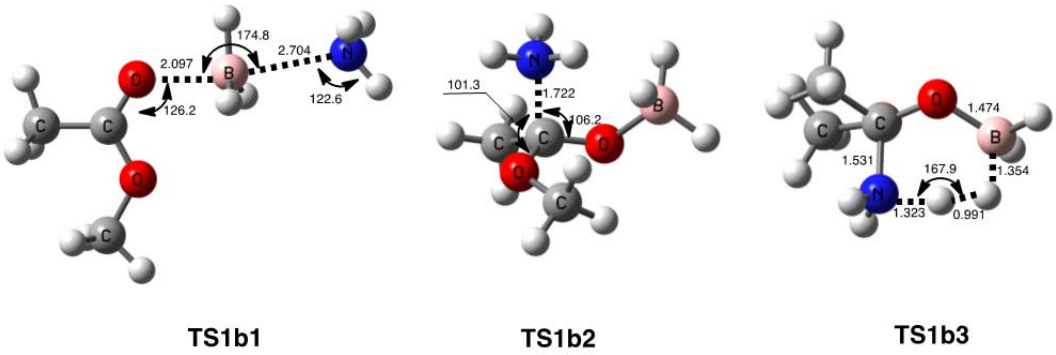

Figure 7.5 B3LYP/6-31+G(2d,p) geometrical parameters of three transition states in mechanism 2. Bond lengths and bond angles are given in angstrom and degree, respectively.

A schematic potential energy profile for the release of the first mole of H_2 via mechanism 2 is demonstrated in **Figure 7.6** below. The activation barriers, $\Delta G^{\ddagger}$ of steps **1**, **2** and **3** are 92.8, 76.2 and 30.0 kJ mol^{-1}, respectively. Since step **1** has the highest $\Delta G^{\ddagger}$, it is thus the rate-determining step. Notably, the activation barrier of step **3** is considerably low as compared to steps **1** and **2**, suggesting that the hydrogen release from the intermediate **1b3** is particularly facile. The explanation for this energetic favour may be attributed to two reasons: (i) intermediate **1b3** is a zwitterion, which contains both the positive and negative charges within its molecule, thus it tends to release one proton at the NH_3 positive group and one hydride at the BH_3 negative group to remove localised charges; (ii) the structure of **1b3** particularly favours the interaction between the proton of NH_3 group and the hydride of BH_3 group. In this structure, the proton is oriented toward the hydride and both the proton and the hydride are in close proximity. Consequently, the NH_3^+ group, carrying positive charge, readily releases one proton, while the BH_3^- group, carrying negative charge, readily contributes a hydride. As a result, the activation barrier required for this H_2 elimination is low.

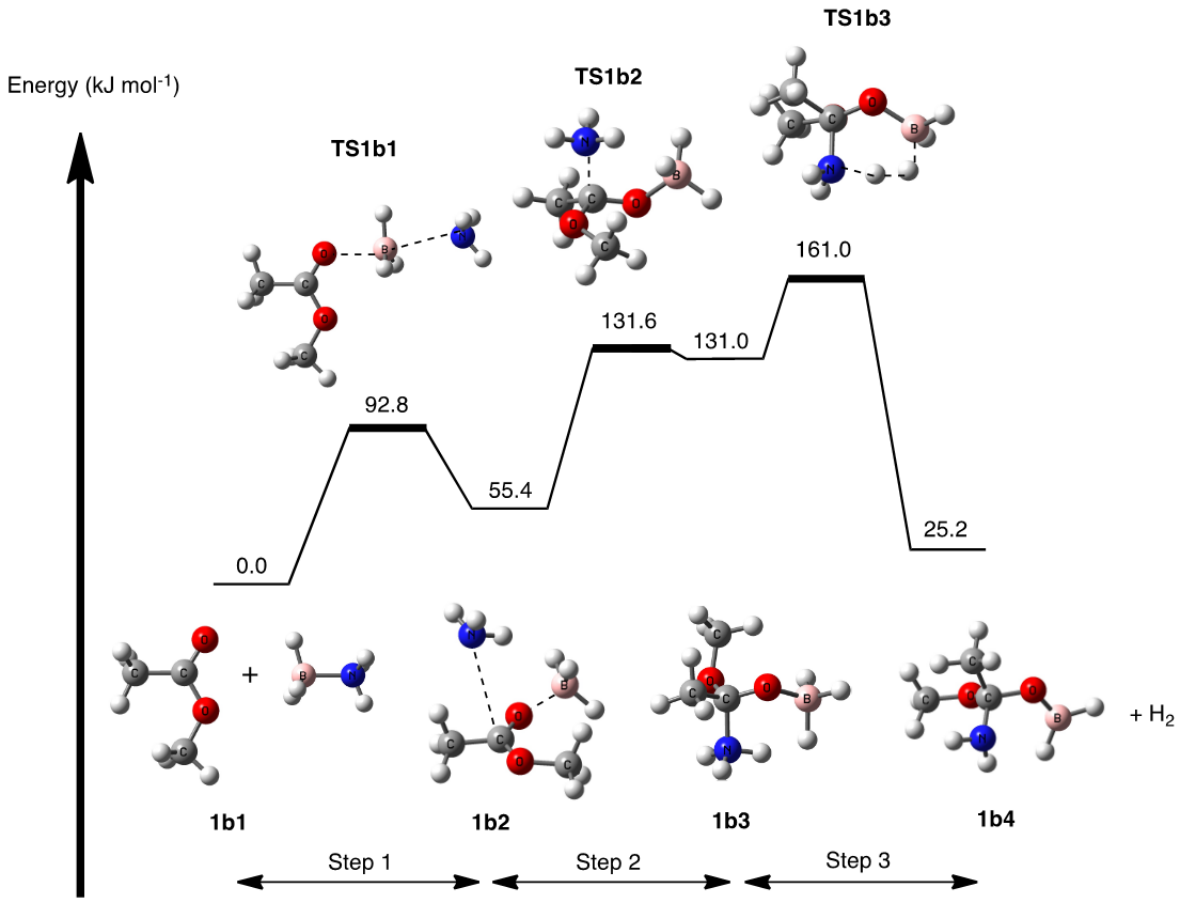

Figure 7.6 Schematic potential energy profile showing the H_2 release via mechanism 2. Relative Gibbs free energies are given in kJ mol^{-1} from B3LYP/6-31+G(2d,p).

The schematic potential energy profiles of the two mechanisms, given in **Figure 7.3** and **7.6**, reveal that the mechanism 2 is kinetically more favourable than the mechanism 1, and thus the first H_2 release is more likely to proceed through the mechanism 2. The rate-determining step of the mechanism 1 costs as much as 171.7 kJ mol^{-1}; whereas the rate-determining step of the mechanism 2 only requires 92.8 kJ mol^{-1}. This significant difference could be explained by two reasons. Firstly, in the mechanism 1, the rate-determining step involves the interaction between the oxygen atom of the carbonyl group of CH_3COOCH_3 and the hydrogen atom of the NH_3 group of AB. This interaction leads to the formation of two entities – carbocation and anion - carrying two opposite charges. Consequently, it requires much more energy than the rate-determining step of the mechanism 2 in which there is no opposite charge entities

formed. Secondly, in the rate-determining step of the mechanism 1, the leaving group is $H_3B\text{-}NH_2$ whereas, in mechanism 2, the leaving group is the NH_3 molecule. It is certainly a better leaving group than the $H_3B\text{-}NH_2$ anion due to the fact that, NH_3 carries no charge while $H_3B\text{-}NH_2$ carries the negative charge and this charge is poorly delocalised, resulting in the unstable anion.

To compare the kinetic properties of the first H_2 release between an AB molecule and our model, we have calculated the activation energies needed to eliminate one hydrogen molecule from an AB molecule at the same level of theory and basis set. Our calculations have revealed that a neat AB requires a significantly higher activation barrier of 141.1 kJ mol^{-1}, as compared to 92.8 kJ mol^{-1} required with our model. These results suggest that the H_2 release process in the PAB20 and PAB80 occurs more readily and rapidly than in the neat AB. Interestingly, these findings are in excellent agreement with the experimental data, which showed that the PAB20 and PAB80 started to release H_2 at lower temperature than the neat AB.

7.3.2 Stage 2a of Hydrogen Release

Stage **2a** begins by the formation of a key molecule, the four-membered ring intermediate **2a2**, shown in **Scheme 7.3**. This molecule is of our central interest since it leads to the release of the second H_2 release. **Scheme 7.3** below summarises all possible reactions occurred in **Stage 2a**.

Two intermediates **1a4** and **1b4**, formed at the end of Stage **1**, can generate the key intermediate **2a2** via the two transition states **TS2a1** and **TS2a1'** (**Figure 7.7**),

respectively. The pathway via **TS2a1** requires an activation barrier of 144.5 kJ mol^{-1} while the pathway via **TS2a1'** only need 44.7 kJ mol^{-1}.

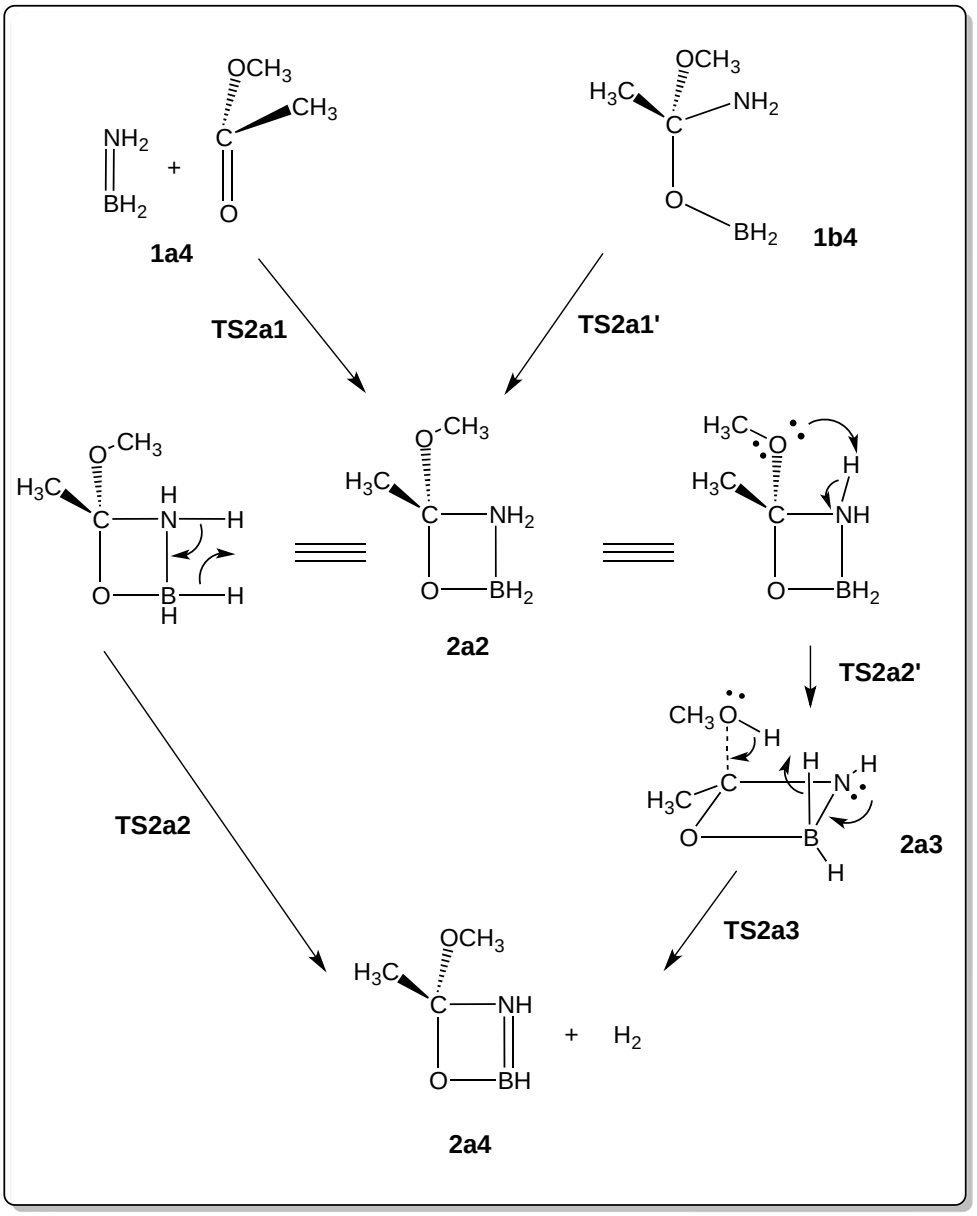

Scheme 7.3 Overall scheme for the two feasible mechanisms in Stage **1**.

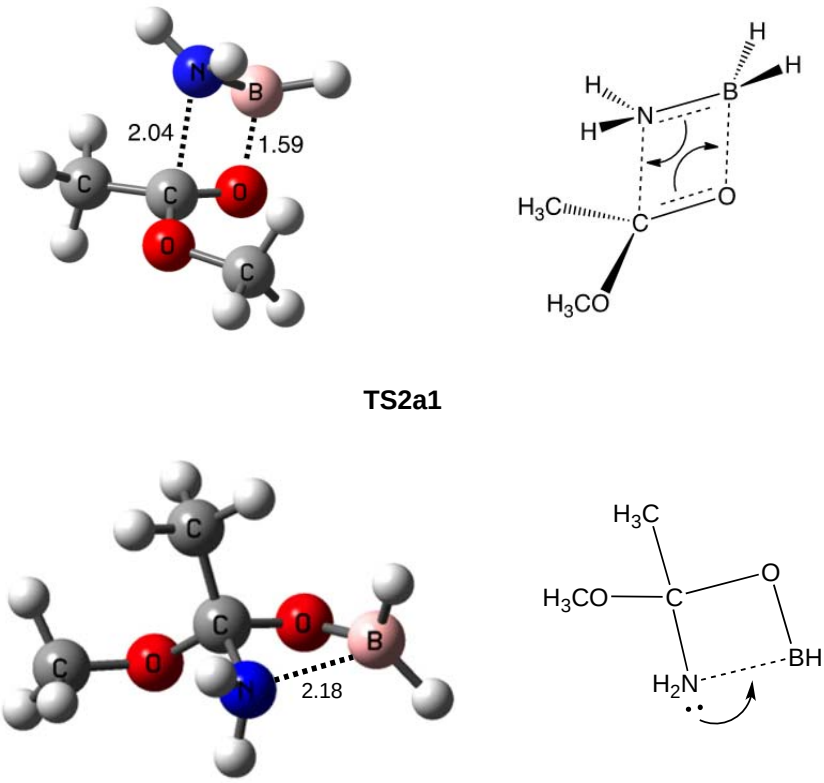

Figure 7.7 B3LYP/6-31+G(2d,p) optimised structure of the two transition states **TS2a1** and **TS2a1'** involved in the four-membered ring closure reactions. Bond lengths are given in angstrom.

To gain a better understanding on why a considerably higher activation barrier is required to proceed through **TS2a1** than in the case of **TS2a1'**, we have analysed HOMO and LUMO involved (**Figure 7.8**) in the ring closure reactions of **1a4** and **1b4**. It should be noted that, the HOMO and LUMO are delocalised over all atoms in the molecule; however, only the lobes at the nitrogen and boron atoms are of our interest since they will take part in the aforementioned intramolecular cyclisation. **Figure 7.8** reveals that in the case of **1a4**, both the HOMO and LUMO can perfectly overlap to form the B-N bond since they have similar shapes and signs (indicated in red lobes), which are similar to p-type atomic orbitals at the nitrogen and boron atoms. Thus, this overlap is energetically favourable, and requires a low energy. On

the contrary, the HOMO and LUMO of **1b4** does not have similar shapes and signs. Consequently, it needs more energy to overlap, and thus the activation barrier required to form the transition state **TS2a1'** is much higher than the energy needed to produce the transition state **TS2a1**.

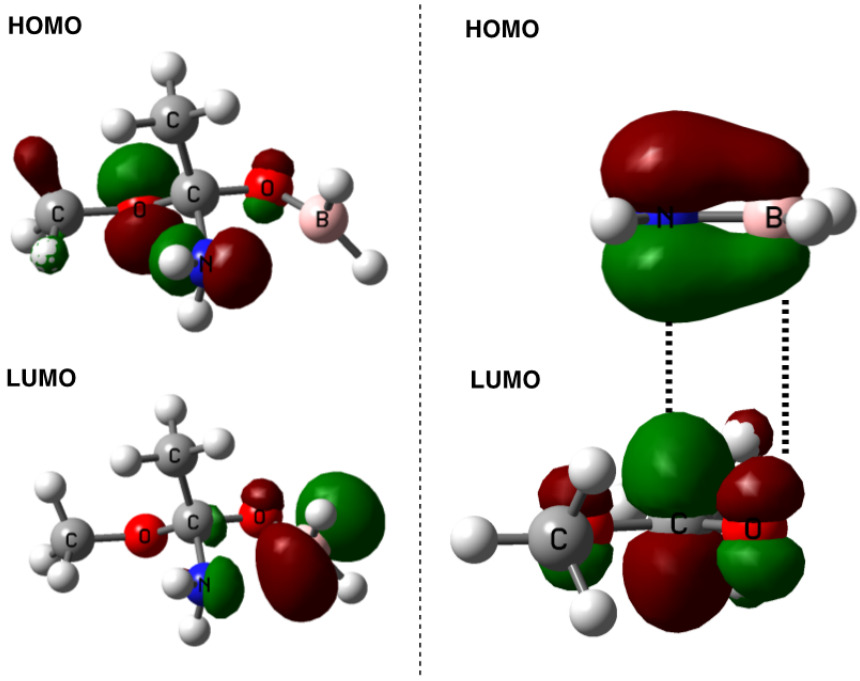

Figure 7.8 The HOMO and LUMO involved in four-membered ring formation from **1a4** and **1b4**.

We have explored two possible dehydrogenation mechanisms of the key molecule **2a2**. In the first mechanism, one hydrogen molecule is released in a familiar concerted reaction in which the N-H and B-H bonds breakage and the H-H bond formation occur in a single step. Only one transition state, **TS2a2**, shown in **Figure 7.9** is involved. As expected, the calculated activation barrier for this single step is fairly high, which is 167.4 kJ mol^{-1}. This high activation barrier may be attributed to the simultaneous breakage of two σ bonds N-H and B-H.

Competing to this one-step mechanism is the two-step mechanism in which one proton is initially transferred to the CH_3O group via transition state **TS2a2'**, subsequently this proton reacts with one hydride of the B-H group to release one H_2 molecule via transition state **TS2a3**. These two transition states are indicated in **Figure 7.10**. The calculated activation barriers for these two steps are 113.2 and 207.1 kJ mol^{-1}, respectively. The second step has an extremely higher activation barrier than that of the first step. It is due to the concomitant breakage of the two stable σ bonds O-H and B-H in the second step while only one σ bond N-H is broken in the first step.

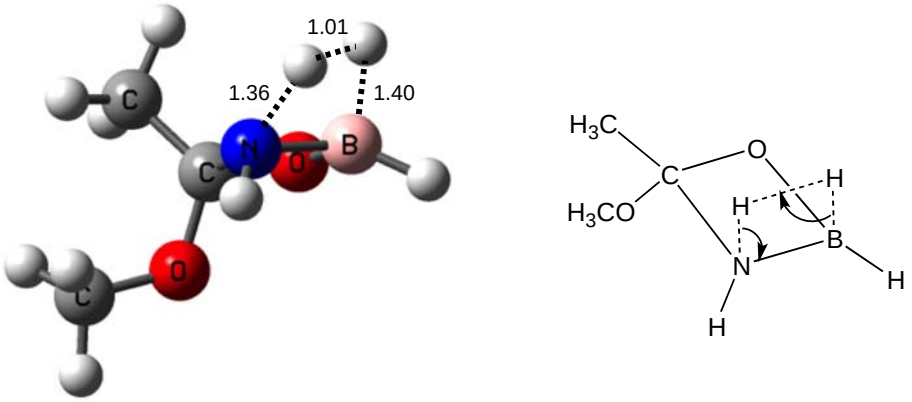

Figure 7.9 B3LYP/6-31+G(2d,p) optimised structure of the transition state **TS2a2** involved in the mechanism 1. Bond lengths are given in angstrom.

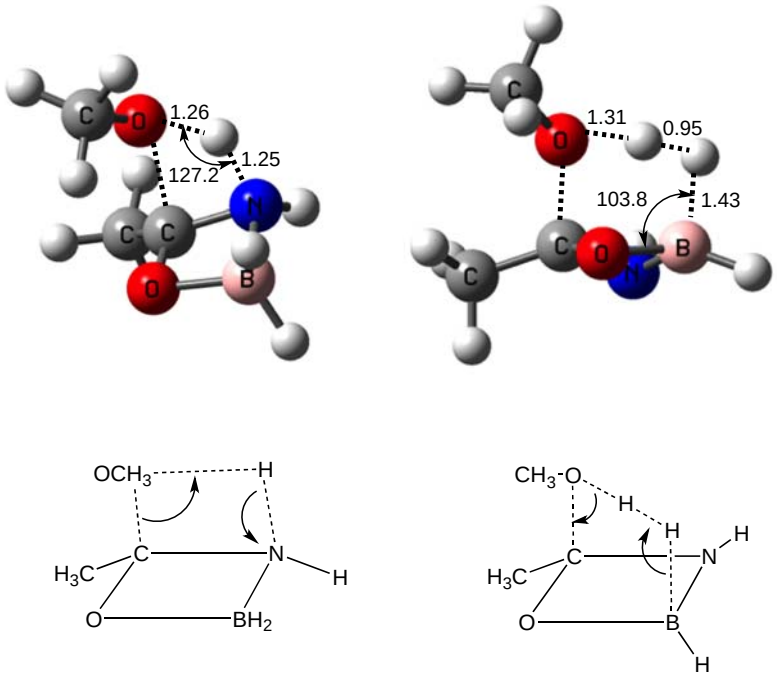

Figure 7.10 B3LYP/6-31+G(2d,p) optimised structure of the two transition states involved in the mechanism 2, **TS2a2'** (left) and **TS2a3** (right). Bond lengths and bond angles are given in angstrom and degree, respectively.

To bring together all the steps and related energies involved in Stage **2**, a schematic energetic profile is given in **Figure 7.11**. As earlier presented, there are two possible pathways that lead to the formation of the key intermediate **2a2**. The first pathway starting from **1a4**, proceeds through the addition reaction of the NH_2BH_2 molecule onto the CH_3COOCH_3 molecule. The second pathway beginning with **1b4**, undergoes the intramolecular cyclisation of the NH_2 and BH_2 groups. **Figure 7.11** clearly shows that the second mechanism is particularly energetically favourable since the activation barrier required for **TS2a1'** formation is considerably low, which is only 44.7 kJ mol^{-1}. On the contrary, the first mechanism proceeding through **TS2a1** from **1a4** requires a considerably higher activation barrier of 144.5 kJ mol^{-1}. Furthermore, as shown in the previous section **7.3.1**, the pathway leading to the formation of **1b4** is kinetically more favourable than the pathway leading to the

formation of **1a4**. Therefore, it is likely that the key intermediate **2a2** is mainly yielded from **1b4**.

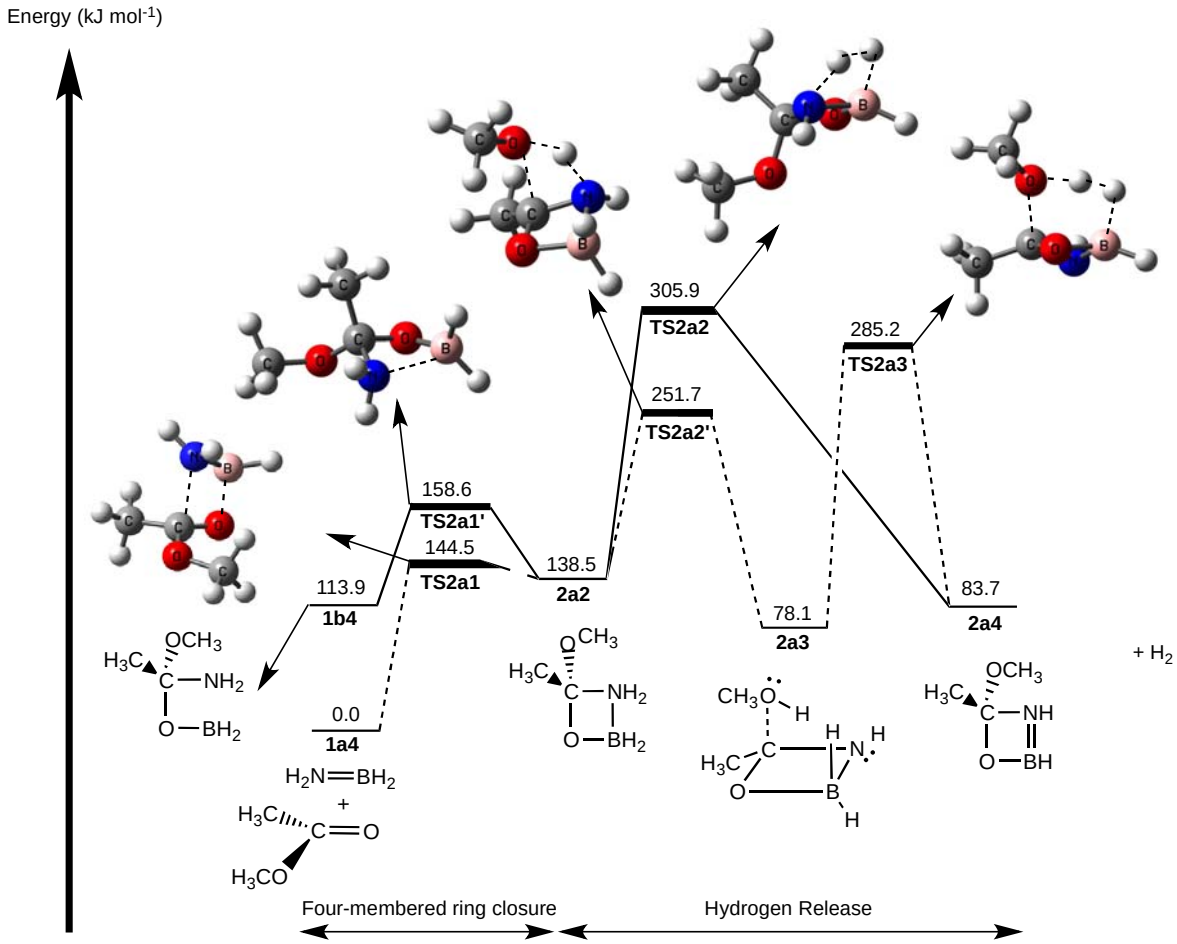

Figure 7.11 Schematic energy profile for mechanism 1 and 2 shows two possible pathways leading to the formation of the key molecule **2a2** and another two possible pathways leading to the hydrogen release from this key molecule. The pathways, which are kinetically less favourable, are indicated in dashed lines.

After the key intermediate **2a2** has been formed, it probably proceeds through two other possible pathways to eliminate a hydrogen molecule as earlier described in detail and now summarised in **Figure 7.11**. The first pathway proceeds through the transition state **TS2a2** while the second pathway proceeds through the two transition states **TS2a2'**, **TS2a3** and the intermediate **2a3**. Although the sole step of the first

pathway requires a fairly high activation barrier of 167.4 kJ mol^{-1}, it is still lower than the activation barrier of the second step of the second pathway, which requires 207.1 kJ mol^{-1}. With these results, it could be concluded that the H_2 elimination from the key molecule **2a2** is likely to proceed through the first pathway via **TS2a2**.

7.3.3 Stage 2b of Hydrogen Release

Stage **2b** involves the participation of the second NH_3BH_3 in the dehydrogenation of Model **2**, leading to the release of the second equivalent of H_2. The reactions of Stage **2b** can be divided into four stages, i.e. Stage **2b1, 2b2, 2b3** and **2b4**. All the reactions involved in these four stages are summarised in **Scheme 7.4**. Stage **2b1** involves the addition reactions of the AB molecule onto the intermediate **1b4**, formed at the end of Stage **1**, to generate the intermediate **2b2**. Then, the elimination of two moles H_2 at two AB-based groups, i.e. the NH_2BH_3 and BH_2NH_3 groups of the newly formed intermediate **2b2** occurs in Stage **2b2**. The intramolecular cyclisation, which occurs in Stage **2b3**, generates the six-membered ring intermediate **2b5** characterised by two groups, the NH_2-BH_2 and the C-O groups. Finally, the elimination of another mole of H_2 from this six-membered ring takes place in Stage **2b4**.

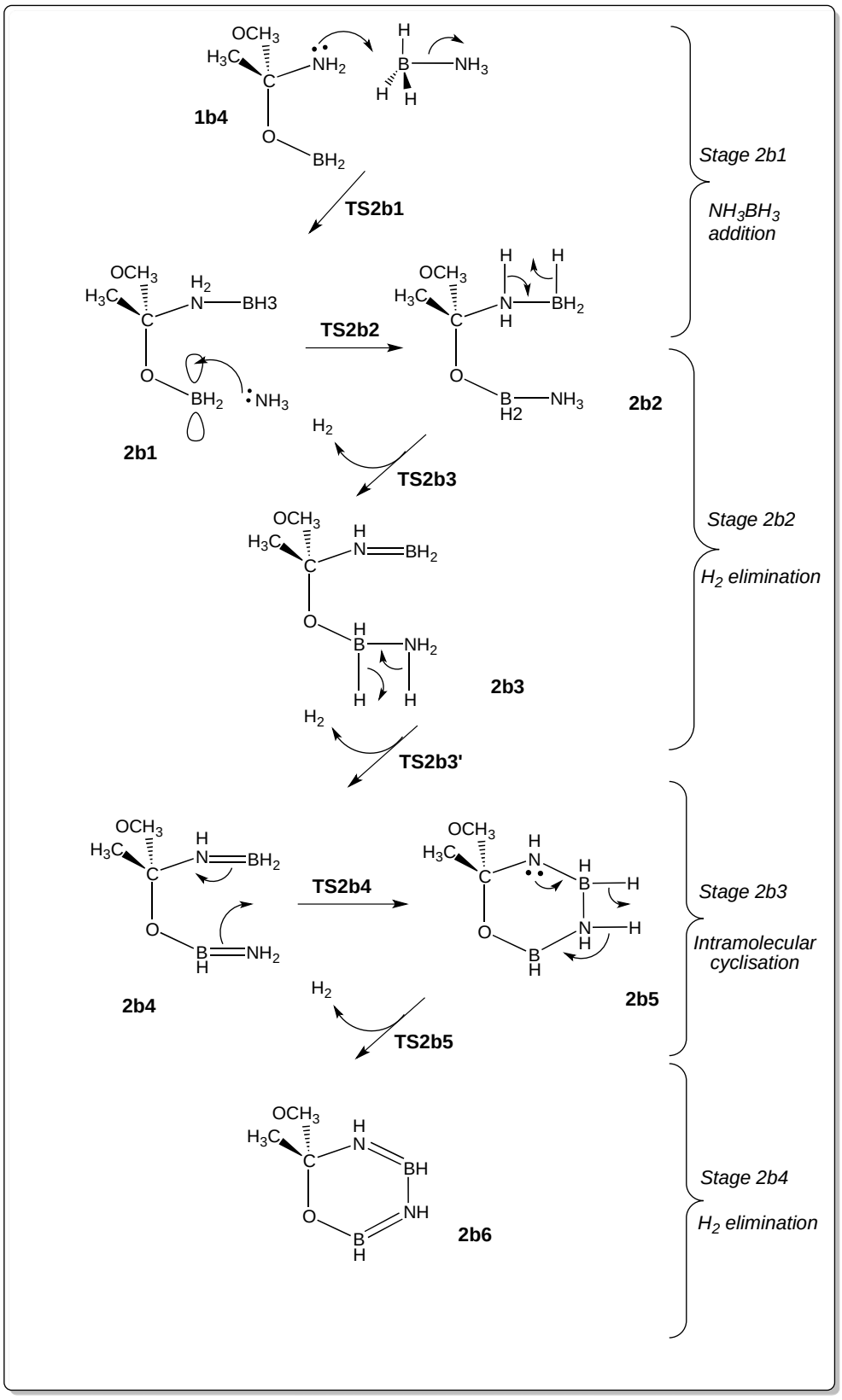

Scheme 7.4 Overall scheme of the second equivalent H_2 being released from Model **2** in the presence of the second AB molecule.

7.3.3.1 Stage 2b1

The addition of NH_3BH_3 onto the intermediate **1b4** proceeds through two steps. In the first step, the intermediate **1b4**, which possesses a nucleophilic NH_2 group with a lone pair of electron, attacks at the BH_3 group of the NH_3BH_3 molecule via transition state **TS2b1** (**Figure 7.12**), resulting in the leaving of the NH_3 group. The activation barrier of this step is 87.3 kJ mol^{-1}, which implies that this reaction may readily occur. It may be attributed to two reasons: (i) The NH_2 group with a lone pair of electron is a strong nucleophilic group; (ii) NH_3 is a good leaving group since it is a neutral molecule. This leaving group NH_3, which possesses a lone pair of electrons, will then be attracted by the BH_2 group of the intermediate **2b1**, which has an empty valence orbital, via transition state **TS2b2 (Figure 7.12**), leading to the formation of the compound **2b2**. The activation barrier of this second step is significantly lower, which is only 21.3 kJ mol^{-1} as compared to 87.3 kJ mol^{-1} at the first step. The newly formed compound **2b2** possesses two AB-based groups, i.e. the NH_2BH_3 and BH_2NH_3 groups. These two groups will take part in the dehydrogenation reactions described in detail in Stage **2b2** below.

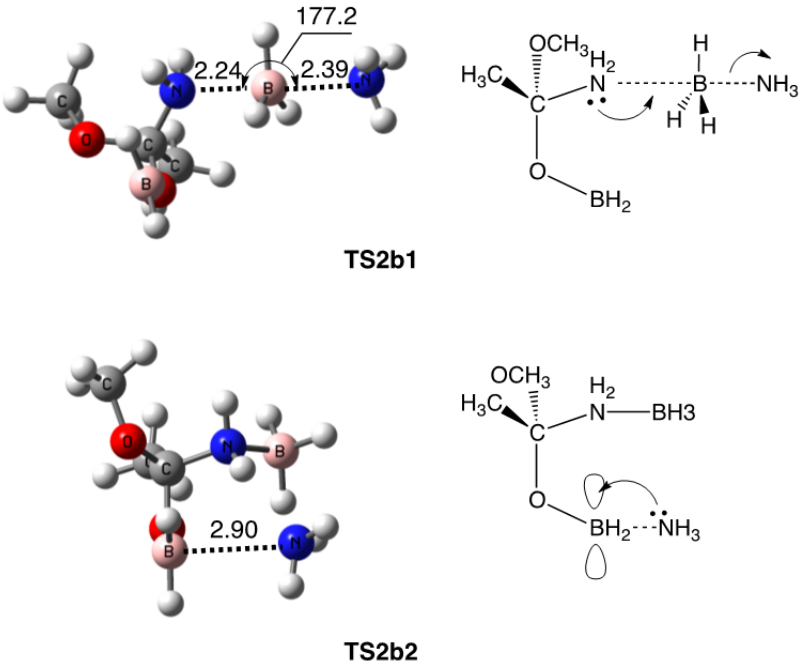

Figure 7.12 B3LYP/6-31+G(2d,p) optimised structures of the transition states **TS2b1** and **TS2b2**. Bond lengths and bond angles are given in angstrom and degree, respectively.

7.3.3.2 Stage 2b2

Stage **2b2** involves the elimination of H_2 from the compound **2b2**, which has been formed at the end of Stage **2b1**. This compound possesses two AB-groups, i.e. the NH_2BH_3 and BH_2NH_3 groups; these two groups may readily release another two moles of H_2. Due to their similar structures, we propose the same concerted mechanism for the dehydrogenation, in which two bond N-H and B-H are broken simultaneously with new H-H bond formation.

Figure 7.13 below shows transition state **TS2b3**, leading to one H_2 molecule released from NH_2BH_3 group. Also, similar transition state for the dehydrogenation at BH_2NH_3 group has been successfully optimised.

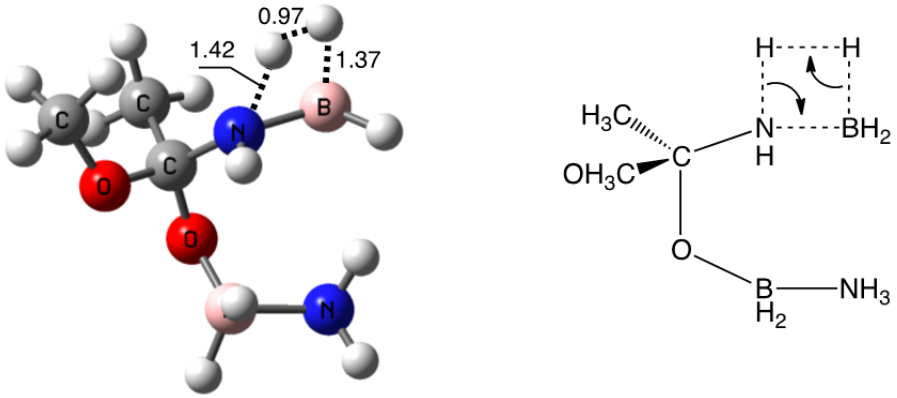

Figure 7.13 B3LYP/6-31+G(2d,p) optimised structure of **TS2b3**. Bond lengths are given in angstrom.

7.3.3.3 Stage 2b3

As we have seen in Chapter **4**, **5** and **6**, the double bond N=B is very active due to the polarisable property. As a result, the nitrogen atom carries a partially positive charge while the boron atom carries a partially negative charge. These two opposite charges encourage the nitrogen and boron atoms of the intermediate **2b4** to take part in an intramolecular cyclisation via transition state **TS2b4** (**Figure 7.14**), generating the six-membered ring intermediate **2b5**. The calculated activation barrier, which is only 68.9 kJ mol^{-1}, confirms the predicted ease of this cyclisation. The formation of this six-membered ring **2b5** now opens a facile way for the next hydrogen release due to the fact that the hydrogen at the BH_2 and NH_2 units of the six-membered ring turns to sp^3 hybridisation from sp^2 hybridisation in the open-chained intermediate **2b4**.

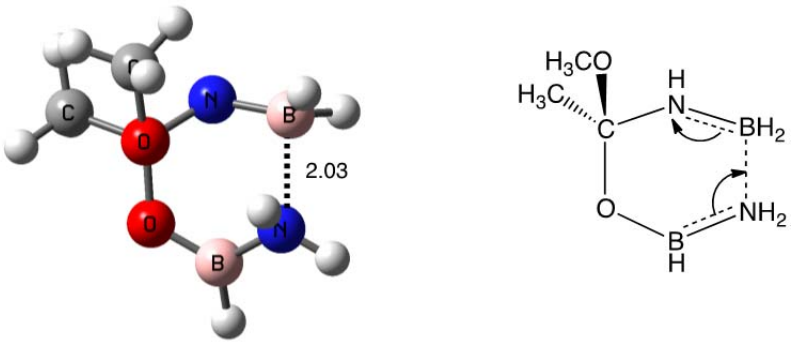

Figure 7.14 B3LYP/6-31+G(2d,p) optimised structure of **TS2b4** leading to the formation of six-membered ring. Bond length is given in angstrom.

7.3.3.4 Stage 2b4

Similar to Stage **2b2**, the dehydrogenation in Stage **2b4** proceeds through the concerted mechanism, in which two N-H and B-H bonds are broken concomitantly with the formation of H-H bond via transition state **TS2b5**, shown in **Figure 7.15**. The activation barrier of this step is fairly low, which is 118.1 kJ mol^{-1}.

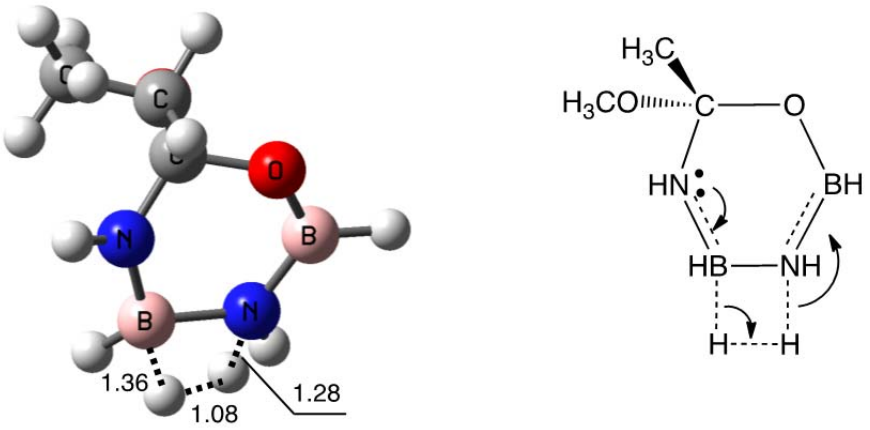

Figure 7.15 B3LYP/6-31+G(2d,p) optimised structure of the transition state **TS2b5**. Bond lengths are given in angstrom.

The formation of the six-membered ring elucidates the ability of the composites to suppress boracic impurity generation. NHBN binds strongly with the carbonyl functional group of the polymer through covalent bonds. This is particularly effective in preventing any NHBH oligomerisation that may yield volatile harmful products such as borazine.

A schematic energy profile for the pathway that leads to the elimination of three moles of H_2 in Stage **2b** is demonstrated in **Figure 7.16**. Notably, the two steps involved in Stage **2b1**, which result in the first two moles of H_2 being released, have significantly higher activation barriers than any other steps. Thus, they completely control the overall rate of the H_2 release in Stage **2b**. Regarding the thermodynamic properties of the dehydrogenation reactions, **Figure 7.16** clearly reveals that the dehydrogenation is particularly energetically favourable. The Gibbs free energy of the reaction is -135.6 kJ mol^{-1}. This may be attributed to three moles of H_2 released, which increases considerably the overall entropy of the reaction. In addition, the product, which possesses a six-membered ring featured by the conjugation between two π N=B bond and the lone pair of electron of oxygen atom, contributes to enthalpy decrease of the reaction. However, it should be noted that the negative value of Gibbs free energy implies that this pathway is essentially irreversible.

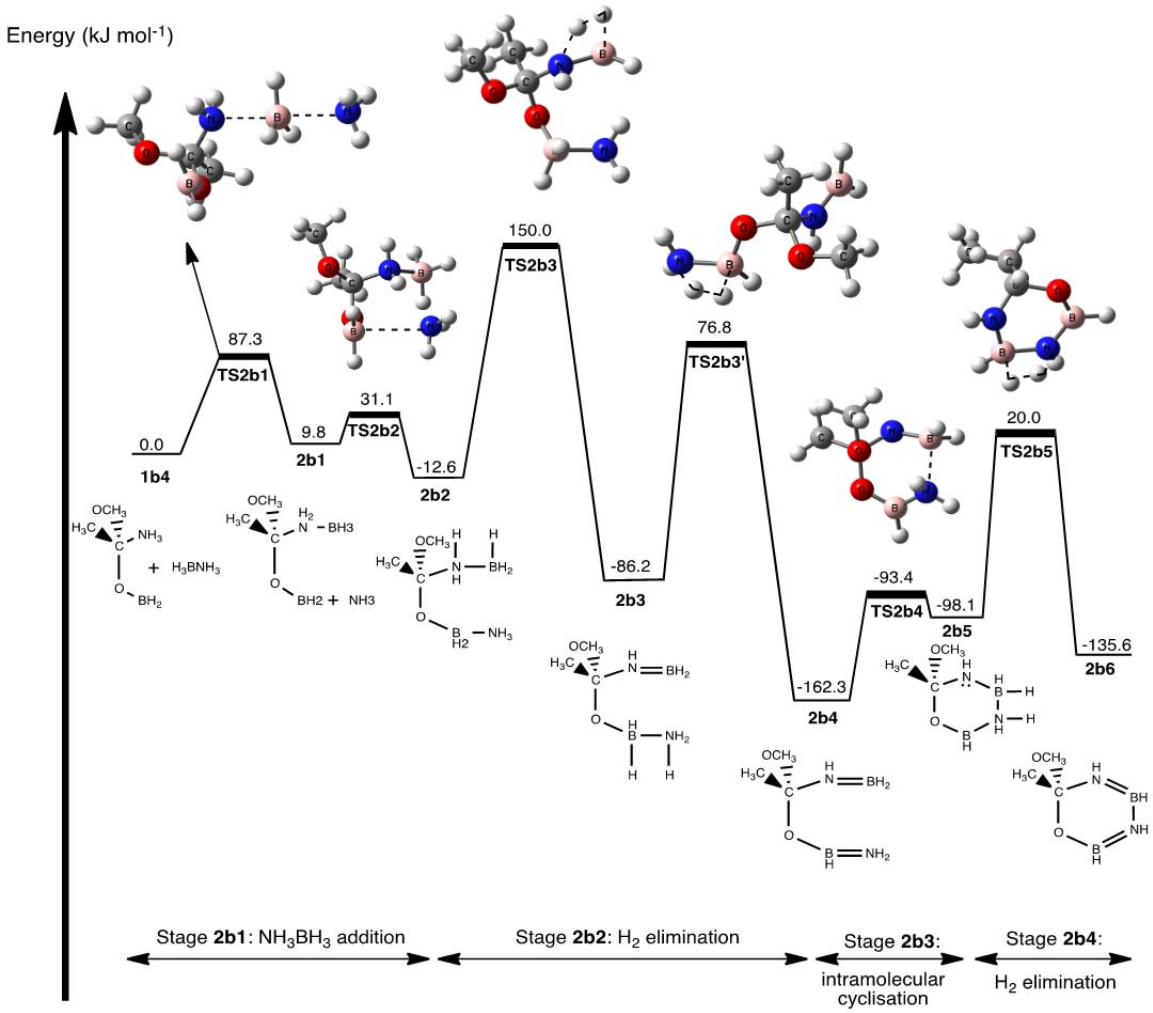

Figure 7.16 Schematic potential energy profile shows the pathway leading to the release of the second equivalent H_2 in Stage **2b**. Relative Gibbs free energies are given in kJ mol^{-1} from B3LYP/6-31+G(2d,p).

7.4 Conclusions

This chapter has explored the possible dehydrogenation mechanisms of PAB20 and PAB80 based on the two simplified models: (i) model **1** comprised of one CH_3COOCH_3 molecule and one NH_3BH_3 molecule; (ii) model **2** including one CH_3COOCH_3 molecule and two NH_3BH_3 molecules. We have carefully examined two stages of the dehydrogenation, corresponding to two equivalent of H_2 released as experimentally observed. Some important results will be highlighted in the following:

Our comprehensive study presented in section **7.3.1** on the first H_2 release has elucidated the critical role of the carbonyl functional group in facilitating the hydrogen release. The carbonyl functional group initially aided in breaking the B-N bond of the AB molecule. The leaving NH_3 group then reattached to the carbon atom of the carbonyl group of CH_3COOCH_3 to yield a zwitterion. The zwitterion with a particular structure accommodated the interactions between the proton and the hydride, resulting in the low activation barrier of the hydrogen release step. Our calculations confirmed that this mechanism involved significantly lower activation barriers than that of AB, suggesting that the PAB20 and PAB80 could release H_2 at lower temperature than AB. These findings are in good accord with J. Chen *et al.*'s experimental observations.

Additionally, our study has provided an explanation on the capability of the composites in suppressing borazine impurities. We have indicated that in stage **2a** (see Section **7.3.2**) and **2b** (see Section **7.3.3**), the formation of four and six-membered rings characterised by NH-BH groups and C-O group helped trap the NHBH molecule. This might be a particularly effective prevention of any NHBH oligomerisation. Thus, it helped avoid the release of any harmful volatile by-products such as borazine.

In the following chapter, we will continue to investigate a fairly similar composite based on amide functional group. Then, we will suggest some new materials based on these composites. In particularly, we will theoretically examine the dehydrogenation of these composites to establish the relations between different

functional groups and their effectiveness in facilitating H_2 release. These findings may help in designing better composites for hydrogen storage purpose.

References

[1] F. H. Stephens, V. Pons, and R. T. Baker, *Dalton Trans.*, vol. 25, p. 2613, 2007.

[2] J. M. Yan, X. B. Zhang, S. Han, H. S. Shioyama, and Q. Xu, *Angew. Chem. Int. Ed.*, vol. 47, p. 2287, 2008.

[3] Y. Lin, W. L. Mao, and H. K. Mao, *Proc. Natl. Acad. Sci. USA*, vol. 106, p. 8113, 2009.

[4] A. Gutowska et al., *Angew. Chem. Int. Ed.*, vol. 44, p. 3578, 2005.

[5] A. Feaver et al., *J. Phys. Chem. B.*, vol. 111, p. 7469, 2007.

[6] L. Li et al., *Adv. Funct. Mater.*, vol. 19, p. 265, 2009.

[7] C. A. Jaska, K. Temple, A. J. Lough, and I. Manners, *J. Am. Chem. Soc.*, vol. 125, p. 9424, 2003.

[8] M. C. Denney, V. Pons, T. J. Hebden, D. M. Heinekey, and K. I. Goldberg, *J. Am. Chem. Soc.*, vol. 128, p. 12048, 2006.

[9] F. Y. Cheng, H. Ma, Y. M. Li, and J. Chen, *Inorg. Chem.*, vol. 46, p. 788, 2007.

[10] P. M. Zimmerman, A. Paul, Z. Zhang, and C. B. Musgrave, *Angew. Chem. Int. Ed.*, vol. 48, p. 2201, 2009.

[11] M. E. Bluhm, M. G. Bradley, R. Butterick, U. Kusari, and L. G. Sneddon, *J. Am. Chem. Soc.*, vol. 128, p. 7748, 2006.

[12] Z. T. Xiong et al., *Nat. Mater.*, vol. 7, p. 138, 2008.

[13] X. D. Kang et al., *Adv. Mater.*, vol. 20, p. 2756, 2008.

[14] J. Spielmann, G. Jansen, H. Bandmann, and S. Harder, *Angew. Chem. Int. Ed.*, vol. 47, p. 6290, 2008.

[18] J. Zhao et al., *Adv. Mater.*, vol. 22, pp. 394-397, 2010.

[15] M. T. Weller, P. F. Henry, V. P. Ting, and C. C. Wilson, *Chem. Commun.*, no. 21, pp. 2973-2989, 2009.

[16] H. L. Jiang, S. K. Singh, J. M. Yan, X. B. Zhang, and Xu. Q., *Chem. Sus. Chem.*, vol. 3, no. 5, pp. 541-549, 2010.

[17] T. Umegaki, J. M. Yan, X. B. Zhang, H. Shioyama, and N. Xu, Q. Kuriyama, *International Journal of Hydrogen Energy*, vol. 34, no. 5, pp. 2303-2311, 2009.

CHAPTER 8

POLYACRYLAMIDE-CONFINED AMMONIA-BORANE AND OTHER SIMILAR COMPOSITES: A COMPUTATIONAL STUDY

8.1 Introduction

In the previous chapter, we have examined the dehydrogenation mechanisms of poly(methyl acrylate)-confined ammonia-borane (PMA-AB). Our investigations have shed light on the critical role of the carbonyl functional group in facilitating the hydrogen release. More specifically, this carbonyl group initially breaks the N-B bonds of the AB molecule, and then reassembles NH_3 and BH_3 into a zwitterion. These structural changes not only help orient the proton toward the hydride but also make the proton of NH_3^+ group more protic and the hydride of BH_3^- group more hydridic. Consequently, hydrogen release process readily occurs. In addition to the improvement of dehydrogenation property, this compound was reported to efficiently suppress the emission of the boracic impurities. This pioneering composite has indeed stimulated further efforts to synthesise other analogous compounds with hopes that they may exhibit better dehydrogenation properties.

Recently, the similar polymer hydrogen storage composite based on polyacrylamide and ammonia-borane (PAM-AB) was successfully synthesised through a simple sol-mixing method. Interestingly, the dehydrogenation properties of

this composite was also reported to promote significantly in contrast to pure ammonia borane, justified by its low onset H_2-release temperature of 75^oC without induction period and complete depression of the emission of the boracic impurities [1-7]. Although tremendous efforts have been made to examine the dehydrogenation mechanisms of this composite, not much information has been obtained [8].

Despite the encouraging improvement in the dehydrogenation properties of this composite, NH_3 release during the dehydrogenation reaction is a major drawback since it can poison the vehicle motor. Thus, metal chlorides such as $CaCl_2$, $MgCl_2$ and $ZnCl_2$, which are Lewis acid, were introduced to PAM-AB with hopes that they will react with NH_3 – a Lewis base. This approach indeed led to an impressive depression of NH_3 evolution. Surprisingly, it was observed that the presence of these metal halides enabled the dehydrogenation of the polymeric composite to occur at a significantly lower temperature as compared to both the PAM-AB system and the neat AB, in conjunction with enhanced hydrogen purity. For comparison, the peaks of the first H_2 release in the neat AB, PAM-AB system and PAM-AB-$ZnCl_2$ system are at 125^oC, 110^oC and 100^oC, respectively. These results have raised a question on the actual role of these metal halides: how do these metal halides suppress ammonia evolution and lower the dehydrogenation temperature of the composite PAM-AB simultaneously? To answer this question, in Section 8.3.1, we will firstly examine the dehydrogenation mechanisms of the first H_2 release from the PAM-AB composite. Then the effect of metal halides on the dehydrogenation and their capability for facilitating the hydrogen release from the PAM-AB composite will be investigated. Finally, in an attempt to design better composites, in Section 8.3.2, we will propose some other composites based on other functional groups such as thionyl, amide,

chloride acid, etc. Then the activation barriers of the first H_2 release from these compounds will be examined. The relationship between their structures and capability for the facilitation of H_2 release will be established.

The findings presented in this chapter will provide a deeper understanding on the dehydrogenation of PAM-AB with and without the presence of metal halides. Additionally, they will elucidate the effect of different functional groups such as carbonyl, thionyl, amide groups, etc. on the dehydrogenation. Based on these results, this study may effectively aid in guiding the synthesis of novel composites that may exhibit much better dehydrogenation properties.

8.2 Computational Methods

Similar to the preceding chapters, the density functional theory method B3LYP in combination with 6-31+G(2d,p) basis set was employed to optimise all the equilibrium structures and transition states in the gas phase of all systems in this study. The activation barriers $\Delta G^{\ddagger}$ of reactions involved at the standard condition 298 K, 1 atm were also computed. Intrinsic reaction coordinates (IRC) were utilised to confirm the identity of the linking reactant and product from a transition state. All calculations were performed with the Gaussian 09 software packages.

8.3 Results and Discussions

8.3.1 Dehydrogenation Mechanism of PAM-AB and PAM-AB-Metal Halides

As mentioned in the previous chapter, since the reaction is unlikely to occur at the main chain of the polymer, thus we replace the main chain of the polymer with a methyl group to reduce a great amount of calculations while the nature of the reaction is likely unchanged. Therefore, our calculations are based on the model comprised of one CH_3CONH_2 molecule and one NH_3BH_3 molecule.

The structural similarity between the methyl acrylate and acrylamide molecules lends us strong confidence to propose a similar dehydrogenation mechanism as investigated in the previous chapter. **Figure 8.1** clearly shows similarities such as the bond lengths of two carbonyl groups and the angles of C-C-N and C-C-O in both two structures.

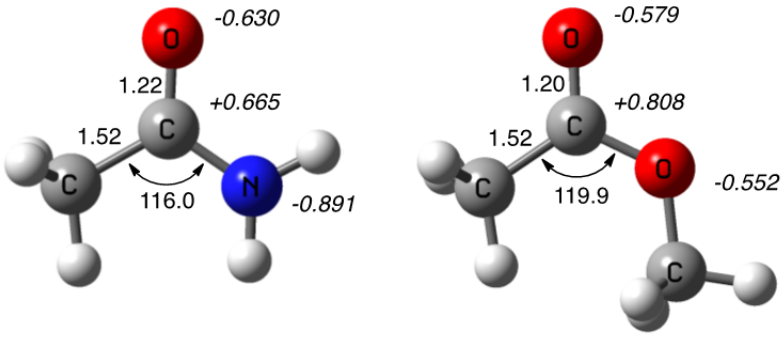

Figure 8.1 B3LYP/6-31+G(2d,p) optimised structures of CH_3CONH_2 (left) and CH_3COOCH_3 (right) show their structural similarities. Bond lengths and bond angles are given in angstrom and degree, respectively. NBO charges are also given (in *italic*).

As shown in the previous chapter, the carbonyl group, C=O and the methoxi group, OCH_3 take part and have great effect mainly on the first stage of the hydrogen release. Thus, in this chapter, we only concentrate on the first stage to investigate the effect of two groups C=O and NH_2 of the CH_3CONH_2 molecule on the dehydrogenation properties.

The first stage of hydrogen release proceeds through two steps: (i) the carbonyl group attacks BH_3 group in a S_N2-like reaction, resulting in the elimination of the NH_3 group from AB via the transition state **TS1** (**Figure 8.2**); (ii) The leaving group NH_3 provides one proton while BH_3 contributes one hydride, leading to one mole of H_2 released via transition state **TS2** (**Figure 8.2**). It should be noted that different from the CH_3COOCH_3 and AB system, we could not locate any tetrahedral intermediate in which NH_3 covalently binds with the carbon atom of the carbonyl group of the CH_3CONH_2 molecule at this first stage of H_2 release. Instead, only weak interaction between NH_3 and the carbon atom of the carbonyl group has been successfully optimised as shown in **Figure 8.3**. It may be attributed to the strong conjugation between NH_2 and C=O group. This strong conjugation prevents the addition of NH_3 group onto the carbon of C=O group since it will lead to the significant loss of conjugation energy.

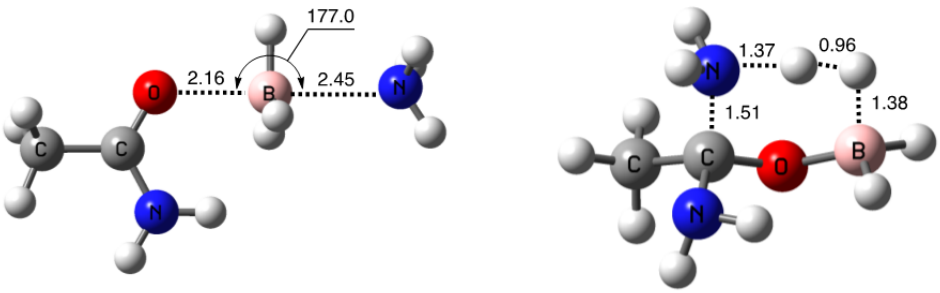

Figure 8.2 B3LYP/6-31+G(2d,p) optimised structures of transition states **TS1** (left) and **TS2** (right) involved in the first stage of H_2 release.

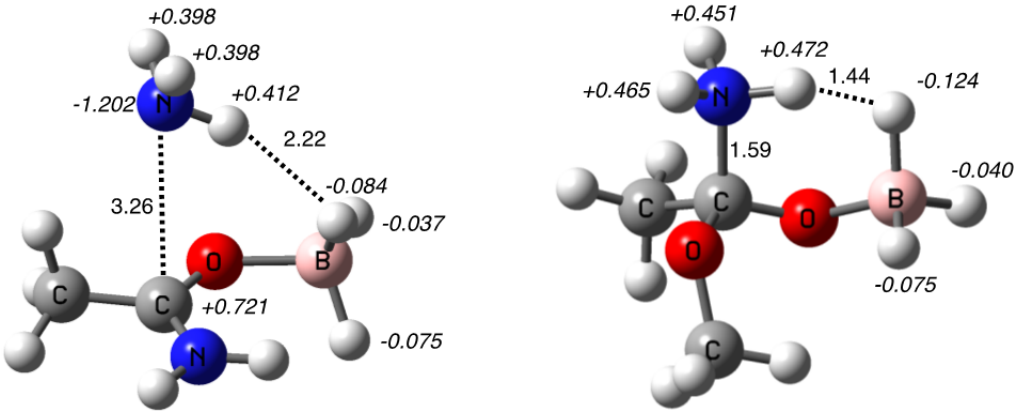

Figure 8.3 B3LYP/6-31+G(2d,p) optimised structures of two intermediates formed after the reaction between NH_3BH_3 and CH_3CONH_2 (left) and CH_3COOCH_3 (right).

The activation barrier of the first step is 94.3 kJ mol^{-1}, which is similar to the calculated activation barrier of the same step in the first H_2 elimination reaction of the CH_3COOCH_3 and AB system investigated in the previous chapter. Notably, the activation barrier of the second step is fairly high, which is 130.4 kJ mol^{-1}. This activation barrier is much higher than the activation barrier of the same step in the reaction between CH_3COOCH_3 and AB. As indicated earlier, at this current system, NH_3 does not bind to the carbon atom of the carbonyl group to form a zwitterion as occurred in the case of the CH_3COOCH_3 and AB, thus the hydrogen of NH_3 does not exhibit strong protic character. Consequently, it requires more energy to release H_2.

We then examine the effect of different metal halides on the activation barriers of these two steps. We have calculated the activation barriers of two steps based on the systems of CH_3COOCH_3, NH_3BH_3 and MCl_2 (M=Mg, Zn, Ca). The results are tabulated in **Table 8.1**.

Table 8.1 Activation Energies of the first and second steps of H_2 released in the presence of metal halides.

Metal halide	Activation Energy of the first step (kJ mol^{-1})	Activation Energy of the second step (kJ mol^{-1})
$MgCl_2$	83.5	17.2
MgF_2	78.8	25.3
$ZnCl_2$	87.9	16.5
ZnF_2	85.7	10.1
$CaCl_2$	89.1	20.0

The results in **Table 8.1** clearly show that the presence of the metal halides slightly lowers the activation barrier of the first step. More impressively, the metal halide drastically lowers the activation of the hydrogen release step, which is the rate-determining step in the dehydrogenation of the CH_3CONH_2-AB system. While the activation barrier of the second step without metal halides is 130.4 kJ mol^{-1}, these metal halides now can reduce it to as low as 10.1 kJ mol^{-1}. With these results, the first step becomes the rate-determining step in the dehydrogenation of the CH_3CONH_2-AB-Metal halide systems. Notably, the activation barrier of this rate-determining step is significantly lower than that of the CH_3CONH_2-AB system. Consequently, the hydrogen release is more readily to occur when metal halides are present.

Figure 8.4 helps elucidate the impressive capability of these metal halides in lowering the activation barrier of the hydrogen release step and suppressing the NH_3 evolution. The figure clearly shows that, the presence of these metals halides open the way to the formation of zwitterions, in which the NH_3 group now carries positive charge while the BH_3 group bears negative charge. Metal halides act as Lewis acids, and thus readily accept a lone pair of electrons on the nitrogen of the NH_2 group of CH_3CONH_2, forming metal-nitrogen bonds. These bindings help break the conjugation between the lone pair of the electrons on the nitrogen atom of the NH_2 group and the π bond of the C=O group. As discussed earlier, this conjugation is the hindrance to the addition of NH_3 onto the carbon atom the carbonyl group. However, this conjugation are now broken. Consequently, NH_3 readily adds onto the carbon of C=O group to form a zwitterion, which eliminates hydrogen easily. The short distance, which is 1.57 Å, between the carbon of the C=O group and the nitrogen of the NH_3 group, suggests that NH_3 covalently binds to the carbon atom, thus it is unlikely that NH_3 can readily release.

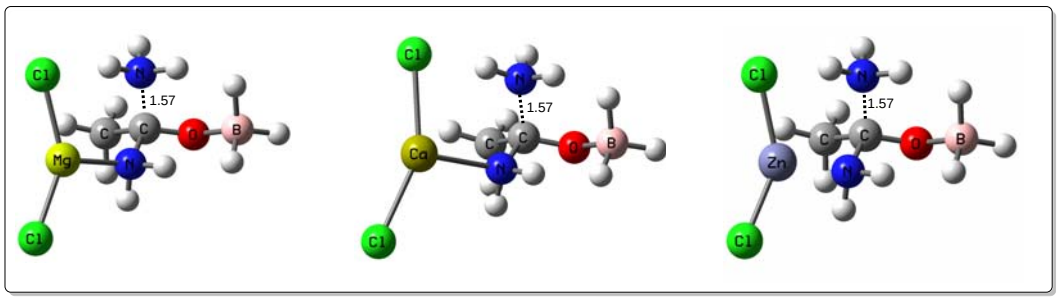

Figure 8.4 B3LYP/6-31+G(2d,p) optimised structures of the complex between several metal halides including $MgCl_2$, $CaCl_2$, $ZnCl_2$ and CH_3CONH_2-NH_3BH_3.

It should be noted that $MgCl_2$, $ZnCl_2$ and $CaCl_2$ have been experimentally examined while the other two metal halides, MgF_2 and ZnF_2 are our proposed

replacements for $MgCl_2$ and $ZnCl_2$. Our calculations have suggested that among other metal halides investigated, MgF_2 and ZnF_2 are likely to work more efficiently. It may be due to the fact that MgF_2 and ZnF_2 are stronger Lewis acid among the five metal halides considered. Their strong acidity can be attributed to the presence of fluoride – the most electronegative element.

In summary, in this section we have examined the dehydrogenation mechanism of the first H_2 release for two systems: (i) CH_3CONH_2-AB; (ii) CH_3CONH_2-AB and metal halides including $MgCl_2$, $ZnCl_2$, $CaCl_2$, MgF_2 and ZnF_2. In comparison with the CH_3COOCH_3 and NH_3BH_3 system examined investigated in the previous chapter, we have found out that replacement of CH_3O group with NH_2 group increases the activation barrier of the hydrogen release step, thus it's more difficult to release H_2 from CH_3CONH_2 and NH_3BH_3 system. However, the presence of metal halides, due to their Lewis acid properties, has changed drastically the nature of reactions, leading to the formation of zwitterions. Consequently, the CH_3CONH_2-AB-Metal halide systems are capable of suppressing NH_3 evolution and lowering significantly the activation barriers of all steps involved, thus facilitate the hydrogen release.

8.3.2 Effects of Different Functional Groups on the Dehydrogenation of AB:

Our mechanistic study on the dehydrogenation of the composites thus far has shown the central role of the functional groups such as $COOCH_3$ and $CONH_2$ in the facilitation of H_2 release. Apart from these two examples, many other functional groups such as ketone, thionyl, chloride etc. may also facilitate the dehydrogenation.

Unfortunately, to date, there have been no experimental and theoretical researches carried out on other functional groups. Thus, our aim is to systematically examine the dehydrogenation reactions of AB in the presence of different functional groups. Based on that, the correlation between the property of these functional groups and their capability of facilitating the hydrogen release will be established. These findings might have a great impact on designing other composites that possess better dehydrogenation properties.

In Section 8.3.2.1 below, varied carbonyl-based compounds including $CH_3CONHCH_3$, CH_3CONH_2, CH_3COCl, $CH_3COOC(CH_3)_3$, CH_3COCH_3 and $CH_3COC(CH_3)_3$ will be first examined. Then, in Section 8.3.2.2, we will replace the carbonyl groups of all the aforementioned compounds with thinoyl group C=S. These newly created thionyl-based compounds will also be investigated.

8.3.2.1 Effects of Varied Carbonyl-based Compounds on the Dehydrogenation of AB

We suppose that the aforementioned carbonyl-based compounds proceed through the same dehydrogenation mechanism as the two carbonyl compounds investigated in the previous chapter and earlier in this chapter. There are two possible mechanisms for the first H_2 release. The first mechanism proceeds through the interaction between the NH_3 group of AB molecule and the carbonyl group of the carbonyl-based compounds, which is followed by the hydrogen release step. Alternatively, in the second mechanism, the BH_3 group of AB molecule first interacts with the carbonyl group of the carbonyl-based compounds, which is followed by the hydrogen release step. Between these two mechanisms, the second mechanism

involves lower activation barriers, thus the dehydrogenation reactions are likely to proceed through. Thus, we only focus on this mechanism when examining the aforementioned carbonyl-based compounds. The following chart (**Figure 8.5**) shows the activation barriers of the rate-determining step of the second mechanism that the carbonyl-based compounds proceed through.

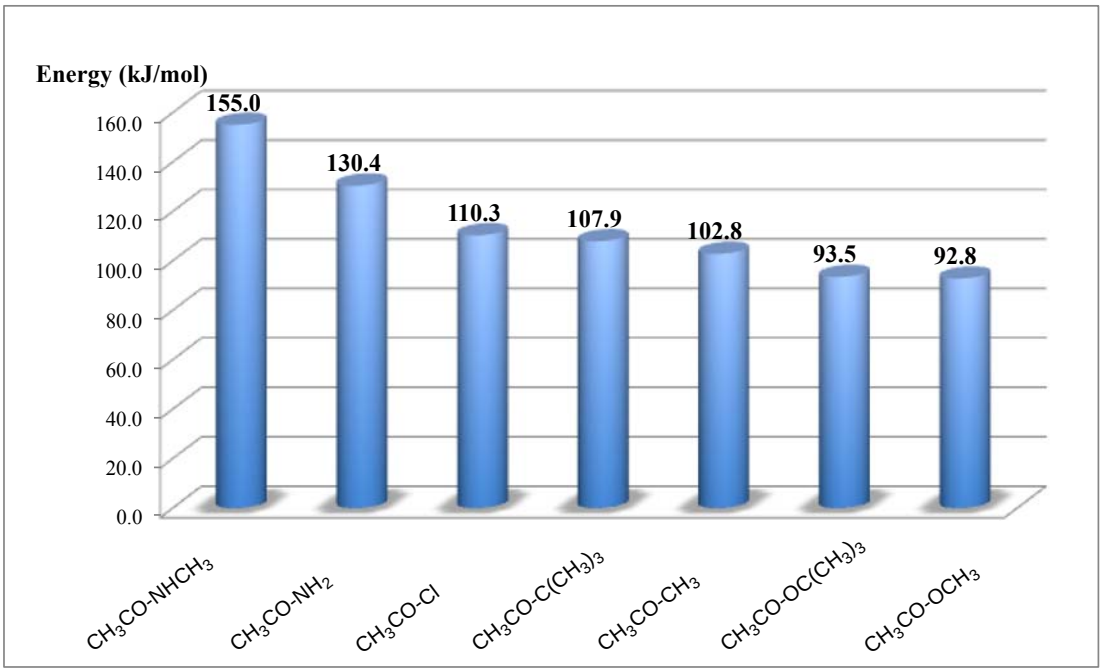

Figure 8.5 Activation energies of the rate-determining steps of the carbonyl-based compounds.

The trend is obviously seen on the chart. The activation energies are descending from left to right of the chart when going through N-methylamide, amide, chloride acid, *t*-butyl ketone, CH_3COOCH_3, acetone and *t*-butyl ester. It should be noted that, for N-methylamide and amide compounds, the rate-determining step is the second step (of the mechanism 2) while it is the first step for all the other compounds. For both N-methylamide and amide, the formation of zwitterions, which are of utmost important to facilitate the hydrogen release in the next step, are prevented by the

conjugation between the lone pair of electrons on the nitrogen atoms and the π bond of the carbonyl groups. Consequently, the activation energies of the hydrogen release step, are 155.0 and 130.4 kJ mol^{-1} for N-methylamide and amide, respectively. These values exceed the activation energies in step 1, which are 87.1 and 83.9 kJ mol^{-1} for N-methylamide and amide, respectively.

For other functional groups, since step 1, in which the nucleophilic oxygen atom attacks the AB molecule, is the rate-determining step, thus the charges on the oxygen atoms are a critical factor to consider. NBO charge analysis has been carried out to find the correlation between the charges of the oxygen atoms of varied functional groups and the activation barriers of step 1 (**Table 8.2**).

Table 8.2 NBO charges on the oxygen atoms of varied carbonyl-based compounds.

Compound	NBO charge on O atom
CH_3CO-Cl	-0.486
CH_3CO-CH_3	-0.551
CH_3CO-$C(CH_3)_3$	-0.556
CH_3CO-OCH_3	-0.579
CH_3CO-$OC(CH_3)_3$	-0.582

Among the five compounds, the two ester compounds have the most negatively charged O atoms. In fact, the activation energies related to these two compounds have smallest values, 92.8 and 93.5 kJ mol^{-1}, respectively. Two ketone compounds have less negative charge on O atom than two ester compounds. Those values help explain why the activation energies of those ketones are higher, 102.8 and 107.9 kJ mol^{-1} respectively. Finally the chloride compounds has the least negative

charge on O atom, corresponding to the highest activation energies among five mentioned compounds, 110.3 kJ mol^{-1}. These results suggest that the compound possesses the carbonyl group with more nulceophilic oxygen will be more effective in lowering the dehydrogenation temperature.

8.3.3.2 Effects of Varied Thionyl-based Compounds on the Dehydrogenation of AB

As shown in the previous section, the nucleophilicity of the oxygen atom of the carbonyl group determines the kinetics of the rate-determining step. Thus, to further improve the kinetics of these composites, a stronger nucleophilic group such as C=S group should be employed. In this section, the effects of varied thionyl-based compounds on the kinetics of the rate-determining step will be investigated.

Similarly, we suppose that the aforementioned thionyl-based compounds might proceed through the same dehydrogenation mechanism as the carbonyl-based compounds. The activation barriers of the rate-determining step for the first H_2 release from these systems are indicated in the chart of **Figure 8.6**. Notably, the chart reveals that among seven thionyl-based compounds, CH_3CSCH_3 has the lowest activation barrier of the rate-determining step. It even has a slightly lower activation barrier as compared to that of CH_3COOCH_3. This result implies that CH_3CSCH_3 might be a better candidate to design a better composite for hydrogen storage purpose than those two composites investigated in the previous chapter.

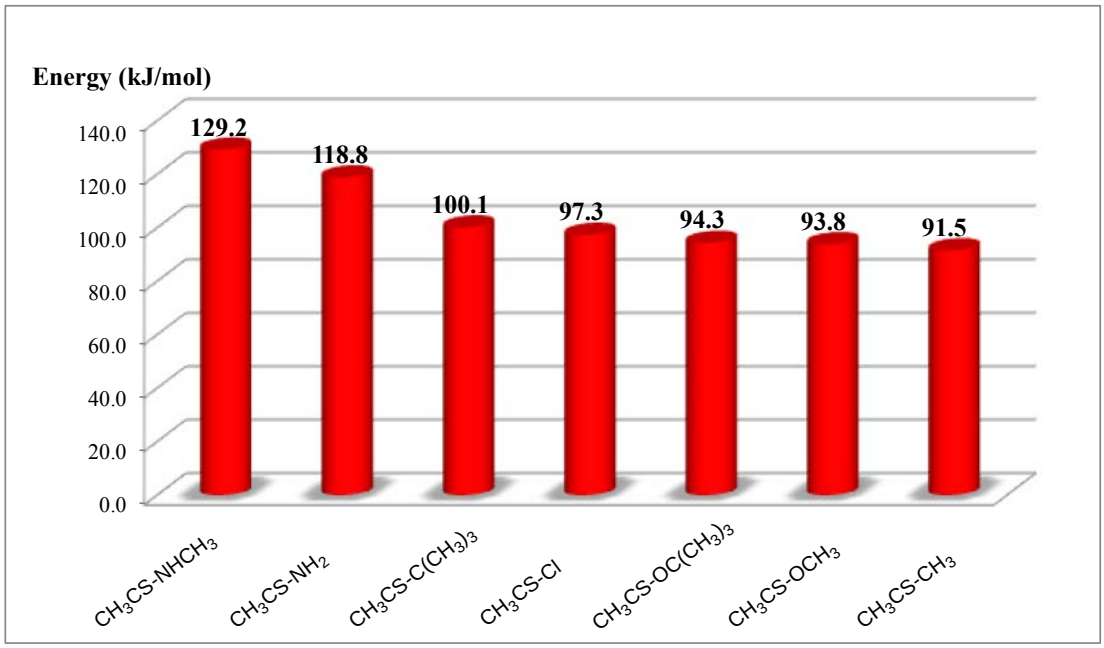

Figure 8.6 Activation energies of the rate-determining steps of thionyl-based compounds.

The activation barriers of the rate-determining step of all the aforementioned carbonyl and thionyl-based compounds have been shown on the chart of **Figure 8.7**. **Figure 8.7** clearly reveals that all the carbonyl-based compounds have higher activation barriers of the rate-determining steps than the thionyl-based compounds. These results suggest that the thionyl-based composites are likely to release hydrogen at lower temperature.

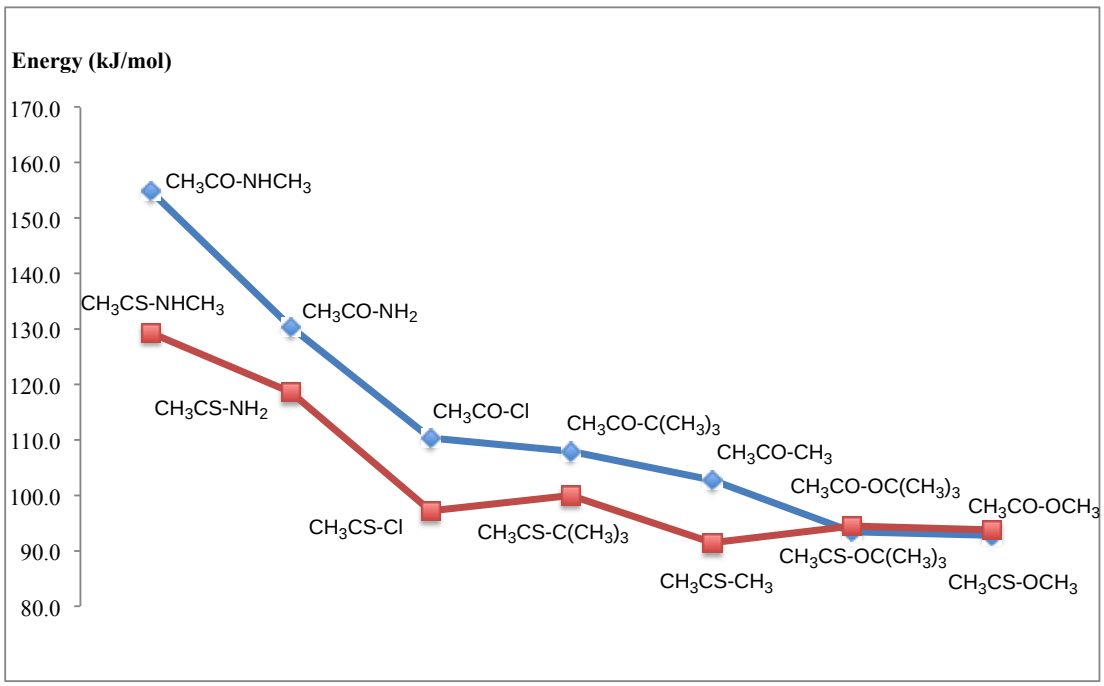

Figure 8.7 Activation energies of the rate-determining steps of varied carbonyl and thionyl-based compounds.

The differences between the activation barriers of these thionyl-based and carbonyl-based compounds could be explained as the following:

For N-methylthioamide and thioamide compounds, these two thionyl-based compounds could generate the zwitterions, which facilitate the hydrogen release (see Chapter 7 and Section 8.3.1). To produce the zwitterions, the double bond C=S, and thus the conjugation between C=S and the lone pair of electrons on the nitrogen atom will be lost. This type of conjugation requires less energy to break than the conjugation between the C=O group and the lone pair of electrons on the nitrogen atom of the NH_2 and the $NHCH_3$ groups. The conjugation formed by the C=O group and the lone pair of electrons on the nitrogen atom is more stable because the lone pair of electrons on the nitrogen atom reside at 2p orbital, which has equal energy with the energy of the C=O π bond.

For other compounds, the rate-determining step is the first step, which involves the attack of the lone pair of electrons on the sulfur atom to the boron atom of the BH_3 group of AB, the reason can be explained in the following diagram:

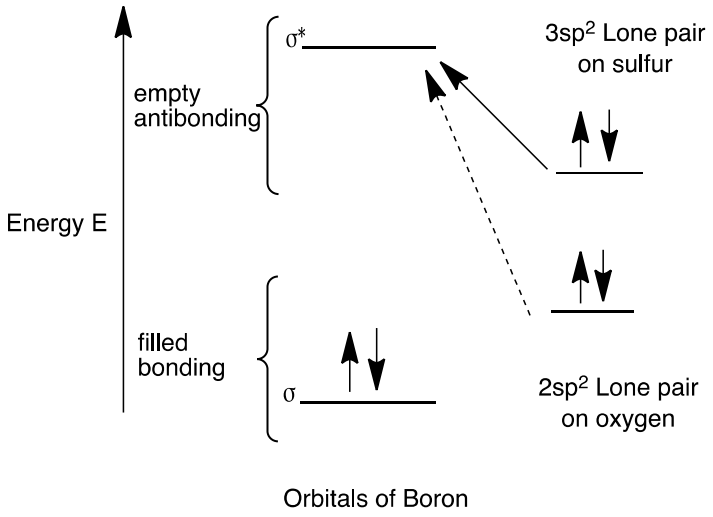

Figure 8.8 Simplified diagram to illustrate the relative nucleophilicity of S and O atom toward B.

To form the bond S-B or O-B, the sulfur and oxygen must donate their $3sp^2$ and $2sp^2$ lone pairs, respectively to the empty antibonding of boron. However, the orbital containing the lone pair of electrons on sulfur has higher energy than the orbital containing the lone pair on oxygen, thus it donates their electrons to the empty antibonding of boron more easily due to the smaller energy gap. This explains why sulfur is a better nucleophile than oxygen.

8.4 Conclusions

In this chapter, we have comprehensively investigated possible mechanisms of the first hydrogen release from the novel and intriguing composites, poly acrylamide-

confined ammonia-borane (PAM-AB) with and without metal halides additives. Our calculations were based on the simplified models composed of CH_3CONH_2; NH_3BH_3 and metal halides including MgF_2, $MgCl_2$, $CaCl_2$, ZnF_2 and $ZnCl_2$.

It was experimentally observed that these metal halides effectively lower the dehydrogenation temperature as compared to neat AB and successfully suppressed NH_3 release. Our models have succeeded in explaining these observations. Our calculations based on these models have showed that the presence of the metal halides helped impressively lower the activation barrier of the hydrogen release step. Metal halides act as Lewis acid, thus they can bind with the nitrogen atom of the $CONH_2$ group. This binding, in turn, breaks the conjugation between the electron pair on the nitrogen of the NH_2 and the CO groups. This breakage opens the way for the facile addition of NH_3 onto the carbon of the carbonyl group to form a zwitterion. As a result, the proton of the NH_3 group gains its acidity, thus readily combines with one hydride of BH_3 group to release a H_2 molecule. In particular, we have suggested another two possible metal halides such as ZnF_2 and MgF_2.which are possibly more effective in facilitating the hydrogen release than the other three experimentally examined metal halides including $MgCl_2$, $ZnCl_2$, and $CaCl_2$.

Finally, we have systematically examined the effects of varied carbonyl and thionyl-based compounds on the dehydrogenation of ammonia-borane. Notably, our results have indicated that employing thionyl-based compounds might help lower the dehydrogenation temperature since these compounds indeed lowered the activation barriers.

The findings in this chapter not only shed light on the dehydrogenation mechanism of the synthesised composite but also provided some helpful suggestions on other possible better composites that may release H_2 at lower temperature. Thus, it paves the way for future synthesis of composites with better dehydrogenation properties.

References

[1] Graetz, *J. Chem. Soc. Rev*, vol. 38, p. 73, 2009.

[2] P. Chen and M. Zhu, *Mater. Today* , vol. 11, p. 36, 2008.

[3] J. Irvine, *J. Mater. Chem.*, vol. 18, p. 2295, 2008.

[4] M. Felderhoff, C. Weidenthaler, R. von Helmolt, and U. Eberle, *Phys. Chem. Chem. Phys.*, vol. 9, p. 2643, 2007.

[5] F. Baitalow, J. Baumann, G. Wolf, K. Jaenicke-Rossler, and G. Leitner, *Thermochim. Acta*, vol. 391, p. 159, 2002.

[6] G. Wolf, J. Baumann, F. Baitalow, and F. P. Hoffmann, *Thermochi. Acta*, vol. 343, p. 19, 2000.

[7] G. Wolf, J. C. van Miltenburg, and U. Wolf, *Thermochim. Acta*, vol. 317, p. 111, 1998.

[8] S. F. Li, Z. W. Tang, Y. B. Tan, and X. B. Yu, *J. Phys. Chem. C*, vol. 116, pp. 1544-1549, 2012.

CHAPTER 9

GENERAL CONCLUSIONS AND PERSPECTIVES

A thirst for energy to fuel the rapid and robust development of our global economy has led to the over-exploitation and over-usage of our precious non-renewable natural resources such as fossil fuels. These on-going actions lead to the accelerated depletion of the global fossil fuel reserves which in turn give rise to serious climate changes, threatening the existence and future of mankind. Therefore, the search for other cleaner and more sustainable sources of energy is more important today than ever before. One such energy source is hydrogen, which is also the most abundant element in the universe; however numerous attempts to physically store hydrogen on board commercial vehicles have failed. Thus, the attention has now been shifted to the research of chemical hydrogen storage materials such as ammonia-borane, metal hydrides, intermetallic hydrides, etc; to be able to tap into the vast potential that hydrogen has as a long term energy source for man in the future to come.

Ammonia-borane, NH_3BH_3 (denoted as AB) has gained much interest as a promising candidate among other chemical hydrogen storage materials due to its high gravimetric hydrogen capacity (19.6 wt%). However, the chemical challenges for effective utilisation of AB as a practical hydrogen storage material remain great. One problem is that AB exhibits slow thermal kinetic behaviour below 100^oC, it also produces several detrimental volatile by-products which includes borazine $(HNBH)_3$

and diborane (B_2H_6) upon dehydrogenation. In view of these problems, tremendous efforts have been devoted to investigating the various possible approaches to further improve the dehydrogenation properties of ammonia-borane. Two current outstanding approaches are: (i) the integration of alkaline or alkaline earth metals to NH_3BH_3, resulting in the formation of metal amidoboranes such as $LiNH_2BH_3$, $Mg(NH_2BH_3)_2.NH_3$ and $LiBH_4.MgCl_2.NH_3$; (ii) the utilisation of polymer to confine ammonia-borane. Both these approaches have been reported to significantly improve the dehydrogenation properties of ammonia-borane. However, it must be noted that the detailed dehydrogenation mechanisms have not been fully understood, as such, the main aim of my thesis was to comprehensively investigate the dehydrogenation mechanisms of these novel compounds, to elucidate the role of metals and polymers in facilitating the hydrogen release process.

Density Functional Theory (DFT) calculations based on the hybrid functional, in conjunction with the 6-31+G(2d,p) basis set, were employed to determine the fundamental properties of those novel compounds which include their geometries, electronic and thermochemical parameters. All DFT calculations were performed using the Gaussian 09 suite of programs. For each system considered, the potential energy surface related to the hydrogen release has been systematically constructed, and thus the possible molecular mechanisms for hydrogen release from these compounds are now elucidated.

The results of my thesis have been implicitly organised into two main parts. The first part, comprising Chapter **4, 5** and **6**, concentrates on the investigation of the dehydrogenation mechanisms of various metal amidoboranes including $LiNH_2BH_3$,

$Mg(NH_2BH_3)_2.NH_3$ and $LiBH_4.MgCl_2.NH_3$. The second part, which includes Chapter **7** and **8**, deals with the dehydrogenation mechanism of an intriguing novel class of polymer-confined ammonia-borane.

For the first part of the thesis, we have examined the analogous two-step mechanisms that these metal amidoboranes could have undergone. The first step was a hydride transfer from the borane group to the ammonia group. The second step was the hydrogen release. It was shown that the first step is the rate-determining step, in other words, the hydride transfer step was the most important step. One interesting result that emerged from the study is the critical role that metals play in these investigated complexes; they were able to facilitate the hydrogen release step by carrying one hydride to another proton in close proximity. Thus, the temperature ranges for hydrogen release of these compounds are significantly lower as compared to ammonia-borane.

Apart from these metal amidoboranes, our mechanistic studies presented in the second part of the thesis revealed that novel amino borane-based polymers such as poly(methyl acrylate)-confined ammonia-borane and polyacrylamide-confined ammonia-borane are also very promising hydrogen storage candidates. We found that the carbonyl functional group was of utmost importance in the facilitation of the hydrogen release. Their capability of lowering the dehydrogenation temperature is based on totally different mechanisms from the metal amidoboranes. Initially, the carbonyl group aided in breaking the B-N bond of the AB molecule to reassemble the NH_3 and BH_3 groups into a zwitterion. This zwitterion carries both the positively and negatively charged groups, thus it is very active. Furthermore, it has a particular

structure that accommodates the interaction between the proton of the NH_3 group and the hydride of the BH_3 group. Consequently, the hydrogen release was readily achieved.

In an attempt to find suitable additives and design new materials to further improve the dehydrogenation properties of polyacrylamide-confined ammonia-borane, we have examined different metal halides such as $MgCl_2$, MgF_2, $ZnCl_2$, ZnF_2, $CaCl_2$, all of which are Lewis acids. Our calculated results have indicated that among these selected metal halides, MgF_2 and ZnF_2 seemed to be the better candidates for improving the dehydrogenation properties of this ammonia-borane based polymer.

Additionally, we have comprehensively investigated a numerous carbonyl and thinoyl-based groups such as amide, ketone, and chloride acid to find the most effective functional group in facilitating hydrogen release. Interestingly, we have found that there could be better materials for facilitating hydrogen release instead, such as thionyl-based polymers.

To recap all the results, our findings from Chapters **4** to **8** have shown that the system examined above have improved siginificantly the dehydrogenation properties of ammonia-borane through the two different mechanisms: (i) in the metal amidoboranes, that is, polarising the proton of the NH_3 group and the hydride of the BH_3 group. (ii) in the polymer-confined ammonia-borane, that is, forming the zwitterion to accommodate the interaction between the proton and the hydride.

Our present work constitutes a theoretical contribution to the study of the chemical properties and molecular mechanisms for hydrogen release of a number of

compounds based on ammonia-borane that possess very strong potentials for effective chemical hydrogen storage. It has provided a comprehensive understanding regarding the dehydrogenation mechanisms of these novel compounds; paving the way to further explore new compounds, which may possibly have better hydrogen release properties than those compounds investigated.

It should be duly noted that for the study done, the potential energy surfaces were mainly constructed from the enthalpies evaluated at 0 K. Also, the energy surfaces obtained correspond to only the gas phase situation. The effects of the liquid- or solid-state conditions are not fully taken into account. These would inevitably affect the results of situations that actually occur in reality, whereby other factors such as entropies, temperatures, and medium effects would have great significance on. Nevertheless, the intrinsic features that we have derived from the static potential energy surfaces in this study have already provided us with essential information pertaining to the outcome of the hydrogen release processes considered.

Our future work is to continue to investigate the above-mentioned systems; however, media effects will have to be incorporated to better explain the hydrogen release in real reaction. The perspectives opened from this work are essentially based on the above results, and these will definitely lead to many new avenues in future. The class of metal amidoboranes possess rich chemistry and still contain hidden mysteries yet to be uncovered; they should certainly be pursued further with more detailed studies and research. These further studies on the BH_3NH_3 system are necessary to find out its behaviour in different combinations with other metals. It would be interesting to investigate systematically the combination of ammonia-borane

with other possible alkaline and alkaline earth metals such as Na and Ca. These metal amidoboranes may then be incorporated into the polymers in the hope that the new compounds may inherit interesting properties of these two classes of compounds and produce a much better hydrogen storage material.